

Unsteady Flow and Force Development in the case of a Circular Cylinder

Pascal Gehlert

Department of Engineering
University of Cambridge

This dissertation is submitted for the degree of
Doctor of Philosophy

Declaration

I hereby declare that except where specific reference is made to the work of others, the contents of this dissertation are original and have not been submitted in whole or in part for consideration for any other degree or qualification in this, or any other university. This dissertation is my own work and contains nothing which is the outcome of work done in collaboration with others, except as specified in the text and Acknowledgements. This dissertation contains fewer than 65,000 words including appendices, bibliography, footnotes, tables and equations and has fewer than 150 figures.

Pascal Gehlert
July 2021

Abstract

Unsteady Flow and Force Development in the case of a Circular Cylinder

Pascal Gehlert

The time varying nature of many real flows has a strong effect on the resulting force experienced by aerodynamic bodies, where the transient force response can readily exceed the steady-state equivalent. This therefore poses a significant threat to small drones as well as larger aircraft that can be subjected to highly unsteady flow fields. Sensing the flow and using predictive modelling to mitigate the unsteady forces shows potential, yet requires a detailed knowledge of the aerodynamic principles at play. This work is a fundamental study into the underlying mechanisms involved in low Reynolds number unsteady aerodynamics to help facilitate future low order models (LOMs). Specifically, the focus is on the development of the unsteady force, by exploring the origin and evolution of boundary layer vorticity as well as the impact of free vorticity located in the flow.

Four sets of experiments are conducted in the towing tank facilities at the University of Cambridge using a rotating and translating circular cylinder as well as a flat plate. To capture the fluid dynamic response, force balance and planar particle image velocimetry (PIV) measurements are acquired in combination, at Reynolds numbers between 4000 and 20000. It is found that whilst the potential flow ‘added mass’ vortex sheet distribution around a stationary object immersed in an accelerating freestream is correct in shape, it ascribes the vortex sheet to the wrong origin. Instead, the vortex sheet is found to develop as a result of external vorticity that is created at the interface between the moving freestream and the quiescent surrounding. Moreover, the evolution of the boundary layer vortex sheet is investigated around a translating and rotating cylinder. The vortex sheet contributions due to kinematics and free vorticity are experimentally recovered. It is further proposed that the vortex sheet contribution due to free vorticity can be decomposed into a local and far-field component. Examining the vortex sheet strength at the unsteady separation point, which has been used in literature explicitly or implicitly to predict unsteady separation, shows that it is strongly affected by the instantaneous velocity, rotation rate and far-field vorticity. Accounting for these contributions collapses the strength of the vortex sheet at the unsteady separation point for the kinematics studied, even as the flow field evolves. In future this may provide avenues with which to predict unsteady separation. Furthermore, the rate at which vorticity sheds from the surface of an object is linked to the boundary layer vortex sheet components. When the unsteady separation point is known, this makes it possible to predict the vorticity shedding rate only from the motion kinematics and the boundary layer vortex sheet.

To minimise computational effort for LOMs, only the most dominant flow physics are ideally modelled. To help determine which flow features therefore need to be incorporated in an LOM, a methodology to approximate the force due to an individual flow structure is proposed. A study of a cylinder encountering a sharp-edged transverse gust explores the force caused by external vorticity located within the gust shear layers. The rigid shear layer assumption inherent in Küssner’s model is found to overestimate the related non-circulatory gust force. However, the discrepancy remains small compared to the total force.

I would like to dedicate this thesis to my loving family.

Acknowledgements

The author would like to sincerely thank Professor Holger Babinsky for his incredible support in all aspects of this work. From his breadth of knowledge, to his unerring patience and refreshing directness, making sure that my explanations were at least remotely understandable. I could have not wished for a better supervisor.

This project would have not come to where it is without the help of Dr Simon Corkery, whose technical insights were invaluable and who helped ensure that my experimental escapades did not result in a flooded lab. Also thank you to Dr Anya Jones and Dr Will Graham for the helpful technical discussions. Thank you to all the aero-lab technicians for not despairing at my many odd design choices and for always providing a helping hand. To all my lab mates, thank you for brightening up every day, whether in the office, the lab or at conferences, through jokes, witty comments or helpful advice. A special thank you to Ignacio Andreu Angulo, for the many fruitful conversations and the time spent together in the lab.

I also need to say a tremendous thank you to my parents for their unwavering support, enduring my moods and for always being there no matter what! And finally, thank you to the kindest, most understanding medic, for being there along the way.

The author also wishes to acknowledge the Engineering and Physical Sciences Research Council (EPSRC) for providing financial support.

Table of contents

List of figures	xv
List of tables	xxi
Nomenclature	xxiii
1 Introduction	1
1.1 Motivation	3
2 Literature Review	5
2.1 Steady and Unsteady Aerodynamics	5
2.2 Potential Flow	7
2.2.1 Vortex Sheets	8
2.3 Unsteady Forces	11
2.3.1 Bernoulli Equation	11
2.3.2 Vortex Force	12
2.3.3 Impulse Method	14
2.3.4 Advanced Force Formulations	15
2.4 Low Order Models	15
2.4.1 Added Mass - Non-Circulatory Force	16
2.4.2 Küssner's Model - Transverse Gust	17
2.5 Predicting the Unsteady Separation Point	20
2.5.1 Leading Edge Suction Parameter	21
2.5.2 Vorticity as a Proxy for Unsteady Separation	23
2.6 Vorticity Shedding Rate	24
2.7 Circular Cylinder	26
2.8 Summary: Literature Review	27
2.9 Approach and Aims	28
3 Experimental Methodology	31
3.1 Towing Tank Facility	31

3.2	Force Measurements	32
3.2.1	Errors	33
3.3	Particle Image Velocimetry	34
3.3.1	Implementation	34
3.3.2	Errors	36
3.4	Experimental Set-Ups	38
3.4.1	Cylinder	38
3.4.2	Multi-Body - Cylinder + Plate	42
3.4.3	Scoop	43
3.4.4	Gust Rig	44
3.5	Measuring the Boundary Layer Vortex Sheet	46
3.6	Summary: Experimental Methodology	47
4	Boundary Layer Evolution	49
4.1	The Boundary Layer Vortex Sheet: A Theoretical Overview	49
4.1.1	γ_{am}^{nc} and γ' : Vortex Sheets due to Kinematics	50
4.1.2	γ^{shed} : Vortex Sheet due to Shed Vorticity	54
4.1.3	γ_{ext}^{nc} : Vortex Sheet due to Externally Generated Vorticity	57
4.1.4	Summary	60
4.2	Experimental Study: Vortex Sheet due to External Vorticity	60
4.2.1	Flow Velocity Impinging on Stationary Plate	62
4.2.2	Recovering the Vortex Sheet Contribution	64
4.2.3	Summary	67
4.3	Evolution of the Boundary Layer Vorticity and its Contributions	67
4.3.1	Surge Only, Case c0	68
4.3.2	Translation and Rotation, Case c2, $\alpha = 2.5$	72
4.3.3	Scaling the Boundary Layer Vortex Sheet Strength	76
4.3.4	Translation and Rotation, Case c1a, $\alpha = 1$	78
4.3.5	Comparison of Vortex Sheet Strength at Separation	80
4.3.6	Summary	80
4.4	Summary: Boundary Layer Evolution	81
5	Vorticity Shedding	83
5.1	Vorticity Flux and Shedding Rate in Terms of Vortex Sheet Contributions	83
5.2	Experimental Investigation into Cylinder Vortex Shedding	88
5.2.1	Measuring the True Shedding Rate	88
5.2.2	Shed Circulation Prediction	88
5.2.3	Rate at which Vorticity is Shed	90
5.2.4	Exploring the Evolution of the Vorticity Shedding Rate	91

5.3	Summary: Vorticity Shedding	92
6	Flow Patterns and Force Generation	95
6.1	Alternate Vortex Shedding and Lift Generation	95
6.2	Prandtl and the Theoretical Maximum Lift	99
6.3	Summary: Flow Patterns and Force Generation	100
7	Unsteady Force Contributions	103
7.1	Unsteady Force Decomposition	104
7.2	Experimental Force Isolation	110
7.2.1	Force on an Individual Object - Experimental Implementation	111
7.2.2	Cylinder in Isolation	112
7.2.3	Circular Cylinder in Vicinity of a Small Flat Plate Wing	114
7.2.4	Circular Cylinder in Vicinity of a Large Flat Plate Wing	115
7.3	Summary: Unsteady Force Contributions	117
8	Cylinder-Gust Encounter	119
8.1	Introduction	119
8.2	Theoretical Sharp-Edged Gust Encounter	120
8.2.1	Flat Plate	120
8.2.2	Circular Cylinder	122
8.2.3	Accounting for further Gust Idealization	125
8.3	Experimental Gust Encounter	127
8.3.1	Recovering the Cylinder Gust Vortex Sheet	127
8.3.2	Non-Circulatory Gust Force	131
8.4	Summary: Cylinder-Gust Encounter	134
9	Conclusions and Future Work	135
9.1	General Comments	135
9.2	Boundary Layer and Free Vorticity	136
9.3	Unsteady Force Response	137
9.4	Recommendations and Future Work	138
	References	141
	Appendix A Reconciling Force Calculations with Legacy Theory	147
A.1	Steady Flow: Kutta-Joukowski Lift	147
A.2	Accelerating Flow	149

List of figures

1.1	Turbulence intensity in the atmospheric boundary layer. After [62, 97].	1
1.2	Examples of MAVs.	2
2.1	Different flow states about an aerofoil section.	5
2.2	The unsteady force fluctuates, whilst the steady-state force remains invariant in time.	6
2.3	A boundary layer around a flat plate can be replaced by an infinitely thin vortex sheet.	9
2.4	Circulatory vortex sheet due to shed vorticity and non-circular contributions due to translation and external vorticity.	10
2.5	Counter-rotating potential vortex pair.	13
2.6	Approximation of the steady-state flow field around a surging wing and its starting vortex.	13
2.7	A real flow field comprises of many individual sources of vorticity rather than just a counter-rotating vortex pair.	14
2.8	Broken-line theory used to represent a flat plate entering a sharp-edged gust.	18
2.9	The Küssner force and its constituent parts. After von Karman and Sears [96] and adapted from Corkery [14].	19
2.10	Schematic illustration of an aerofoil together with its velocity components and the pitching location. The camber distribution $\chi(x)$ and a LEV and TEV are also indicated. The induced velocity components $\frac{\partial\Phi_{TEV}}{\partial x}$ and $\frac{\partial\Phi_{TEV}}{\partial y}$ from the TEV feature as well. \dot{h} is the plunge velocity, U the instantaneous velocity, β the angle of attack and ac the distance from the leading edge to the pivot location.	22
2.11	Schematic illustration of how the LESP is implemented in a panel method code to determine when vorticity is shed from the leading edge.	23
2.12	Accumulation of circulation within the LEV, fed by the separating shear layer.	25
3.1	Towing tank.	31
3.2	Overview of the experimental set-ups.	32
3.3	Force balance.	33
3.4	Schematic illustration of a generic PIV set-up.	34
3.5	Overview of experimental set-up.	35

3.6	Missing velocity vectors can be accounted for by assigning the boundary condition to the cylinder and interpolating between the measured flow field and cylinder surface velocity.	36
3.7	Cylinder assembly.	38
3.8	Experimental set-up.	39
3.9	Experimental set-up in the water tank.	39
3.10	Experimental configurations. The angle definition around the cylinder is also indicated.	40
3.11	Kinematic profile of the cylinder. Case c3a, $Re = 20\,000$, $\alpha = 3$	41
3.12	C_l when an endplate two times the cylinder diameter and when no endplate is fitted. .	41
3.13	Schematic illustration of the cylinder and plate assembly.	42
3.14	Experimental set-up.	42
3.15	Scoop and stationary plate arrangement.	43
3.16	PIV top view.	43
3.17	Experimental set-up.	44
3.18	Gust flow field.	45
3.19	‘Wedge’ discretization used to compute γ^b	46
3.20	Schematic illustration showing how shed vorticity can incorrectly be associated with γ^b .	47
4.1	Vortex sheet contributions.	50
4.2	Vortex sheet distribution around a translating cylinder. Non-dimensionalizing with instantaneous velocity collapses the vortex sheet strength.	51
4.3	Coordinate transformation mapping a plate onto a cylinder.	53
4.4	Theoretical vortex sheet due to translation and rotation for a flat plate.	54
4.5	Calculating the vortex sheet due to free vorticity.	55
4.6	Uniform freestream induced by a pair of counter-rotating vortices around a stationary cylinder. The complex potentials $(F_1(z), F_{1,m}(z), F_2(z), F_{2,m}(z))$ for each vortex are indicated.	58
4.7	Non-circulatory added mass vortex sheet for a surging plate.	61
4.8	Schematic illustration of a translating scoop creating an accelerating flow field around a stationary plate.	62
4.9	Normalised vorticity field used to calculate the velocity at the plate. Scoop has moved $s/c = 1$	63
4.10	u -velocity component recovered by considering only vorticity along the scoop edge, normalised by final scoop translation velocity. $s/c = 1$. Contours are from -1.5 to 1.5.	63
4.11	Velocity trace comparison between the <i>effective</i> velocity impinging on the flat plate, recovered from the vorticity created at the interface between the quiescent and accelerated flow field, to the <i>scoop</i> and <i>idealised</i> velocity profile. The shaded area indicates scoop acceleration.	64
4.12	Vorticity contours and vortex sheet development.	65

4.13	Averaged vortex sheet due to external scoop vorticity compared to the theoretical added mass distribution.	66
4.14	Schematic illustration showing how external vorticity within the wind tunnel wall boundary layer or the gust shear layers is included in the field of view. If treated incorrectly, this may result in the wrong force prediction by an LOM.	67
4.15	Normalised vorticity contours as the cylinder translates, case c0.	69
4.16	Flow field and vortex sheet shortly after the cylinder has begun to surge.	69
4.17	Evolution of γ^b , case c0. Line colour changes from red to blue as s/D increases. Circles and triangles mark the unsteady separation point on the lower and upper cylinder surface.	70
4.18	γ_{am}^{nc} recovered experimentally and compared to the theoretical distribution.	71
4.19	Evolution of γ^b at the separation point.	71
4.20	Vorticity contours as the cylinder translates from right to left, case c2.	72
4.21	Boundary layer vortex sheet and constituent parts. Circles mark the separation point. Line colour transitions from red to blue with increasing s/D	73
4.22	Effect of local and far-field vorticity.	74
4.23	Variation of $\gamma_{far-field}^{shed}$ and γ_{local}^{shed} as a vortex moves away from the cylinder.	75
4.24	Schematic illustrating the calculation of $\gamma_{far-field}^{shed}$	76
4.25	Line colour transitions from red to blue with increasing s/D . Circle marks the separation location. Case c2.	76
4.26	Evolution of the adjusted boundary layer vortex sheet and its strength at the separation point, case c2.	77
4.27	Normalised vorticity contours as the cylinder begins to translate and rotate. Case c1a.	78
4.28	Circles and triangles indicate the separation point. s/D increases in steps of 0.5 as the line colour changes from red to blue. Case c1a.	79
4.29	Development of uncorrected and adjusted vortex sheet strength at separation point for all kinematic cases. Legend applies to both graphs, where hollow symbols correspond to the raw strength.	80
5.1	Schematic illustration of a boundary layer that forms along a wall and subsequently separates.	84
5.2	Schematic illustration of the boundary layer velocity profile and vorticity an infinitesimal distance upstream and downstream of the separation point.	86
5.3	Schematic illustration of the dependency of $\dot{\Gamma}_{shed}$ on the surface vortex sheets.	87
5.4	Relationship between boundary layer velocity and vorticity on either side of a spinning cylinder subjected to incoming flow.	87
5.5	Schematic illustration of how Γ_{shed} is calculated.	88

5.6	Comparison of computing Γ_{shed} by using the <i>vortex sheet method</i> and by directly interrogating the vorticity field. Shaded regions identify the difference between the two <i>alternative</i> measurement techniques. Legend applies to both figures.	89
5.7	Absolute rate at which vorticity is shed into the flow.	90
5.8	Schematic illustration showing positive vorticity located at ‘infinity’ reducing the shedding rate by lowering γ^b	91
5.9	Raw and adjusted rate at which vorticity is shed. Absolute values are plotted. . .	92
6.1	Schematic representation of the flow field around a surging cylinder. Simplified distributions of γ^b and γ^{shed} are also shown. Numbers indicate the corresponding time steps.	96
6.2	Flow field and γ^b and γ^{shed} development for a surging and clockwise rotating cylinder. Each number corresponds to one instance in time, with the colours matching accordingly.	98
6.3	Vortex at infinity of strength $\Gamma = 4\pi Ua$ causes $\gamma^b = \gamma^r$, theoretically leading to $\dot{\Gamma}_{shed} = 0$	100
7.1	Deflection of gust shear layer as a cylinder approaches.	104
7.2	Schematic illustration of a flow field containing a translating cylinder as well as cylinder-shed ω^{shed} and external vorticity ω^{ext}	105
7.3	Time variation of γ_{ext}^{nc} and deflection of a free vortex as this passes by a cylinder. . . .	110
7.4	Schematic illustration of the tempting (yet incorrect) approach to calculate the force acting on a single object, part of a multi-body flow field, by only considering the impulse created by the vorticity associated with the individual object.	111
7.5	Schematic illustration of a flow field grouped into two sections, one encompasses cylinder related vorticity ω^{cyl} and a second includes only external vorticity ω^{ext} . . .	112
7.6	Vorticity contours around a translating cylinder, case m1.	113
7.7	Force history, case m1.	113
7.8	Vorticity contours of the cylinder and plate, case m2. The dashed line marks the region within which vorticity is associated with the cylinder.	114
7.9	Force history, case m2.	115
7.10	Vorticity contours of the cylinder and plate, case m3. The dashed line marks the region within which vorticity is associated with the cylinder.	116
7.11	Force history, case m3.	117
8.1	Flat plate sharp-edged gust encounter. Note that even for infinitely thin gust shear layers, gust entry (and exit) takes place over one chord length.	120
8.2	Schematic illustration of a thin flat plate entering a gust and its $\gamma_{Küss}^{nc}$ distribution. . .	121

8.3	The non-circulatory vortex sheet created around a flat plate immersed in a transverse freestream is identical to the vortex sheet created by the mirror image of the vorticity residing within the gust shear layers.	122
8.4	Cylinder entering a rigid non-deforming gust.	123
8.5	Force coefficient contributions as the cylinder or plate intersects the rigid gust shear layers when entering and exiting a top-hat gust.	124
8.6	Schematic illustration indicating the change in transverse momentum as the cylinder enters the gust.	124
8.7	Variations of the gust shear layer: The velocity profile for the Küssner and smeared gust are indicated as well as the non-zero velocity outside the gust.	125
8.8	Effect of smeared gust shear layers.	126
8.9	Schematic illustration of a cylinder inside an idealised rigid top-hat shaped gust. . . .	127
8.10	Normalised vorticity field used to calculate γ^{shed} for case g1, $GR = 0.5$	128
8.11	Comparison between the theoretical and experimental distribution of γ_{gust}^{nc}	129
8.12	Flow field and non-circulatory gust vortex sheet γ_{gust}^{nc} as a result of extending the gust shear layers and masking any cylinder-shed vorticity. Case g1, $GR = 0.5$	130
8.13	Vorticity contours of a circular cylinder entering a top-hat shaped gust at $GR = 0.5$ (a-c), $GR = 1.0$ (d-f), $GR = 1.5$ (g-i).	131
8.14	Theoretical and experimental forces acting on the cylinder.	132
A.1	Schematic illustration of the steady-state flow field. A single vortex has been shed to infinity and a uniform freestream is induced by two external vortices.	148
A.2	Schematic illustration of the flow field due to an external vortex pair that induces uniform freestream at the location of the cylinder.	149

List of tables

- 3.1 PIV measurement error estimation (in pixels), using work by Raffel et al. [72] and Nobach and Bodenschatz [64]. 37
- 3.2 Summary of the test cases. s_{acc} represents the acceleration distance and $s_{\Omega_{\infty}}$ the distance required to reach terminal angular velocity, Ω_{∞} 40
- 3.3 Overview of multi-body test cases. 43
- 3.4 Summary of the cylinder-gust cases. 46

Nomenclature

Acronyms

EP	Endplate
GR	Gust ratio
LE	Leading edge
LESP	Leading edge suction parameter
LEV	Leading edge vortex
LOM	Low order model
MAV	Micro aerial vehicle
PIV	Particle image velocimetry
RMS	Root mean square
RPM	Revolutions per minute
TEV	Trailing edge vortex

Greek Symbols

χ	Camber line
$\dot{\Gamma}_b$	Boundary layer vorticity flux
γ_{gust}^{nc}	Non-circulatory gust vortex sheet
ω^b	Boundary layer vorticity
ω^{ext}	Externally created vorticity
ω^{shed}	Shed vorticity
α	Rotation ratio

β	Angle of attack
δ	Boundary layer height
δw_{gust}	Gust shear layer width
δ_2	Momentum thickness
δ_3	Energy thickness
$\dot{\Gamma}$	Vorticity flux / Time rate of change of circulation
$\dot{\Gamma}_{shed}$	Shedding rate of circulation
ϵ_{bias}	Bias PIV error
ϵ_{rms_0}	PIV error due to variation in particle diameter
ϵ_{rms_δ}	PIV error due to particle displacement
ϵ_{rms_ρ}	PIV error due to particle density
ϵ_{rms_i}	PIV error due to variation in particle intensity
ϵ_{PIV}	PIV error
Γ	Circulation
γ	Vortex sheet
γ_{sep}^b	Boundary layer vortex sheet strength at the separation point
γ^r	Vortex sheet due to rotation
γ_{sep}^r	Rotational vortex sheet strength at the separation point
γ^b	Boundary layer vortex sheet
γ^{nc+r}	Combination of added mass vortex sheet contribution (translation) and rotational component
$\gamma_{Küss}^{nc}$	Küsser's non-circulatory vortex sheet
γ_{am}^{nc}	Added mass vortex sheet
γ_{ext}^{nc}	Vortex sheet due to external vorticity
$\gamma_{gust:PIV}^{nc}$	Gust vortex sheet calculated from gust shear layer vorticity
$\gamma_{gust:PV\ extension}^{nc}$	Gust vortex sheet calculated from gust shear layers extended by point vortices

γ_{sep}^{nc}	Non-circulatory vortex sheet strength at the separation point
γ^{shed}	Vortex sheet due to shed vorticity
$\gamma_{far-field}^{shed}$	Vortex sheet due to shed vorticity located in the ‘far-field’
γ_{local}^{shed}	Vortex sheet due to ‘local’ shed vorticity
γ_{sep}^{shed}	Vortex sheet strength at the separation point due to shed vorticity
Γ_{∞}	Steady-state strength of a shed vortex
$\Gamma_{\text{advected past line}}$	Shed circulation computed by integrating vorticity advected past line
$\Gamma_{\text{sum flow field}}$	Shed circulation computed by integrating vorticity field
Γ_{ext}	Strength of an <i>externally</i> created vortex
Γ_{shed}	Shed circulation
κ	Doublet strength
μ	Dynamic viscosity
ν	Kinematic viscosity
Ω	Angular velocity
ω	Vorticity
Ω_{∞}	Steady-state angular velocity
$\bar{\Gamma}_{shed}$	Adjusted shedding rate of circulation
$\bar{\gamma}^b$	Adjusted boundary layer vortex sheet
$\bar{\gamma}_{sep}^b$	Adjusted boundary layer vortex sheet strength at the separation point
Φ	Potential function
ϕ	Angle from horizontal to a point in space
ψ	Streamfunction
ρ	Density
θ	Radial cylinder surface position
ζ	Position in the complex plane, $\zeta = \varepsilon + i\eta$

Roman Symbols

\dot{h}	Plunge velocity
\dot{U}	Acceleration
\mathbf{F}	Force vector
\mathbf{U}_b	Body velocity vector
B_b	Body boundary
F_i	Inertial force
$G(s/c)$	Küssner function
I_{ext}^{nc}	Impulse created by vortex sheet due to external vorticity
I^{cyl}	Impulse created by cylinder vorticity
I_{gust}^{nc}	Impulse created by non-circulatory gust vortex sheet
R_b	Region associated with body
R_{cyl}	Region associated with cylinder
R_{ext}	Region associated with external vorticity
R_{plate}	Region associated with plate
R_{wing}	Region associated with wing
S	Suction
U_b	Body velocity in x -direction
U_{γ^b}	u -velocity field induced by the boundary layer vortex sheet
$U_{\omega^{ext}}$	u -velocity field induced by external vorticity
$U_{\omega^{shed}}$	u -velocity field induced by shed vorticity
U_{cyl}	u -velocity field induced by cylinder vorticity
U_{field}	u -velocity field
V_x, V_y	Voltage in x and y -direction
$W(x, t)$	Downwash function

\mathbf{e}_n	Normal unit vector
\mathbf{F}_a	Aerodynamic force
\mathbf{I}	Impulse
\mathbf{n}	Normal vector
\mathbf{r}	Position vector
\mathbf{u}	Velocity field
$\widehat{C}_{l\text{Küssner}}^{nc}$	Uncorrected non-circulatory Küssner force
a	Cylinder radius
A_0	Fourier coefficient from linear thin airfoil theory, equivalent to the LESP
A_0 to A_k	Fourier coefficients in thin airfoil theory
ac	Distance from leading edge to pivot point
B_L	Fluid domain boundary
B_{LEV}	Boundary enclosing LEV
c	Chord length
C_d	Drag coefficient
C_l	Lift coefficient
D	Cylinder diameter
d	Distance
$F(z)$	Complex potential
$F_1(z), F_2(z)$	Complex potential due to free vortices
F_n	Normal force
F_s	Suction force
F_x	Force in the x -direction
F_y	Force in the y -direction
$F_0(z)$	Complex potential representing freestream about a cylinder

$F_{1,m}(z), F_{2,m}(z)$	Complex potential due to mirror vortices
F_{am}	Added mass force
$F_{ref}(z)$	‘Reference’ complex potential
H_{32}	Modified shape factor used to predict unsteady separation
I^b	Impulse due to boundary layer vortex sheet
I^{ext}	Impulse due to external vorticity
I^{shed}	Impulse due to shed vorticity
I_x, I_y	Impulse in the x and y -direction
I_y^{nc}	Impulse in y -direction due to the non-circulatory vortex sheet created by external vorticity
L	Lift force
L_{ext}	Lift force created by a region of external vorticity
m	Parameter related to boundary layer shape
m_{us}	Unsupported mass
p	Pressure
R_L	Region associated with fluid
R_{el}	Region associated with an element of vorticity
Re	Reynolds number
s	Translation distance
s_n	Segment length
s_{acc}	Acceleration distance
t	Time
U	Translation / free-stream velocity
u	Velocity in x -direction
u_θ^b	Average boundary layer velocity
U_∞	Steady-state translation / free-stream velocity

u_θ	Tangential velocity
u_θ^e	Boundary layer edge velocity
u_θ^{cyl}	Cylinder wall velocity
U_n	Normal velocity
U_b	u-velocity component of a travelling body
V	Transverse gust velocity
v	Velocity in y-direction
V_{cyl}	Cylinder volume that has entered gust
V_{init}	Transverse velocity upstream of first gust shear layer
w	Velocity in z-direction
z	Position in the complex plane, $z = x + iy$
z_{mir}	Complex position of mirror vortex
C_l^{fb}	Lift coefficient measured by force balance during gust encounter
$C_{l_{Küssner}}^{nc, smeared}$	Lift coefficient associated with non-circulatory gust force assuming smeared gust shear layers
C_l^{nc}	Lift coefficient associated with non-circulatory gust force
$C_{l_{Küssner}}^{nc}$	Corrected non-circulatory Küssner force
$C_{l_{gust}}^{nc}$	Lift coefficient associated with experimentally recovered non-circulatory gust force
$C_{l_{\delta V_{cyl}}}^{nc}$	Lift coefficient associated with body volume effect

Chapter 1

Introduction

Aerodynamics has come a long way since the milestone endeavours pioneered by Otto Lilienthal [52, 104] and the Wright Brothers [13], who first developed heavier-than-air flight in their quest to satisfy the ambition of non-ground-bound mobility. Since then, aerodynamic designs have become ever more complex and intricate. New innovations have focused on the big as well as the small, with large aircraft such as the Airbus A380 at one end of the spectrum and miniature micro aerial vehicles (MAVs) at the other. These technological advances have come hand in hand with significant steps in aerodynamic understanding, in particular in regards to steady-state flight, experienced during cruise for example. Unfortunately, aerodynamic flow fields are not always time invariant but can instead change extremely quickly. To make matters worse, the unsteady or time-varying nature of the flow is not confined to the fringes of the aerodynamic envelope but it is ubiquitous in the world around us, from cricket or footballs exhibiting a highly variable flight path if thrown or struck correctly to the dynamic flow contained within the atmospheric boundary layer. In the latter, the variation in velocity at each instance in time (turbulence intensity) can be as high as 50 % in rough city terrain as shown in figure 1.1. The main concern that comes from such rapidly changing flows is that they can create a

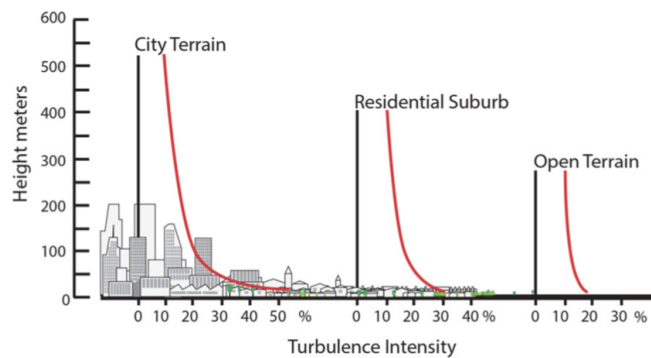
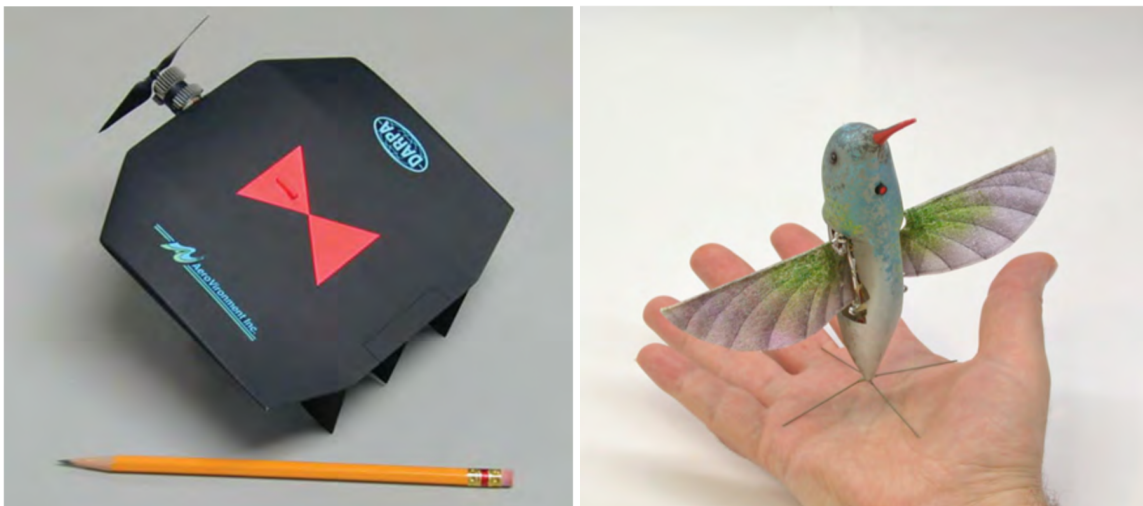


Fig. 1.1 Turbulence intensity in the atmospheric boundary layer. After [62, 97].

highly dynamic loading on any immersed object or structure, whilst at the same time, the increased

complexity makes them considerably more difficult to understand and model. As such, wind or water turbines can suffer from fatigue failure due to dynamic loading created by fluctuating incoming velocities and may even need to be turned off to avoid damage in especially gusty conditions, when the most energy could otherwise be created [35]. Similarly to the unsteady dynamics observed around turbines, transient flow also affects full scale aircraft. To avoid a sudden loss of control created by the quickly varying flow within an aircraft wake, long landing intervals are required at airports, to not put human life at risk. Moreover, novel lightweight, large-span drones such as the Aquila Facebook project, are also subjected to the risks posed by quickly varying flows. This was experienced first hand when then Aquila drone crashed after encountering a gust whilst approaching its landing site during its maiden flight [12].

A further area where an improved understanding of unsteady aerodynamics is of particular interest is MAVs. Their autonomous capabilities make them ideal candidates for reconnaissance without risking human lives in disaster relief efforts, surveillance, observing wildlife as well as in the future of goods delivery. Since each use case benefits from a unique set of design variables to optimize performance, three main classes of MAVs have been developed: fixed wing, rotary and flapping wings. Examples of a fixed wing and flapping wing drone are shown in figure 1.2. Unfortunately, the size and flight speed of MAVs make them extremely susceptible to unsteady effects, where their mission profiles are compromised by having to fly in aerodynamically ‘dirty’ environments [98, 99, 101]. The effect of such flow variations is further amplified due to the high relative ratio between the velocity of the flow disturbance and the comparatively low speed at which MAVs fly [98]. Additional unsteady effects are created by rotary wing motion as well as by the rapid acceleration and deceleration of flapping wings.



(a) Fixed wing Black Widow [32].

(b) Flapping wing NanoHummingbird [39].

Fig. 1.2 Examples of MAVs.

Given the widespread impact of unsteady flow and the danger posed by the resulting variable force evolution, a next critical milestone to be reached in aerodynamics is an ability to confidently tackle and combat the time varying nature of fluid flows and the associated force response. An improved understanding of the physics involved opens the door for quick optimisation strategies, or alternatively creates a possibility to pre-emptively mitigate the forces created by gusts, thereby expanding the working range of aerodynamic objects. To achieve the almost instantaneous force prediction required for such endeavours, time expensive computational fluid dynamic simulations or experiments are understandably not viable approaches. Instead, low order models (LOMs) that represent the force response in form of simple equations are an alternative approach that enable real time force predictions. One approach to inform such models uses ‘artificial intelligence’ or ‘machine learning’ to develop simplified representations of the true flow field. The downside of this method is that it often acts like a black-box. Whilst the results are applicable to the data sets on which the models are trained, it is difficult to determine if and how the predictions may be applied to other scenarios. Alternatively, LOMs can be developed by distilling the flow physics to simpler, more tractable problems of only the most dominant contributions and solving each individually using aerodynamic theory. This enables rapid flow and force predictions, whilst retaining the ability to learn about the fundamental phenomena at play, and may therefore be a preferred alternative. For a successful implementation of this approach, a detailed knowledge of the underlying aerodynamic principles is key, since LOMs may only have access to basic flow properties and minuscule errors in modelling the flow can have large ‘butterfly’ effects that may render the final result inconclusive.

1.1 Motivation

The motivation for this research stems from the objective to better understand unsteady flow in order to inform gust mitigation strategies employed by LOMs for larger aircraft or small MAVs. By feeding an LOM flow field data, acquired by sensors scanning the flow to all sides of an aerodynamic flyer, a pre-emptive gust control methodology, counteracting the force spike, can be implemented. The main aim of this thesis is therefore to explore the key principles involved in the flow and force development of unsteady low Reynolds number aerodynamics, to provide a solid basis for the design of future LOMs. Moreover, the use case of sufficiently accurate LOMs may extend beyond real time gust control and may further enable rapid design and optimisation strategies for any geometry subjected to unsteady flow conditions. In addition, the fundamental nature of this research enables a more thorough understanding of the underlying principles of unsteady aerodynamics that can be used as building blocks for future advances. Due to the nascency of the field of research and the significant involved complexity, this thesis will restrict itself to strictly two-dimensional flow, in a bid to simplify the analysis and to enable a more clear view of the basic principles at play.

Chapter 2

Literature Review

2.1 Steady and Unsteady Aerodynamics

In steady aerodynamics, the flow field is considered to remain invariant in time. A common example of this is fully attached flow around a wing, as schematically shown in figure 2.1a. Alternatively, if variations about the mean are small, steady separation, as illustrated in figure 2.1c, can also often be approximated by a time averaged representation. In unsteady flow on the other hand, a significant evolution of the flow is observed and a strong time dependency is thereby introduced. This is particularly relevant at the low Reynolds numbers at which MAVs operate (below 70000), since the boundary layer on a wing remains laminar until the beginning of pressure recovery and is therefore prone to separating [53]. Examples of such unsteady phenomena can be the formation of a leading edge vortex (LEV) or trailing edge vortex (TEV), as shown in figure 2.1b. These vortices are created when the boundary layer leaves the wing surface from the leading or trailing edge and forms a separating shear layer, which rolls up into a vortical structure [109]. The vortices grow rapidly and detach from the surface, initiating a cascade of ever changing flow states [25], which under certain conditions may eventually asymptote to steady separation observed in figure 2.1c. Alternatively, and depending on the object geometry and the nature of the surrounding flow field, the unsteady dynamics may prevail indefinitely and vortices shed from either side of the object at regular intervals, establishing the commonly observed alternating shedding pattern downstream of bluff bodies [58, 68].

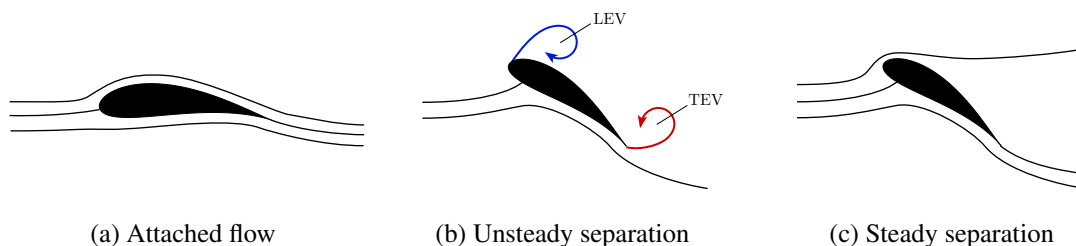


Fig. 2.1 Different flow states about an aerofoil section.

Further differences between steady and unsteady flow appear when closely examining the point at which the flow detaches from an object's surface. Prandtl [70] proposes that steady separation, in two dimensions and from a stationary surface, occurs when the skin friction at the surface approaches zero, whilst the separation point remains fixed. Moore [63], Rott [80] and Sears and Telionis [86] however suggest that this is no longer applicable for unsteady separation, where the separation point may move. Rather than using zero skin friction at the wall to indicate separation, they propose an MRS-criterion. This states that unsteady flow detachment occurs when the shear stress goes to zero somewhere within the fluid, whilst simultaneously the velocity parallel to the surface matches the speed of the separating structure.

Moreover, tied to the fluctuating nature of the flow field, the force response on an immersed object sees an equally variable time development, as schematically illustrated in figure 2.2. Kramer [41] is credited with being the first to document such unsteady force effects by studying dynamic stall on aerofoils. He noticed peak lift values which exceeded the maximum steady-state lift of an aerofoil when the flow direction in a wind tunnel was suddenly changed by a cascade of upstream slats. Whilst there was some initial criticism of his results by Francis and Cohen [28], who suggested that the force may have been affected by additional flow disturbances created by the moving slats, the significant overshoot in steady-state lift is nowadays a common observation, with a cohort of studies confirming Kramer's results [8, 27, 83].

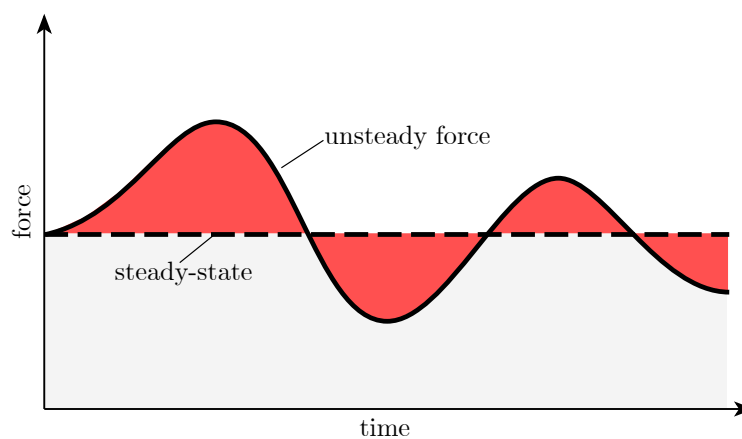


Fig. 2.2 The unsteady force fluctuates, whilst the steady-state force remains invariant in time.

Compared to steady-state flow, the transient nature of unsteady aerodynamics makes it significantly more difficult to model the flow as well as to predict its effect on any immersed objects. Yet, a thorough understanding of the concepts at play is crucial for a continued improvement and development of all aerodynamic fliers or structures that are subjected to such unsteady conditions.

2.2 Potential Flow

One approach to better understand unsteady flow and the related force response is to use potential flow theory, since it provides a simplified way to represent real viscous flow. At the same time, potential theory allows for analytical solutions, or alternative numerical formulations, that can be computed rapidly, and it is therefore also well suited for LOM applications. Potential flow itself is described by Anderson [3] as incompressible, inviscid and irrotational. For the use case throughout this thesis, where two-dimensional potential flow theory is relied on heavily, the constraint that the flow must be incompressible is met since the envisaged applications of this work are low speed flows, where the Mach number remains below 0.30, and density variations are therefore restricted to below 5% [3]. Thus, the related *continuity equation* reads

$$\nabla \cdot \mathbf{u} = 0. \quad (2.1)$$

\mathbf{u} represents the velocity vector field and may further be expressed as the gradient of the potential function Φ ,

$$\mathbf{u} = \nabla \Phi. \quad (2.2)$$

Combining equation 2.1 and equation 2.2 yields

$$\nabla^2 \Phi = 0. \quad (2.3)$$

Moreover, a streamfunction ψ can be defined that runs orthogonal to Φ . Its strength remains constant along a streamline and it can therefore be used to represent the instantaneous path taken by a particle. It is defined such that the volume flow rate passing between any two points is equal to the difference between the streamfunction $\Delta\Psi = \psi_2 - \psi_1$. From this it follows that if $d\mathbf{l}$ is a two-dimensional vector between two points and e_z is a unit vector in the z -direction,

$$\begin{aligned} d\psi &= \mathbf{u} \times d\mathbf{l} \cdot \mathbf{e}_z \\ &= u dy - v dx. \end{aligned} \quad (2.4)$$

As a result, the gradient of ψ in the x and y -direction gives the u and v velocity respectively,

$$\frac{\partial \psi}{\partial y} = u, \quad \frac{\partial \psi}{\partial x} = -v. \quad (2.5)$$

Furthermore, due to the flow being irrotational, the vorticity is expressed as

$$\boldsymbol{\omega} = \nabla \times \mathbf{u} = 0. \quad (2.6)$$

Inserting equations 2.5 into 2.6 yields,

$$\nabla^2 \psi = 0. \quad (2.7)$$

Equations 2.3 and 2.7 represent Laplace's equation, which is a second order, linear partial differential equation. The importance for the work within this thesis is that solutions to Laplace's equation may be linearly superimposed. This makes it possible to replicate the true flow field through a superposition of individual *potential flow elements*. As an example, a superposition of the streamfunction representing a uniform freestream as well that for a doublet of strength $\kappa = 2\pi Ua^2$, where U represents the instantaneous velocity and a the cylinder radius, recovers the streamlines about a cylinder. Likewise, free vorticity located in a viscous flow field can be represented by point vortices with potential and streamfunction

$$\Phi = \frac{\Gamma}{2\pi}\phi, \quad \psi = -\frac{\Gamma}{2\pi}\ln r, \quad (2.8)$$

where ϕ and r refer to a point in space in terms of radians and distance. Γ represents circulation and using Stokes theorem can be written as

$$\Gamma = \int \omega dA = \oint \mathbf{u} \cdot d\mathbf{l}. \quad (2.9)$$

Effectively Γ is a measure of the total sum of all vorticity contained within a closed loop [3]. It can either be obtained by directly 'adding' the vorticity within the domain multiplied by an elemental area dA or by integrating the velocity vector aligned with the vector segment $d\mathbf{l}$ of the bounding curve. Both of these methods will be used extensively throughout the thesis. For inviscid flow, Kelvin [40] showed that circulation is conserved if a loop is taken around a region of fluid and enforced to travel with the same fluid particles such that it may deform in time. In regards to viscous flow, circulation is conserved if the loop, enclosing a region of fluid, is taken such that it avoids crossing any regions where shear stresses are significant [51, 108].

Lastly, and used frequently throughout the thesis, a complex potential $F(z)$ can be formed by combining the potential and streamfunction according to

$$F(z) = \Phi + i\psi. \quad (2.10)$$

2.2.1 Vortex Sheets

On the surface of an object, the no-slip condition creates a shear stress acting on passing fluid elements. The fluid parcels are *rotated* by this shear force, through which a region of vorticity is created, commonly referred to as the boundary layer [3]. To represent such viscous boundary layers in potential flow, Saffman [81] describes that a discontinuous jump in velocity can be assumed to occur over an infinitesimally short distance, as to not violate irrotationality. This creates an infinitely thin approximation of the boundary layer in form of a vortex sheet,

$$\gamma = u_2 - u_1. \quad (2.11)$$

Its strength matches the vorticity distribution of the original viscous boundary layer and enforces the no-through flow condition at every position along its length, thereby itself becoming a streamline. As a consequence, any object can be represented by a vortex sheet γ^b located on its surface, as schematically illustrated for an infinitely thin flat plate in figure 2.3. The absence of any attributed *thickness* with this vortex sheet, however, means that it does not capture the wall normal distribution of vorticity that existed in the original boundary layer.

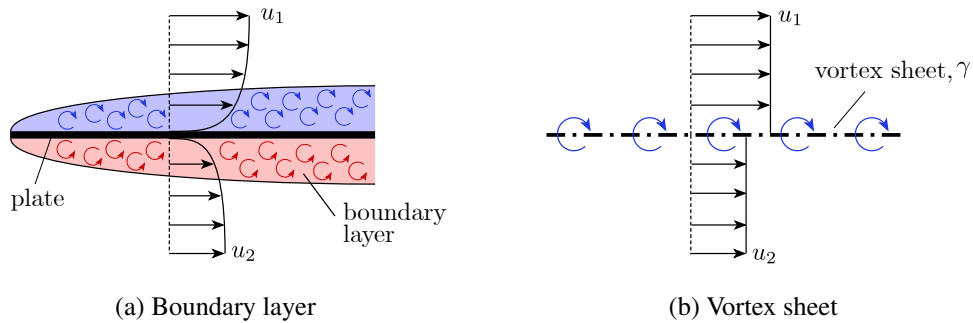


Fig. 2.3 A boundary layer around a flat plate can be replaced by an infinitely thin vortex sheet.

Potential flow theory models a true viscous flow field by superposing individual flow elements. This can be done by using a selection of singularities such as sinks, sources, doublets. To represent the flow field around a body surrounded by vorticity, Milne-Thomson [60] showed that in potential flow this can be modelled by representing free vorticity as point vortices and positioning corresponding ‘mirror’ vortices within the body. Thereby a streamline in the shape of the body is created and thus the no-through flow condition is enforced along its surface. Alternatively, Eldredge [23] or Graham et al. [31] suggest that the velocity at the location of the object, induced by the aforementioned singularities, can be viewed as a slip velocity, which can be associated with a vortex sheet.

To illustrate this general concept of superposition, let us imagine a flow around a translating and pitching plate, where vorticity sheds from the leading and trailing edges and rolls up into a respective LEV and TEV. In addition, some *external* vorticity that was created by an external mechanism also populates the flow field. This complex viscous flow can now be represented in potential flow by superposing several independent components. One contribution comes from the inviscid flow around a flat plate at an angle of incidence. A second component results from a rotating plate in inviscid quiescent fluid. To include the contributions due to free vorticity, we imagine a stationary flat plate surrounded by the LEV and TEV as well as the externally generated vorticity. As discussed above, Eldredge [23] and Graham et al. [31] now propose that each of these contributions create a slip velocity along the plate surface, and that the surface vortex sheet γ^b can therefore equally be imagined to consist of individual flow components. Each surface vortex sheet contribution is inextricably linked to the associated potential flow field component and the latter can be used to determine the former.

In the example of the plate, potential flow can be used to compute the slip velocity between the inviscid flow field and the moving plate surface. An *added mass* vortex sheet γ_{am}^{nc} is created by plate translation, as shown in the top left corner of figure 2.4. The net circulation of γ_{am}^{nc} is zero and it is therefore categorised as a *non-circulatory* vortex sheet. Initially, while the plate is at rest, γ_{am}^{nc} is zero everywhere. As the plate accelerates, the vortex sheet grows and, as will be later discussed, this development of the vortex sheet can be linked to an added mass force, thus giving the vortex sheet its name. Plate rotation creates a further slip velocity along the plate surface, resulting in an associated vortex sheet contribution γ^r . In contrast to γ_{am}^{nc} , the net circulation of γ^r depends on the body around which it forms. For an infinitely thin flat plate, the net circulation of the vortex sheet is zero, whereas it is finite for a body of volume, due to a need to conserve circulation. To verify that this ‘bookkeeping’ of the respective contributions to the total boundary layer vortex sheet is representative of the true viscous flow, Corkery et al. [16] showed that we can identify the same translational and rotational vortex sheet contributions in potential flow as well as experimentally.

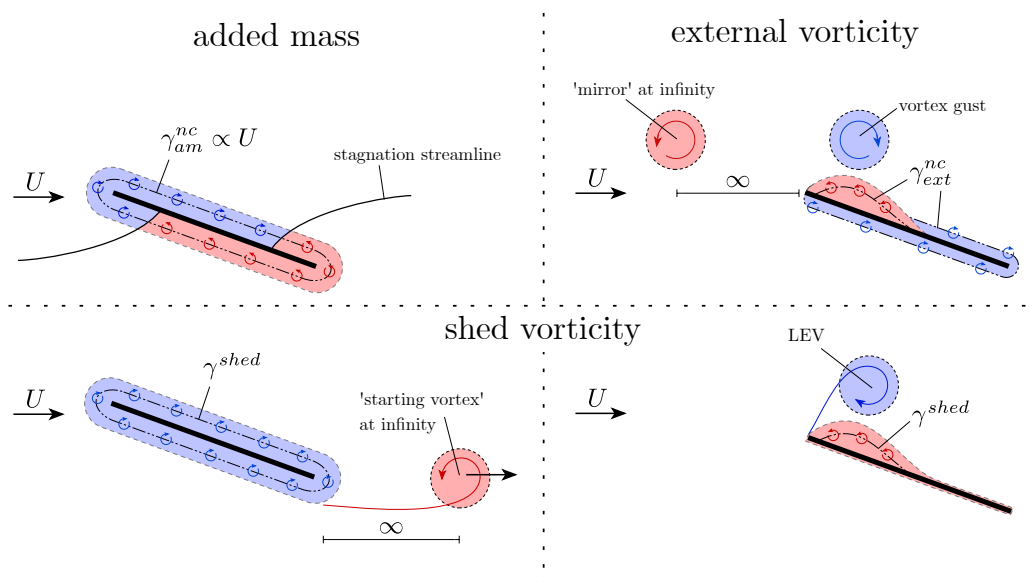


Fig. 2.4 Circulatory vortex sheet due to shed vorticity and non-circular contributions due to translation and external vorticity.

Vorticity shed from the leading and trailing edge leads to the development of an additional vortex sheet contribution γ^{shed} , as schematically illustrated in the lower half of figure 2.4. To conserve circulation within the complete flow field, vorticity of the opposite sign as that being shed needs to be located within the surface vortex sheet [40]. γ^{shed} can therefore be understood as a ‘mirror image’ of shed vorticity and since its net circulation is not necessarily zero, it is referred to as *circulatory*.

Similarly, if vorticity that was not originally shed by the plate is present in the flow, then this external vorticity generates a ‘mirror’ vortex sheet contribution γ_{ext}^{nc} on the plate surface [14], as shown in the top right of figure 2.4. Since in general, the global flow field is assumed to have zero net circulation (ie. equal parts of positive and negative circulation), it follows that the net circulation of external vorticity is also zero [40] and γ_{ext}^{nc} is therefore considered to be *non-circulatory*.

2.3 Unsteady Forces

Modelling the flow itself is often just a prerequisite to predict the forces acting on the object in question. Our focus therefore now shifts to methodologies devised to calculate forces from a flow field. The importance and relevance to the aerodynamics community has led to a large number of theories to be developed, with a short overview provided by Rival and van Oudheusden [77]. The approaches presented next are by no means an exhaustive list but aim to recognize the most important methodologies relevant to this work.

2.3.1 Bernoulli Equation

A classical and widespread approach to calculate the force using potential theory is to utilize the unsteady Bernoulli equation. It is used to recover the pressure field, which in turn is subsequently integrated around the surface of the object to evaluate the relevant forces. To derive the unsteady Bernoulli equation, we begin with classical aerodynamic theory. The equations of motions are given by the Navier-Stokes equations, which when written in vector form, where body forces are ignored, and applied to an infinitesimal small region of incompressible Newtonian fluid are

$$\rho \frac{D\mathbf{u}}{Dt} = -\nabla p + \mu \nabla^2 \mathbf{u}. \quad (2.12)$$

The scalar pressure field is represented by p and μ is the dynamic viscosity. In inviscid flow, $\mu = 0$ and equation 2.12 simplifies to the Euler equation

$$\rho \left(\frac{\partial \mathbf{u}}{\partial t} + \mathbf{u} \cdot \nabla \mathbf{u} \right) = -\nabla p. \quad (2.13)$$

By using equation 2.2, relating the velocity field \mathbf{u} to the potential function, as well as $\mathbf{u} \cdot \nabla \mathbf{u} = \frac{1}{2} \nabla |\mathbf{u}|^2$, since the flow is irrotational, the Euler equation can be re-written as

$$\nabla \left(\rho \frac{\partial \Phi}{\partial t} + \frac{1}{2} \rho |\mathbf{u}|^2 + p \right) = 0. \quad (2.14)$$

From this it follows that

$$\underbrace{\rho \frac{\partial \Phi}{\partial t}}_{\text{transient}} + \underbrace{\frac{1}{2} \rho |\mathbf{u}|^2}_{\text{dynamic}} + \underbrace{p}_{\text{static}} = f(t), \quad (2.15)$$

where $f(t)$ represents an arbitrary time dependent function. In the case of steady flow, the time variation of the potential is zero and the steady Bernoulli equation is

$$\frac{1}{2}\rho|\mathbf{u}|^2 + p = f. \quad (2.16)$$

In potential flow, the force acting on an object can now be found by evaluating the pressure p and integrating this around the surface of the object. In viscous flow, the Bernoulli equation is applicable in regions where the flow is irrotational. If the Reynolds number is sufficiently high, the boundary layer is thin and thus has a negligible effect on the curvature of the surrounding inviscid flow. The pressure on the body surface therefore closely matches that outside of the boundary layer and equation 2.15 can be used to compute the forces. Unsteady separation, where vorticity is transported away from the objects surface and into the outer flow via a separating shear layer, however, significantly affects the ability of this method to recover the forces.

2.3.2 Vortex Force

Monitoring the motion and strength of vortical filaments can provide an alternative method to compute the forces acting within a domain. This is because circulation can be linked to velocity using the Biot-Savart law, which in three-dimensions reads [81]

$$\mathbf{du} = \frac{\Gamma}{4\pi} \frac{\mathbf{dl} \times \mathbf{r}}{|\mathbf{r}|^3}. \quad (2.17)$$

\mathbf{du} represents the incremental velocity vector at a point in space, whilst \mathbf{r} is the vector from the vortex centre to this same location and \mathbf{dl} represents an element of the vortex filament. In two-dimensions, and applicable to the flow fields considered throughout this thesis, the Biot-Savart law simplifies to $u_\theta = \Gamma/(2\pi|\mathbf{r}|)$, where u_θ is the tangential velocity induced by the vortex. The velocity of the flow directly links to its momentum and thus the force can be computed by assessing the time variation of momentum. Lamb [46] shows that the momentum (or impulse) created by a pair of counter-rotating vortices of equal and opposite strength in two-dimensional flow, as shown in figure 2.5, is given by

$$I = \rho\Gamma d, \quad (2.18)$$

where d is the distance between the two vortices. The momentum of the fluid changes when these vortices move apart or when their strength is modified. The force F required to do so, is therefore the time rate of change of momentum, such that

$$F = \rho \left(\underbrace{\Gamma \dot{d}}_{\text{motion}} + \underbrace{d \dot{\Gamma}}_{\text{creation}} \right), \quad (2.19)$$

where the *dot* signifies differentiation with respect to time. The first term describes the force contribution created by the relative motion between the two vortices, whilst the second is due to a change in vortex strength.

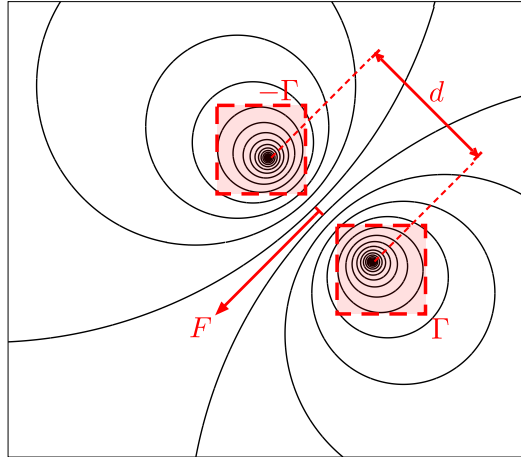


Fig. 2.5 Counter-rotating potential vortex pair.

As a simplified example, a wing at a small angle of incidence travelling at constant velocity, such that it has shed a starting vortex a long time ago, and where the flow is fully attached, can be represented by a pair of equal and opposite point vortices as shown in figure 2.6. From equation 2.19 it follows that a force is created when the distance between the wing and the starting vortex increases or when the strength of the point vortices changes. In steady flow, the strength of the point vortices is invariant ($\dot{\Gamma} = 0$), and the distance between them increases at the speed of the travelling wing ($\dot{d} = U$). The lift force acting on the wing is therefore

$$L = -\rho U \Gamma, \quad (2.20)$$

This recovers the commonly known *Kutta-Joukowski* lift force and in literature is referred to as *vortex lift* [69] or *circulatory lift* [90].

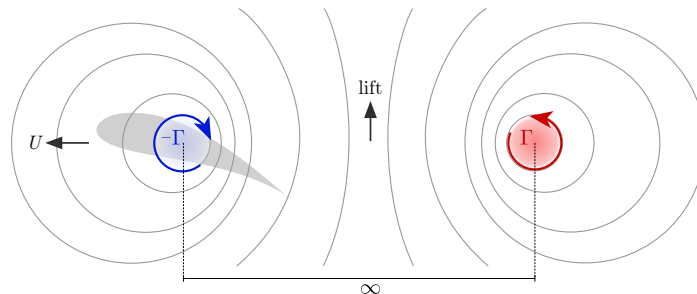


Fig. 2.6 Approximation of the steady-state flow field around a surging wing and its starting vortex.

2.3.3 Impulse Method

Under normal circumstances, a real flow field consists of more than a single counter rotating vortex pair and is instead populated by multiple distributions of vortical flow, as schematically illustrated in figure 2.7¹. The *impulse method* developed by Wu [107] extends the principles derived by Lamb [46] to a general theory that relates the forces acting within a fluid domain to the rate of change in position and strength of any contained vorticity. As such, the theory is applicable to inviscid as well as viscous flow with a discrete or continuous vorticity distribution.

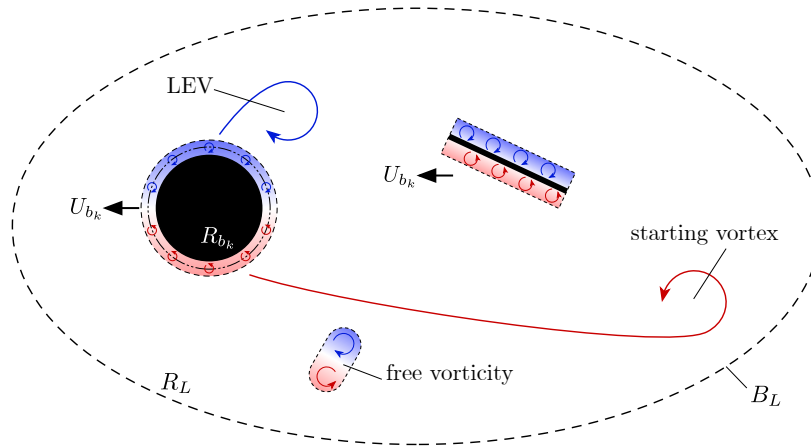


Fig. 2.7 A real flow field comprises of many individual sources of vorticity rather than just a counter-rotating vortex pair.

Wu assumes that the flow velocity at the domain boundary B_L approaches zero as well as that circulation is conserved, such that all vorticity contained within the enclosed region R_L sums to zero,

$$\int_{R_L} \omega dR = 0. \quad (2.21)$$

The domain can include an arbitrary number of bodies of area R_b , where each object is treated as a continuum with the surrounding fluid. When any objects sets into motion and travels at velocity \mathbf{U}_{b_k} , vorticity is assumed to develop in its boundary layer before eventually advecting into the surrounding flow. Rotation creates circulation, equal to twice the angular velocity due to body rotation, within the object. Moreover, since circulation must be conserved, boundary layer vorticity of the opposite sign is created along the surface. The aerodynamic force \mathbf{F}_a created within the domain is expressed as

$$\mathbf{F}_a = -\rho \left(\frac{d}{dt} \int_{R_L} \mathbf{r} \times \omega dR - \sum_{k=1}^N \frac{d}{dt} \int_{R_{b_k}} \mathbf{U}_{b_k} dR \right). \quad (2.22)$$

¹Any flow where the net circulation is zero can effectively be treated as an infinite sum of vortex pairs. The impulse approach could therefore be understood as an integral version of Lamb's [46] result.

The first term in equation 2.22 is the force due to *vortex moment* resulting from vortex motion and growth. The second term is a ‘force correction’ and stems from the assumption that fluid extends into each body. Acceleration of an object causes the fluid within it to accelerate to match the body velocity \mathbf{U}_{b_k} and thereby creates a contribution to the change in momentum. This is captured by the vortex moment (first term in equation 2.22) and thus needs to be removed, in order to recover the true aerodynamic force.

In its basic form, however, only the total force acting within the domain can be identified using the impulse method, rather than the contribution of an individual flow feature. Furthermore, it is also not possible to determine the force that acts only on a single object that is part of a multi-body flow field. Moreover, the formulation itself does of course not predict the development of the flow and can only be applied to flow field measurements or simulations, hence still requiring a predictive model to provide the input for the force calculation.

2.3.4 Advanced Force Formulations

Building on Wu’s formulation, Noca et al. [65, 66] limited the analysis to a finite domain by introducing surface integrals along a control volume boundary. However, the limitation remains that only the total force within the domain can be identified. Bai et al. [7] expand on this to recover the force acting on a single object within a multi-body flow system, whilst Kang et al. [38] take this further still. They propose a ‘minimum domain impulse theory’ to isolate the forces, using only a limited region of the flow field without the need for surface integrals along domain boundaries. Still however, this does not allow for an individual force contribution due to a specific flow phenomenon to be determined. Li and Wu [49] make progress in this respect by developing vortex maps that relate the force created by a vortex to its position and velocity. However, because the impact that this vortex has on the surrounding flow is neglected, this approach does not capture its complete effect.

2.4 Low Order Models

LOMs aim to model a flow using the least amount of information possible, in order to achieve fast computational speeds. By being sufficiently rapid and accurate, this enables real time control of MAVs and other aerodynamic flyers subjected to unsteady aerodynamic environments. In most cases, LOMs distil the physics and the governing equations into simpler, more tractable problems to meet these demands. Moreover, only the most dominant effects contributing to the force are included, in a bid to save computational resources. As such, the true flow field is often abstracted to the bare minimum that must be included; unfortunately however, identifying what these necessary parts are, is not always entirely obvious. One approach to construct a LOM is to split the force into a *circulatory* as well as into a *non-circulatory* component. Both contributions can subsequently be solved independently and are superposed thereafter. Whilst the circulatory component can be attributed to flow field

vorticity shed by the object itself, as discussed using the example of a wing and the starting vortex in section 2.3.2, the non-circulatory contribution is often related to an added mass force as well as recently, to external vorticity [14].

When calculating the total force by evaluating and combining a range of individual force contributions, it is crucial that we are aware of the true origin of each force component. Otherwise we may accidentally consider the same force multiple times. Therefore before we proceed, we will take a closer look at the historic understanding of the added mass force.

2.4.1 Added Mass - Non-Circulatory Force

The added mass force has been extensively discussed in the aerodynamics community since the beginning of the 19th century. Notable contributions include Green [33], Lamb [46], Darwin [18], Thompson [92], Blevins [10], Sarpkaya and Isaacson [85] and Brennen [11]. As its name suggests, the added mass force describes an increase in force required to accelerate an object when this is surrounded by a fluid compared to when it is accelerated in a vacuum. An intuitive explanation for this phenomena is provided by Darwin [18]. He proposes that as an object moves, it drags a region of fluid with it, which he refers to as the *drift volume*. To accelerate the object, an applied force must therefore not only accelerate the object itself but also the surrounding fluid.

Mathematically, the added mass force can be found from a kinematic or unsteady Bernoulli approach. In the following derivation, we follow the latter for the canonical case of an accelerating cylinder. In potential flow, we can represent a surging (forward moving) cylinder of radius a by a doublet, such that the cylinder surface potential reads

$$\Phi = Ua \cos \theta. \quad (2.23)$$

θ takes a value between 0 and 2π and describes a radial surface location measured counter-clockwise from the x -axis. From equation 2.23 it follows that the time derivative of the surface potential is

$$\frac{\partial \Phi}{\partial t} = \dot{U}a \cos \theta. \quad (2.24)$$

The static pressure on the cylinder surface can now be obtained by re-arranging the unsteady Bernoulli equation (2.15), such that

$$p = -\rho \frac{\partial \Phi}{\partial t} - \frac{1}{2} \rho |\mathbf{u}|^2 + f(t). \quad (2.25)$$

Integrating the pressure along the surface of the cylinder surface B_b gives the force \mathbf{F} acting on the cylinder

$$\mathbf{F} = - \oint_{B_b} p \mathbf{n} dl. \quad (2.26)$$

Here \mathbf{n} is a unit vector normal to the surface, $\mathbf{n} = \cos \theta + i \sin \theta$. Inserting equation 2.25 for pressure into our force expression (2.26) yields

$$\mathbf{F} = \rho \oint_{B_b} \left(\frac{\partial \Phi}{\partial t} + \frac{1}{2} |\mathbf{u}|^2 - \frac{1}{\rho} f(t) \right) \mathbf{n} dl. \quad (2.27)$$

Due to the symmetry of the problem, the second and third term on the right of equation 2.27 integrate to zero when evaluating the force in the x -direction. Likewise, the pressure forces cancel exactly in the y -direction, yielding zero lift force. Using the fact that $dl = a d\theta$, the drag force is given by

$$F_x = \rho a \int_0^{2\pi} \frac{\partial \Phi}{\partial t} \cos \theta d\theta. \quad (2.28)$$

Combining equation 2.24 with equation 2.28 ultimately yields the added mass force

$$F_x = \rho \pi a^2 \dot{U}. \quad (2.29)$$

The added mass force is therefore proportional to the acceleration rate, whilst the ‘added mass’ is equal to the cylinder volume. It is worth noting that it is not generally the case that the added mass matches the volume displaced by the object and this is merely a coincidence for the cylinder.

Of course, an added mass force is not unique to an accelerating cylinder. It exists equally for a flat plate; a geometry that is frequently used to model wings and thus a common geometry in unsteady models. Using the same approach as described above for the cylinder, Pitt Ford [69] derived the added mass force in the x and y -direction for an accelerating flat plate at an angle of attack β relative to the direction of acceleration,

$$F_x = \rho \pi \frac{c^2}{8} \dot{U} (1 - \cos 2\beta), \quad (2.30)$$

$$F_y = \rho \pi \frac{c^2}{8} \dot{U} \sin(2\beta). \quad (2.31)$$

The net force acts normal to the plate chord and once the forces and the velocity are resolved accordingly, yields

$$F_n = \rho \frac{\pi c^2}{4} \dot{U}_n, \quad (2.32)$$

where \dot{U}_n represents the acceleration in the chord normal direction. As before, the added mass force is directly related to body acceleration and this definition will be used rigorously throughout later parts of the thesis.

2.4.2 Küssner’s Model - Transverse Gust

Within the atmospheric boundary layer, there exist a large cohort of variations in flow velocity [98], created by natural turbulence or flow interactions with mountains, trees or skyscrapers, to name a few

examples. The force response created on a body is highly dependent on both the velocity distribution within these gusts as well as on the orientation at which they encounter the body. Watkins et al. [99] found that the most dangerous flow disturbance for MAVs is created by a transverse gust hitting a drone from above, since it creates significant unsteady loading that pushes the MAV into the ground.

A LOM which analytically approximates the force when a wing encounters a transverse gust is Küssner's model [43, 44], which employees a non-circulatory / circulatory force decomposition. To reduce the complex aerodynamics to a more tractable problem, a number of assumptions simplify the gust encounter. The wing is modelled by a flat plate at zero angle of incidence and any perturbations due to the transverse gust are assumed to be small. Moreover, the delimiting gust edges are considered to be infinitely thin and rigid, such that there is no coupled interaction between the plate and the gust. Ultimately, vorticity is assumed to only shed from the plate trailing edge, where it remains on the same horizontal plane and advects away at the freestream velocity.

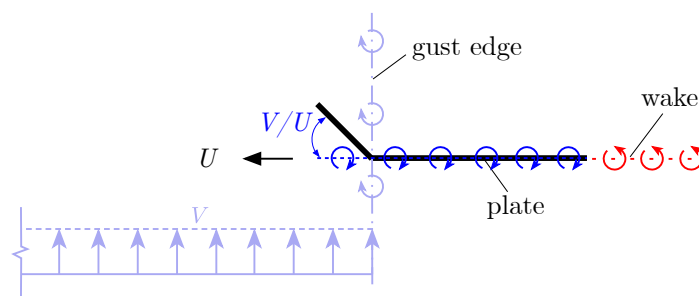


Fig. 2.8 Broken-line theory used to represent a flat plate entering a sharp-edged gust.

Gust entry occurs over one chord length, during which successively more of the plate is located within the gust. To represent the plate, von Karman and Sears [96] use a 'broken line' theory, as schematically shown in figure 2.8. It is assumed that the plate experiences a step change in angle of attack and moving camber point as the gust edge advances. The changing angle of incidence as well as camber cause the circulation around the plate to grow. An appropriate amount of vorticity must therefore be released into the flow to conserve circulation. Moreover, vorticity shed from the trailing edge further affects the developing force, because it induces a downwash onto the wing. Thereby, it reduces the effective angle of attack and thus delays the rate at which circulation and thus lift increases. The individual force contributions are shown in figure 2.9. A circulatory steady-state force arises as a result of the developing bound circulation. Neglecting any effects of downwash, it increases non-linearly during gust entry and reaches a steady-state once the complete plate is located within the gust. A further circulatory force is created by the wake and may be described as a 'lift deficit' due to the induced downwash onto the wing. In addition, a non-circulatory force has a significant contribution during gust entry and is historically attributed to an added mass force [96]. Interestingly, we note that no body or fluid acceleration has taken place, and the added mass force classification

therefore appears non-intuitive. In fact for thin flat plates, Corkery [14] suggests that the origin of this force should be attributed to external vorticity created at the interface of the gust and its surrounding rather than to any non-existent acceleration.²

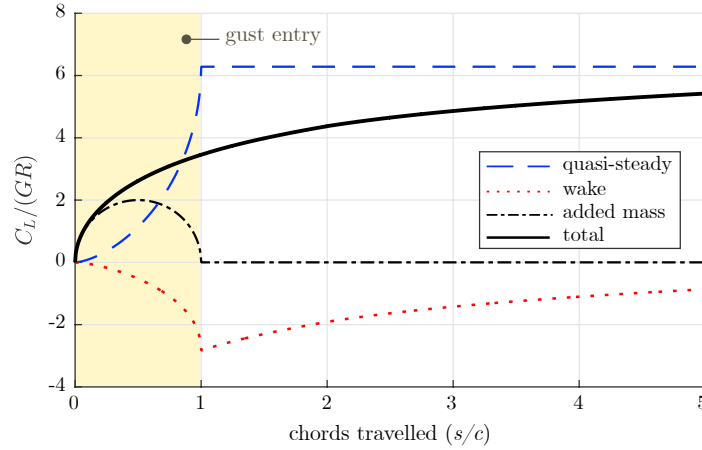


Fig. 2.9 The Küssner force and its constituent parts. After von Karman and Sears [96] and adapted from Corkery [14].

The summation of all three contributions yields the total force, which Leishman [48] writes as

$$C_l = 2\pi \frac{V}{U} G(s/c). \quad (2.33)$$

$G(s/c)$ is the Küssner function, approximated by Bisplinghoff et al. [9] as

$$G(s/c) = \frac{4(s/c)^2 + 2(s/c)}{4(s/c)^2 + 5.64(s/c) + 0.8}, \quad (2.34)$$

where s represents the distance travelled by the wing. Andreu-Angulo et al. [4] show that for plate-gust encounters at low gust ratios up to around 0.5, the model shows good agreement with experimental results. At higher gust ratios, a significant divergence from the theoretical results is observed. The reasons for this mismatch are difficult to identify, since a variety of assumptions have been made simultaneously in the derivation of Küssner's model. One clear candidate responsible for the inaccuracies of the model, particularly at high gust ratios GR , is the fact that leading edge separation is not accounted for. In addition, the impact of gust distortion is not well understood and it remains to be seen whether an inclusion of the related dynamics equally contribute to the divergence of the model. Moreover, many real aerodynamic shapes are not simple flat plates but have some attributed volume. The effect which this has, especially on the non-circulatory force during gust entry (and exit), can further lead to possible errors of the theory.

²A closer inspection of this is provided in chapters 4 and 8.

2.5 Predicting the Unsteady Separation Point

The circulatory force created by shed vorticity has a significant impact on the overall force response. Whilst approaches like the impulse method can retrospectively calculate the force from the development of the vorticity field, they require knowledge of the flow field history. LOMs like the Küssner model, artificially ascribe a separation point and motion profile to any vorticity that leaves the boundary layer as an input for the force computation. This approach can achieve sufficient accuracy for sharp-edged objects such as flat plates, where the separation point is clearly defined. Many real life objects however, have a smooth surface where the location of unsteady separation varies. This complicates the prediction of the unsteady separation point, which is a prerequisite for an accurate representation of the flow field and the subsequent force computation.

A well known approach to predict the location of separation is Thwaites' method. Thwaites [94] defined a parameter m , which relates to the shape of the boundary layer given by its velocity profile,

$$m = \frac{\delta_2}{u_\theta^e} \frac{\partial^2 u}{\partial y^2} \Big|_{y=0} = -\frac{\delta_2^2}{v} \frac{du_\theta^e}{dx}, \quad (2.35)$$

where u is the velocity variation within the boundary layer, u_θ^e represents the boundary layer edge velocity and δ_2 is defined as the momentum thickness,

$$\delta_2 = \int_\delta \left(1 - \frac{u}{u_\theta^e}\right) \frac{u}{u_\theta^e} dy. \quad (2.36)$$

Separation is found to occur when $m = 0.09$, as this corresponds to zero wall shear stress and thereby identifies the beginning of flow reversal in steady flow. As shown by the MRS-criterion, zero shear at the wall does not necessarily identify separation in unsteady flow, and therefore restricts the applicability of this method to steady flow.

An alternative method to identify the laminar unsteady separation point is presented by Ramanathan et al. [73]. The authors propose a modified shape factor H_{32} , which represents the ratio between the energy thickness δ_3 ,

$$\delta_3 = \int_\delta \left(1 - \left(\frac{u}{u_\theta^e}\right)^2\right) \frac{u}{u_\theta^e} dy \quad (2.37)$$

and the momentum thickness δ_2 , such that

$$H_{32} = \frac{\delta_3}{\delta_2}. \quad (2.38)$$

The authors perform a range of a pitching NACA0012 and SD7003 simulations, with which they illustrated the potential for H_{32} to predict unsteady separation. Unfortunately however, LOMs do

not have access to such detailed velocity data within the boundary layer and can only identify more basic flow variables, preventing an implementation of a H_{32} -based unsteady separation model. One boundary layer property however that is easily obtainable, even for LOMs, is the boundary layer vorticity. It develops as the flow field evolves and feeds any vortices that are shed [109]. In the following we therefore assess how boundary layer vorticity, implicitly or explicitly, has been used in the past to attempt to predict unsteady separation.

2.5.1 Leading Edge Suction Parameter

Ramesh et al. [75] introduced the leading edge suction parameter (LESP) to predict unsteady separation. They propose that whenever the LESP exceeds a predetermined critical value at the leading edge, unsteady separation is initiated. This stems from the idea that a maximum suction force, F_s , can be sustained before the flow separates. This leading edge suction force is defined by Garrick [29] as

$$F_s = \pi \rho S^2, \quad (2.39)$$

where S is:

$$S = \lim_{x \rightarrow LE} \frac{1}{2} \gamma(x) \sqrt{x}. \quad (2.40)$$

The vortex sheet distribution $\gamma(x)$, expressed as a Fourier series, is derived from thin aerofoil theory [21] and in cylindrical coordinates is formulated as

$$\gamma(\theta) = 2U_\infty \left(A_0 \frac{1 + \cos \theta}{\sin \theta} + \sum_{n=1}^N A_n \sin n\theta \right), \quad (2.41)$$

where

$$x = \frac{c}{2} (1 - \cos \theta). \quad (2.42)$$

The local coordinate frame is defined such that at the leading edge $x = 0$ and $\theta = 0$ and at the trailing edge $x = 1$ and $\theta = \pi$. The Fourier coefficients, A_0 and A_k , are a function of the local downwash, $W(x, t)$,

$$A_0 = -\frac{1}{\pi} \int_0^\pi \frac{W(x, t)}{U(t)} d\theta \quad (2.43)$$

$$A_k = \frac{2}{\pi} \int_0^\pi \frac{W(x, t)}{U(t)} \cos k\theta d\theta, \quad (2.44)$$

where $U(t)$ is the instantaneous velocity. Assuming a camber line distribution $\chi(x)$ and the presence of a LEV and TEV in the flow field, the downwash acting on a wing can be written as

$$W(x,t) = \frac{\partial \chi}{\partial x} \left(U \cos \beta + \dot{h} \sin \beta + \frac{\partial \Phi_{\text{LEV}}}{\partial x} + \frac{\partial \Phi_{\text{TEV}}}{\partial x} \right) - U \sin \beta - \dot{\beta}(x-ac) + \dot{h} \cos \beta - \frac{\partial \Phi_{\text{LEV}}}{\partial y} - \frac{\partial \Phi_{\text{TEV}}}{\partial y}. \quad (2.45)$$

$\frac{\partial \Phi}{\partial y}$ and $\frac{\partial \Phi}{\partial x}$ are the induced velocities normal and tangential to the chord where ϕ is the corresponding potential. The other symbols correspond to the definition of the aerofoil shown in figure 2.10.

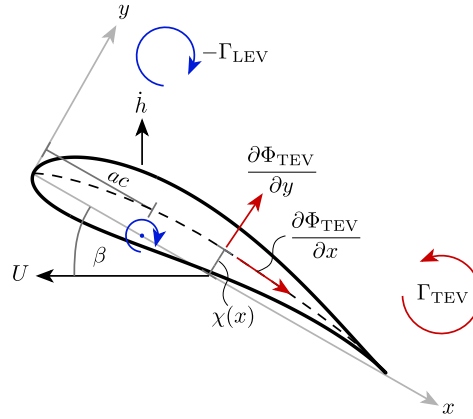


Fig. 2.10 Schematic illustration of an aerofoil together with its velocity components and the pitching location. The camber distribution $\chi(x)$ and a LEV and TEV are also indicated. The induced velocity components $\frac{\partial \Phi_{\text{TEV}}}{\partial x}$ and $\frac{\partial \Phi_{\text{TEV}}}{\partial y}$ from the TEV feature as well. \dot{h} is the plunge velocity, U the instantaneous velocity, β the angle of attack and ac the distance from the leading edge to the pivot location.

Substituting $\gamma(\theta)$, equation 2.41, into equation 2.40 as x approaches the leading edge ($\theta \rightarrow 0$) leads to

$$S = \sqrt{c}UA_0(t). \quad (2.46)$$

The LESP is now simply taken as A_0 by Ramesh et al. [75], since it gives a non-dimensional measure of the suction force,

$$LESP(t) = A_0(t). \quad (2.47)$$

Depending on the instantaneous strength of the LESP, steady or intermittent separation can now be predicted and used to model for example a plunging and translating plate, as schematically shown in figure 2.11.

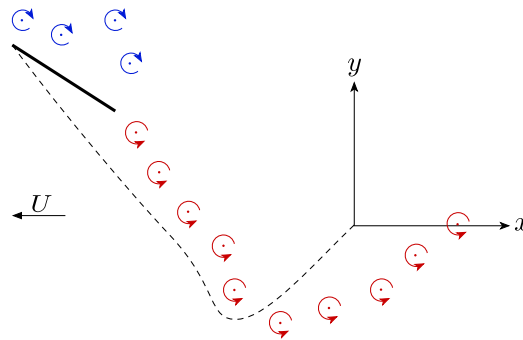


Fig. 2.11 Schematic illustration of how the LESP is implemented in a panel method code to determine when vorticity is shed from the leading edge.

Even though the LESP is often calculated directly from the leading edge pressure, Eldredge [24] shows that it is intrinsically linked to the boundary layer vorticity and that it can be calculated from this. Ramesh [74] further shows that the LESP can be related to the velocity at the leading edge, by expanding the singularity using asymptotic matching of an outer solution, based on thin linear airfoil theory, and an inner solution, formed by evaluating flow past a parabola. Moreover, whilst the LESP has been shown to be successful at predicting flow detachment, trailing edge separation [76] and increased aerofoil pitch rates [19] can modify the critical value at which unsteady separation occurs. Furthermore, changing LESP strength has been documented by Deparday and Mulleners [19] during vortex shedding as well as by He and Williams [34]. The latter investigated the progression of the LESP during attached and separated turbulent surging flow states past an aerofoil. Therefore, whilst the LESP under certain conditions seems a good proxy through which unsteady separation can be predicted, the underlying behaviour remains somewhat unclear. A more thorough understanding of its development, for example obtainable through knowledge of the boundary layer vortex sheet, due to the link between LESP and surface vorticity, could facilitate a more accurate interpretation and confident application.

2.5.2 Vorticity as a Proxy for Unsteady Separation

Other means to predict unsteady separation have focused more directly on boundary layer vorticity or vorticity that has just been shed. Melius et al. [59] investigate whether there is a critical value of surface vorticity associated with flow separation. They argue that a sufficient accumulation of vorticity would entrain enough fluid to cause flow reversal and thus eject small scale vortices. In their experiments, a scaled turbine blade model is pitched in a wind tunnel whilst the surface vorticity at the location of separation is recorded. The authors find a critical value of normalized vorticity, $|\omega^*| = |\omega c / U_\infty|$, after which separation occurs. Whilst the data is rather noisy and one might argue that a single measurement point is susceptible to errors, it is nonetheless interesting to note that there is a consistent increase in surface vorticity with a related critical value, even when the separation point

moves.

Moreover, when rotating a surging wing at variable pitch rates, Deparday and Mulleners [19] observe that the amount of vorticity contained within the LEV remains comparable, even as the pitch rate changes. Since shed vorticity emanates from the boundary layer, this further suggests that there may be a link between the local boundary layer vortex sheet strength and the unsteady separation location.

It therefore appears worth noting that there exist numerous attempts to predict unsteady separation by either explicitly or implicitly leveraging boundary layer vorticity. This is an attractive parameter, as it can be obtained even from simple LOMs. However, because the underlying reasons for the evolution of the boundary layer, especially at the separation point, remain obscure, this makes finding a ‘separation indicator’ difficult and more due to luck rather than as a result of a systematic and coordinated analysis.

2.6 Vorticity Shedding Rate

A further parameter that needs to be modelled by an LOM is the rate at which new vorticity leaves the surface of an object and sheds into the flow. This is because the creation of new vorticity significantly affects the rate of change of momentum of the flow, and thus the force, as well as the time evolution of the flow field as a whole. Eldredge and Jones [25] as well as Wojcik and Buchholz [105] suggest that the rate at which vorticity sheds and increases the strength of a LEV contained within a domain B_{LEV} , as shown in figure 2.12, can be found from a vorticity balance. Beginning from the Navier-Stokes equation (2.12) and taking the curl of each element in the equation, yields the vorticity equation,

$$\frac{D\boldsymbol{\omega}}{Dt} = (\boldsymbol{\omega} \cdot \nabla)\mathbf{u} + \nu \nabla^2 \boldsymbol{\omega}, \quad (2.48)$$

where $\nu = \mu/\rho$ is the kinematic viscosity. Integrating the spanwise components of each term in equation 2.48 and applying the divergence theorem leads to

$$\dot{\Gamma} = - \int_{B_{LEV}} \mathbf{n} \cdot \mathbf{u} \omega_z dl + \int_{B_{LEV}} \nu \frac{\partial \omega_z}{\partial n} dl + \int_{B_{LEV}} \mathbf{n} \cdot \boldsymbol{\omega} \omega dl. \quad (2.49)$$

The second term on the right hand side represents the diffusive flux and is only non-zero on the boundary aligned with the body. It however is assumed to be small compared to the vorticity fed into the LEV through the separating shear layer. The final term describes vortex tilting and is zero in two-dimensional flow. Eldredge and Jones [25] shows that by assuming vorticity to be divergence-free, the net spanwise convective flux and the stretching of spanwise vorticity cancel and they have therefore been omitted from equation 2.49. Moreover, variations of the viscous flux along the boundary are assumed to be small, and the respective terms have therefore also been removed in equation 2.49.

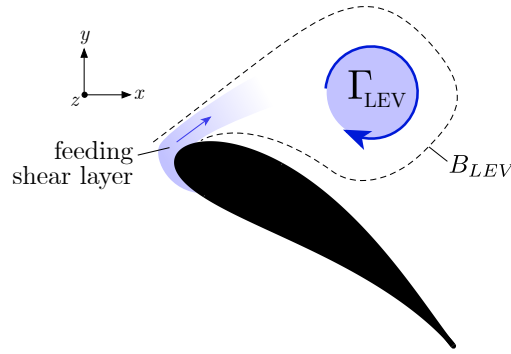


Fig. 2.12 Accumulation of circulation within the LEV, fed by the separating shear layer.

In the absence of *vorticity annihilation*, a process by which secondary vorticity of the opposite sign is created downstream of the separation point and drawn into the LEV [105], the rate of change of circulation in the separating vortex should be equal to the vorticity flux in the boundary layer just upstream of the separation point. Xia and Mohseni [109] suggest that at the separation point, the complete boundary layer vorticity (represented as a vortex sheet) flows into the separating shear layer, where the boundary layer vorticity flux is written as

$$\dot{\Gamma} = \int_{\delta} \omega(y) \frac{1}{2} u(y) dy. \quad (2.50)$$

When the surface of the object is stationary, this simplifies to

$$\dot{\Gamma} = \frac{1}{2} u_{\theta}^e{}^2, \quad (2.51)$$

where u_{θ}^e is the boundary layer edge velocity. Equation 2.51 frequently features in literature. Didden [20] and Sarpkaya [84], amongst others, derive similar equations, for which varying degrees of success at correctly estimating the rate of shed vorticity have been reported upon implementation [26, 57].

Moreover, not only does the strength of a LEV effect the force response but its motion dynamics have been found to be equally important [2]. As such, methods to stabilise the LEV, preventing it from bursting, have become topics of interest. Here it has been observed by Widmann and Tropea [102] as well as by Wong and Rival [106], that a key parameter involved in the dynamics of the released vortex is the strength of the separating shear layer that feeds the LEV. This in turn has led to an interest in developing simple ways to model the rate at which vorticity is shed. In regards to this, Li et al. [50] and Shumway and Jones [88] noticed that during the early stages of vortex formation, the shedding rate of vorticity has a significant dependency on the effective angle of attack as well as on the relative velocity at the leading edge due to the kinematics and the freestream flow. As the vortex grows and begins to drift downstream, this relationship however fades. Phenomenological trends as those described by Li et al. [50] and Shumway and Jones [88] are extremely useful when building future LOMs. However, a more underlying insight into why these work would go to even

greater lengths of helping explore when the resulting models are valid and when they no longer reflect the true dynamics.

2.7 Circular Cylinder

The simplicity of a flat plate has made it a favoured geometry with which to mathematically, computationally and experimentally study unsteady flows. However, many real geometries like wings are not infinitely thin but are of finite volume with a rounded leading edge. A fixed separation point due to sharp edges, as is the case for flat plates, is therefore generally an exception rather than the norm. Understanding and capturing the effects due to a moving separation point as well as body volume is therefore crucial to better comprehend real unsteady flows.

A spinning and surging circular cylinder appears as an ideal candidate with which to investigate these dynamics. It is geometrically simple enough to be modelled analytically in potential flow, whilst at the same time emulating a lifting body and generating a sufficiently time varying flow as well as force response. Furthermore, the boundary layer is found to remain laminar below a Reynolds number of approximately 100 000 [79], and thus emulates the conditions on MAV wings. Circular cylinders have long been a regular feature in aerodynamic literature, where early interest in the geometry was created by the Magnus effect, which describes the generation of force due to a rotating and translating cylinder. The effect was first studied by Robins in 1742 [36]. More than 100 years later, in 1852 Magnus published his first paper on the topic, which led to the effect, perhaps falsely, being associated with his name [54]. Since then, it has been researched and implemented in real applications in various shapes and forms, see the review by Seifert [87]. Perhaps more relevant for the current research is the strongly varying unsteady flow field that can be created by adjusting the ratio between cylinder spin (angular velocity times cylinder radius, Ωa) and relative freestream velocity, U_∞ , $\alpha = \frac{\Omega a}{U_\infty}$, (see Badr and Dennis [6], Coutanceau and Menard [17], Badr et al. [5], Padrino and Joseph [67]). The unsteady flow field can be grouped into two main categories. For α less than around two, alternate vortex shedding takes place from either side of the cylinder [45, 61]. When α exceeds this value, successive vortex shedding is suppressed and only one initial starting vortex is shed as the cylinder begins its kinematic motion [45]. Moreover, due to the link between the force response and the growth as well as advection of vorticity, it follows that the lift response of the cylinder mirrors the vortex shedding behaviour. Cyclic loading is observed during alternate vortex shedding, whilst the lift force asymptotes to a steady-state value when only a starting vortex forms [55]. The ability to create a varying flow field using a single geometry and simply adjusting the rotation ratio makes for an ideal experimental case study and this will be leveraged throughout the thesis.

2.8 Summary: Literature Review

Unsteady aerodynamics is categorized by a rapidly changing flow field. Key characteristics of such flows are found to be rapidly evolving leading and trailing edge vortices, which are fed by separating shear layers that emanate from unsteady separation points. In contrast to steady flow, unsteady separation is observed to no longer be fixed to a specific position along a surface, where the skin friction goes to zero, but it is free to move. To complicate matters further, the transient force resulting from this flow field has been shown experimentally to readily exceed the steady-state equivalent and thereby creates a highly variable loading on any immersed structure or object. The present work is therefore largely motivated by the aim to better understand these unsteady flow fields, in order to help develop low order models that predict the unsteady force response in real time and can thus be used to mitigate the resulting transient forces.

To achieve the necessary computational speeds required for such LOMs, the real viscous flow field needs to be simplified to a more tractable problem. One approach by which this has been achieved in the past is through potential flow theory. Here, the true flow field is recreated by superposing individual flow solutions. Whilst free vorticity can be represented through point vortices, it has been argued that the viscous boundary layer can be replaced by an infinitely thin vortex sheet that is located on the body surface and enforces the no-throughflow condition everywhere along it. Moreover, similar to how the flow field can be represented by a number of individual components, the boundary layer vortex sheet on a thin flat plate has equally been represented as a superposition of discrete components, which have been recovered under experimental conditions. Grouping the surface vortex sheet into separate contributions was subsequently used to better understand the force development, since the impulse method, a common approach to predict forces, links the rate of change in strength and position of vorticity to a force response. Thus, by understanding the origin and underlying reasons behind the development of vorticity, a better assessment of the force evolution should be possible.

Vorticity is created in the boundary layer and from this sheds into the flow field. Isolating the unsteady separation point and the rate at which vorticity sheds is therefore crucial for an accurate force prediction and appropriate approaches are thus frequently discussed in literature. Unfortunately, unsteady flow is found to complicate predictions of the unsteady separation point, as observed for Thwaites' theory, which does well only in steady-state conditions. Evaluating the velocity profile of the boundary layer has been shown to be successful in predicting the unsteady separation point, however, LOMs do not have access to such detailed flow field data. Vorticity on the other hand, is accessible to LOMs and has been used implicitly, in form of the LESP criterion, as well as explicitly in literature, to better understand unsteady separation. It is however noted that a lack of knowledge regarding the development pattern of boundary layer vorticity still complicates the search for a universally valid separation criterion.

LOMs not only need to correctly predict the force, but they must also do this in near to real time, if they hope to successfully alleviate the danger posed by gusts. As a consequence, LOMs such as the Küssner model, developed for transverse gust encounters, ideally only model the most dominant force effects, in order to not unnecessarily prolong the computation. In a bid to reduce the necessary calculations, Küssner invoked a number of assumptions that simplify the flow field. Unfortunately however, determining how much individual flow phenomena contribute to the force and thus which simplifying assumptions have a negligible effect on the force computation, is not always straight forward. This is because existing methods that calculate the force response have a limited ability to determine the force due to an individual flow feature, making it difficult to assess which flow contributions affect the force most strongly, and should therefore be included in the LOM.

To better understand many of these underlying aerodynamic principles to develop improved LOMs, simple thin flat plates are at the heart of most investigations discussed in literature. Many aerodynamics shapes however, have some attributed volume. The developed theories must necessarily be equally viable for such geometries. A rotating and translating circular cylinder is therefore found to be an ideal test candidate; it is far removed from a thin flat plate and able to create a range of varying flow fields simply by adjusting the rotation ratio. Moreover, the absence of any sharp edges creates a dynamically moving unsteady separation point and together with its finite volume, creates the opportunity to verify and extend idealised theories for thin flat plates to real life objects.

2.9 Approach and Aims

The complete scope of unsteady aerodynamics, from flapping wings, pitch, plunge surge combinations, gust encounters of variable velocity profiles, renders any attempt at including a complete assessment within this thesis impossible. Therefore, rather than exploring each possible permutation, we restrict ourselves to accelerating objects and top-hat shaped transverse gust encounters. The significant flow separation around a circular cylinder and the considerable non-circulatory forces generated through acceleration as well as by the transverse gust provides an exhaustive representation of many real viscous flows. The thesis therefore aims to illuminate the underlying principles using basic flow experiments where the subsequent findings can thereafter, be applied independently to each unique situation.

The overarching questions that we aim to explore are:

1. What flow dynamics elucidate a boundary layer vortex sheet contribution around an object of volume and what affects its evolution globally?
2. How does the vortex sheet strength develop at the unsteady separation point?

3. What is the connection between different boundary layer vortex sheet contributions and the rate at which vorticity sheds at the unsteady separation point and how does this relate to the observed unsteady force and flow field dynamics?
4. How does an external flow feature contribute to the force response of an object and can the resulting theory be used to understand the limitations of the rigid gust assumption inherent to Küssner's model?

To unravel the underlying dynamics, an experimental approach is chosen. Two-dimensional flow is assumed throughout the thesis and the experiments are restricted, for the most part, to the rotation and surge of a circular cylinder. Its attributed volume and ability to create varying flow fields with moving unsteady separation points is thought to be an ideal platform from which to investigate the related unsteady mechanisms. In addition, to introduce further unsteadiness into the flow field that is not due to variable motion kinematics, the cylinder is subjected to a transverse gust encounter. Moreover, an assessment of the force response is elucidated by including external objects in the flow field, which increase the complexity of the flow by creating and shedding their own vorticity.

The remaining thesis is structured, such that the experimental set-up developed precisely for this investigation is described in chapter 3. Thereafter, we take a closer look at the theoretical background of the boundary layer vortex sheet as well as its evolution globally, and at the unsteady separation point, in chapter 4. The link between the boundary layer vortex sheet and the rate at which vorticity sheds is explored thereafter in chapter 5. An assessment of how the findings relate to real flow patterns and force generation is made in chapter 6. The force contribution due to an individual flow feature is extracted in chapter 7 before the developed methodology is used to assess a cylinder-gust encounter in chapter 8.

Chapter 3

Experimental Methodology

A range of different experiments are developed and performed within the University of Cambridge Towing Tank facilities to better understand the nature of unsteady flow. The water towing tank facility at the core of this research is described in section 3.1. Force balance measurements and particle image velocimetry (PIV) provide insight into the underlying mechanisms at play and are described in sections 3.2 and 3.3. A number of experimental set-ups are developed and used throughout this investigation. The circular cylinder model is described in section 3.4.1. A multi-body flow field arrangement comprising of a cylinder and a flat plate is discussed in section 3.4.2. To replicate a uniform freestream impinging on a stationary flat plate, a ‘scoop’ experiment is developed and outlined in section 3.4.3. Ultimately, Küssner’s sharp edged gust encounter is replicated using the apparatus detailed in section 3.4.4. The measurement of the boundary layer vortex sheet is an integral part of this study and a description of the method in section 3.5 precludes the chapter.

3.1 Towing Tank Facility

The experiments conducted throughout this investigation utilise the towing tank facility at the University of Cambridge. A schematic image of the 9 m long, 1 m wide towing tank is shown in figure 3.1, which is filled up to a height of 0.8 m. A servo motor driven carriage, with a maximum speed of 4 ms^{-1} , runs along the length of the tank and serves as the mounting point for the force balance, to which various geometries can be attached.

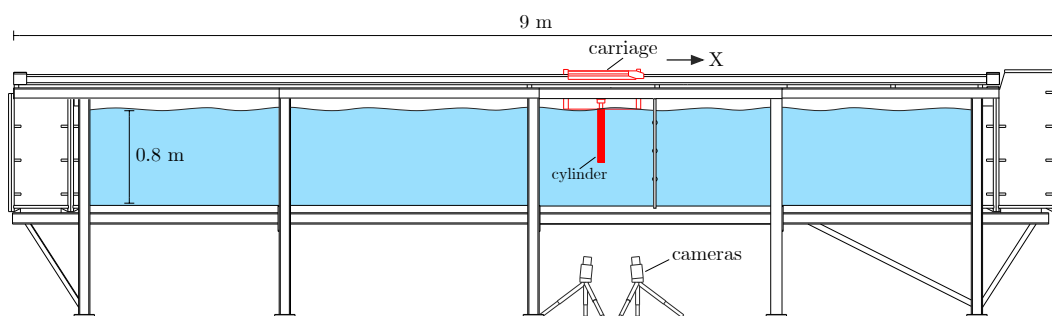


Fig. 3.1 Towing tank.

Compared to air, water has a number of advantages that make it the preferred medium for investigations into unsteady aerodynamics. For the same Reynolds number, the speed required in water is only 7.7 % of that needed in air, due to the difference in kinematic viscosity ν between the two fluids. Further to this, forces are amplified by a factor of 3.7 at the same Reynolds number [69]. The reduced velocity and higher force magnitude allow for more accurate measurements. This is because the slower kinematic motions can be more successfully executed, whilst at the same time, the force signal to noise ratio is reduced. Furthermore, the towing tank has the additional benefit that low turbulence intensities can easily be achieved, since it is not the fluid that must be set into motion but rather the object. After a 15 minute settling time, the turbulence intensity is below the noise of the PIV measurements when the field of view is sufficiently large [37].

The kinematics of the carriage are measured using a linear quadrature encoder with a step resolution of 1 mm as well as with an onboard ADXL354 accelerometer. The data is sampled at a rate of 3000 kHz using Lab View and a 16-bit data National Instruments data acquisition card.

A simplified schematic illustration of the four different experiments conducted within the towing tank facility is shown in figure 3.2. A circular cylinder is either accelerated and rotated in isolation or in unison with a flat plate. Alternatively, the cylinder is subjected to a transverse sharp-edged gust. A further experiment comprises of a stationary flat plate surrounded by an accelerating freestream created by a translating *scoop*.

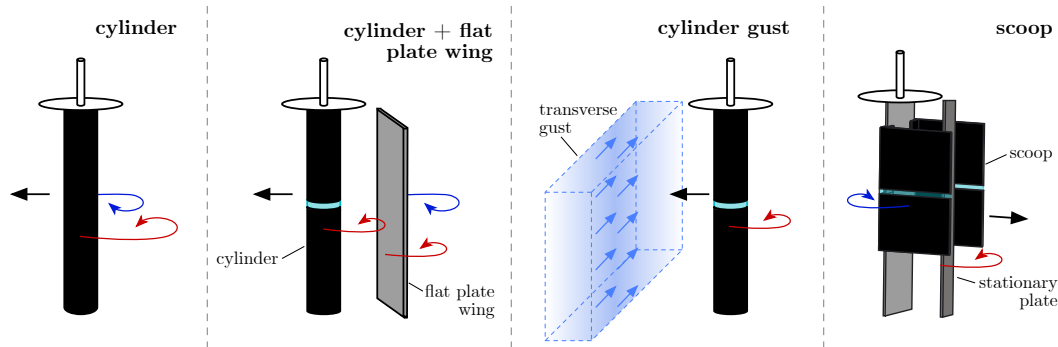


Fig. 3.2 Overview of the experimental set-ups.

3.2 Force Measurements

Force measurements are conducted using the two component force balance shown in figure 3.3. It uses a Flow Dynamics strain gauge based load cell with a resolution of 0.01 N in the drag (x) and lift (y) direction. The top plate is fixed to the carriage, whilst the bottom is free to move and serves as the mount for the cylinder. It is designed such that it transmits the in-plane forces, whilst rejecting those created by the bending moment acting on the attached cylinder [14].

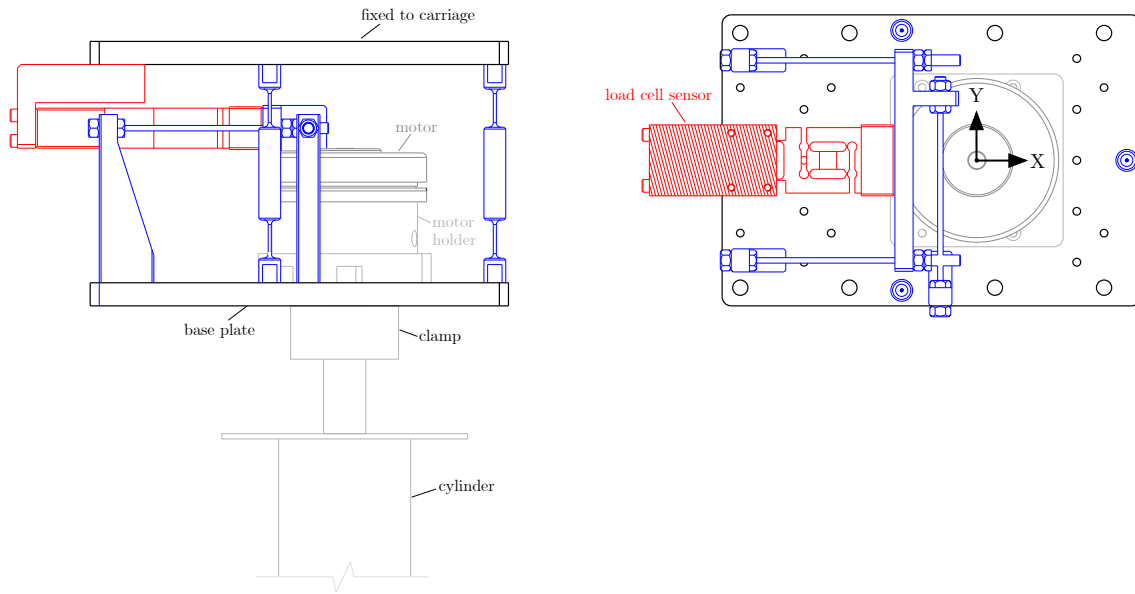


Fig. 3.3 Force balance.

The load cell is calibrated in-situ to ensure an accurate relationship between the recorded voltage signal and the applied force. The voltage (V_x , V_y) is recorded for both channels, whilst an incremental known force is applied via a pulley system and a set of free weights in either the x or y -direction to achieve a representative calibration. A linear relationship is observed for the active channel throughout, leading to a calibration slope of $F_x = 44.6384V_x$ and $F_y = 64.4996V_y$ in the x and y -direction respectively.

When the carriage accelerates, an inertial force component F_i arises in the x -direction, which affects the drag measurements. This force is created by all ‘unsupported’ parts of the force balance that are not fixed to the carriage as well as by the cylinder. To isolate the aerodynamic force, the inertial contribution must be removed from the total measured force. F_i is computed using the instantaneous acceleration \dot{U} and the unsupported mass of the force balance assembly, m_{us} ;

$$F_i = m_{us}\dot{U}. \quad (3.1)$$

3.2.1 Errors

An error in the force measurements can arise from cross-talk between the two load channels. As a force is applied along one direction, the load measured in the perpendicular axis is also affected. This can occur because of structural deformation as the load is applied or because of a slight misalignment of the sensor elements. The maximum error as a result of cross-talk is 0.8 % of the applied load [14].

A second error affects the load measurements when the load is at an offset from the sensor elements. The bending moment created between the top and bottom plate of the force balance causes

a deflection and subsequent loading of the load cell sensors. The error is quantified by applying a load at various offsets from the load cell. At a cylinder length of 0.48 m, the maximum error is found to be approximately 1 % [14]. Combined, the order of magnitude of the errors is sufficiently small as to not affect the results throughout this investigation.

3.3 Particle Image Velocimetry

Particle image velocimetry (PIV) is a non-intrusive technique that measures the fluid velocity within a region of interest. A schematic illustration of a generic PIV set-up is shown in figure 3.4. A laser and the appropriate lenses create a thin light sheet, which illuminates a measurement domain. Small seeding particles, which track the fluid motion, are suspended in the working fluid which is usually air or water. The particles reflect a small amount of light as they are illuminated by the laser and thus become visible to a camera that is ideally positioned normal to the laser sheet. The laser and the camera are pulsed in rapid succession to obtain a time series of photos between which the particles move a small distance. Each frame is divided into a series of interrogation windows, which feature a small subset of the photographed seeding particles. A cross-correlation algorithm is subsequently applied to determine by how much the particles have moved between successive frames. From this, the velocity vector for each interrogation window can be reconstructed, thus ultimately yielding the complete velocity field.

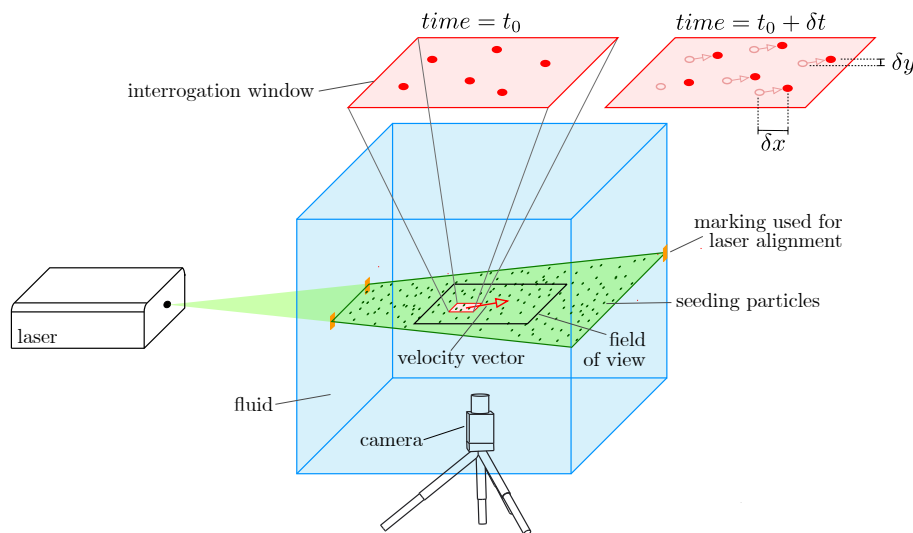


Fig. 3.4 Schematic illustration of a generic PIV set-up.

3.3.1 Implementation

Measuring the development of the unsteady velocity field is key throughout this investigation. An overview of the PIV set-up is shown in figure 3.5. An Nd:YLF dual cavity Litron PIV300 series laser acts as the light source. It produces a pulsed laser with a wavelength of 527 nm, a maximum energy

output per pulse of 20 mJ and a pulse nominal width of 150 ns. To create the light sheet, the laser beam is split into two just after it has been emitted. The first part passes through a laser arm and is shone into the test section as a horizontal plane from the same side. The second beam passes below the tank and a series of mirrors and lenses transform it into a light sheet that shines into the tank from the opposite side. Together, both light sheets illuminate the complete horizontal plane at the midspan of the test geometry and thereby re-create the dual-laser sheet configuration first developed by Stevens and Babinsky [91]. The light sheets are aligned using three photo-luminescent markers positioned on the tank windows. Two of these are positioned on one side of the tank, whilst the third is located on the opposite side, as shown in figure 3.4. The markers define the desired laser plane, which is initially determined using a low-power, auto-levelling laser. The laser alignment is performed whilst the water tank is filled, as there is a mismatch of the refractive index between water and air. At a temperature of 20°C, the refractive index of water is 1.33 whilst that of air is unity. The difference in refractive index would cause the laser sheets to deflect if the angles of incidence are not perpendicular to the tank windows. The focal point of the laser beams is adjusted such that the focus is always at the centre of the tested geometry. This gives an approximate maximum thickness of 1 mm for the laser sheet at the edges of the field of view.

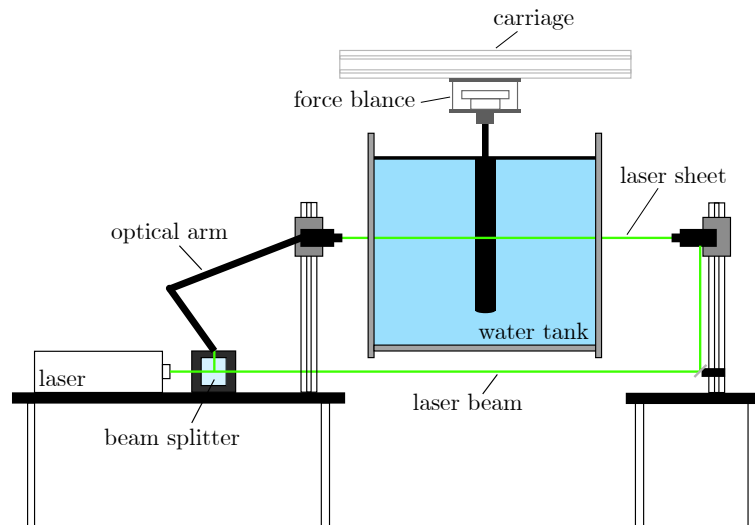


Fig. 3.5 Overview of experimental set-up.

The water is seeded with titanium dioxide (TiO_2) particles with a maximum diameter of $45\mu\text{m}$. TiO_2 particles have the advantage that they have a high reflectivity and low settling rate in water. Furthermore, Pitt Ford [69] found that the fluid tracking error, which may occur when the acceleration created by an applied pressure gradient differs between the fluid and the particles, is negligible for the particle sizes and velocities considered.

To acquire data across the entire observation window, two high-speed Phantom M310 cameras are positioned below the tank for all instances. The sampling rates are adjusted between 400 - 1200 Hz respectively, to ensure that the particle displacement is between 3 - 4 pixels for all test cases.

The commercial LaVision Flowmaster 2D system is used for the cross-correlation process which is applied to both camera images independently. Thereafter, the two resulting vector fields are stitched together to yield a complete representation of the flow field without any shadow regions. The adaptive interrogation window initially has a size of 48×48 pixels, to reduce the signal to noise ratio. In an iterative procedure, it decreases to 16×16 pixels during its final pass. The interrogation window overlap is 50 %. The final PIV vector spacing is 1.9 mm for any cylinder cases, 1.8 mm for the multi-body flow field, 2.6 mm for the scoop experiment and 3.8 mm for the gust studies.

The boundary layer is of key importance throughout this work. In particular we are interested in boundary layer vorticity, not however in the specific boundary layer velocity distribution. Unfortunately, laser reflections from surfaces can cause missing velocity data in the surrounding flow field (ie. in the boundary layer). To recover the missing velocity vectors, we linearly interpolate between the measured velocity field and the known surface velocity of the object, as illustrated in figure 3.6. This methodology preserves the magnitude of vorticity located in the boundary layer. An error in the surface normal distribution of vorticity arises, as this cannot be accurately recovered. However, since reflections only extend approximately 1 - 2 mm into the flow field, the associated error in the wall normal vorticity distribution is small and does therefore not adversely affect the results.

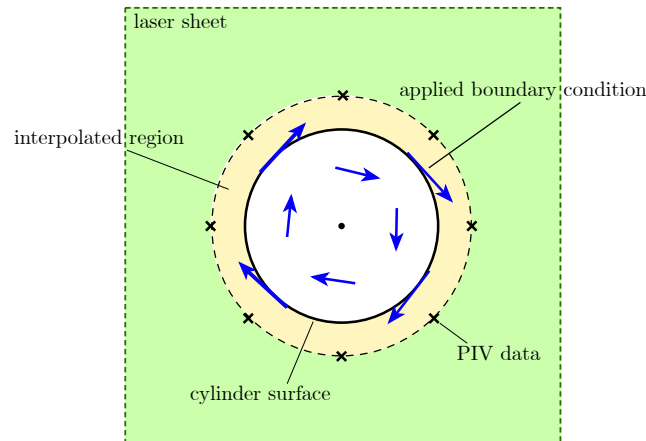


Fig. 3.6 Missing velocity vectors can be accounted for by assigning the boundary condition to the cylinder and interpolating between the measured flow field and cylinder surface velocity.

3.3.2 Errors

To provide the best possible input for the PIV cross-correlation algorithm, which is easily affected by spurious increases or variations in light intensity [72], a background subtraction is performed on the

original images captured by the cameras, which minimizes stray light and reflections. On top of this, the light intensity of each pixel contained within a moving window of 12×12 pixels is normalized, in order to remove any sudden changes in brightness.

Unfortunately, PIV measurements are affected by numerous additional sources of errors. One of the most dominant errors is referred to as peak-locking and occurs when light reflected from a particle is only captured by a single pixel on the camera sensor. In this case, it is not possible to determine, where within the pixel the particle is located [72]. To avoid this, the focus of the cameras is adjusted so that each particle diameter is smeared over at least 2 pixels. The sub-pixel position can now be identified, by applying a Gaussian fit to the light intensity.

Work by Raffel et al. [72] and Nobach and Bodenschatz [64] investigates further sources of errors by using synthetically created particles, where individual parameters are changed and the effect on the total root mean square (RMS) error is evaluated. One source of error identified from this is a consistent bias in the pixel displacement ϵ_{bias} that occurs when particle pairs are lost between successive interrogation windows. Further sources of random error come from the variation in particle diameter ϵ_{rms_0} , the displacement of particle images $\epsilon_{\text{rms}_\delta}$, the particle density within each interrogation window $\epsilon_{\text{rms}_\rho}$ as well as from a change in particle intensity when it moves perpendicular to the light sheet ϵ_{rms_i} :

$$\epsilon_{\text{PIV}} = \epsilon_{\text{bias}} + \epsilon_{\text{rms}_0} + \epsilon_{\text{rms}_\delta} + \epsilon_{\text{rms}_\rho} + \epsilon_{\text{rms}_i}. \quad (3.2)$$

An estimate of each error, based on the work by Raffel et al. [72] and Nobach and Bodenschatz [64], is provided in table 3.1.

ϵ_{bias}	ϵ_{rms_0}	$\epsilon_{\text{rms}_\delta}$	$\epsilon_{\text{rms}_\rho}$	ϵ_{rms_i}
-0.01	0.04	0.01	0.025	0.10

Table 3.1 PIV measurement error estimation (in pixels), using work by Raffel et al. [72] and Nobach and Bodenschatz [64].

At an average particle displacement of 4 pixels, the random error is 0.175 pixels or 4.3 %. By averaging the resulting velocity field obtained from the multiple repeats of each individual test case, the random error reduces according to $1/\sqrt{N}$, where N is the number of repeated runs [1]. Accounting for the bias error of 0.25 %, a total error of the order of 2 % is obtained. This compares well to the error estimate of 3 % provided by the inbuilt DaVis error tool, which evaluates the shift in correlation peak when mapping an interrogation window back to its original position according to the calculated displacement vector [103].

3.4 Experimental Set-Ups

The unsteady flow field is investigated using a variety of individual experimental set-ups, all aimed at isolating and interrogating specific phenomena. The cylinder described in section 3.4.1 is the most prominent part of the testing suite and is used to study the development of the unsteady boundary layer and the shedding rate. A modified set-up including both a cylinder and a flat plate wing described in section 3.4.2 investigates force production, whilst further insight into the boundary layer development is elucidated through the scoop experiment described in section 3.4.3. Ultimately, the set-up used to study cylinder-gust experiments is described in section 3.4.4.

3.4.1 Cylinder

A schematic diagram of the cylinder build is shown in figure 3.7. The cylinder is made from a hollow carbon fibre tube that sits on two bearings. These are attached to a hollow, load bearing, aluminium tube which is clamped to the force balance. A carbon fibre drive shaft is housed inside this tube and connects to an EC synchronous motor via a rotary coupling. The motor itself is mounted to the force balance and fitted with a digital encoder to measure the angular velocity. The drive shaft further attaches to a 3D printed plug at the far end of the cylinder, which in turn connects to the outer cylinder shell and transmits the rotary motion. The design aims to separate the two bearings, around which the cylinder rotates, as much as possible to achieve a smooth rotation with minimum eccentricity, minimizing vibrations which might contaminate the force measurements. The cylinder diameter D is either 0.04 m or 0.06 m and the span is 0.48 m. The skim plate leads to an effective cylinder aspect ratio of 16 or 24 respectively.

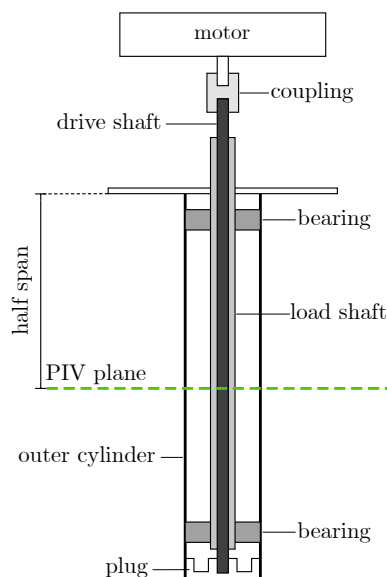


Fig. 3.7 Cylinder assembly.

The cylinder is vertically mounted to the force balance fixed to the carriage as shown in figure 3.8a. The top of the cylinder is in-line with the skim plate and any bridging is avoided to not affect force measurements. A top view of the camera and laser arrangement is shown in figure 3.14b. The two horizontal light sheets illuminate the flow on either side of the cylinder and the two cameras below, are positioned upstream and downstream of the cylinder to capture the complete surrounding flow field.

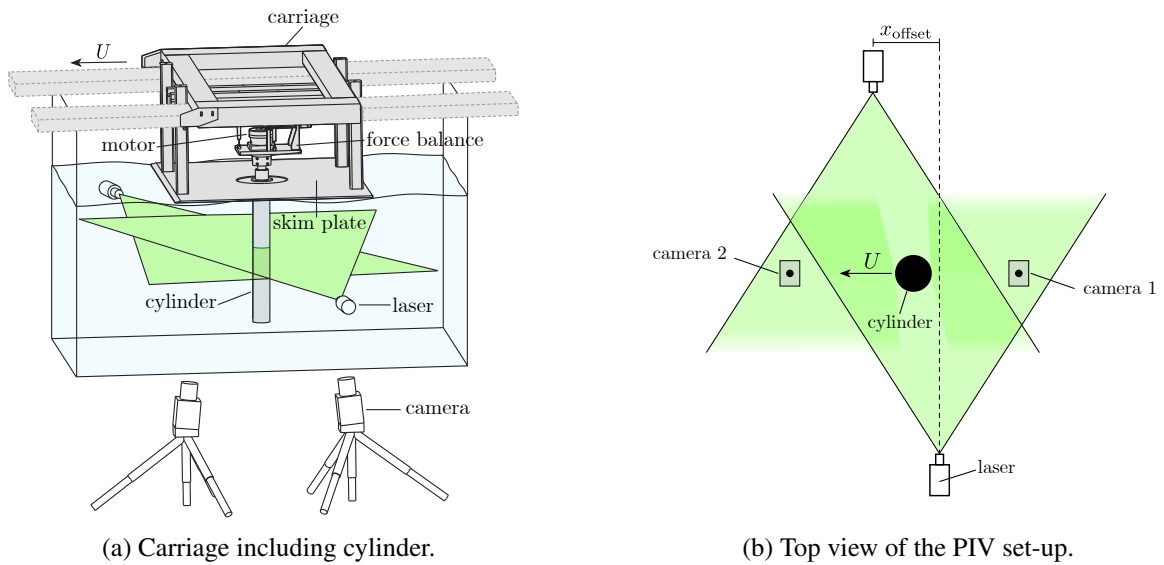
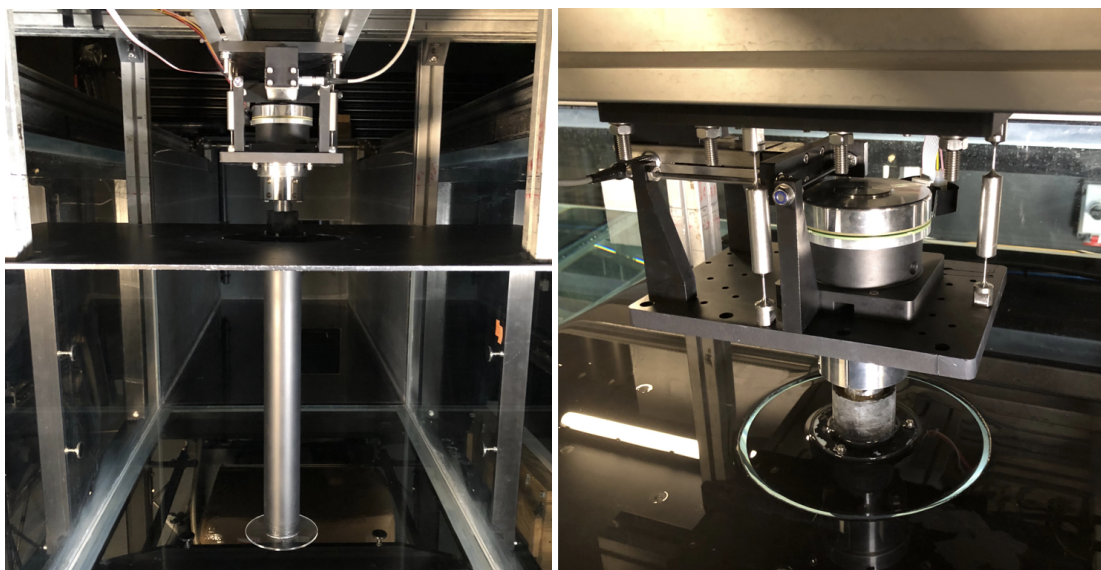


Fig. 3.8 Experimental set-up.

The complete set-up in the towing tank as well as a close-up of the motor mounted to the force balance is shown in figure 3.9. To improve the contrast between the illuminated particles and the surrounding fluid in the camera images used for the PIV measurements, the set-up is painted matte black as much as possible to minimize light scattering.



(a) Cylinder mounted to the carriage.

(b) Motor mounted to the force balance.

Fig. 3.9 Experimental set-up in the water tank.

Cylinder Kinematics

As part of this thesis, a number of cylinder kinematics are explored. The motions can be grouped into two main categories, as schematically illustrated in figure 3.10. The first set comprises of translation (also referred to as ‘surge’) only. Here, the cylinder accelerates linearly over a set distance s_{acc} from a stationary start to a final steady-state velocity, U_{∞} . The second kinematic group includes translation as well as rotation. The cylinder simultaneously begins to accelerate and rotate from a stationary start, where steady-state rotation is reached almost instantaneously. The details of the motion profiles are presented in table 3.2. Test cases c0, c1a, c1b and c2 will be analysed in detail in chapters 4 and 5. The more ‘extreme’ case c3a is used to test whether the presence of an endplate has a significant effect on the force results as well as to evaluate how accurately the experimental motion profile matches the theoretical ideal scenario.

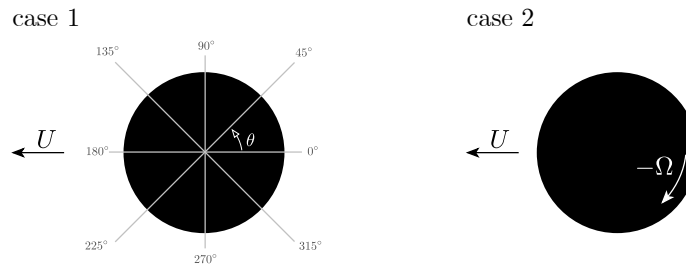


Fig. 3.10 Experimental configurations. The angle definition around the cylinder is also indicated.

Case	α	RPM	U_{∞} (ms ⁻¹)	Re	s_{acc}/D	$s_{\Omega_{\infty}}/D$	a (m)
c0	0	0	0.43	20000	3	-	0.03
c1a	1	153	0.32	10000	2	0.25	0.02
c1b	1	137	0.43	20000	2	0.15	0.03
c2	2.5	385	0.32	10000	2	0.23	0.02
c3a	3	411	0.43	20000	2	0.31	0.03

Table 3.2 Summary of the test cases. s_{acc} represents the acceleration distance and $s_{\Omega_{\infty}}$ the distance required to reach terminal angular velocity, Ω_{∞} .

Figure 3.11 shows an example of a cylinder motion, comparing the demanded and measured velocity, acceleration and RPM for case c3a where $Re = 20000$ and $\alpha = 3$, averaged over 5 runs. The ideal and experimental velocity trace match well throughout the motion, with some vibrations being noticeable during the steady-state region, as seen in figure 3.11a. The uncertainty associated with the instantaneous velocity is 1 %. The real acceleration overshoots and at the end of the acceleration phase decays to zero over some distance, compared to the ideal ‘top-hat’ case, as presented in figure 3.11b.

The rotation rate of the cylinder matches well to the ideal case, figure 3.11c, however, takes a finite distance before the steady-state region is reached.

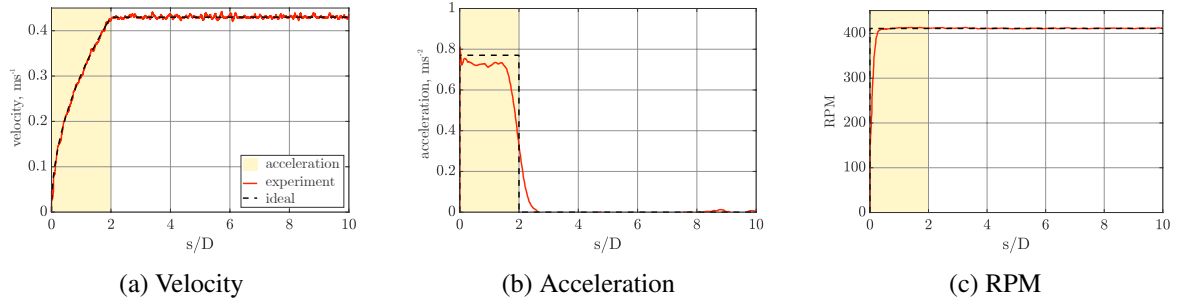


Fig. 3.11 Kinematic profile of the cylinder. Case c3a, $Re = 20\,000$, $\alpha = 3$.

Effect of an Endplate

The weakening effect of winglets or endplates on the wingtip vortex is well documented in the aerodynamic community [42, 47, 78, 89, 100]. Similarly, endplates can be used on rotating cylinders, where an endplate two times the diameter of the cylinder greatly reduces the pressure variation at the tip compared to the midspan [93]. Using an endplate at the free end of the cylinder reduces the scope of the PIV measurements, as the cameras need to be arranged such that the endplate does not obscure their field of view. It is therefore investigated whether an endplate needs to be used or whether it does not significantly alter the flow for the cases studied.

The comparison of the lift response with and without an endplate for $\alpha = 1$ and $\alpha = 3$ is shown in figures 3.12a and 3.12b, respectively. When $\alpha = 1$, C_l features a series of peaks and troughs with successively decreasing amplitude. The behaviour and steady-state lift force is identical with and without the endplate. At the higher rotation ratio of 3, C_l increases steadily until it eventually asymptotes to a constant value. A significant difference in the steady-state force is observed. For low translation distances, however, the effect of the endplate is minimal. The results therefore suggest that for the kinematic motions and short translation distances studied here, the force evolution is not significantly affected by an endplate and this is therefore not required for the experiments conducted.

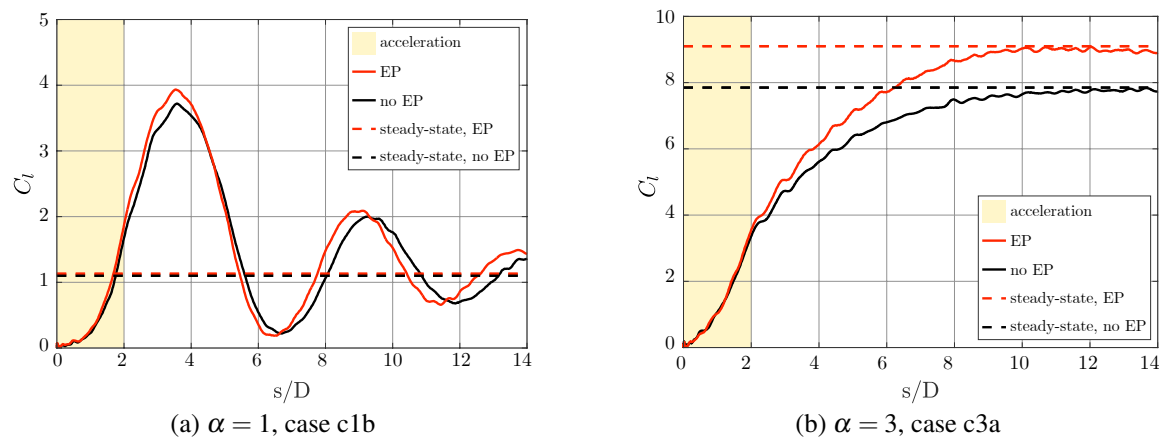


Fig. 3.12 C_l when an endplate two times the cylinder diameter and when no endplate is fitted.

3.4.2 Multi-Body - Cylinder + Plate

The force development in a multi-body flow field is investigated using a simultaneously surging cylinder and a flat plate wing, as shown in figure 3.13. The cylinder is mounted to the force balance such that it is flush with the skim plate and has the same dimensions outlined in section 3.4.1, a diameter and span of 0.06 m and 0.48 m, respectively. However, to ensure complete optical access to the entire flow field, the construction of the cylinder differs. The cylinder consists of a single outer shell which is made from clear see-through acrylic. It is painted matt black everywhere apart from a small region around the midspan, as to allow the laser sheet to pass through.

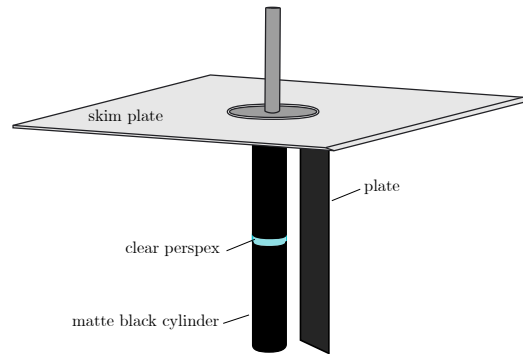
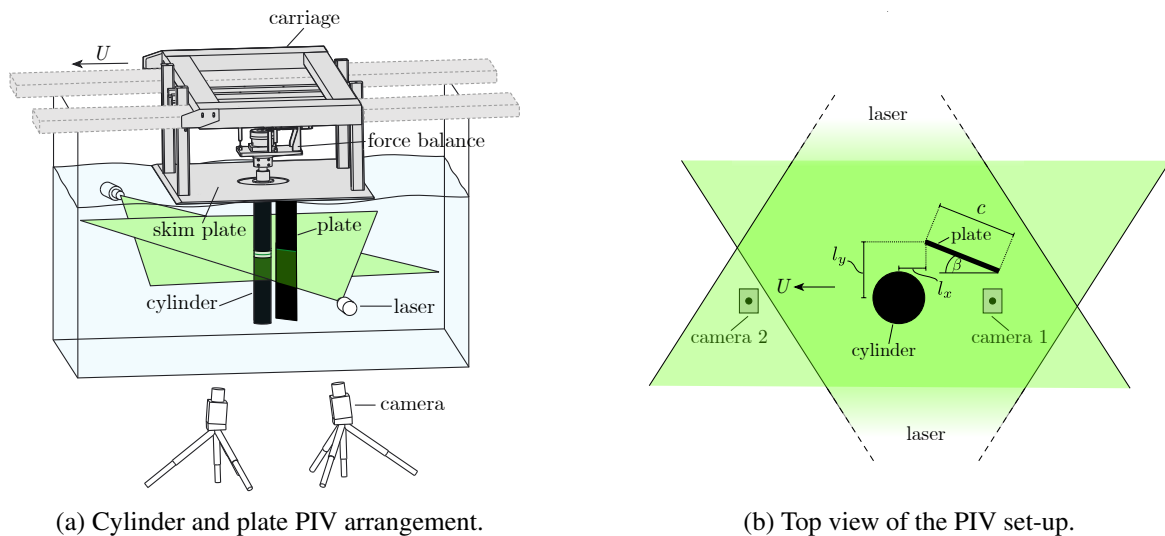


Fig. 3.13 Schematic illustration of the cylinder and plate assembly.

The complete set-up in the towing tank and a top-view of the arrangement is shown in figure 3.14. A dual light sheet is once again used to eliminate any shadow regions and two cameras below the tank capture the complete field of view. The aluminium flat plate is mounted to the skim plate and positioned such that the leading edge is offset by l_x and l_y from the cylinder centre, whilst it is orientated at an angle of attack β . The span is the same as the cylinder and it has a chord length, c and width, w . It is painted matte black to reduce reflections from the laser.



(a) Cylinder and plate PIV arrangement.

(b) Top view of the PIV set-up.

Fig. 3.14 Experimental set-up.

Multi-Body Kinematics

Three different tests are performed, as presented in table 3.3. In the first test case, the cylinder is linearly accelerated in isolation over a distance s_{acc} of two diameters to a final velocity U_∞ of 0.43 ms^{-1} , reaching a Reynolds number of 20000. In the second case, the cylinder kinematics are unchanged but a flat plate wing, $c = 0.045$, at an angle of attack β of 40° , is mounted a short distance downstream. For the final test case, the small wing is replaced by a larger plate orientated at $\beta = 22^\circ$ where $c = 0.09 \text{ m}$. The linear acceleration is performed over half a cylinder diameter and $U_\infty = 0.22 \text{ ms}^{-1}$, such that the cylinder based Reynolds number is 10000.

Case	Description	β (deg)	c (m)	w (m)	l_x/D	l_y/D	s_{acc} (s/D)	U_∞ (ms^{-1})	Re
m1	cyl	-	-	-	-	-	2	0.43	20000
m2	cyl + plate	40	0.045	0.003	0.3	1.2	2	0.43	20000
m3	cyl + plate	22	0.09	0.003	0.3	1.0	0.5	0.22	10000

Table 3.3 Overview of multi-body test cases.

3.4.3 Scoop

To generate an accelerating flow field around a stationary flat plate in an otherwise quiescent fluid, a ‘scoop’ is designed as shown in figure 3.15. A carbon fibre plate is equipped with two forward directed side skirts that enclose the region around a stationary flat plate. The side skirts are 3D printed using ABS plastic and extend 0.135 m in front of the flat plate. They have a thickness of 0.005 m, a total span of 0.235 m and a width of 0.14 m. A see-through piece of perspex is placed at the midspan location of the side skirts to allow the laser sheet to illuminate the complete flow field. The aluminium stationary flat plate has a span of 0.48 m, a thickness of 0.005 m and a chord length c of 0.045 m, resulting in an effective aspect ratio of 21 due to the presence of the skim plate. All surfaces, except the perspex, are painted matte black to minimize reflections contaminating the PIV images.

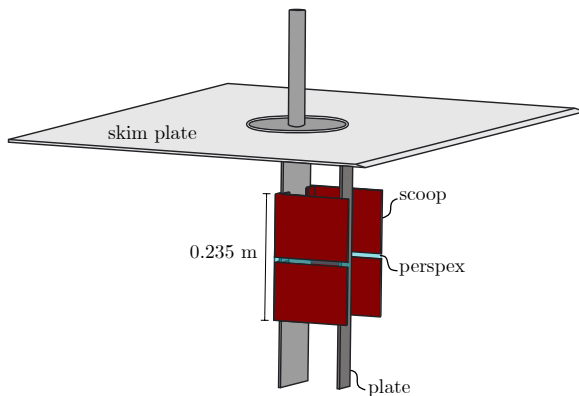


Fig. 3.15 Scoop and stationary plate arrangement.

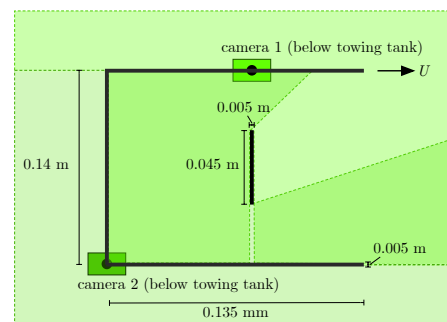


Fig. 3.16 PIV top view.

To remove any shadow regions, the camera arrangement shown in figure 3.16 is used. Camera 1 is aligned with one of the side skirts as well as the stationary flat plate. This provides the optical access to the region extending to the back wall of the scoop and the opposing skirt. To capture the remaining flow field, camera 2 is placed at the opposing corner, such that it is in line with the back of the scoop as well as the second side skirt, when the scoop is in its initial starting position. Together, the cameras are now able to capture the complete flow field, where the final velocity vectors are the result of 8 runs, which are processed independently and averaged thereafter.

Scoop Kinematics

The scoop, which is mounted to the carriage, accelerates at a constant rate over a distance of one plate chord (0.045 m) to a final velocity of 0.11 ms^{-1} , or an equivalent Reynolds number of 4000, whilst the plate is held in place by an external support.

3.4.4 Gust Rig

To investigate force generation during a body gust encounter, the gust rig developed by Corkery [14] is used in conjunction with the towing tank, as shown in figure 3.17. The cylinder with the transparent midspan described in section 3.4.2 is mounted to the carriage and towed through the open section of the gust rig to simulate a transverse, top-hat shaped gust encounter. The gust rig itself consists of an outlet and a collector, which are connected to each other via a pump, and generates a flow perpendicular to the motion of the carriage. A gap in the collector allows for the laser sheet to pass through and illuminate midspan of the cylinder as shown in figure 3.17b

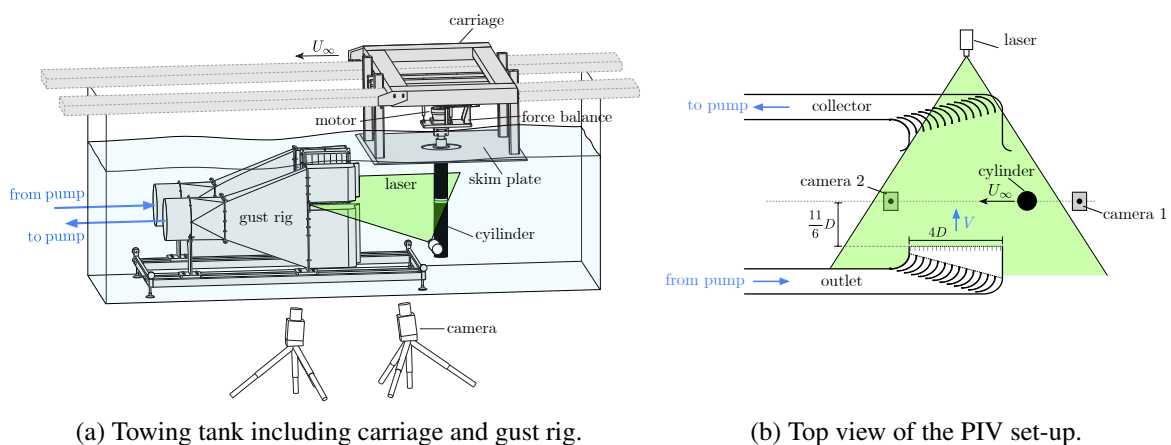


Fig. 3.17 Experimental set-up.

The gust is 600 mm high and 0.24 m wide, equating to a width of $4D$. This is sufficient to reach 70 % of the transient response in Küssner's theory for a flat plate [14]. The cylinder centre passes the outlet at a distance of 0.11 m; ($11/6D$) and the top of the outlet is 0.03 m below the skim plate to avoid any clashes.

The transverse gust flow is created by a 2.25 kW 3-phase motor, which drives an axial flow pump through a pulley configuration with a gear ratio of 2.25:1. A frequency inverter is used to allow continuous adjustment of the gust strength. The flow velocity is dependent on pump RPM and increases linearly until 800 RPM after which the pump appears to stall. This leads to an approximate maximum velocity of 0.4 ms^{-1} [14].

The vorticity contours of the gust flow are shown in figure 3.18a. The path taken by the cylinder centre as it traverses the gust is also indicated. The transverse velocity profile normalised by the average gust velocity, v/\bar{V} , is shown in figure 3.18b at various stream-normal locations inside the gust. It is observed that the gust shear layers diffuse with distance from the gust outlet, leading to a less sharp gust profile. At the location where the cylinder crosses the gust, the shear layer width, δw_{gust} , is approximately $0.5D$. Furthermore, some gust non-uniformity is observed within the gust and a small yet non-zero velocity V_{init} is recorded outside the gust.

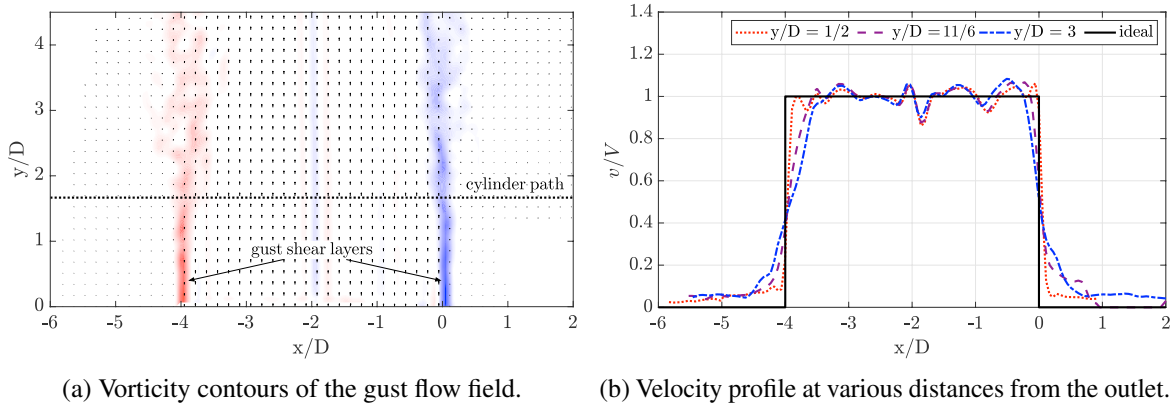


Fig. 3.18 Gust flow field.

Cylinder Kinematics and Gust Ratios

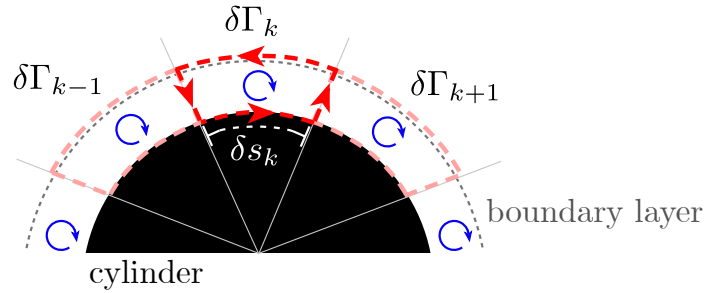
The cylinder centre is initially located $1.4D$ upstream of the gust outlet. From a stationary start, the cylinder accelerates within $0.5D$ to its final velocity of 0.129 ms^{-1} , equivalent to a Reynolds number of 6000. Three different nominal gust ratios, 0.5, 1 and 1.5, are explored, as summarized in table 3.4. The actual gust velocities, however, differed slightly from the target value, as also indicated in table 3.4. Any cylinder forces presented later are therefore normalised by the actual gust ratio rather than by the ideal gust strength.

Case	GR_{true}	GR_{nominal}	U_{∞}	Re
g1	0.42	0.5		
g2	0.94	1.0	0.129	6000
g3	1.55	1.5		

Table 3.4 Summary of the cylinder-gust cases.

3.5 Measuring the Boundary Layer Vortex Sheet

Measuring the boundary layer vortex sheet, which derives from the boundary layer vorticity, is at the core of this investigation. Despite the fact that the boundary layer velocity distribution is not fully resolved, it is possible to determine the boundary layer vorticity magnitude as long as the tangential boundary layer edge velocity as well as the body surface motion is known. To robustly compute the vortex sheet strength experimentally, the body surface and the surrounding flow field are split up into k elements or wedges, as shown in figure 3.19.

Fig. 3.19 'Wedge' discretization used to compute γ^b

The circulation contained within each discrete element is computed by integrating the velocity, \mathbf{u} , aligned with the contour of each element,

$$\delta\Gamma_k = \oint \mathbf{u} \cdot d\mathbf{l}. \quad (3.3)$$

The velocity along the cylinder surface is set to the true wall velocity and linear interpolation is used to obtain the flow velocity along the remaining integration path, as it cannot be guaranteed that PIV velocity vectors lie exactly on the specified contour of each element. The vortex sheet strength is ultimately obtained by dividing $\delta\Gamma_k$ by the segment length δS_k ,

$$\gamma_k = \frac{\delta\Gamma_k}{\delta S_k}. \quad (3.4)$$

Near the separation point or when the separating vortex is located in very close proximity to the body surface, vorticity that has already been shed can sometimes erroneously be included in the

calculation of γ^b , as schematically illustrated in figure 3.20, and leads to an incorrect vortex sheet distribution. This occurs when shed vorticity resides within the contour of the elements used to find γ^b . In light of this, the height of the 70 elements used to discretize the cylinder surface is adjusted accordingly and set to $\delta y = D/15$. Increasing the number of elements results in the same distribution albeit with more noise [14].

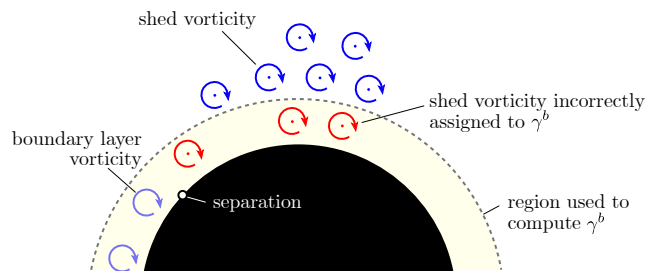


Fig. 3.20 Schematic illustration showing how shed vorticity can incorrectly be associated with γ^b .

3.6 Summary: Experimental Methodology

The chapter describes the equipment and measurement techniques used during this study. A water towing tank is at the core of the experiments, to take advantage of Reynolds number scaling effects. Force data is acquired using a two-component force balance, whilst the flow field is assessed using planar PIV. Here, a dual light-sheet and camera arrangement are employed to capture the complete flow field. A surging and rotating cylinder is utilized to study the development of the boundary layer vorticity, since different rotation ratios can significantly affect the unsteady flow field without requiring a change in geometry. The boundary layer development is further assessed using a scoop, which creates an accelerating freestream around a stationary flat plate. The force development in a multi-body flow field is analysed by positioning a flat plate in close proximity to the circular cylinder mounted to the force balance. To further study the unsteady force development, a gust rig is used to create a transverse top-hat shaped gust profile. Measuring the boundary layer vortex sheet is an integral part of this study. To robustly compute this distribution, the body surface and surrounding flow field are discretized into a series elements, making it possible to determine the vortex sheet strength at each location.

Chapter 4

Boundary Layer Evolution

A boundary layer forms along the surface of an object and develops as the unsteady flow field evolves. From the literature review we learnt that the force acting on an object is linked to the rate at which vorticity moves and changes in strength. In this regard, boundary layer vorticity plays an important role. Not only does its distribution evolve when the kinematics of the object change or the flow field develops, but it also acts as a source of free vorticity during unsteady separation. Predicting the unsteady separation point has consequently been of substantial interest to the aerodynamics community, where boundary layer vorticity is, directly or indirectly, involved in many of the proposed strategies. Understanding the evolution of the boundary layer vorticity is therefore crucial to form a complete picture of the unsteady flow field that we aim to approximate through low order models. To progress with this endeavour, we focus on the boundary layer vortex sheet and its constituent parts throughout this chapter. We begin by revisiting the vortex sheet distribution from a theoretical perspective in section 4.1. Thereafter, we explore how the boundary layer vortex sheet is created during an accelerating freestream in section 4.2, in order to isolate the effect of externally created vorticity. Having familiarised ourselves with the true origin of the boundary layer vorticity, we analyse the development of the boundary layer vortex sheet distribution and its strength at the separation point in section 4.3. This aims to elucidate the reasons for the vortex sheet behaviour as the unsteady flow field develops and how this ties into the strength observed at the unsteady separation point.

4.1 The Boundary Layer Vortex Sheet: A Theoretical Overview

Boundary layer vorticity arises in viscous flow because of the no-slip condition along an object's surface. In potential flow it is possible to represent this vorticity as an infinitely thin vortex sheet that enforces the no-penetration condition [81]. From the literature review we found that distinct portions of the boundary layer vortex sheet can be attributed to individual kinematics or flow phenomena. A simplified schematic overview of the individual vortex sheet components around a circular cylinder is shown in figure 4.1. Translation creates an added mass vortex sheet γ_{am}^{nc} with zero net circulation, whilst a further boundary layer vortex sheet contributions can be attributed to rotation, γ^r . Free

vorticity residing within the flow field creates an additional contribution to the boundary layer vortex sheet, and is divided into two groups. One arises because of vorticity shed by the cylinder itself γ^{shed} , whilst a second results from externally created vorticity γ_{ext}^{nc} . The former is classified as a *circulatory* vortex sheet, since its net circulation can be non-zero, whilst γ_{ext}^{nc} is of *non-circulatory* nature since its total circulation is always zero.

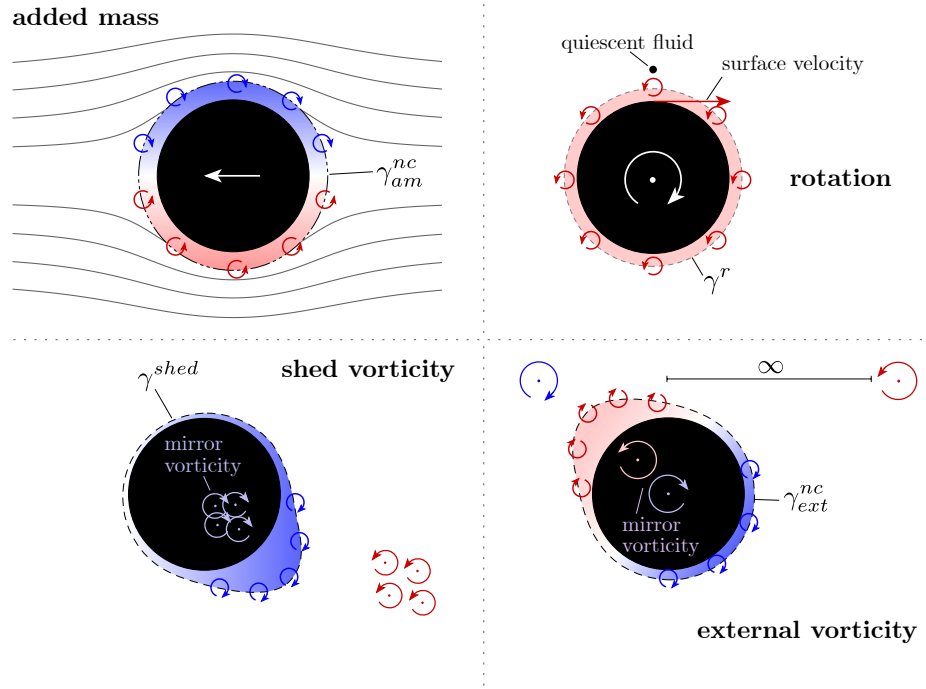


Fig. 4.1 Vortex sheet contributions.

4.1.1 γ_{am}^{nc} and γ^r : Vortex Sheets due to Kinematics

γ_{am}^{nc} : Vortex Sheet due to Translation

When an object begins to translate, a non-circulatory *added mass* vortex sheet γ_{am}^{nc} is created. Its name derives from the fact that the sheet has zero net circulation and that its rate of change can be linked to an added mass force as the body accelerates [16, 31]. In potential flow it is usually assumed that the fluid domain extends into the object. The flow field is viewed to be correct external to the body, whereas the internal distribution arises somewhat arbitrarily depending on the mathematical construction of the problem. Here, we instead assume that the velocity within the cylinder is the prescribed kinematic motion. It follows that the vortex sheet is the slip velocity between the external flow, u_θ and the true cylinder wall velocity u_θ^{cyl} ,

$$\gamma_{am}^{nc} = u_\theta - u_\theta^{cyl}. \quad (4.1)$$

To obtain the external tangential velocity, we first represent the cylinder by a doublet, such that on the cylinder surface the potential reads

$$\Phi = Ua \cos \theta. \quad (4.2)$$

Thereafter, the gradient of the potential in the circumferential direction gives u_θ . For this we differentiate the potential with regards to θ , where this represents a position on the cylinder surface in terms of angle (alternatively $x = a \cos \theta$), and divide by the cylinder radius a ,

$$u_\theta = \frac{1}{a} \frac{d\Phi}{d\theta} = -U \sin \theta. \quad (4.3)$$

When the cylinder travels at a velocity U , the internal velocity along the surface is $u_\theta^{cyl} = U \sin \theta$. The vortex sheet, equal to the slip velocity, is consequently

$$\gamma_{am}^{nc} = -2U \sin \theta. \quad (4.4)$$

A graphical and quantitative representation of this distribution is shown in figure 4.2. If we account for the instantaneous velocity U then it follows from equation 4.4 that the vortex sheets for different U collapse onto a single distribution. Moreover, before any unsteady separation occurs, the boundary layer vortex sheet is entirely governed by the body geometry and the kinematic motion.

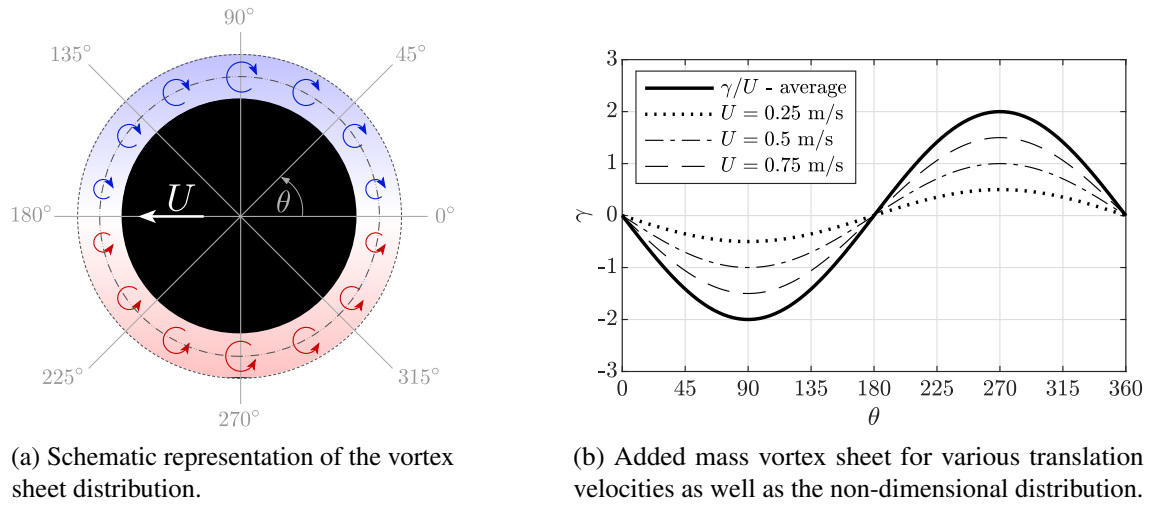


Fig. 4.2 Vortex sheet distribution around a translating cylinder. Non-dimensionalizing with instantaneous velocity collapses the vortex sheet strength.

By evaluating the time variation of the vortex sheet distribution γ_{am}^{nc} , the related force response in the x -direction can be calculated.¹ To do so, we follow Wu's approach discussed in section 2.3.3. First, we find the impulse

$$I_x = \oint_{B_b} y \gamma_{am}^{nc} dl, \quad (4.5)$$

¹The force is zero in the y -direction, due to the symmetry of the flow around the cylinder.

which, using $y = a \sin \theta$ and $dl = a d\theta$, can be re-written as:

$$I_x = a^2 \oint_0^{2\pi} \gamma_{am}^{nc} \sin \theta d\theta. \quad (4.6)$$

Substituting the expression for γ_{am}^{nc} (4.4) yields

$$I_x = -2\pi U a^2. \quad (4.7)$$

The drag force acting on the cylinder is now found by evaluating the time rate of change of the impulse,

$$\begin{aligned} F_x &= -\rho \frac{dI_x}{dt} + \rho \frac{d}{dt} \int_{R_b} -U dR. \\ &= \rho \pi a^2 \frac{dU}{dt}. \end{aligned} \quad (4.8)$$

The result is identical to the added mass force derived in section 2.4.1 using the unsteady Bernoulli equation. This highlights how the added mass force can equally be calculated by assessing the rate of change of γ_{am}^{nc} and thus gives the vortex sheet its name.

γ^r : Vortex Sheet due to Rotation

A further vortex sheet contribution γ^r is created by the rotational motion of the cylinder. A slip velocity exists between the moving cylinder surface u_θ^{cyl} and the quiescent surrounding $u_\theta = 0$. γ^r is therefore equal and opposite to the angular velocity multiplied by the cylinder radius such that,

$$\begin{aligned} \gamma^r &= u_\theta - u_\theta^{cyl} \\ &= -\Omega a. \end{aligned} \quad (4.9)$$

γ_{am}^{nc} and γ^r : Extension to a Flat Plate

Equivalent vortex sheet distributions can be computed for a surging and rotating flat plate. This is achieved by taking the representation of an ellipse in potential flow, as provided by Milne-Thomson [60] or Lamb [46], to the limit case of zero thickness along the minor axis. To do so, potential and streamfunctions are first derived about a circle with unit radius located in the complex ζ -plane, where $\zeta = \varepsilon + i\eta$. Thereafter, the circle is mapped to a plate with chord c in the z -plane using the transformation

$$z = \frac{c}{4} (\zeta + 1/\zeta). \quad (4.10)$$

A visual illustration of the transformation is shown in figure 4.3.

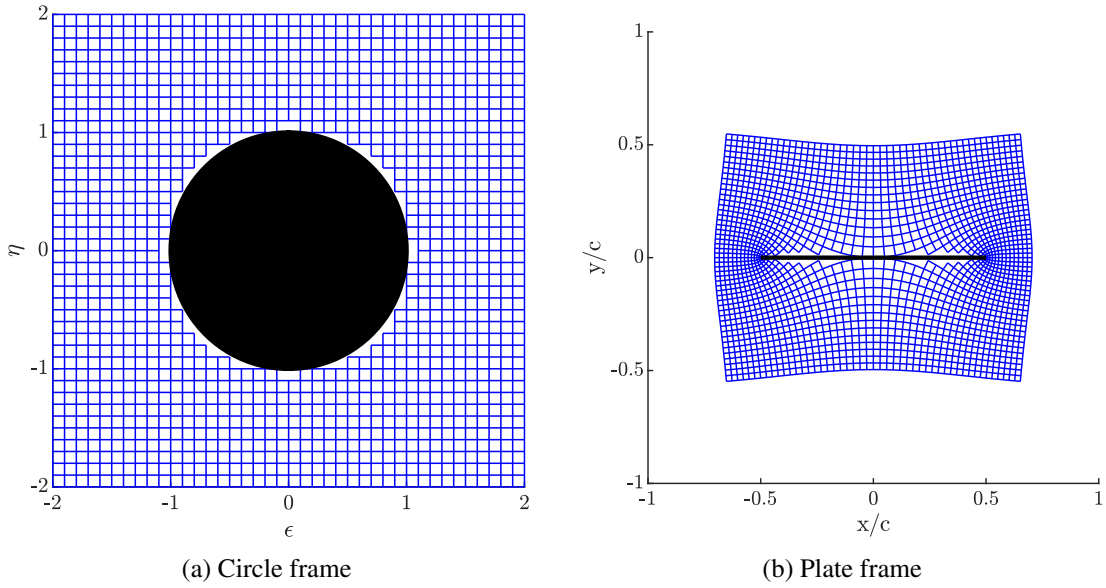


Fig. 4.3 Coordinate transformation mapping a plate onto a cylinder.

The resulting vortex sheet distribution along the plate surface in polar coordinates is

$$\begin{aligned}
 \gamma_{am}^{nc}(\theta) &= u(-\theta) - u(\theta) \\
 &= \underbrace{-2U_n \frac{\cos \theta}{\sin \theta}}_{\text{translation}} - \underbrace{\Omega \frac{c \cos 2\theta}{2 \sin \theta}}_{\text{rotation}}, \tag{4.11}
 \end{aligned}$$

where θ is the argument of ζ and describes a position on the circle surface. In Cartesian coordinates, where U_n and Ω are the plate normal and angular velocities, respectively, the vortex sheet reads

$$\gamma_{am}^{nc}(x) = \underbrace{-2U_n \frac{x}{\sqrt{(c/2)^2 - x^2}}}_{\text{translation}} - \underbrace{\Omega \frac{2x^2 - (c/2)^2}{\sqrt{(c/2)^2 - x^2}}}_{\text{rotation}}. \tag{4.12}$$

Vortex sheets for various normal and angular velocities are shown in figure 4.4, where it is observed that the vortex sheets scale with their respective kinematics. This non-dimensional form allows a single curve to be representative of an entire kinematic range and enables comparisons between different data sets.

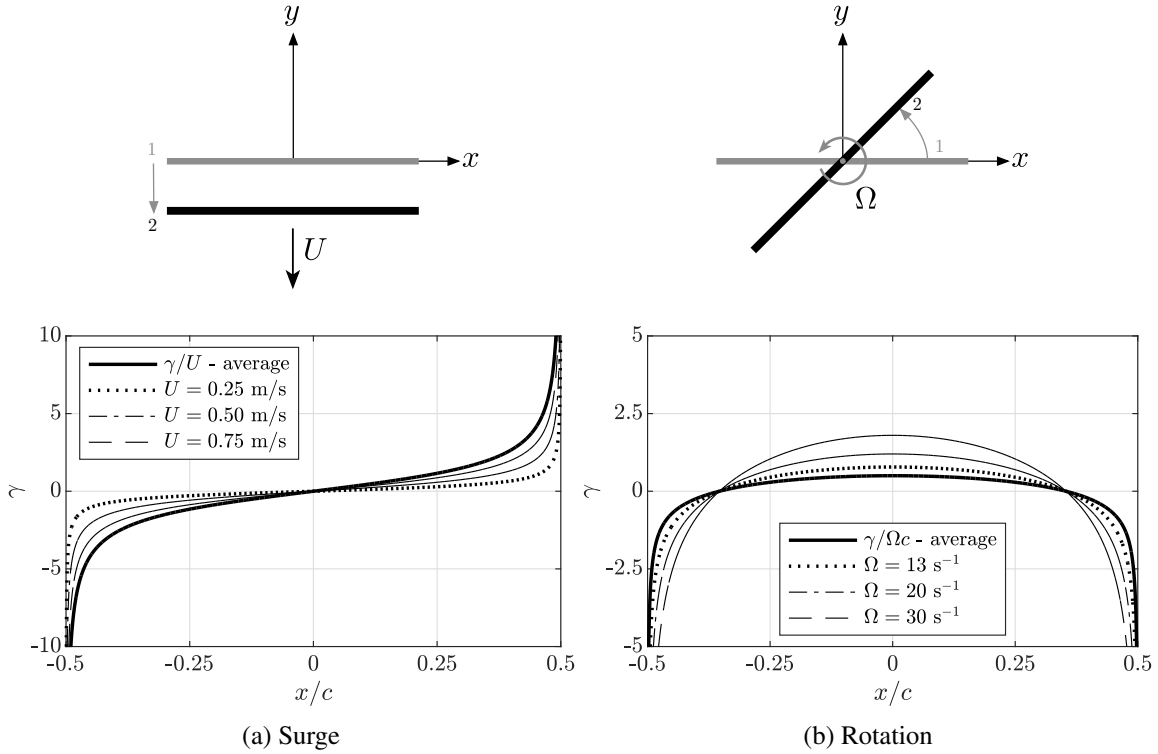


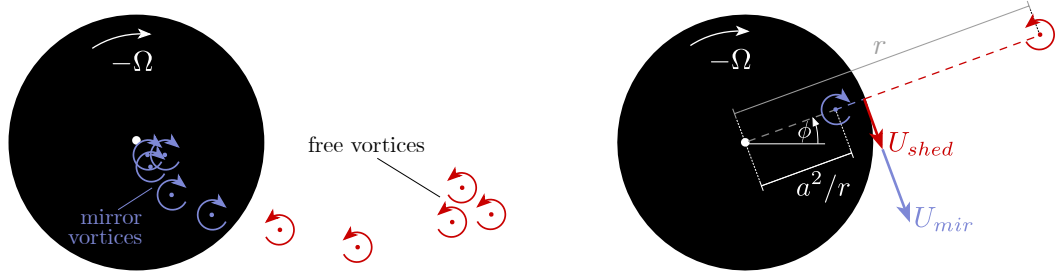
Fig. 4.4 Theoretical vortex sheet due to translation and rotation for a flat plate.

4.1.2 γ^{shed} : Vortex Sheet due to Shed Vorticity

When the boundary layer separates, vorticity is shed and carried into the outer flow via the detached shear layer. In a real viscous flow, any shed vorticity must have an equal and opposite mirror image located in the boundary layer, in order to conserve circulation [40]. Since we choose to model the flow using potential flow theory, free vorticity, which is labelled as such when it is not part of the boundary layer and is instead distributed in the surrounding flow field, can be represented by an element of vorticity or a point vortex. Following the workings outlined by Milne-Thomson [60] and Graham et al. [31], and using a singularity approach to represent the flow field, each element of free vorticity has a mirror image within the cylinder at position

$$z_{k,mir} = \frac{a^2}{r_k} e^{i\phi_k}, \quad (4.13)$$

where a is the cylinder radius, r_k is the distance between the element of free vorticity and the cylinder centre and ϕ_k is the angle from the horizontal to this element, as shown in figure 4.5. Placing a mirror vortex inside the cylinder conserves the circulation of the flow field and enforces the no-penetration condition due to the corresponding free vortex by forming a closed streamline at the cylinder surface [31].



(a) Free vortex elements and their respective mirror images.

(b) Induced velocity along the cylinder surface due to a free and mirror vortex pair.

Fig. 4.5 Calculating the vortex sheet due to free vorticity.

Alternatively, a vortex sheet approach can be used to enforce the no-throughflow condition. The circulatory vortex sheet γ^{shed} arises from the slip velocity induced by each vortex pair as shown in figure 4.5b. Mathematically, the tangential velocity induced by a vortex pair at the surface may be calculated by first forming the complex potential $F_k(z)$ due to the free vortex and its mirror image located within the cylinder,

$$F_k(z) = -i \frac{\Gamma_k}{2\pi} \ln \left(\underbrace{\frac{z - z_k}{z - z_{k,mir}}}_{\text{mirror image}} \right), \quad (4.14)$$

free vorticity

where the complex potential for the vortex pair is defined as $F_k(z) = \Phi_k + i\psi_k$. Here Φ_k represents the potential and ψ_k the streamfunction. The complex potential is now differentiated with respect to z to obtain the u_k and v_k velocity components,

$$u_k - iv_k = \frac{dF}{dz} = i \frac{\Gamma_k}{2\pi} \frac{z_{k,mir} - z_k}{(z - z_{k,mir})(z - z_k)}. \quad (4.15)$$

We are reminded that $z = ae^{i\theta}$ defines a position on the cylinder surface, whilst $z_k = r_k e^{i\phi_k}$ refers to the position of the free vortex in the flow field, and $z_{k,mir} = \frac{a^2}{|z_k|} e^{i\phi_k}$ defines the location of the mirror vortex inside the cylinder. It follows that the contribution to the vortex sheet can be calculated from the tangential velocity $u_{\theta,k}$ induced by free vorticity in the flow field and its mirror images within the cylinder,

$$\gamma_k^{shed}(\theta) = u_{\theta,k}. \quad (4.16)$$

The flow field may be populated with N free vortices, each of which contribute to the circulatory vortex sheet. γ^{shed} can therefore be found by linearly superposing the individual contributions,

$$\gamma^{shed} = \sum_{k=1}^N \gamma_k^{shed}. \quad (4.17)$$

γ^{shed} for a Flat Plate

To compute the equivalent circulatory vortex sheet for a flat plate, conformal mapping is first used to transform the plate into a cylinder. A circle with radius $a = c/4$ in the ζ -plane, is linked to a plate of length c in the z -plane through the transformation

$$z = \zeta + \frac{(c/4)^2}{\zeta}. \quad (4.18)$$

The conditions affecting the circle in the mapped plane are unchanged to those experienced by the plate. Circulation is conserved and the no-throughflow condition remains enforced on the circle surface. Identical to the process discussed earlier for the cylinder, the global conservation of circulation and the local circle boundary condition due to an element of free vorticity Γ_k at ζ_k is enforced by placing a single mirror vortex of opposite magnitude $-\Gamma_k$ at $\zeta_{k,mir} = \frac{a^2}{|\zeta_k|} e^{i\phi_k}$ within the circle [31]. The slip velocity created by each vortex pair along the circle surface is subsequently found and related back to the original reference frame of the plate to give the circulatory vortex sheet distribution along the plate surface.

The complex potential for the vortex pair, written as $F_k(\zeta) = \Phi_k + i\psi_k$, where Φ_k still represents the potential and ψ_k the streamfunction, is

$$F_k(\zeta) = -i \frac{\Gamma_k}{2\pi} \ln \left(\frac{\zeta - \zeta_k}{\zeta - \zeta_{k,mir}} \right). \quad (4.19)$$

Differentiation with regards to z gives the velocities in the plate reference frame

$$u_k - iv_k = \frac{dF_k}{dz} = \frac{dF_k}{d\zeta} \frac{d\zeta}{dz}, \quad (4.20)$$

which when evaluated yields,

$$u_k - iv_k = \frac{i\Gamma_k}{2\pi} \frac{\zeta^2(\zeta_{k,mir} - \zeta_k)}{(\zeta^2 - (c/4)^2)(\zeta - \zeta_{k,mir})(\zeta - \zeta_k)}. \quad (4.21)$$

Since we assume the plate to be aligned horizontally, the tangential velocity u_k along the plate surface is equivalent to the slip velocity and can therefore be used to obtain γ^{shed} . Inserting the definition of

the circle surface $\zeta = ae^{i\theta}$ into equation 4.21 gives

$$u_k(\theta) = \frac{-\Gamma_k}{\pi c \sin \theta} \frac{(c/4)^2 - |\zeta_k|^2}{|\zeta_k|^2 - \frac{1}{2}|\zeta_k|c \cos(\theta - \phi_k) + (c/4)^2}, \quad (4.22)$$

where θ represents the angle from the horizontal to a location on the circle surface in the ζ -plane and transforms to the plate surface in the z -plane according to $x = (c/2) \cos \theta$. The vortex sheet created by the vortex pair is subsequently found by evaluating the difference in slip velocity on either side of the infinitely thin plate

$$\gamma_k^{shed}(\theta) = u_k(-\theta) - u_k(\theta), \quad (4.23)$$

where $0 \leq \theta \leq \pi$. The process above may be repeated for all N free vortices in the flow field. Through linear superposition, the individual contributions are added together to give the total circulatory vortex sheet distribution,

$$\gamma^{shed} = \sum_{k=1}^N \gamma_k^{shed}. \quad (4.24)$$

4.1.3 γ_{ext}^{nc} : Vortex Sheet due to Externally Generated Vorticity

The vortex sheets explored so far have been created as a result of kinematic motion of the body or due to vorticity shed by the object. The final scenario that we would like to consider is what happens to the boundary layer vortex sheet when free vorticity is produced by external means. This idea is explored by considering a stationary object immersed in an accelerating freestream. Vorticity is created at the interface between the bulk fluid motion and its surroundings. This could occur at the boundary between a moving and quiescent fluid or in the boundary layer that forms along a wind tunnel wall. Conceptually, there is no difference between this *externally* created vorticity and the vorticity that is shed by the body itself discussed in section 4.1.2.

To illustrate this idea, we can imagine a freestream to be created by two point vortices (of strength $\pm \Gamma$) located above and below ($\pm \eta$) a cylinder, as graphically illustrated in figure 4.6. The vortex pair induces a freestream at the location of the cylinder, which approaches uniformity when the vortices are an infinite distance from the cylinder. In turn a vortex sheet is required to enforce the no-throughflow condition along the cylinder surface.

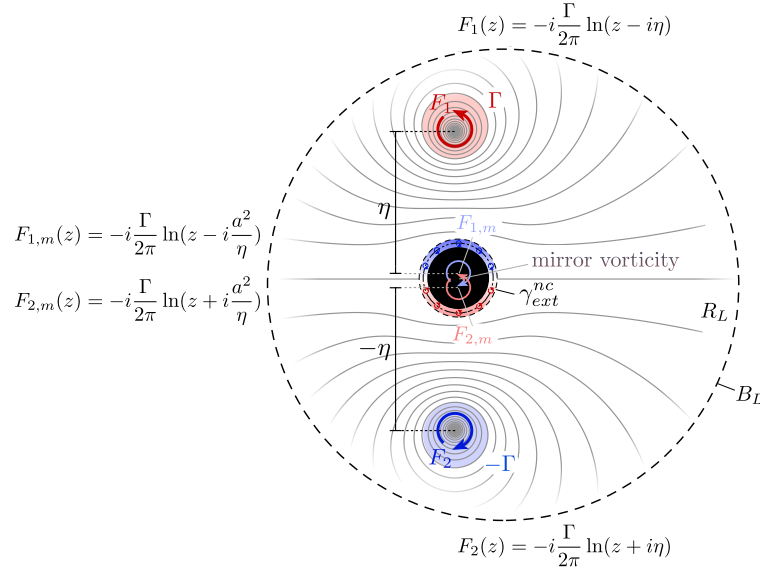


Fig. 4.6 Uniform freestream induced by a pair of counter-rotating vortices around a stationary cylinder. The complex potentials ($F_1(z)$, $F_{1,m}(z)$, $F_2(z)$, $F_{2,m}(z)$) for each vortex are indicated.

The theoretical distribution of the vortex sheet created through the external pair of counter-rotating point vortices can be calculated by following the steps outlined by Corkery [14]. The U -velocity induced by the vortex pair along the y -axis is given by

$$U(y) = \frac{\Gamma}{\pi} \left(\frac{\eta}{\eta^2 - y^2} \right). \quad (4.25)$$

To induce a uniform freestream, the vortices need to be infinitely far away from the cylinder. At this distance, the strength required to induce a velocity U at $y = 0$ is

$$\Gamma = \pi\eta U. \quad (4.26)$$

Each vortex located at z_1 and z_2 has a mirror image at $z_{1,m} = a^2 z_1 / |z_1|$ and $z_{2,m} = a^2 z_2 / |z_2|$. They are of equal and opposite strength and thereby conserve the circulation of the flow field. At the same time, they form a closed streamline on the cylinder surface, thereby enforcing the no-throughflow condition. The complete flow field is represented by the complex potential

$$\begin{aligned} F_0(z) &= F_1(z) + F_{1,m}(z) + F_2(z) + F_{2,m}(z) \\ &= -i \frac{\Gamma}{2\pi} \ln \left(\frac{(z - i\eta)(z\eta + ia^2)}{(z + i\eta)(z\eta - ia^2)} \right), \end{aligned} \quad (4.27)$$

where $F_1(z)$, $F_{1,m}(z)$, $F_2(z)$, $F_{2,m}(z)$ represent the complex potentials for each of the four vortices, as shown in figure 4.6. Replacing Γ by the vortex strength found in equation 4.26 yields

$$F_0(z) = -iU \frac{\eta}{2} \ln \left(\frac{(z - i\eta)(z\eta + ia^2)}{(z + i\eta)(z\eta - ia^2)} \right). \quad (4.28)$$

To avoid an unbounded infinite solution when taking the limit $\eta \rightarrow \infty$, Corkery [14] shows that we must first create a new complex potential that is zero at $z = a$. We therefore create a reference point at $z = a$ where the complex potential is

$$F_{ref}(z) = -iU \frac{\eta}{2} \ln \left(\frac{(a - i\eta)(a\eta + ia^2)}{(a + i\eta)(a\eta - ia^2)} \right), \quad (4.29)$$

and subsequently take the difference between F_0 and F_{ref} to arrive at the new complex potential

$$\begin{aligned} F(z) &= F_0(z) - F_{ref}(z) \\ F(z) &= -iU \frac{\eta}{2} \ln \left(\frac{(z - i\eta)(z\eta + ia^2)(a + i\eta)(a\eta - ia^2)}{(z + i\eta)(z\eta - ia^2)(a - i\eta)(a\eta + ia^2)} \right). \end{aligned} \quad (4.30)$$

Taking the limit $\eta \rightarrow \infty$, and discarding the arbitrary constant $-2a$ that remains, gives the complex potential

$$F(z) = \underbrace{Uz}_{\text{freestream}} + \underbrace{\frac{Ua^2}{z}}_{\text{doublet}}. \quad (4.31)$$

This is equivalent to the complex potential often used to model a cylinder immersed in a moving fluid, since it is the combination of a uniform freestream and a doublet. It follows that the potential is $\Phi = 2Ua \cos \theta$ and differentiating with respect to the circumferential position gives the tangential velocity,

$$u_\theta = \frac{1}{a} \frac{d\Phi}{d\theta} = -2U \sin \theta. \quad (4.32)$$

The surface vortex sheet is ultimately obtained from the slip velocity between the flow and the stationary cylinder surface,

$$\begin{aligned} \gamma_{ext}^{nc} &= u_\theta - u_\theta^{cyl} \\ &= -2U \sin \theta. \end{aligned} \quad (4.33)$$

The result of equation 4.33 is the same as that of equation 4.4, where the latter was derived for a moving cylinder in quiescent fluid. This shows that the resulting vortex sheet is the same regardless of whether the cylinder surges or is stationary and immersed in a moving freestream. Although this should come as no surprise, since the effective velocity seen by the cylinder is the same in both cases, conceptually this is a major step. It shows that the boundary layer vortex sheet (in the absence of shed vorticity) is either generated directly as a result of object acceleration, where it produces an added mass force, or as the necessary mirror image to external vorticity created at the interface of the accelerating fluid and its quiescent surroundings. The similarity in the created vortex sheet and the

resulting equivalence of the related force therefore also solves the conundrum of how we can have what looks like an added mass force even when the object in question is not accelerating.

4.1.4 Summary

The first part of this chapter provides insight into the creation of boundary layer vorticity and how this can be modelled in a potential flow framework. The boundary layer vortex sheet represents the boundary layer vorticity present in viscous flow. It enforces the no-throughflow condition along the surface, whilst conserving the circulation of the flow field. The boundary layer vortex sheet can be broken down into a series of individual contributions. Each component satisfies the no-penetration condition due to a particular flow feature. One contribution comes from the kinematic motion (surge / rotation) of the object and a further is the result of free vorticity in the flow field. The latter is grouped into a component arising from vorticity shed by the body itself and a contribution attributed to externally created vorticity. An example of the latter is vorticity generated at the interface between a region of moving fluid and a quiescent surrounding fluid. From a potential flow perspective, a uniform freestream impinging on a stationary object can be understood to be created by an external pair of counter-rotating point vortices. The vortex sheet due to this vortex pair is identical to the added mass vortex sheet created when the body surges, even though its origin does not come from any non-existent body acceleration.

The vortex sheet contributions due to translation, rotation and vorticity shed by the body itself have all been experimentally identified for an infinitely thin flat plate by Graham et al. [31] and Corkery et al. [16], amongst others. The correct treatment of the vortex sheet created by an accelerating freestream on the other hand has only been investigated from a theoretical perspective and through a more complex experimental flat plate gust encounter, which required a number of assumptions [14]. The next section therefore aims to unambiguously experimentally verify the origin of the vortex sheet created by an accelerating freestream before moving on to assess the general behaviour of the boundary layer vortex sheet on a circular cylinder thereafter.

4.2 Experimental Study: Vortex Sheet due to External Vorticity

From potential flow we know that a plate surging normal to its chord creates the potential flow streamlines and the vortex sheet shown in figure 4.7. The streamlines are symmetrical about both sides of the plate and equal amounts of positive and negative vorticity are created along surface. The definition of the total boundary layer vortex sheet,

$$\gamma^b = \gamma_{am}^{nc} + \gamma_{ext}^{nc} + \gamma^{shed}, \quad (4.34)$$

was used by Corkery et al. [16] to experimentally recover γ_{am}^{nc} for a surging plate. The authors measured γ^b and γ^{shed} at each time-step, and in the absence of any externally created vorticity, recovered the added mass vortex sheet by re-arranging equation 4.34, giving

$$\gamma_{am}^{nc} = \gamma^b - \gamma^{shed}. \quad (4.35)$$

The result of this is shown in figure 4.7b. Since the vortex sheet scales with instantaneous velocity, γ_{am}^{nc} can be normalised by U at each time step and averaged thereafter to remove noise in the measurements.

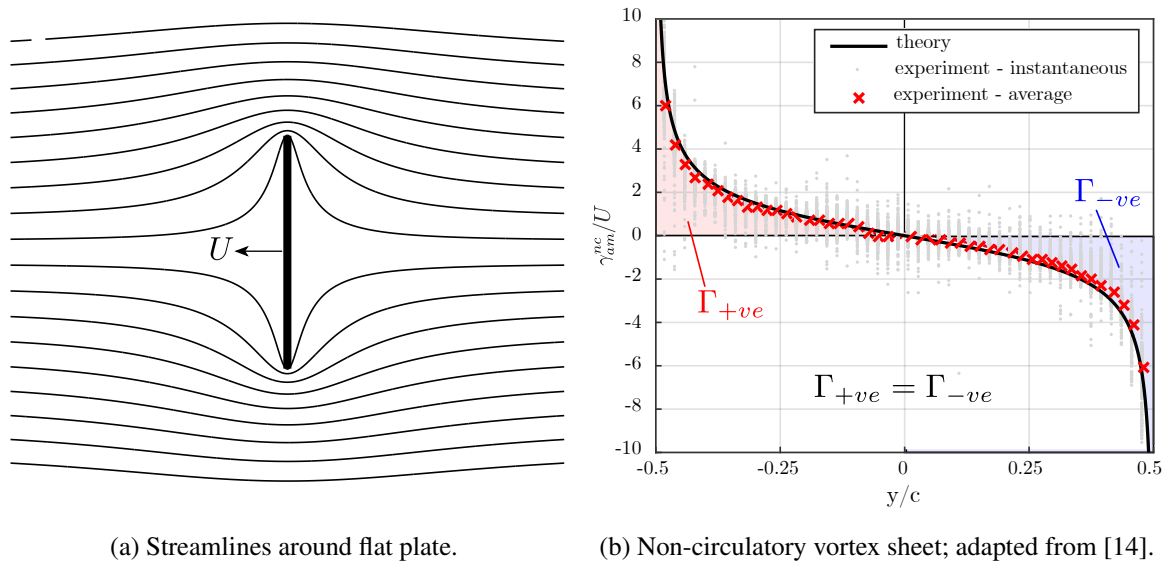


Fig. 4.7 Non-circulatory added mass vortex sheet for a surging plate.

Mathematically, an identical vortex sheet to that recovered for a surging plate is created when a stationary plate is immersed in a uniform freestream, as discussed using the example of a cylinder in section 4.1.3. This intuitively makes sense because the slip velocity along the plate surface is unchanged. We now want to show that the true origin of the vortex sheet comes from the vorticity created at the interface between the moving freestream and the quiescent surrounding, and thereby hope to confirm the theory discussed in section 4.1.3.

To experimentally create a uniform freestream around a stationary plate, we use the *scoop* experiment discussed in section 3.4.3 and shown in figure 4.8. A region of flow is accelerated by surging the *scoop* from left to right, whilst the plate remains stationary. Vorticity forms at the interface between the scoop and the quiescent surrounding and at the same time, a vortex sheet is created on the plate surface. Importantly, this set-up allows us to measure the complete vorticity field and thus makes it possible to unambiguously identify the true origin of the vortex sheet resulting from the impinging flow.

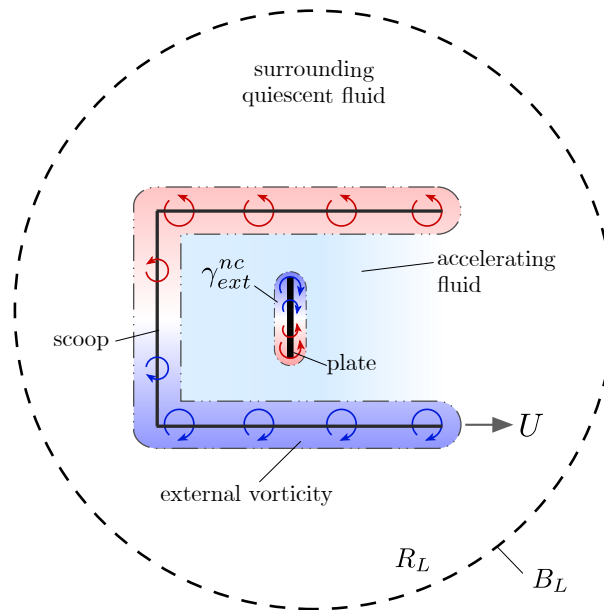


Fig. 4.8 Schematic illustration of a translating scoop creating an accelerating flow field around a stationary plate.

4.2.1 Flow Velocity Impinging on Stationary Plate

In an idealised scenario, the span and width of the scoop are infinite, such that an entirely uniform flow field is created around the stationary flat plate. As such, it would be easy to identify the freestream velocity impinging on the plate, which is required to accordingly scale the theoretical vortex sheet contribution. However, due to the finite nature of the experimental set-up, complete flow uniformity cannot be ensured. A velocity gradient exists in the x -direction within the scoop as it accelerates. The velocity seen by the plate therefore not only changes in time, due to the acceleration of the scoop, but the impinging velocity is also dependent on how far inside the scoop, the plate is located. A conventional approach to determine the velocity seen by the plate would be to perform the same scoop motion in the absence of the plate and record the velocity at the plate position. However, the significant blockage ratio (the ratio between the projected area of the plate and the area enclosed by the scoop A_{plate} / A_{scoop}) of 32 % does not make this a viable option. Instead, we propose to more accurately estimate the *effective* freestream velocity at the plate location by using the measured vorticity field at each instance in time.

As an example, the vorticity contours when the scoop has moved $s/c = 1$ are shown in figure 4.9a. Positive and negative vorticity is seen to form along the upper and lower edge of the scoop, as well as around the plate. To obtain the velocity of the accelerating bulk fluid at the location of the plate, the Biot-Savart law is used, since this links the vorticity distribution to the velocity field, as discussed in

section 2.3.2 and can be applied to a discrete vorticity data set in the form of

$$u_k - iv_k = \sum_{j=1}^N \frac{i\Gamma_j}{2\pi(z_j - z_k)}. \quad (4.36)$$

Here z_k refers to each grid location and z_j to each element of circulation Γ_j , where $k \neq j$. u and v are the induced velocity components in the x and y -direction and z is the position coordinate defined as a complex number.

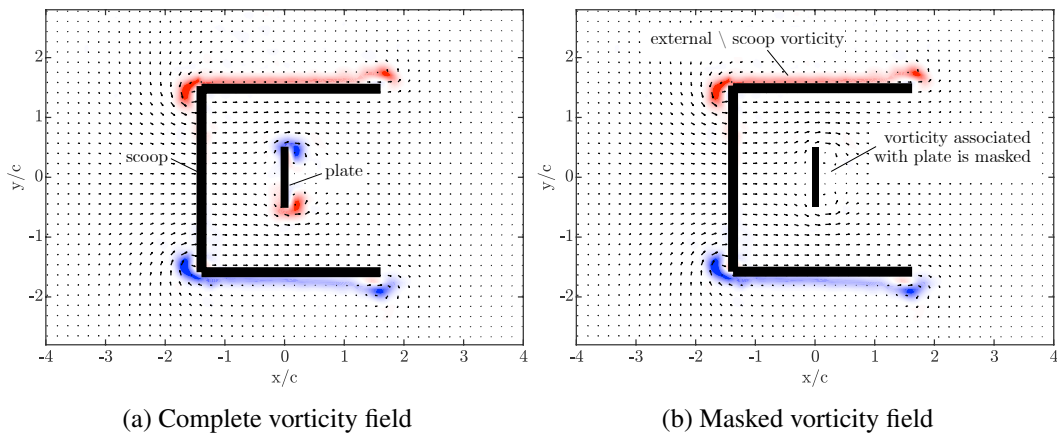


Fig. 4.9 Normalised vorticity field used to calculate the velocity at the plate. Scoop has moved $s/c = 1$.

The Biot-Savart law is applied to any vorticity that is generated along the interface of the moving fluid and the quiescent surrounding (ie. the vorticity along the scoop edge), as shown in figure 4.9b, where any vorticity associated with the plate is masked. The recovered u -velocity component is shown in figure 4.10. A smooth transition from high to low positive velocity is observed within the scoop as well as negative velocity above and below the scoop. The velocity at the mid-chord of the plate can now be extracted and used as the representative *freestream* velocity encountered by the plate.

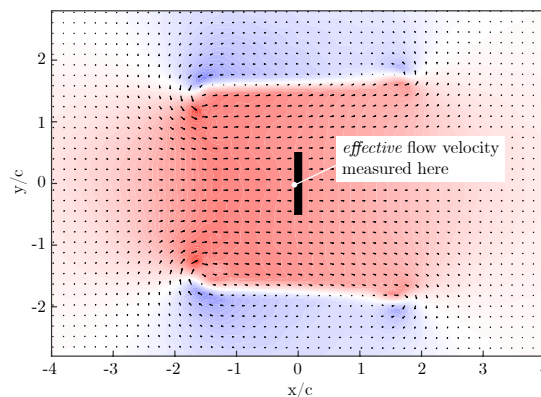


Fig. 4.10 u -velocity component recovered by considering only vorticity along the scoop edge, normalised by final scoop translation velocity. $s/c = 1$. Contours are from -1.5 to 1.5.

The importance of calculating the freestream velocity experienced by the plate using the vorticity generated along the scoop edge is shown in figure 4.11. Here, the velocity input profile to the carriage is compared to the true velocity of the scoop as well as the effective flow velocity at the plate position, calculated using the method described above. Whilst the ideal and the true scoop velocity grow until they reach a constant velocity of 0.11 ms^{-1} at $s/c = 1$, the effective velocity felt by plate increases at a slower rate and only reaches the same terminal velocity at $s/c = 1.6$.

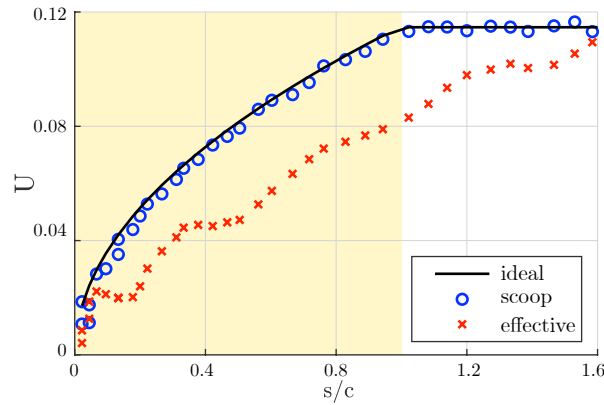


Fig. 4.11 Velocity trace comparison between the *effective* velocity impinging on the flat plate, recovered from the vorticity created at the interface between the quiescent and accelerated flow field, to the *scoop* and *idealised* velocity profile. The shaded area indicates scoop acceleration.

4.2.2 Recovering the Vortex Sheet Contribution

Having found the velocity of the flow impinging on the plate, which is used to determine the theoretical vortex sheet γ_{ext}^{nc} , we can now assess the vortex sheet contribution created by external vorticity resulting from fluid motion. The vorticity contours for three instances in time are shown in figures 4.12a, 4.12c and 4.12e. The positive and negative vorticity along the upper and lower edge of the scoop gets progressively stronger, as the scoop accelerates. At the same time, vorticity begins to shed from either end of the flat plate. To recover the vortex sheet created by the *external* vorticity, the methodology described in section 4.1.2 is applied to any vorticity created by the scoop. The theoretical vortex sheet due to surge (equation 4.12) and the experimental distribution γ_{ext}^{nc} , obtained from the scoop vorticity, are shown in figures 4.12b, 4.12d and 4.12f for the equivalent time steps. Both vortex sheets grow in time as the flow accelerates and match each other throughout.

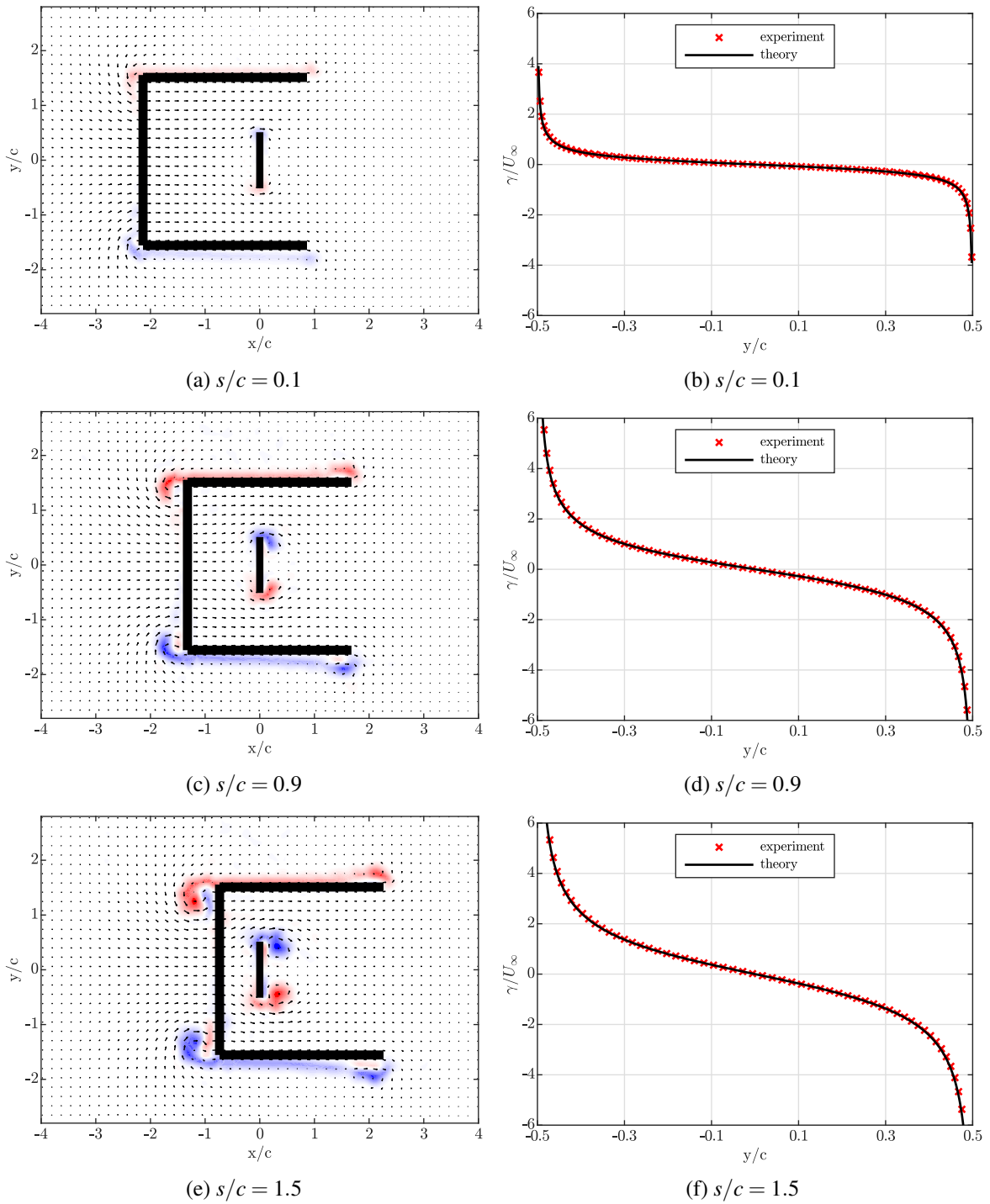


Fig. 4.12 Vorticity contours and vortex sheet development.

The non-circulatory vortex sheet γ_{ext}^{nc} scales with instantaneous velocity. This makes it possible to measure γ_{ext}^{nc} throughout the entire evolution of the velocity field and average it thereafter. The result is shown in figure 4.13 together with the theoretical distribution. A continued close match between

the two is observed, confirming that vorticity created along the interface of a moving fluid and its surrounding leads to a vortex sheet contribution that is identical in shape to that arising due to body translation.

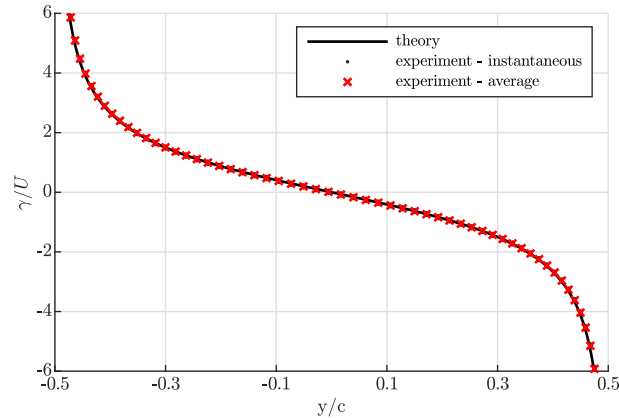


Fig. 4.13 Averaged vortex sheet due to external scoop vorticity compared to the theoretical added mass distribution.

An alternative example of a flow field where vorticity is created *externally* is that of a body encountering a transverse gust as discussed by Corkery [14]. The flow field of limited extent can be considered to be a superposition of a horizontally translating body and a transverse freestream. Vorticity is created in the shear layers that form along the interface between the gust edges and the quiescent fluid. Corkery [14] experimentally showed that when the horizontal flat plate is fully immersed in the gust (ie. a transverse freestream), it has a vortex sheet contribution that looks identical to the added mass component created when the plate translates normal to its chord. Although similar in shape, he attributes this vortex sheet to the external vorticity residing in the gust shear layers. Due to the experimental nature of plate gust encounter performed by Corkery [14], it is impossible to measure the complete vorticity field. The process through which he identifies the vortex sheet created by the gust shear layers therefore relies on a small number of assumptions which may unfortunately have led to some lingering scepticism. The results of the *scoop* experiment presented here, in regards to the vortex sheet created on the flat plate immersed in the accelerating freestream, however, align well to his conclusions and thereby hopefully remove any remaining doubt.

The different origins of the vortex sheets have an important implication when analysing unsteady flows. A double counting of the boundary layer vorticity or even of the force can occur when for example, the field of view captures part of the boundary layer developing on a wind tunnel wall or some of the gust shear layer, as shown in figure 4.14. Computing the force from the vorticity field and additionally (and explicitly) including a further *added mass* force, supposedly created by the moving freestream, causes the same force to be considered twice. It is therefore important to be aware of how the boundary layer vortex sheet is created, to avoid accounting for the same force multiple times.

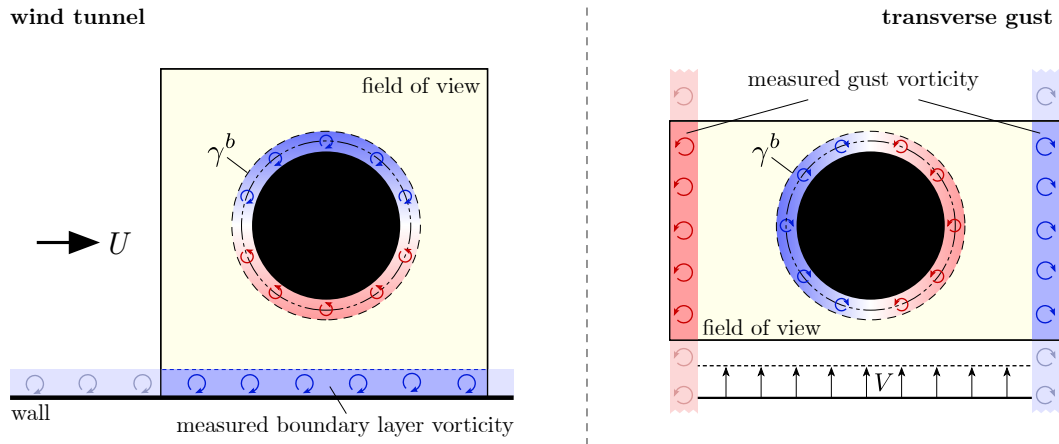


Fig. 4.14 Schematic illustration showing how external vorticity within the wind tunnel wall boundary layer or the gust shear layers is included in the field of view. If treated incorrectly, this may result in the wrong force prediction by an LOM.

4.2.3 Summary

This section investigated the true origin of the vortex sheet contribution that forms when a stationary flat plate is immersed in an accelerating free stream. It is experimentally confirmed that even though the vortex sheet on the plate looks identical to the *added mass* vortex sheet seen when the plate surges, the process by which the vortex sheet is created is fundamentally different. The vortex sheet arises in response to external vorticity forming at the interface between the moving freestream and the quiescent surrounding, rather than due to any non-existent body motion. It can therefore be concluded that the total boundary layer vortex sheet may be represented by four main contributions,

$$\gamma^b = \underbrace{\gamma_{am}^{nc} + \gamma_{ext}^{nc}}_{\text{non-circulatory}} + \underbrace{\gamma^r + \gamma^{shed}}_{\text{circulatory}}. \quad (4.37)$$

γ_{am}^{nc} and γ_{ext}^{nc} are considered to be *non-circulatory*, as their net circulation is zero, whilst γ^r and γ^{shed} contain a finite amount of circulation and are therefore classified as *circulatory*. Together these four contributions make up the total boundary layer vorticity and have now been successfully identified for an infinitely thin flat plate. The next step is to confirm their presence, and importantly our ability to measure them, for an object of finite thickness. Moreover, a change to any of these components affects the total boundary layer vortex sheet strength. This process and its subsequent implications is explored further in the following section.

4.3 Evolution of the Boundary Layer Vorticity and its Contributions

The preceding section identified the core contributions to the boundary layer vortex sheet and showed that these can be measured for an infinitely thin flat plate. The section now aims to build on these

findings, and focuses on evaluating the time dependent evolution of the boundary layer vortex sheet on a surging and rotating cylinder. We aim to explore the behaviour of the individual vortex sheet components, in order to understand how and why the boundary layer vortex sheet evolves in the way it does and how this affects the behaviour at the unsteady separation point. To do so we use the experimental cylinder set-ups discussed in section 3.4.1.

4.3.1 Surge Only, Case c0

The first flow field to be explored is that created by a translating cylinder, case c0, as shown by several ‘vorticity’ snapshots in figure 4.15. The cylinder begins to translate from right to left and linearly accelerates until $s/D = 3$ after which it moves at a constant speed.

Throughout the time period under investigation, the flow is more or less symmetric about the x -axis running through the cylinder center and initially remains attached. An inspection of the time-resolved PIV data suggests that separation becomes clearly visible at approximately $s/D = 0.9$. The unsteady separation points are located on the downstream side of the cylinder, where they slowly move upstream along the cylinder surface as the flow develops and more vorticity is shed. The separating shear layers roll up into two vortices which remain close to the surface throughout the captured motion, whilst growing in size as the translation distance increases.

Before separation is observed at approximately $s/D < 0.9$, the experimental flow field closely resembles potential flow around a circular cylinder. This is demonstrated in figure 4.16a where the streamlines, recovered from the PIV measurements, are reminiscent of those calculated using potential theory. The boundary layer vortex sheet determined at these early instances is plotted in figure 4.16b together with its theoretical equivalent. Whilst the experimental vortex sheet γ^b is obtained using the *wedge* methodology outlined in section 3.5, the theoretical distribution γ_{am}^{nc} is computed from the slip velocity between the cylinder surface and the surrounding potential flow, such that

$$\gamma_{am}^{nc} = -2U \sin \theta, \quad (4.38)$$

as discussed in section 4.1.1. As the cylinder accelerates, the amplitude of the sinusoidal distribution of both the experimental and theoretical vortex sheet grow, and a close match between the two is observed. This is in line with the discussion from section 4.1.1, where it was suggested that prior to separation, the boundary layer vortex sheet is a function of the cylinder geometry and the kinematic motion alone.

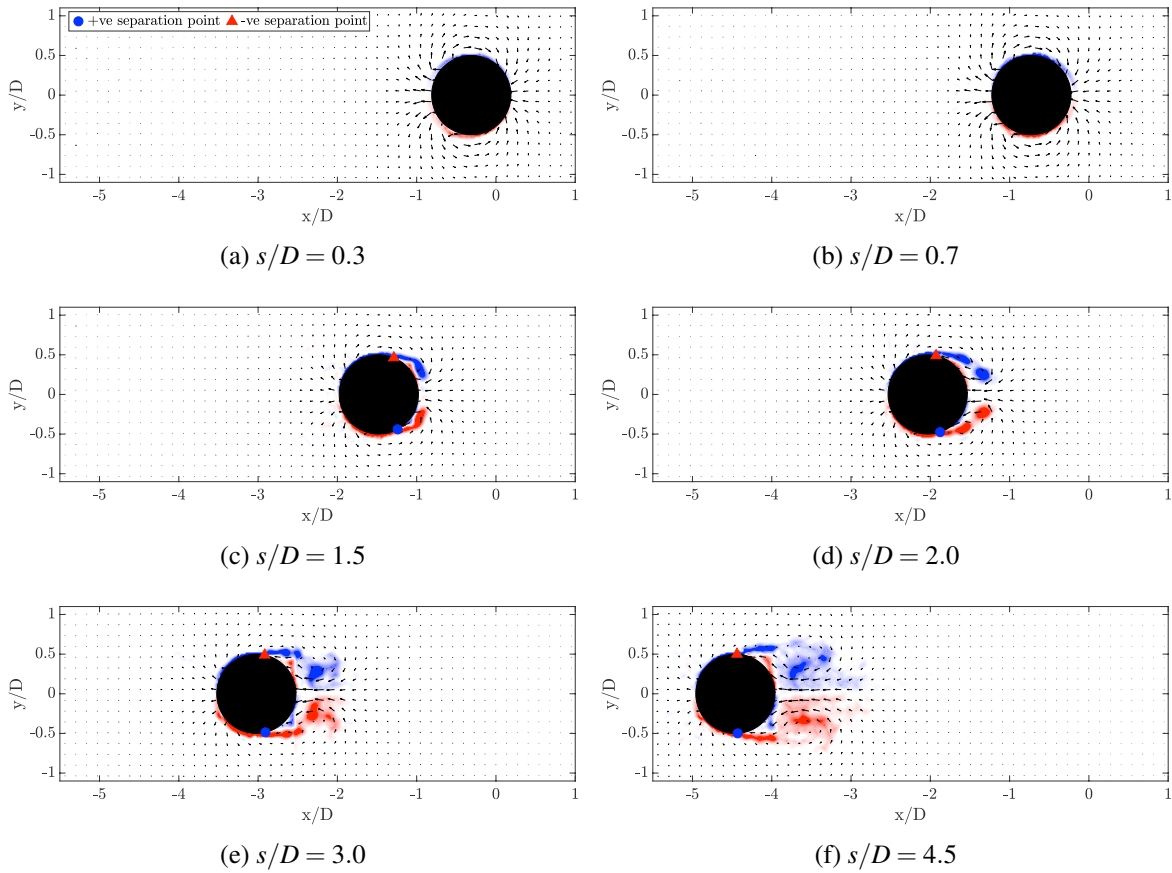
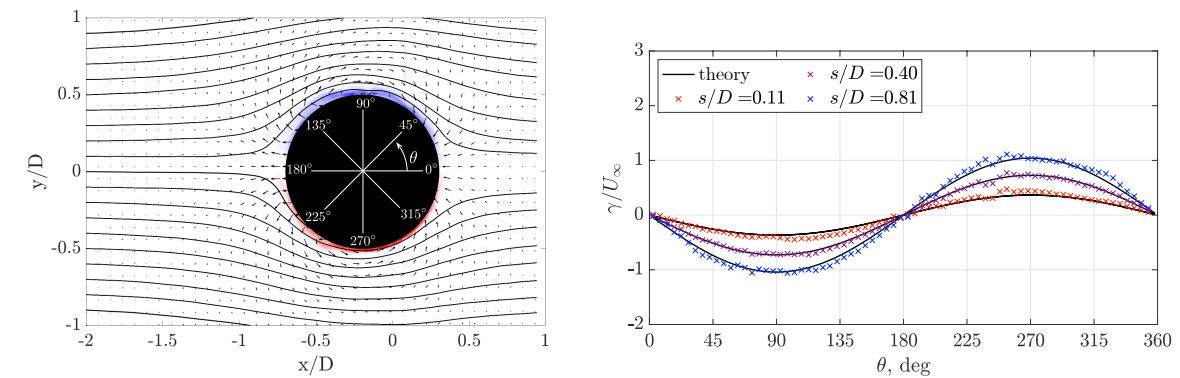


Fig. 4.15 Normalised vorticity contours as the cylinder translates, case c0.



(a) Vorticity contours and streamlines reminiscent of those observed in potential cylinder flow. (b) Theoretical and measured boundary layer vortex sheet at selected time intervals.

Fig. 4.16 Flow field and vortex sheet shortly after the cylinder has begun to surge.

As the cylinder continues to accelerate, the flow separates and vorticity sheds from its surface, as seen in figures 4.15c - 4.15f. This has a significant effect on the boundary layer vortex sheet, as shown in figure 4.17. Once unsteady separation occurs, a sudden sharp drop in magnitude of γ^b occurs. The

location of this drop is marked with a triangle on the upper and a circle on the lower cylinder surface. Relating these positions to the flow field images seen in figure 4.15, where the same locations are marked, shows that the drop in vortex sheet strength coincides with the unsteady separation points where the boundary layer separates.

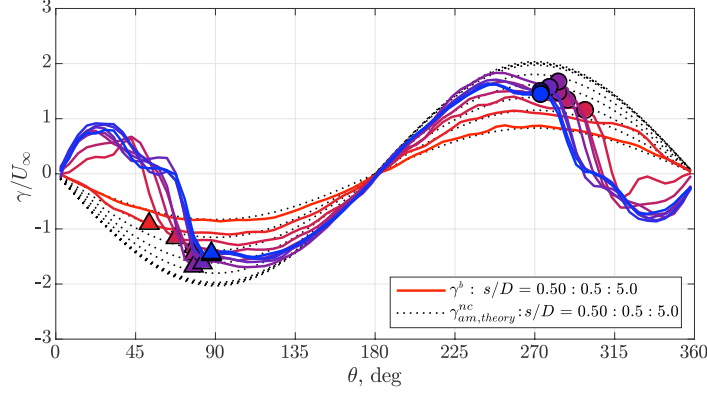


Fig. 4.17 Evolution of γ^b , case c0. Line colour changes from red to blue as s/D increases. Circles and triangles mark the unsteady separation point on the lower and upper cylinder surface.

The difference between the observed surface vortex sheet γ^b and the sinusoidal potential flow distribution γ_{am}^{nc} suggests that an additional contribution to the boundary layer vortex sheet arises when the flow separates and vorticity is carried into the outer flow via the separating shear layer. Once separation occurs, we should therefore be able to represent the viscous boundary layer around a surging cylinder through the superposition of the potential flow vortex sheet γ_{am}^{nc} and that created by shed vorticity γ^{shed} ,

$$\gamma^b = \gamma_{am}^{nc} + \gamma^{shed}. \quad (4.39)$$

To test this hypothesis for a circular cylinder we attempt to calculate γ^{shed} , using the tangential velocity induced by the free and respective mirror vortices, and remove this from the boundary layer vortex sheet γ^b . The result should recover the potential flow vortex sheet γ_{am}^{nc} created through the surge motion of the cylinder,

$$\gamma_{am}^{nc} = \gamma^b - \gamma^{shed}. \quad (4.40)$$

Figure 4.18 shows the recovered instantaneous γ_{am}^{nc} distributions scaled by the relevant freestream velocity at each time step for translation distances $0 < s/D < 5$ as well as the resulting average. It can be seen that the experimental distributions collapse well onto the theoretical vortex sheet and thereby demonstrate that the motion of the cylinder creates a tangible contribution to the boundary layer vortex sheet. Moreover, γ_{am}^{nc} can be experimentally identified even in the presence of external vorticity, where the latter has created its own respective vortex sheet contribution.

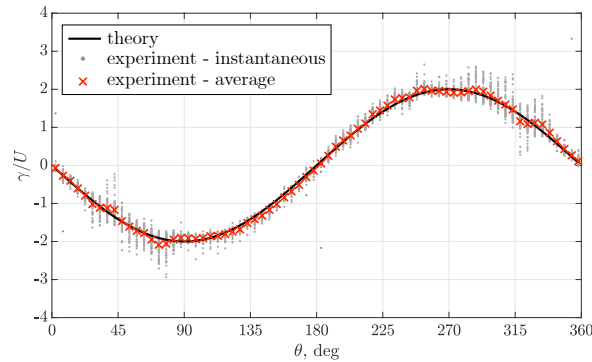


Fig. 4.18 γ_{am}^{nc} recovered experimentally and compared to the theoretical distribution.

Vorticity Development at the Separation Point

Having identified the individual vortex sheet contributions to the boundary layer, we now evaluate the behaviour of the boundary layer vorticity at the unsteady separation point. The absolute strength of the boundary layer vortex sheet at the separation point, γ_{sep}^b , on either side of the cylinder is extracted for each time-step and the result normalised by the final translation velocity (hollow circles), is plotted in figure 4.19. As expected, γ_{sep}^b is similar on either side of the cylinder and once acceleration ceases at $s/D > 3$, γ_{sep}^b remains almost unchanged even as more vorticity sheds and the flow field develops further. It can also clearly be seen in figure 4.19 that whilst the cylinder accelerates, γ_{sep}^b continues to increase. Given that the potential flow vortex sheet strength γ_{am}^{nc} scales with instantaneous velocity, it appears sensible to also scale γ_{sep}^b by U and the result is further included in figure 4.19. When the changing instantaneous velocity is accounted for, the strength of the vortex sheet at the separation point remains almost constant throughout the entire translation distance. This occurs even though the unsteady flow field changes significantly and the unsteady separation point moves almost 40° along the cylinder surface.

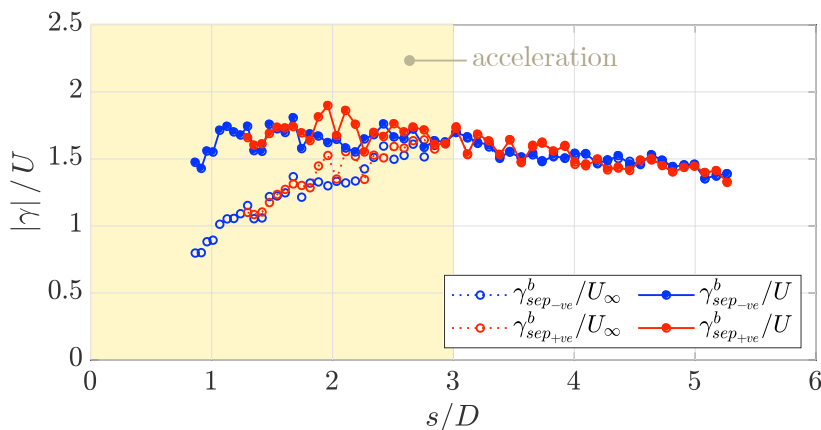


Fig. 4.19 Evolution of γ^b at the separation point.

The almost invariant strength of γ^b/U at the unsteady separation point appears to suggest that there may be a ‘critical’ value of boundary layer vorticity that causes separation. The existence of such a parameter could potentially be useful for the development of low-order models. However, a simple thought experiment demonstrates that this cannot be the case. Imagine a stationary cylinder that begins to rotate in quiescent fluid. Here the ‘rotational’ vortex sheet γ^r develops due to the slip velocity between the moving cylinder surface and the stationary external fluid. In theory, the cylinder can be spun at any speed which in turn leads to any strength of γ^b , without separation ever occurring. To investigate the variation and development of γ_{sep}^b further, we consider a translating as well as rotating cylinder next.

4.3.2 Translation and Rotation, Case c2, $\alpha = 2.5$

The rotation ratio α is set to 2.5 and the boundary layer vorticity is analysed in the same way as for $\alpha = 0$. The cylinder begins to translate and rotate simultaneously from a stationary start and accelerates until $s/D = 2$. Initially, attached positive vorticity is observed within the entire boundary layer created by the rotary motion as seen in figure 4.20a. As the cylinder translates further, shown in figures 4.20b and 4.20c, vorticity detaches all along the downstream surface of the cylinder, and a clearly defined unsteady separation point appears around $s/D = 1$. Shed vorticity subsequently rolls up into a single vortex which drifts away from the cylinder, as shown in figure 4.20d.

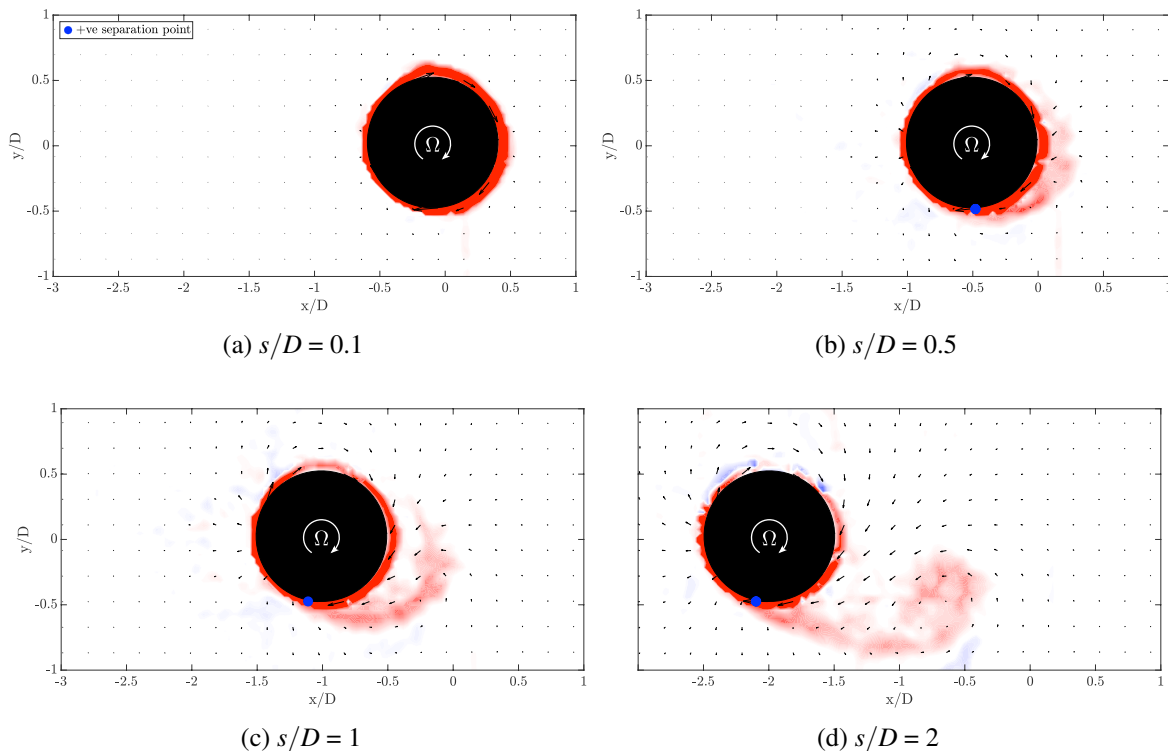


Fig. 4.20 Vorticity contours as the cylinder translates from right to left, case c2.

Once again the boundary layer vortex sheet is extracted and shown at selected intervals in figure 4.21a, where the line colour shifts from red to blue with increasing translation distance. The separation point is indicated with an equivalently colour coded circle. With increasing s/D , the majority of the boundary layer vortex sheet distribution $0 < \theta < 250$, apart from the region downstream of the separation point, appears to shift downwards almost uniformly. A similar trend is observed for the vortex sheet created by shed vorticity, as seen in figure 4.21b.

Moreover, γ^b features a distinctive sinusoidal distribution on the upper cylinder surface and upstream of the separation point. The sinusoidal shape is attributed to γ_{am}^{nc} which we can recover from the flow field using the same methodology that was earlier applied to the surging cylinder. The only difference is that there is now an additional rotational contribution that must be considered, hence

$$\gamma_{am}^{nc} = \gamma^b - \gamma^r - \gamma^{shed}. \quad (4.41)$$

The averaged distribution of γ_{am}^{nc} normalised by instantaneous velocity at each instance in time throughout the captured motion is shown in figure 4.21c. It can be seen that the experimental distribution tracks the theoretical vortex sheet all along the cylinder surface and thereby confirms the physical presence of this added mass vortex sheet contribution as well as that our measurements of γ^r and γ^{shed} are correct.

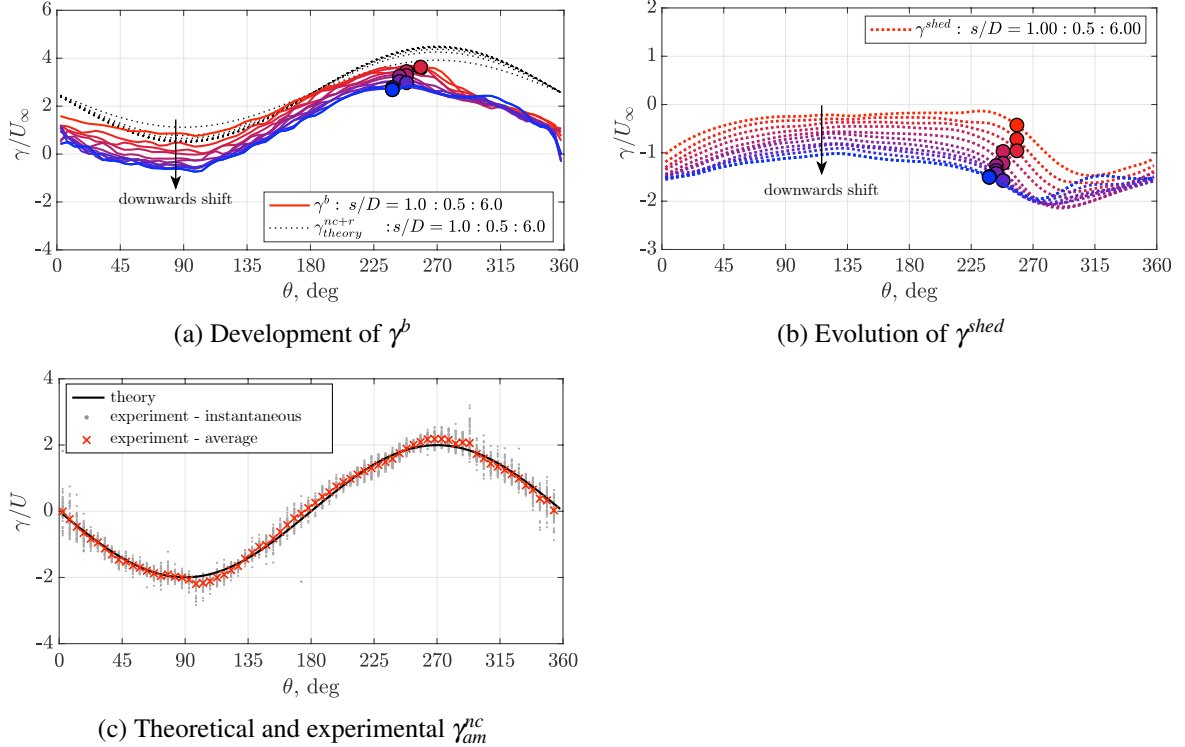


Fig. 4.21 Boundary layer vortex sheet and constituent parts. Circles mark the separation point. Line colour transitions from red to blue with increasing s/D .

Influence of γ^{shed}

At the end of the previous section we noticed a global downwards shift of the boundary layer vortex sheet as the cylinder translated. This coincided with a similar drift spotted for γ^{shed} . Since simultaneously, the vortex sheet contributions due to rotation and translation remained unchanged once acceleration ceases at $s/D = 2$, the change in γ^b appears to be caused by vorticity residing within the outer flow field. We therefore take a closer look at how free vorticity affects the boundary layer vortex sheet in the following passages.

Imagine an external vortex located in close proximity to the cylinder. To calculate its contribution to γ^{shed} , we follow the approach outlined in section 4.1.2. A mirror image of the external vortex is placed inside the cylinder and the induced velocity from the external and the mirror vortex is found all along the cylinder surface. Assuming that the external vortex is close to the cylinder, we observe that the mirror image vortex is well away from the cylinder centre and relatively close to the surface. This has an important effect on the resulting vortex sheet distribution. Close to the external vortex, the induced velocities from either vortex add up, while on the opposite side they tend to roughly cancel, as long as the distance between the cylinder surface and the external vortex is small compared to the cylinder diameter. The resulting vortex sheet is therefore confined to the vicinity of the external vortex whilst almost vanishing elsewhere along the cylinder surface, as shown schematically at the top of figure 4.22.

If the external vortex is instead located infinitely far away, a very different effect is observed. Now the mirror vortex is located at the cylinder centre. The induced velocity from the external vortex approaches zero because of the large distance, whilst the mirror image at the cylinder centre induces an equal velocity all along the surface, giving a vortex sheet of uniform strength, as shown at the bottom of figure 4.22. For convenience, we will refer to the vortex sheet contribution due to vorticity in close proximity to the cylinder as γ_{local}^{shed} and to the component from vorticity far away as $\gamma_{far-field}^{shed}$.

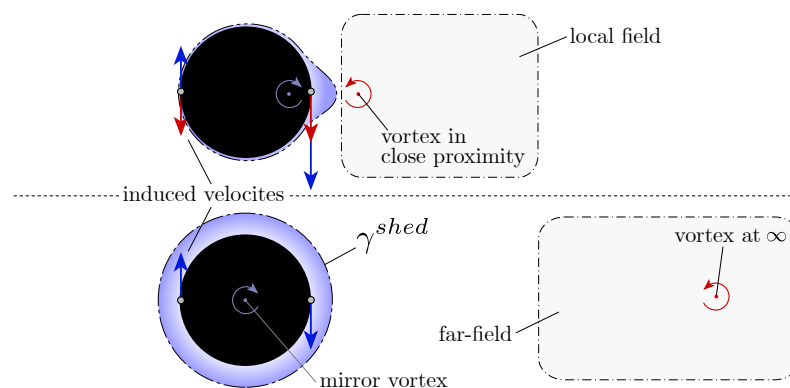


Fig. 4.22 Effect of local and far-field vorticity.

Effectively, any free vortex contributes to both γ_{local}^{shed} and $\gamma_{far-field}^{shed}$ and the distance from the cylinder simply determines the relative balance between the two components; such that

$$\gamma^{shed} = \gamma_{local}^{shed} + \gamma_{far-field}^{shed}. \quad (4.42)$$

For example, whilst a vortex is close to the cylinder, its local contribution dominates. However as it drifts away, γ_{local}^{shed} diminishes and the vortex instead begins contribute more to the far-field component, as shown in figure 4.23.

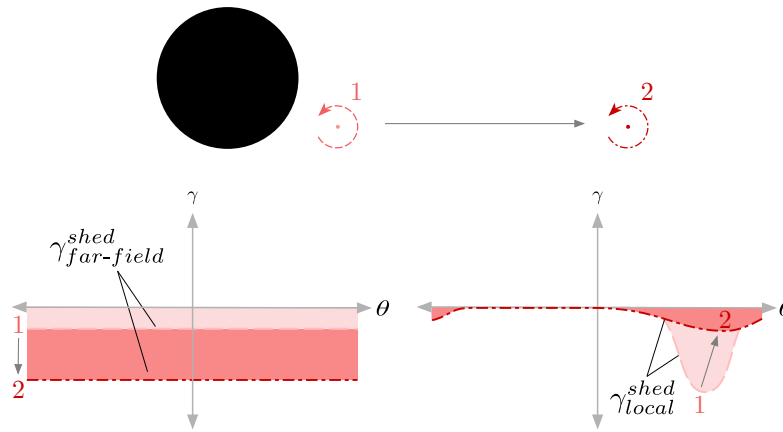


Fig. 4.23 Variation of $\gamma_{far-field}^{shed}$ and γ_{local}^{shed} as a vortex moves away from the cylinder.

The question arises how to distinguish between the local and far-field contributions, as the correct attribution is somewhat arbitrary. For instance, setting a cut-off distance after which vorticity is counted as far-field rather than as local, to determine its respective contribution to γ^{shed} , introduces an additional unknown in the form of the cut-off distance. Instead we propose a simple yet more systematic method to estimate the respective distributions. The far-field contribution to the vortex sheet is found by calculating the velocity induced by the external vortex and its mirror image on the opposite side of the cylinder, as schematically illustrated in figure 4.24. As described earlier, the velocity induced by vorticity in close proximity to the surface will approximately cancel with its mirror image here, whereas this will not occur if vorticity is far away. It follows that γ_{local}^{shed} is the remainder when the far-field contribution, $\gamma_{far-field}^{shed}$ is removed from the total vortex sheet due to shed vorticity γ^{shed} ,²

$$\gamma_{local}^{shed} = \gamma^{shed} - \gamma_{far-field}^{shed}. \quad (4.43)$$

²This methodology estimates $\gamma_{far-field}^{shed}$ for any shape that can be mapped to a cylinder. For irregular objects, where this is not possible, a panel method approach can be used. The vortex sheet created by the k^{th} element of free vorticity is first calculated using the panel method. Thereafter, the strength of this vortex sheet is found at the opposite side on the body surface p_k . The strength of a vortex located at infinity is now calculated that creates an equally strong vortex sheet at p_k . The strength of the vortex at infinity now serves as an approximation of the far-field contribution of the specific vortex element. The process may be repeated for all elements of free vorticity, to arrive at a global estimate.

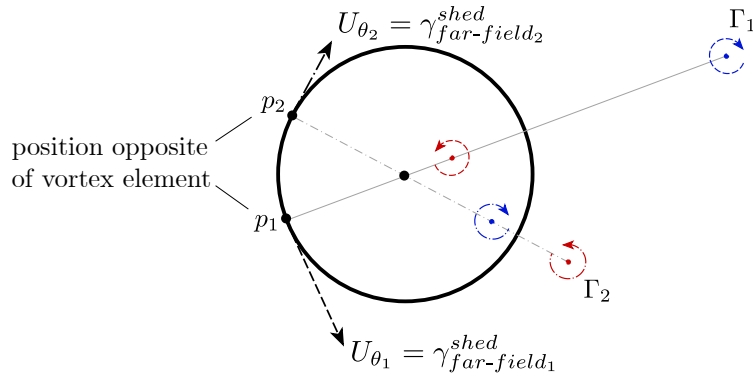


Fig. 4.24 Schematic illustrating the calculation of $\gamma_{far-field}^{shed}$.

Therefore, to better understand the observed drift of γ^{shed} , we now decompose the measured vortex sheet into its respective local and far-field contributions. The original vortex sheet normalised by instantaneous velocity as well as its two individual components are shown in figure 4.25. Whilst γ_{local}^{shed} remains almost unchanged upstream of the separation point for the entire translation distance, $\gamma_{far-field}^{shed}$ is found to gradually become more negative. As a consequence, far-field vorticity therefore appears to be the driving force behind the downwards trend of γ^{shed} . In fact, this is not too surprising. As time passes, more vorticity sheds, moves away from the cylinder and accumulates in the far-field, thereby enhancing its contribution to the vortex sheet.

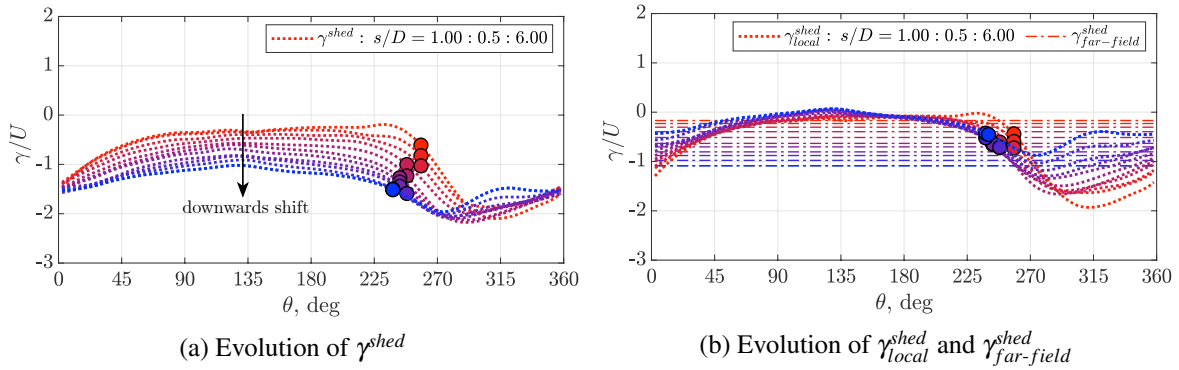


Fig. 4.25 Line colour transitions from red to blue with increasing s/D . Circle marks the separation location. Case c2.

4.3.3 Scaling the Boundary Layer Vortex Sheet Strength

In light of the findings regarding the influence of far-field vorticity on the boundary layer vortex sheet, the evolution of γ^b as well as the development of its strength at the separation point, γ_{sep}^b , are revisited. To do so, a new parameter is formed by subtracting the influence of far-field vorticity and scaling the result with the instantaneous velocity,

$$\bar{\gamma}^b = \frac{\gamma^b - \gamma^r - \gamma_{far-field}^{shed}}{U}. \quad (4.44)$$

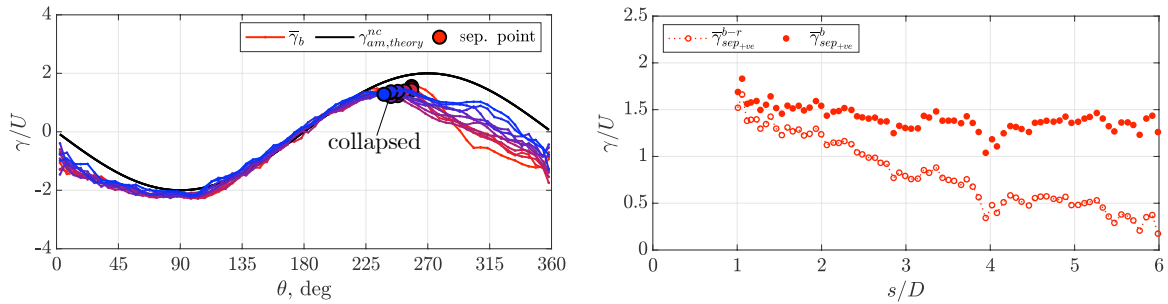
γ^r is also subtracted, as this is entirely independent of U . In other words, $\bar{\gamma}^b$ describes vortex sheet due to translation γ_{am}^{nc} and the effect of vorticity close to the cylinder γ_{local}^{shed} ,

$$\bar{\gamma}^b = \frac{\gamma_{am}^{nc} + \gamma_{local}^{shed}}{U}. \quad (4.45)$$

Figure 4.26a shows that this new vortex sheet strength parameter almost completely collapses the boundary layer vorticity distribution as the cylinder translates. Furthermore, the vortex sheet strength at the separation point also remains much more constant. This is seen more clearly in figure 4.26b where $\bar{\gamma}_{sep}^b$ is extracted for every time-step once separation has been identified. $\bar{\gamma}_{sep}^b$ is compared to, $\bar{\gamma}_{sep}^{b-r}$, the equivalent case where $\gamma_{far-field}^{shed}$ is retained,

$$\bar{\gamma}_{sep}^{b-r} = \frac{\gamma^b - \gamma^r}{U}. \quad (4.46)$$

Whilst $\bar{\gamma}_{sep}^{b-r}$ shows a clear downwards trend, $\bar{\gamma}_{sep}^b$ remains almost invariant.



(a) $\bar{\gamma}^b$ between $1 < s/D < 6$ in steps of 0.5, line colour changes from red to blue with increasing s/D . (b) Development of $\bar{\gamma}_{sep}^{b-r}$ and $\bar{\gamma}_{sep}^b$. Whilst $\bar{\gamma}_{sep}^{b-r}$ reduces, $\bar{\gamma}_{sep}^b$ remains almost invariant.

Fig. 4.26 Evolution of the adjusted boundary layer vortex sheet and its strength at the separation point, case c2.

It may now appear surprising that we did not observe the downwards trend of γ_{sep}^b earlier, when investigating the surging cylinder in figure 4.19, since vorticity is equally shed. The difference to the rotating case however is that vorticity of equal magnitude is shed from either side of the cylinder, creating an approximately symmetric flow field about the x -axis running through the cylinder. Since the vorticity released on either side of the cylinder is of opposite sign, the far-field contribution created by the positive and negative vorticity effectively cancels, thus leading to a more consistent γ_{sep}^b , even before it is scaled according to equation 4.44.

4.3.4 Translation and Rotation, Case c1a, $\alpha = 1$

In the previous example a single vortex sheds and drifts away, with no further vortex being created during the investigated time period. To test the proposed ideas in a more complex situation, the final example consists of a surging and rotating cylinder at a rotation ratio of 1, where alternate vortices are shed from either side of the cylinder.

The clockwise rotating cylinder sheds a single starting vortex from its lower surface which slowly moves away, as seen in figures 4.27b - 4.27c. Thereafter, a second vortex begins to develop along the upper surface of the cylinder and eventually also advects downstream; this is observed in figures 4.27d - 4.27e. As the second vortex advects away, a significant change to the vorticity on the lower side of the cylinder is observed. It no longer forms a shear layer which ‘connects’ the starting vortex to the cylinder surface but instead rolls up into a new vortex and thus establishes the commonly observed alternate shedding pattern.

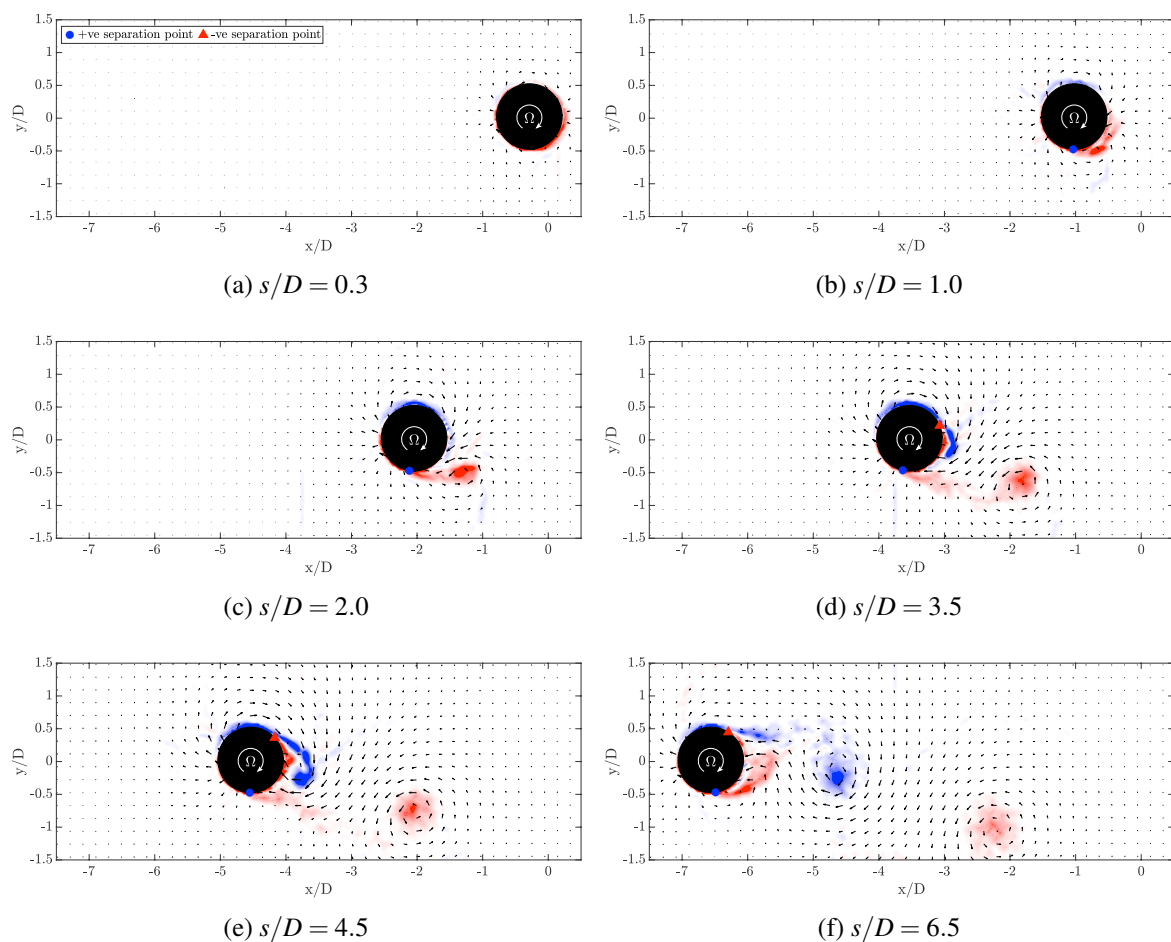


Fig. 4.27 Normalised vorticity contours as the cylinder begins to translate and rotate. Case c1a.

To make the analysis of this unsteady flow field easier, we chose to group the flow into two stages. The ‘development’ period describes the time when the starting vortex is shed from the lower cylinder surface and drifts away, whilst simultaneously a vortex forms along the upper surface, figures 4.27a - 4.27e. The ‘periodic shedding’ stage describes the flow field when the vortex created along the top surface advects away and at the same time a further vortex forms on the bottom side of the cylinder, as shown in figure 4.27f.

During the development period, $\bar{\gamma}^{b-r}$ gradually shifts downwards as seen in figure 4.28a. This coincides with positive vorticity accumulating in the far-field, which creates a negative vortex sheet contribution. During the periodic shedding phase, the opposite is observed as shown in figure 4.28c as $\bar{\gamma}^{b-r}$ moves back upwards. At this point negative vorticity from the second vortex negates the contribution created by the positive vorticity residing within the starting vortex and thus the overall far-field contribution reduces.

The *adjusted* distribution $\bar{\gamma}^b$ is shown in figures 4.28b and 4.28d. Quantifying the effect of far-field vorticity, and excluding its contribution to the boundary layer vortex sheet, removes the overall drift of $\bar{\gamma}^b$ and causes it to collapse throughout the two time periods.

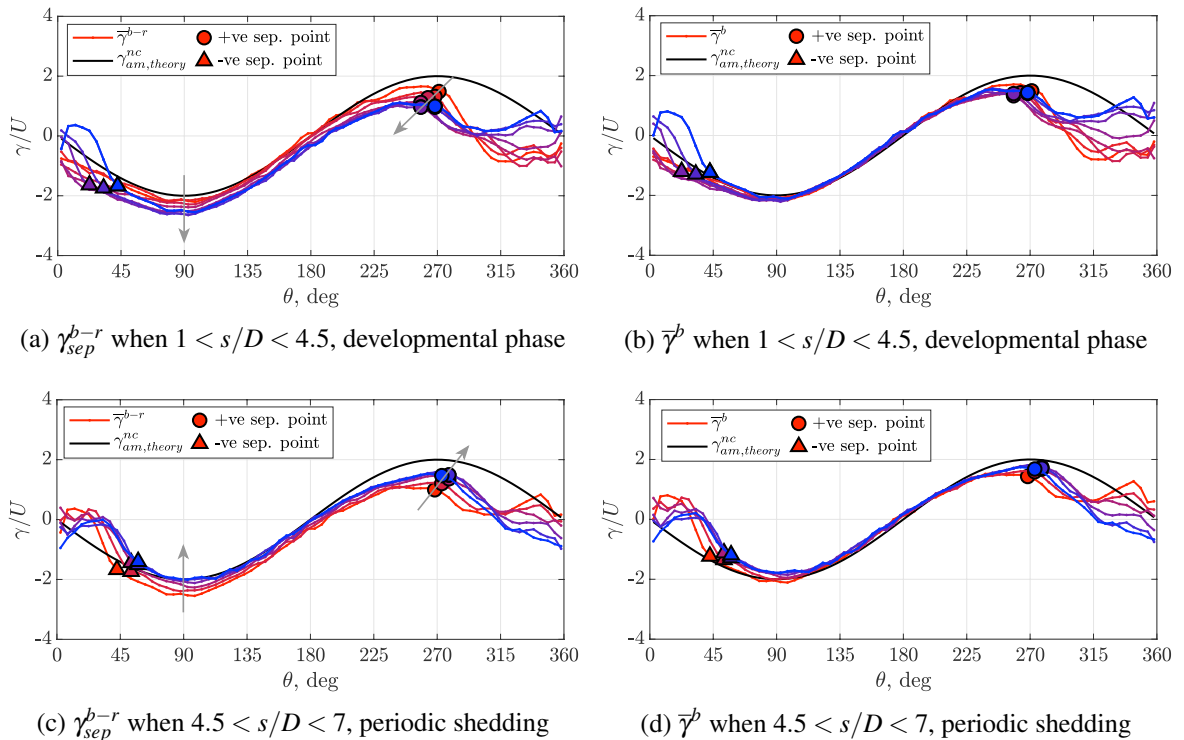


Fig. 4.28 Circles and triangles indicate the separation point. s/D increases in steps of 0.5 as the line colour changes from red to blue. Case c1a.

4.3.5 Comparison of Vortex Sheet Strength at Separation

To visualise and highlight the development of the boundary layer vortex sheet strength at the separation point as the cylinder translates and the flow field evolves, we compare the raw γ_{sep}^b to its adjusted counterpart $\bar{\gamma}_{sep}^b$ for all three kinematic cases in figure 4.29.

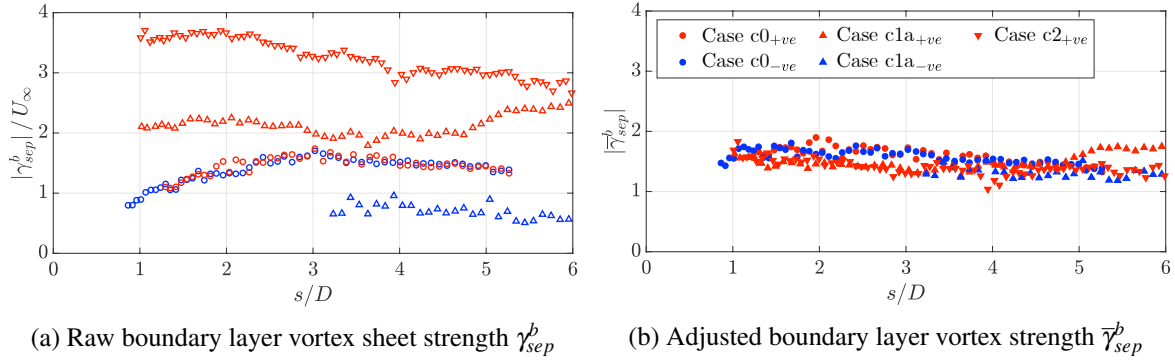


Fig. 4.29 Development of uncorrected and adjusted vortex sheet strength at separation point for all kinematic cases. Legend applies to both graphs, where hollow symbols correspond to the raw strength.

From figure 4.29a it is immediately obvious that the uncorrected vortex sheet strength at the separation point is not always the same, that in some cases it varies considerably with s/D , and that there is no critical value that could predict unsteady flow separation. However, when $\bar{\gamma}_{sep}^b$ is normalised by instantaneous velocity and the effects of rotation rate and far-field vorticity are accounted for, the resulting boundary layer vortex sheet parameter $\bar{\gamma}_{sep}^b$ collapses to an almost constant level as shown in figure 4.29b. Only $\bar{\gamma}_{sep}^b$ along the bottom surface of Case c1a (upright red triangles in figure 4.29b) slightly deviates from this trend at around $s/D = 5$, which coincides with the initial formation of a second vortex shedding from the lower cylinder surface. The emergence of a new vortex, and the early stages of the vortex roll up, significantly change the position of vorticity located in close proximity to the cylinder. This can cause γ_{local}^{shed} , which has so far remained almost invariant, to change and may thus be the reason behind the variation in $\bar{\gamma}_{sep}^b$.

4.3.6 Summary

We explored the development of boundary layer vorticity during unsteady flow by experimentally translating and rotating a circular cylinder in quiescent fluid. Translation creates a boundary layer vortex sheet component that can be calculated from the potential flow solution and is experimentally recovered for bodies of volume in real viscous flow featuring substantial external vorticity.

A further vortex sheet contribution arises when the cylinder spins and as a result of the symmetry of the cylinder is uniform everywhere. When free vorticity is present in the flow field, an additional vortex sheet contribution is created and isolated experimentally. In the potential flow framework it enforces the necessary no-throughflow condition and is found from the slip velocity induced by

the free elements of vorticity and their mirror counterparts residing within the cylinder. It is further proposed that this vortex sheet component can be decomposed into a *local* and *far-field* contribution. Vorticity close to the cylinder creates a vortex sheet contribution that acts only on a small, local portion of the cylinder surface, whilst the far-field component provides a uniform contribution everywhere.

The growth and decline of the boundary layer vortex sheet as a whole can be de-constructed and traced back to the development of its constituent parts, thereby no longer appearing arbitrary. As such, acceleration causes the vortex sheet to grow, whereas an accumulation of vorticity far away from the cylinder creates an oppositely signed uniform vortex sheet component all along the cylinder surface. Normalising by the instantaneous velocity and removing the contribution due to far-field vorticity causes the remaining non-dimensional vortex sheet to remain largely invariant as the unsteady flow field evolves. A similar pattern is observed for the vortex sheet strength at the unsteady separation point. Further removing the effect due to rotation collapses the strength at the separation point between all investigated kinematics, as long as no repeated vortex shedding occurs from the same side of the cylinder. The invariance confirms that we have correctly identified the most prominent factors affecting boundary layer vorticity, bringing us one step closer to understanding unsteady separation and force generation.

Physically however, it is not yet entirely clear why the *adjusted* vortex sheet strength at the separation point remains constant. One hypothesis is that the link between the strength of the boundary layer vortex sheet and unsteady separation is of a secondary nature; meaning that the boundary layer vortex strength is not directly related to flow separation but that it acts as a proxy for the true underlying mechanism at play. An example of this could be that it indirectly provides information about the adverse pressure gradient or the boundary layer health.

In future, these results can hopefully, explicitly or implicitly, enable the prediction of the unsteady separation point. In contrast, the raw strength of the boundary layer vortex sheet cannot be used to indicate unsteady separation, since significant variations in its strength are observed at the unsteady separation point.

4.4 Summary: Boundary Layer Evolution

This chapter explored the origins and behaviour of boundary layer vorticity in unsteady flow through a potential flow framework. A boundary layer vortex sheet is used to represent the vorticity present in the boundary layer and it is subdivided into four main contributions. As such, it builds on work by Corkery [14] regarding infinitely thin flat plates and verifies the true origin of the vortex sheet contribution due to externally created vorticity.

The individual vortex sheet contributions are further identified for a surging and rotating cylinder, confirming their general validity for objects of thickness and are subsequently used to explain the variation of the boundary layer vortex sheet strength as a whole, where in particular acceleration and far-field vorticity are found to play an integral role.

Now that we have gained insight into how boundary layer vorticity is created, the next stage is to investigate the unsteady separation process. Being able to understand and predict the rate at which vorticity is shed into the flow field is crucial when building LOMs, since unsteady separation and free vorticity have a significant impact on the experienced forces. The following chapter will therefore explore the rate at which vorticity is shed into the flow.

Chapter 5

Vorticity Shedding

The rate at which vorticity sheds into the flow, together with its subsequent motion, has a significant effect on the forces. As a consequence, any LOM modelling the flow needs to correctly replicate this behaviour, in order to arrive at an accurate force prediction. In the literature review we discussed that the rate at which vorticity sheds is directly proportional to the boundary layer vorticity flux, which in turn is dependent on the boundary layer vortex sheet. The latter can be broken down into its constituent parts and by analysing the variation of each individual contribution in chapter 4, we gain insight into its development as a whole.

Ideally, we therefore want to express the boundary layer vorticity flux solely in terms of vortex sheet components. This provides a way to estimate the shedding rate only from the knowledge of the individual vortex sheet contributions, when the unsteady separation point is known. Moreover, by linking the rate at which vorticity sheds to the individual components of the boundary layer vortex sheet, the underlying mechanisms affecting the rate at which vorticity is shed into the flow can be explored.

The chapter begins by expressing the boundary layer vorticity flux in terms of vortex sheet contributions in section 5.1, after which the shedding rate is recovered in section 5.2. The chapter concludes by exploring the variation of the shedding rate as the flow field develops in section 5.2.4.

5.1 Vorticity Flux and Shedding Rate in Terms of Vortex Sheet Contributions

A boundary layer is created when viscous flow passes over a surface, as visualised in figure 5.1. Vorticity resides within this boundary layer and is transported at a rate given by the vorticity flux,

$$\dot{\Gamma}_b = \frac{d\Gamma_b}{dt} = \int_{\delta} \omega u \, dn, \quad (5.1)$$

where δ is the boundary layer thickness. ω and u represent the vorticity and velocity distributions in the wall normal n direction [20]. When the flow reaches a separation point, vorticity is no longer transported further along the surface but it is instead ejected into the flow field and thereby acts as a source of for free vorticity [109].

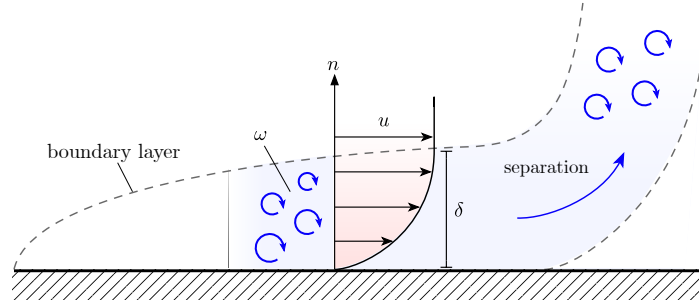


Fig. 5.1 Schematic illustration of a boundary layer that forms along a wall and subsequently separates.

To better understand the rate at which vorticity is shed into the flow field, we will begin by expressing the vorticity flux in the boundary layer, equation 5.1, in terms of only the vortex sheet contributions, such that

$$\dot{\Gamma}_b = f(\gamma_{am}^{nc}, \gamma_{ext}^{nc}, \gamma^r, \gamma^{shed}). \quad (5.2)$$

Thereafter, the result is used to write the vorticity shedding rate in terms of these same vortex sheet parameters. This process will be showcased for a point on the lower half of the cylinder with the coordinate system fixed to the cylinder centre. It can equally be repeated for a position on the upper surface as long as the sign convention is correctly applied. Furthermore, to reduce the clutter in any subsequent equations, we will also assume for the moment that γ^{nc} represents the sum of the non-circulatory vortex sheets γ_{am}^{nc} and γ_{ext}^{nc} .

In line with our approach throughout this thesis, we once again model the flow field using various potential flow contributions. As such, we begin by representing the vorticity distribution within the boundary layer by a vortex sheet γ^b . The vorticity flux therefore becomes

$$\dot{\Gamma} = \gamma^b u_\theta^b, \quad (5.3)$$

where u_θ^b is the average boundary layer velocity. The velocity distribution within the boundary layer is assumed to a first order to be linear,

$$u_\theta^b = \frac{u_\theta^{cyl} + u_\theta^e}{2}. \quad (5.4)$$

Here, u_{θ}^{cyl} is the cylinder wall velocity and u_{θ}^e is the boundary layer edge velocity. The cylinder surface velocity links to the rotational motion of the cylinder,

$$u_{\theta}^{cyl} = -\gamma^r. \quad (5.5)$$

The boundary layer edge velocity u_{θ}^e is affected by the potential flow due to translation, any externally created vorticity γ^{nc} as well as by the velocity induced by shed vorticity γ^{shed} . u_{θ}^e can therefore be expressed as

$$\begin{aligned} u_{\theta}^e &= \gamma^{nc} + \gamma^{shed} \\ &= \gamma^b - \gamma^r, \end{aligned} \quad (5.6)$$

since $\gamma^b = \gamma^{nc} + \gamma^{shed} + \gamma^r$. The average boundary layer velocity can now be found by substituting equations 5.5 and 5.6 into equation 5.4,

$$u_{\theta}^b = \frac{\gamma^b - 2\gamma^r}{2}. \quad (5.7)$$

The vorticity flux is ultimately obtained by inserting the expression for u_{θ}^b (5.7) into equation 5.3,

$$\dot{\Gamma}_b = \gamma^b \frac{\gamma^b - 2\gamma^r}{2}. \quad (5.8)$$

As desired, the result is now a function of only γ^b and γ^r , where the former is dependent on the underlying vortex sheet components, γ^{nc} , γ^r and γ^{shed} .

The rate at which vorticity is shed into the flow $\dot{\Gamma}_{shed}$ can now be approximated by assuming that the vorticity flux is conserved at the separation point [109]. This implies that the difference between the vorticity flux upstream (position 0) and just downstream (position 1) of the unsteady separation point gives the rate at which vorticity is shed. Consequently, the shedding rate can be expressed as

$$\begin{aligned} \dot{\Gamma}_{shed} &= \gamma^b u_{\theta}^b \Big|_0 - \gamma^b u_{\theta}^b \Big|_1 \\ &= \gamma^b \frac{\gamma^b - 2\gamma^r}{2} \Big|_0 - \gamma^b \frac{\gamma^b - 2\gamma^r}{2} \Big|_1. \end{aligned} \quad (5.9)$$

The vorticity and the boundary layer velocity distributions just before and after the separation point are schematically illustrated in figure 5.2. By definition, the velocity at the point of separation is entirely normal to the surface. Therefore, there exists no tangential velocity component that contributes to the surface vortex sheet. Only the slip velocity between the rotating cylinder and nominally quiescent fluid affects γ^b , leaving $\gamma^b = \gamma^r$ at the point of separation.

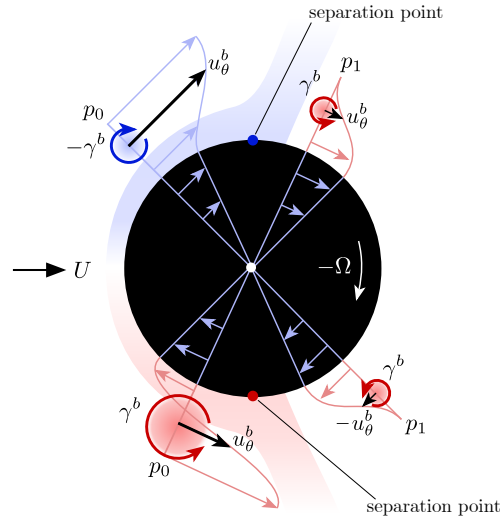


Fig. 5.2 Schematic illustration of the boundary layer velocity profile and vorticity an infinitesimal distance upstream and downstream of the separation point.

Replacing γ^b by its respective vortex sheet components prior to separation and letting $\gamma^b = \gamma^r$ just after separation leads to

$$\dot{\Gamma}_{shed} = \frac{(\gamma_{sep}^{nc} + \gamma_{sep}^{shed})^2}{2} = \frac{(\gamma_{sep}^b - \gamma_{sep}^r)^2}{2}. \quad (5.10)$$

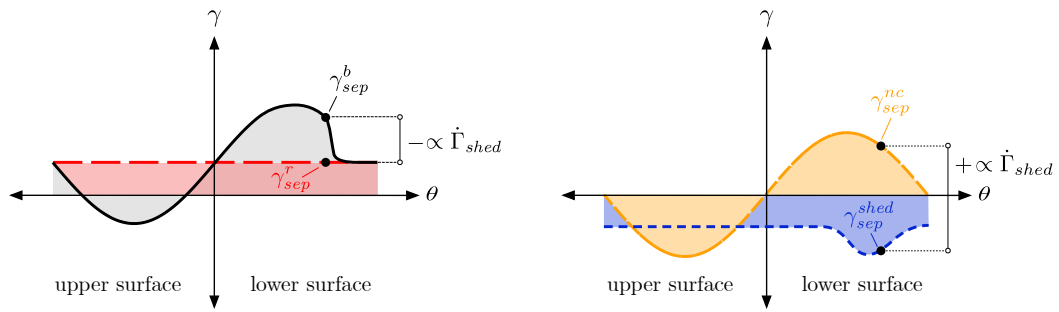
This approach will be referred to as the *vortex sheet method* throughout the thesis and the subscript *sep* evaluates the vortex sheet just before the separation point.¹ In the specific case when $\gamma^r = 0$, the right side of equation 5.10 is similar to the formulations derived by, amongst others, Saffman and Schatzman [82], Sarpkaya [84] and Xia and Mohseni [109]. Schematically, the result of equation 5.10 is visualised in figure 5.3. The amount of circulation shed is directly proportional to the difference between γ_{sep}^b and γ_{sep}^r .

Alternatively, the first formulation of $\dot{\Gamma}_{shed}$ in equation 5.10 shows that

$$\dot{\Gamma}_{shed} = f(\gamma_{sep}^{nc}, \gamma_{sep}^{shed}). \quad (5.11)$$

This implies that the rate at which vorticity sheds is not explicitly dependent on the rotation rate. Whilst rotation of course has an implicit contribution, in that it affects the location of the unsteady separation point, it does not directly contribute to the shedding rate once the unsteady separation point is fixed.

¹When separation occurs on the upper cylinder surface, the shedding rate is the negative of equation 5.10.



(a) Rate at which circulation is shed is equal to the difference between γ^b and γ^r at the separation point.

(b) Rate at which circulation is shed is equal to the sum of γ^{nc} as well as γ^{shed} at the separation point.

Fig. 5.3 Schematic illustration of the dependency of $\dot{\Gamma}_{shed}$ on the surface vortex sheets.

This idea can be visualised by imagining a spinning cylinder in a uniform freestream as shown in figure 5.4. Due to rotation, the slip velocity on the upper surface is reduced, leading to a low vortex sheet strength. On the other hand, the average boundary layer velocity is high. On the bottom surface, the opposite is the case. A high slip velocity leads to a strong vortex sheet, whereas the average boundary layer velocity is low. As a result of this inverse relationship between boundary layer vorticity and velocity, the vorticity flux remains unchanged and in turn, the shedding rate is independent of rotation rate.

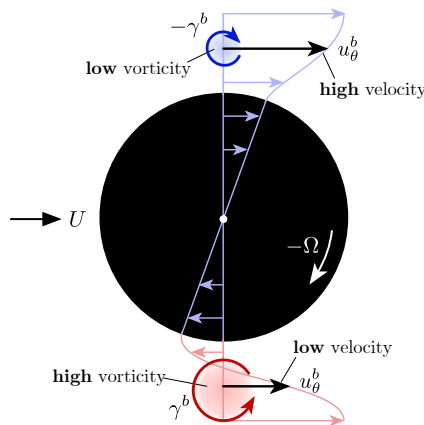


Fig. 5.4 Relationship between boundary layer velocity and vorticity on either side of a spinning cylinder subjected to incoming flow.

5.2 Experimental Investigation into Cylinder Vortex Shedding

We now apply the *vortex sheet method* discussed in the previous section to experimental flow fields around a surging and rotating circular cylinder created using the experimental set-up discussed in section 3.4.1 (cases c0 and c1b), where the cylinder diameter is 0.06 m, with the aim to assess vorticity shedding.

5.2.1 Measuring the True Shedding Rate

To confirm the accuracy of the *vortex sheet method*, we need to be able to compare the predicted rate at which vorticity is shed to the true shedding rate. One *alternative* approach to measure the amount of shed circulation is to integrate the vorticity field associated with vorticity shed from either the top or bottom surface of the cylinder, as schematically shown in figure 5.5a, where any contribution from the boundary layer is excluded. A problem with this method however is that 3-dimensional flow can develop as vorticity leaves the cylinder surface and this can affect the measured circulation. Moreover, errors arise when vorticity leaves the field of view or when it is affected by viscous dissipation. To account for these shortcomings, a second *alternative* method, shown in figure 5.5b, is used to provide a further bound on the shedding rate. The circulation is measured by integrating the vorticity advected past a line that intersects the separating shear layer. An error associated with this approach is that the line is located a short distance away from the cylinder surface and the boundary layer. There is therefore a small time delay between when vorticity is released into the flow field and when it advects past the line. In conjunction we assume that both methods are able to sufficiently minimise effects due to 3-dimensionality, circulation leaving the observed field of view as well as time-lag and thereby bound the real shedding rate.

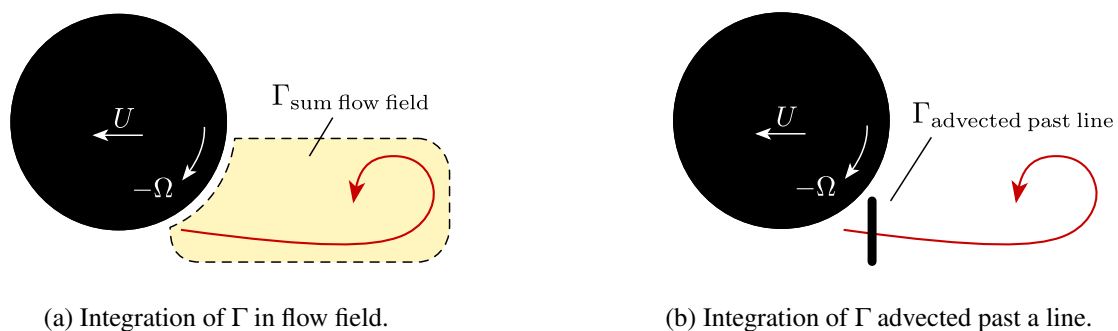


Fig. 5.5 Schematic illustration of how Γ_{shed} is calculated.

5.2.2 Shed Circulation Prediction

A comparison between the amount of shed circulation predicted by the *vortex sheet method* described in section 5.1 and the two *alternative* methods described in section 5.2.1, is shown in figure 5.6 for

the purely translating cylinder as well as for the translating and rotating case. We note that to obtain the magnitude of shed circulation predicted by the *vortex sheet method*, we integrate equation 5.10 in time. This has the added benefit of reducing measurement noise.

From the development of Γ_{shed} we see that unsteady separation occurs simultaneously from both sides of the surging cylinder and from about $s/D = 3$ onwards, when a steady-state velocity is reached, the amount of positive and negative circulation shed into the flow appears to increase approximately linearly for the remainder of the measurement domain. The *vortex sheet method* prediction lies within the bounds created by the *alternative* two methods and thereby shows that it can be successfully used to predict the amount of shed circulation.

When rotation is applied to the cylinder, vorticity first sheds from the lower surface before unsteady separation, at approximately $s/D = 3$, begins on the upper side. The amount of positive circulation shed from the lower surface steadily increases until it begins to taper off at higher translation distances. Moreover, the amount of negative circulation shed from the upper surface increases approximately linearly throughout the observed motion. The amount of shed circulation predicted by the *vortex sheet method* closely follows the results obtained from the two *alternative* measurement techniques. This suggests once more that the proposed *vortex sheet method* is able to successfully predict the rate at which vorticity sheds from the cylinder surface.

An implication from this is that the rate at which vorticity sheds can be used to determine the boundary layer vortex sheet strength at the separation point γ_{sep}^b . This is because the *vortex sheet method* predicts the amount of shed vorticity by using the boundary layer vortex sheet contributions and this relationship can therefore be used to ‘reverse-engineer’ γ_{sep}^b . This may be useful in situations where we would like to recover γ_{sep}^b but are unable to get an accurate boundary layer measurement due to for example experimental limitations

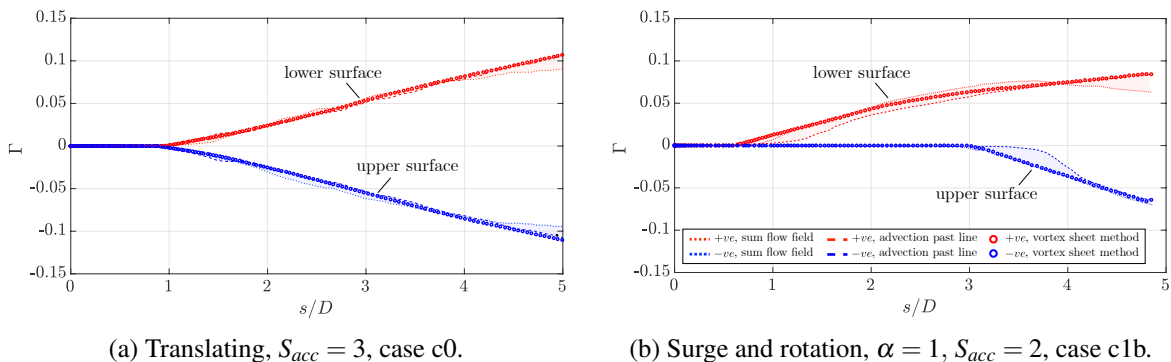


Fig. 5.6 Comparison of computing Γ_{shed} by using the *vortex sheet method* and by directly interrogating the vorticity field. Shaded regions identify the difference between the two *alternative* measurement techniques. Legend applies to both figures.

5.2.3 Rate at which Vorticity is Shed

To take a closer look at how the rate at which vorticity sheds evolves, we plot the shedding rate in figure 5.7 for the surging as well as rotating and translating cylinder. Before delving any deeper into the development of the shedding rate, it must be noted that obtaining the vorticity shedding rate is a rather noisy endeavour. This is because it is either found by differentiating the amount of circulation residing in the flow field, thereby amplifying any noise or alternatively, directly from the vortex sheet strength at the separation point using the *vortex sheet method*. Unfortunately, the latter is itself a sensitive measurement and any noise is once more amplified when performing the *power of 2* operation needed to recover the shedding rate. To give a cleaner picture, a zero-phase shifting filter, with a window size of 0.09 s and 0.06 s respectively, is therefore applied to both kinematic cases. All this is to say that the exact magnitude of the shedding rate at each instance in time should not be viewed from a quantitative perspective. Instead the data presented should be interpreted from a more qualitative standpoint with a focus on general trends.

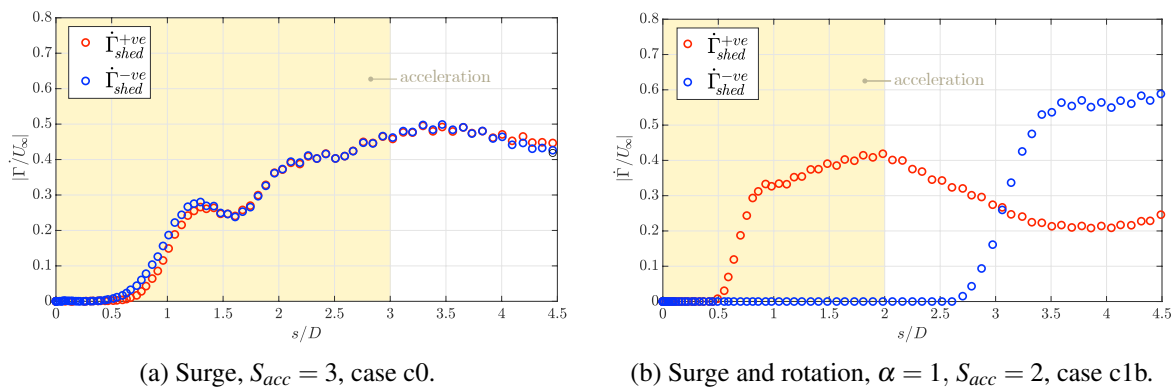


Fig. 5.7 Absolute rate at which vorticity is shed into the flow.

Keeping the sensitivity of the measured shedding rate in mind, let us nonetheless take a look at its development. The surging cylinder sees an initial sharp rise in vorticity shedding rate as unsteady separation begins from both sides of the cylinder. As the cylinder accelerates, the shedding rate continues to increase at a more gradual rate until acceleration ceases at $s/D = 3$, after which the general trend is approximately constant. This coincides with the linear increase of Γ seen earlier in figure 5.6a. Moreover, the shedding rate from both sides of the cylinder is comparable and this is in line with visible observations from the flow field, where two equally sized vortices develop.

Shifting our focus to the surging and rotating cylinder, unsteady separation first begins on the lower surface and the shedding rate increases until $s/D = 2$ when acceleration ceases. Thereafter it gradually decreases until approximately $s/D = 3.5$, where it maintains its level for the remainder of the observed motion. The rate of unsteady separation from the top surface is almost invariant throughout

the captured motion and therefore confirms the findings from figure 5.6b, where an approximately linear increase in the amount of shed circulation residing in the flow field was observed.

5.2.4 Exploring the Evolution of the Vorticity Shedding Rate

In the preceding sections we tracked the total amount of vorticity shed into the flow field from the separation point as well as the shedding rate. We noted that the rate at which vorticity sheds is not always constant but that it varies as the cylinder moves. This is particularly noticeable for the surging and spinning cylinder. We now attempt to reconcile this behaviour by exploiting the link between the shedding rate and the strength of the constituent parts of boundary layer vortex sheet at the unsteady separation point.

In Chapter 4 we discussed how changes to γ_{sep}^b are dominated by acceleration and far-field vorticity. By accounting for both of these effects, the adjusted vortex sheet strength at the separation point remains almost unchanged as the unsteady flow field develops. It therefore appears logical that the shedding rate should equally be affected by these same two parameters, since it itself is governed by γ_{sep}^b , as shown by equation 5.10. This suggests that acceleration increases the shedding rate, whilst far-field vorticity of the same sign as that being shed creates an opposite effect. The latter is schematically illustrated in figure 5.8. Positive vorticity in the far-field creates a negative vortex sheet contribution γ^{shed} all along the cylinder. This shifts γ^b downwards and thus lowers $\dot{\Gamma}_{shed}$, since the difference between γ^b and γ^r at the separation point reduces.

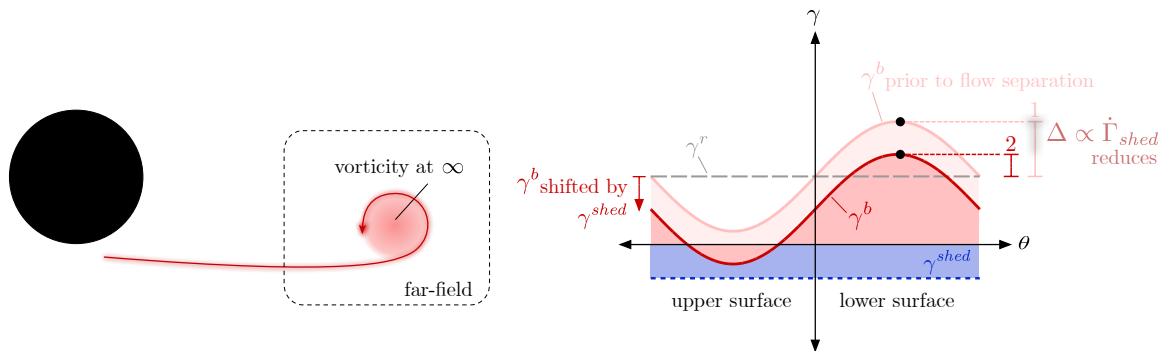


Fig. 5.8 Schematic illustration showing positive vorticity located at ‘infinity’ reducing the shedding rate by lowering γ^b .

We test our hypothesis regarding the influence of acceleration and far-field vorticity on the shedding rate by forming a new parameter $\bar{\Gamma}_{shed}$. This represents the *adjusted* shedding rate where the effect due to far-field vorticity is removed and acceleration is accounted for. Beginning from the definition of the shedding rate given by equation 5.10, where this is written as a function of the non-circulatory vortex sheet component (which in the absence of external vorticity is γ_{am}^{nc} and thus only related to the surge velocity) and the contribution to due shed vorticity, we remove the far-field

contribution $\gamma_{far-field,sep}^{shed}$ and divide by U to arrive at

$$\begin{aligned}\bar{\Gamma}_{shed} &= \frac{\left(\gamma_{sep}^{nc} + \gamma_{sep}^{shed} - \gamma_{far-field,sep}^{shed}\right)^2}{2U} \\ &= \frac{\left(\gamma_{sep}^{nc} + \gamma_{local,sep}^{shed}\right)^2}{2U}.\end{aligned}\quad (5.12)$$

The adjusted and raw shedding rate for the surging cylinder are shown in figure 5.9a, where we see that $\bar{\Gamma}_{shed}$ remains much more constant throughout the captured motion than its uncorrected counterpart. The most notable effect is seen during the acceleration phase, where the general up-trend seen in the raw data (hollow circles) is removed. Far-field vorticity on the other hand, has a negligible effect on the shedding rate. This is because the flow field is symmetrical about the x -axis and equal amounts of positive and negative vorticity are shed, causing each to cancel the effect of the other.

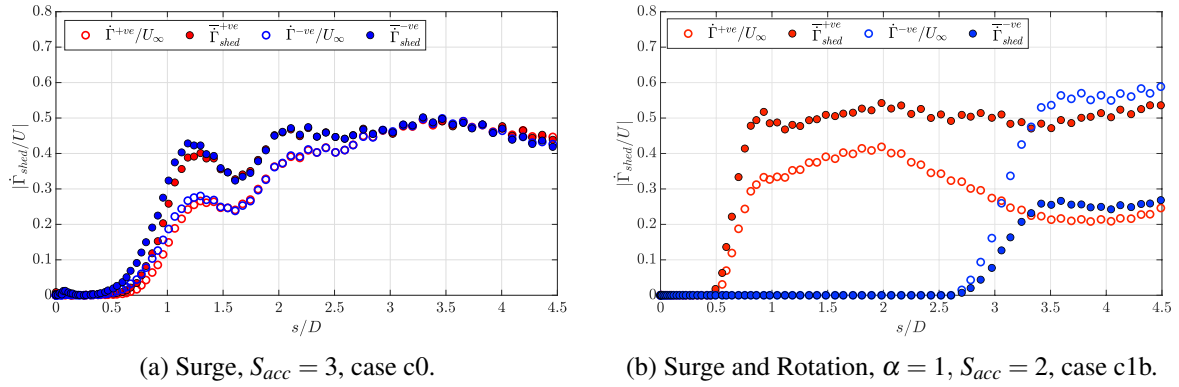


Fig. 5.9 Raw and adjusted rate at which vorticity is shed. Absolute values are plotted.

$\bar{\Gamma}_{shed}$ as well as the original shedding rate for the surging and rotating cylinder are shown in figure 5.9b. In section 5.2.3 we noticed a highly variable shedding rate of positive vorticity from the bottom half of the cylinder. As demonstrated in figure 5.9b, when accounting for acceleration and far-field vorticity, the *adjusted* shedding rate is entirely constant and all fluctuations are removed.

The observed invariance of $\bar{\Gamma}_{shed}$ for both kinematic cases therefore confirms our hypothesis, that acceleration increases the shedding rate, whilst far-field vorticity, of the same sign as that being shed, reduces $\bar{\Gamma}_{shed}$.

5.3 Summary: Vorticity Shedding

The chapter explored the rate at which vorticity is shed from the unsteady separation points on a surging and rotating cylinder. A key concept discussed is that the shedding rate can be expressed solely in terms of the boundary layer vortex sheet contributions. This shows that the rate at which vorticity

leaves the boundary layer and enters the surrounding flow field is proportional to the difference between the total boundary layer vortex sheet and the rotational component at the separation point. Alternatively, it is a function of the sum of the non-circulatory vortex sheet and that due to shed vorticity. Experimental measurements of the vortex sheets make it possible to recover the amount of circulation shed and thereby validate the proposed theory. A consequence from this is that the shedding rate itself can be used to estimate the vortex sheet strength at the separation point. This may be useful in situations when accurate boundary layer measurements are not possible.

The rate at which vorticity is shed into the flow varies as the cylinder translates. This development can be attributed to a changing instantaneous translation velocity as well as to far-field vorticity. As an example, acceleration increases the shedding rate, whilst it is reduced when vorticity of the same sign as that being shed populates the far-field. By proposing an *adjusted* shedding rate, this idea can be experimentally confirmed, where this new parameter remains invariant throughout the captured motion of the cylinder.

The implications of these findings regarding alternate vortex shedding from bluff bodies, lift creation as well as the theoretical maximum lift of a spinning cylinder are discussed in the following chapter.

Chapter 6

Flow Patterns and Force Generation

This chapter is a short excursion into the world of lift generation and flow patterns. The idea is to reconcile our findings from Chapters 4 and 5 with observable phenomena in the real world. Specifically, we focus on how lift and the respective flow structures around a circular cylinder arise by viewing the development through the lens of vortex sheets. In particular with the idea in mind that the vortex sheet strength at the separation point, and directly tied to this, variations of the shedding rate, appear to be strongly affected by far-field vorticity. The chapter first explores how an alternate vortex shedding pattern develops as well as how lift is generated in section 6.1 before associating the results with the theoretical maximum lift proposed by Prandtl [71] in section 6.2.

6.1 Alternate Vortex Shedding and Lift Generation

We begin by assessing the evolution of the flow field around a surging circular cylinder as well as the related force response. When the cylinder first sets into motion, the flow is initially fully attached and boundary layer vorticity develops along the cylinder surface. By once more applying potential flow theory, the vorticity in the boundary layer can be represented by a boundary layer vortex sheet γ^b that enforces the no-throughflow condition. As the cylinder continues to surge, equal amounts of vorticity are shed from either side of the cylinder, creating a symmetric flow field, as schematically depicted on the left in figure 6.1, and labelled accordingly with a 1. The numbers in the figure correspond to individual time steps, and we will use these to help guide us through the example. The boundary layer vortex sheet now consist of a sinusoidal contribution due to translation as well as a component arising from shed vorticity γ^{shed} . A simplified schematic representation of both γ^b and γ^{shed} is further included in figure 6.1, where the related distributions are once again marked with a 1. The symmetry of the flow causes both vortex sheets to be equal and opposite on the upper and lower cylinder surface.

From the impulse method we know that a lift force is created when the y -momentum of the flow field changes. This can be caused by elements of vorticity moving relative to each other in the

x -direction or when new vorticity is shed. Due to the symmetry of the flow field about the x -axis, the net vertical impulse at each x -location is zero and therefore no lift force is created.

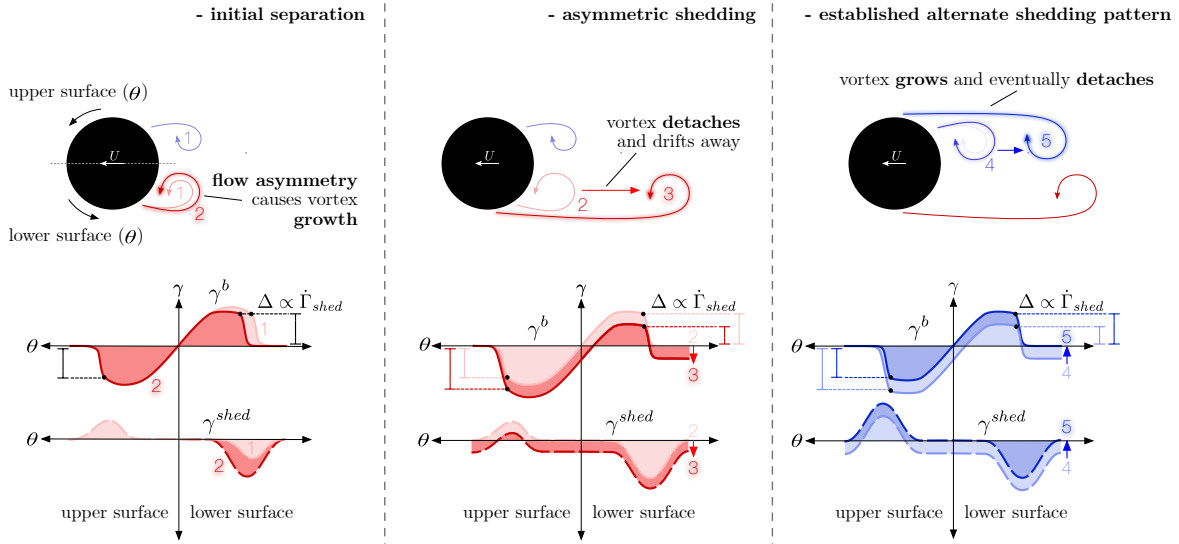


Fig. 6.1 Schematic representation of the flow field around a surging cylinder. Simplified distributions of γ^b and γ^{shed} are also shown. Numbers indicate the corresponding time steps.

The question therefore arises how the transition of the flow field to an alternate shedding pattern occurs. The state change begins with the fact that although qualitatively the flow appears symmetric during the initial stages, there can exist a small difference between the exact unsteady separation point, the shedding rate and how the flow develops on either side of the cylinder. This could be caused by a different surface roughness, a slight asymmetry in the circular cylinder or small variations of the flow field due to the stochastic nature of turbulence. Therefore, to illustrate how such an imbalance can lead to alternate vortex shedding, we consider the case where the unsteady separation point is the same on both sides of the cylinder but where the shedding rate at the bottom is slightly increased. This causes more positive vorticity to shed, which in turn rolls up into a stronger positively signed vortex and this is schematically included on the left in figure 6.1 and marked as time step 2. Vorticity is still located in very close proximity to the cylinder and therefore γ^{shed} increases in the local vicinity to the vortex, as indicated on the left in figure 6.1. With time, some of this positive vorticity begins to drift away from the cylinder, as shown in the middle segment of figure 6.1. At this point, shed vorticity starts to populate the far-field and begins to create a substantial negative far-field vortex sheet contribution $\gamma_{far-field}^{shed}$, which as we discussed in chapter 4, uniformly affects the entire cylinder surface.

The presence of the far-field vortex sheet contribution has two significant implications, which shape the future flow development. The first is that it affects the rate at which positive vorticity is shed from the lower cylinder surface. This is because the far-field vortex sheet contribution causes the entire boundary layer vortex sheet to shift downwards, as illustrated in the centre of figure 6.1

(labelled as time step 3). As a result, the shedding rate $\dot{\Gamma}_{shed}$ becomes less. This is because $\dot{\Gamma}_{shed}$ is proportional to the difference between γ_{sep}^b and γ_{sep}^r , and this reduces when the boundary layer vortex sheet is affected by $\gamma_{far-field}^{shed}$ as discussed in chapter 5. Moreover, the rate at which vorticity sheds into the flow determines whether the separating shear layer rolls up into a vortex. This is because a high shedding rate, leads to a high localised magnitude of shed vorticity. This in turn induces a sufficiently strong *circular* flow causing any shed vorticity to roll up into a vortex. Conversely, when the strength of shed circulation is too low, the separating shear layer does not form a vortex and instead drifts away from the cylinder.

Furthermore, $\gamma_{far-field}^{shed}$ not only affects unsteady separation from the bottom cylinder surface, but it also influences how negative vorticity sheds from the opposite side. While the difference between γ_{sep}^b and γ_{sep}^r reduces as a result of $\gamma_{far-field}^{shed}$ on the bottom cylinder surface, it becomes larger on top, and thereby causes negative vorticity to shed at an increased rate. As a result, the newly shed vorticity induces sufficient *circular* flow and rolls up into a vortex as shown in time step 4 on the right of figure 6.1. Eventually, as this negatively signed vortex grows, parts of it move further away from the cylinder and begin to contribute to the far-field vortex sheet, labelled as time step 5 in figure 6.1. This initiates the reverse of the process previously described. As negative vorticity begins to also populate the far-field, this negates the vortex sheet contribution created by positive vorticity already residing there. In turn, the contribution from $\gamma_{far-field}^{shed}$ becomes less negative and γ^b is shifted back upwards. As a result, the shedding rate from the upper surface reduces, whilst simultaneously the shedding rate from the lower surface increases. This causes the separating shear layer from the bottom surface to roll up into a vortex once more and thus establishes the alternating vortex shedding pattern. The imbalance in the shedding rate from the upper and lower surface as well as the time delay between positive and negative vorticity moving away from the cylinder, creates a changing impulse and thus leads to the sinusoidal variation in lift force.

Moving on from this and using the same approach, let us now explore the force and flow development when spin is applied to the surging cylinder. Imagine a cylinder that impulsively surges from right to left as well as rotates in the clockwise direction. Even though spin is often equated with a lift force this is not an immediate result in unsteady flow and it should be clearly noted that this idea only works when we assume fully developed potential flow. The reasons behind this are illuminated as part of the following discussion.

When the cylinder has just begun its motion, and no vorticity has yet been shed into the flow, the time rate of change of the impulse is zero and therefore no lift force acts on the cylinder. This is because even though the solid body motion creates negative circulation within the cylinder, a positive vortex sheet of matching strength forms along the surface, such that the net circulation is zero.

Instead, the effect by which spin creates a lift force is that it causes unequal amounts of vorticity to be shed from the upper and lower cylinder surface. In line with the previous example of the surging cylinder, when the rotating cylinder begins its motion, positive vorticity first sheds from the lower surface as shown in the top right corner of figure 6.2, where this instance in time is marked accordingly with a 1. A boundary layer vortex sheet γ^b and its constituent parts develop accordingly, with γ^b and γ^{shed} also included in figure 6.2. The boundary layer vortex sheet consists of the sinusoidal distribution from γ_{am}^{nc} , a uniform contribution due to rotation γ^r and a localised component γ^{shed} created by the starting vortex residing in close proximity to the cylinder. With time, the starting vortex drifts away from the cylinder, as shown on the left in figure 6.2 and labelled with a 2. This increases the negative far-field vortex sheet contribution and causes γ^b to shift downwards. As discussed for the surging cylinder, this reduces the difference between γ_{sep}^b and γ_{sep}^r and thus lowers the shedding rate. At the same time, the shift in γ^b causes the vortex sheet strength to become more negative on the upper surface. At some point, a critical threshold is reached and unsteady separation is initiated from the upper surface as shown at step 3 in figure 6.2. The newly shed vorticity rolls up into a vortex and eventually drifts downstream as illustrated by step 4 in the same figure. Identical to the phenomena discussed for the surging cylinder, the negative vorticity drifting away from the cylinder opposes the far-field contribution induced by the positive starting vortex. γ^b therefore shifts upwards once again. This reduces the rate at which negative vorticity sheds from the top surface, whilst increasing the amount of positive vorticity leaving the bottom half of the cylinder. Since the positive vorticity is now sufficiently strong to induce the necessary *circular* flow, the separating shear layer rolls up into a new vortex and thus establishes an alternating shedding pattern.

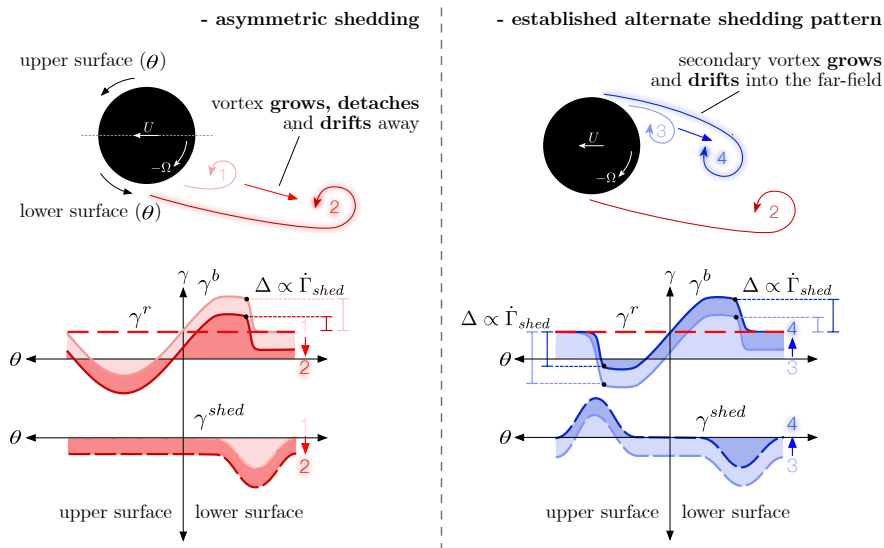


Fig. 6.2 Flow field and γ^b and γ^{shed} development for a surging and clockwise rotating cylinder. Each number corresponds to one instance in time, with the colours matching accordingly.

The lift force acting on a cylinder is tied to the rate of change of the vertical flow impulse, which as discussed earlier, is created by flow field asymmetry and a delay between when positive and negative vorticity sheds. A parameter that has a direct effect on this behaviour is the rotation ratio of the cylinder. This is because it governs the amount of either positively or negatively signed vorticity that can be shed before vorticity of the opposite sign is also released into the flow field.

For example, when a cylinder moves from right to left, a high clockwise rotation ratio creates a strong positive γ^r vortex sheet contribution, shifting γ^b upwards. In turn, a substantial amount of positive vorticity must now shed from the bottom cylinder surface before γ^{shed} is strong enough to cause γ^b to become sufficiently negative on the top surface, for separation to commence. When this occurs, it marks maximum lift, which reduces thereafter as more negative vorticity sheds. Conversely, a low rotation ratio only requires a small amount of positive vorticity to be shed before the boundary layer has been sufficiently shifted for separation to occur from the top cylinder surface. Since less positive vorticity has been shed into the flow before negative vorticity also populates the flow field, a lower rate of change of vertical impulse is created and thus the peak force is reduced.

6.2 Prandtl and the Theoretical Maximum Lift

Staying with the topic of force creation, the vortex sheet approach can also be used to evaluate the maximum theoretical lift, which a spinning cylinder should be able to achieve. Prandtl [71] and Goldstein [30] argued that this maximum is reached when the stagnation points around a circular cylinder collapse and move away from the surface and into the flow. Since the streamlines form a closed loop around the cylinder, the shedding of any further circulation is theoretically prevented. This theory is based on potential flow and since it therefore substantially simplifies the flow it should not come as a surprise that this threshold is only of theoretical nature. In fact Tokumar and Dimotakis [95] for example experimentally exceeded this theoretical value by more than 20 %.

Aware of the limitations of this upper bound idea, we nonetheless proceed to derive the equivalent result using the vortex sheet approach. Imagine an impulsively started cylinder surging from right to left whilst simultaneously rotating clockwise, as shown on the left in figure 6.3. When unsteady separation occurs, the rate at which vorticity is shed is proportional to $\gamma^b - \gamma^r$ at the unsteady separation point. This suggests that once both of these vortex sheet components have the same strength at the unsteady separation point, no more vorticity is shed into the flow. The maximum difference between γ^b and γ^r is equal to the amplitude of the sinusoidal vortex sheet contribution arising from translation, and this is $2U$ on the bottom cylinder surface.

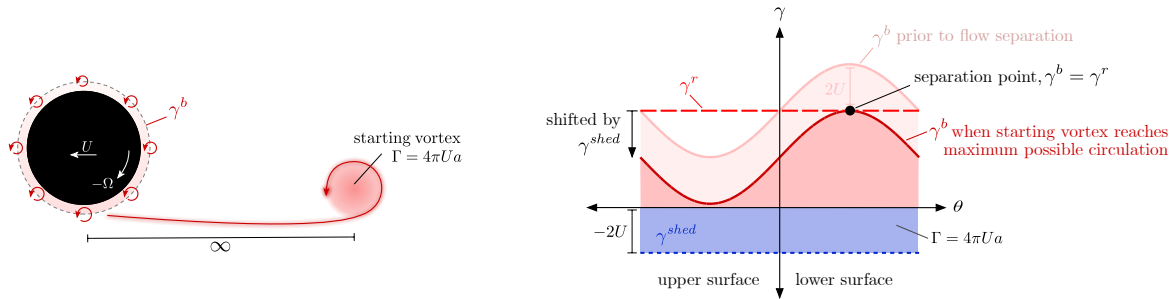


Fig. 6.3 Vortex at infinity of strength $\Gamma = 4\pi Ua$ causes $\gamma^b = \gamma^r$, theoretically leading to $\dot{\Gamma}_{shed} = 0$.

If we now assume that positively signed vorticity sheds from the lower side of the cylinder and moves infinitely far away, then this creates a negative uniform vortex sheet contribution all along the cylinder surface. When the total amount of shed circulation reaches $4\pi Ua$, the strength of the corresponding uniform vortex sheet is $-2U$ everywhere. This causes the maximum of γ^b to equal γ^r and thereby theoretically prevents any further positive vorticity to be released into the flow. If the rotation ratio of the cylinder is below two, negative vorticity would form on the upper cylinder surface and could be shed into the flow. This however, has no impact on the maximum lift, since the shedding of negative vorticity would only serve to reduce the experienced lift force.

The total circulation of cylinder and its boundary layer vortex sheet is equal and opposite to that of the shed circulation residing at infinity. The system can therefore be represented as two point vortices of equal and opposite magnitude moving apart at a constant velocity U_∞ . It follows that the steady-state potential flow lift is $L = \rho U_\infty \Gamma$. Replacing Γ with the maximum theoretical circulation $4\pi Ua$, yields

$$C_l = 4\pi. \tag{6.1}$$

This maximum lift coefficient is identical to that proposed by Prandtl but derived purely from a vortex sheet perspective. As noted earlier, this theoretical limit does not hold in real viscous flow. Instead the main aim of the above derivation was to reconcile the current conceptual ideas with historical approaches to flow analysis and force prediction.

6.3 Summary: Flow Patterns and Force Generation

This chapter explored the flow patterns around a circular cylinder as well as the force creation from a vortex sheet perspective. Even though the flow around many bluff bodies is symmetrical to begin with, an alternating vortex shedding pattern often develops with time. This cyclic behaviour can be linked to the imbalance of positive and negative vorticity located far away from the object. When more positive than negative vorticity is located in the far-field, the boundary layer vortex sheet on a circular cylinder is uniformly reduced and becomes more negative. This reduces the rate at which positive vorticity leaves one side of the cylinder surface, whilst simultaneously increases the rate

at which negative vorticity is released from the other side. The opposite is the case when the imbalance shifts in favour of negative far-field vorticity and thereby creates the alternate shedding pattern.

Moreover, the vortex sheet concept can provide a theoretical upper bound on the steady-state lift that can be achieved by a surging and rotating circular cylinder. The rate at which vorticity is shed from the cylinder surface tends to zero when the difference between the total boundary layer vortex sheet and the rotational contribution at the separation point approaches zero and thereby limits the maximum achievable lift force. By calculating the amount of shed circulation required to shift the boundary layer vortex sheet such that it matches the rotational vortex sheet contribution, the theoretical maximum lift can be obtained and this is found to match the potential flow steady-state lift threshold predicted by Prandtl.

The previous chapters investigated the origins of boundary layer and flow field vorticity, the process by which vorticity is shed and how this knowledge can be applied to real life examples. To further advance LOMs it is now time to take a detailed look into how the vorticity field must be treated to calculate specific force contributions. This is the next step on our journey to better understand these unsteady flow fields and we explore this in the following two chapters.

Chapter 7

Unsteady Force Contributions

When studying unsteady flow it is often necessary to predict the forces acting on an object as well as to understand why these arise. This is particularly important for LOMs, since these are in many cases designed by reducing the governing equations to simple linear formulations that can be solved at a low computational cost. The underlying physics are split up into a series of separate components, where a simple model is used to approximate each. To ensure that the individual parts of an LOM complement each other and arrive at a suitable force prediction, a good understanding of the process by which the forces are created is therefore necessary. This requires first an understanding of vorticity creation, as discussed in the previous chapters, and secondly, insight into how a particular flow feature contributes to the force. Together both of these ensure that each force contribution is only considered once and that the minimum number of computations are performed.

Having explored vorticity creation, this chapter focus on identifying how much a specific flow structure contributes to the total force. LOMs ideally limit their analysis to only the most dominant flow features in order to save resources. Being able to quantify whether a flow structure has a strong or negligible contribution to the force can therefore help decide whether it should make up part of the LOM or if it can be ignored instead. Examples of this could be whether the deflected path taken by a vortex as it passes a wing needs to be modelled or whether gust shear layer deflection during a body-gust encounter, as shown in figure 7.1, creates a sufficient force to warrant its inclusion in an LOM.

From a more global perspective, understanding how flow structures influence the force can help interpret experimental or computational results. As an example, Martínez-Muriel and Flores [56] found that the peak force experienced by a wing, as externally created vortices of various sizes and strengths pass by at different distances, scales with the average velocity induced on the wing by the vortex. Unfortunately, the authors could not provide an explanation for this observed relationship. In situations like this, knowledge as to how a particular flow structure affects the force can be useful to provide a more complete picture and holistic understanding of why certain patterns exist and

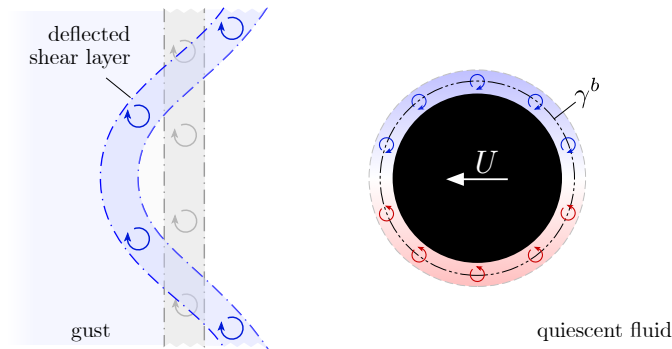


Fig. 7.1 Deflection of gust shear layer as a cylinder approaches.

importantly, what their limitations may be.

This chapter therefore focuses on isolating the force due to a specific flow feature. The theoretical path by which this can be achieved is outlined in section 7.1. As part of the derivation, the force acting on an object is expressed in terms of its constituent parts, thereby also enabling us to recover the force affecting an individual object in a multi-body flow field. We subsequently use this flow arrangement to test our theory in section 7.2, since our calculations of the force acting on a single object can be compared to physical force balance measurements.

7.1 Unsteady Force Decomposition

As a recap, Lamb [46] shows that the impulse created by a pair of counter-rotating vortices of equal and opposite strength in 2-dimensional flow is given by

$$I = \rho \Gamma d, \quad (7.1)$$

where ρ is the fluid density, Γ is the circulation and d is the distance separating the vortices. The momentum or impulse of the fluid changes when these vortices move apart or when their strength changes. The force, F , is therefore the time rate of change of the impulse I ,

$$F = \rho \left(\underbrace{\Gamma \dot{d}}_{\text{motion}} + \underbrace{d \dot{\Gamma}}_{\text{creation}} \right), \quad (7.2)$$

where the first term describes the force contribution created by the relative motion between the two vortices, whilst the second is due to a change in vortex strength.

A real flow field cannot always be grouped into pairs of counter-rotating vortices, however, the same theoretical approach can nonetheless be applied; for example by considering the flow to consist of many incremental vortex pairs, where their effect is summed¹. This is the basis of the *impulse approach*, where Wu's [107] implementation of this concept can be illustrated, without loss of generality, by assuming the 'body' of interest to be a circular cylinder. Consider a 2-dimensional flow field, where a single cylinder is travelling horizontally in a region R_L , and enclosed by a boundary B_L far away, as illustrated in figure 7.2.

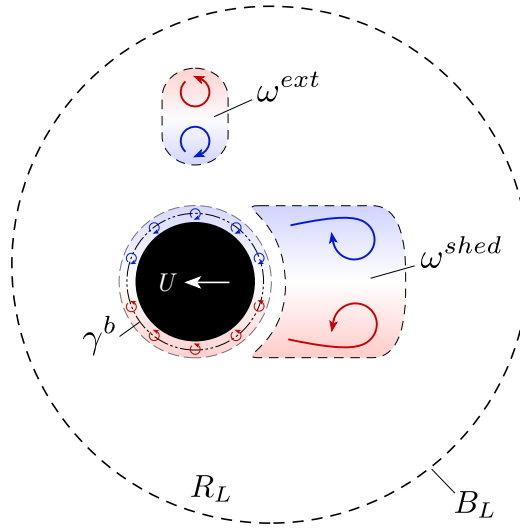


Fig. 7.2 Schematic illustration of a flow field containing a translating cylinder as well as cylinder-shed ω^{shed} and external vorticity ω^{ext} .

The flow field consists of cylinder-shed and external vorticity, where the latter could be created by a localised region of moving fluid such as a gust. The complete vorticity field is assumed to be contained within R_L , yielding

$$\int_{R_L} \omega dR = 0. \quad (7.3)$$

Furthermore, the flow is otherwise quiescent, such that the velocity on the boundary B_L is zero. The aerodynamic force acting within the domain B_L is

$$\mathbf{F}_a = -\rho \left(\frac{d}{dt} \int_{R_L} \mathbf{r} \times \omega dR - \frac{d}{dt} \int_{R_b} \mathbf{U}_b dR \right), \quad (7.4)$$

where ρ is the density of the fluid and is for simplicity is assumed to be constant throughout and \mathbf{r} is the position vector. R_b represents the region occupied by the cylinder, and \mathbf{U}_b is the instantaneous velocity vector of the cylinder. As a reminder, the first term on the right of equation 7.4 is the force arising from the rate of change of vorticity. The second term is required because Wu assumes that fluid is distributed throughout the entire flow field, including the region occupied by the cylinder. As

¹The flow is assumed to be linear, consisting of a superposition of all individual vortex elements [81].

this accelerates, the momentum of the fluid contained within the cylinder changes. The additional force contribution resulting from this needs to be removed to recover the correct aerodynamic force.

Unfortunately, in its current formulation only, the total force acting within the boundary B_L can be determined. This is what we now seek to rectify in the following derivation by reformulating equation 7.4, such that the force due to a specific flow structure can be identified. As a starting point, equation 7.4 is applied to a horizontally travelling cylinder and re-written in terms of lift and drag,

$$\begin{aligned} L &= \rho \frac{d}{dt} \int_{R_L} I_y dR \\ D &= -\rho \frac{d}{dt} \int_{R_L} I_x dR + \rho \frac{d}{dt} \int_{R_b} U_b dR. \end{aligned} \quad (7.5)$$

where I_y and I_x represent the impulse,

$$I_y = x\omega, \quad I_x = y\omega. \quad (7.6)$$

We proceed by making use of the fact that in potential flow we can ‘construct’ the complete flow field by superposing individual flow solutions that are based on vortex elements. Thus we can represent the viscous flow field in potential flow terms, where we choose to split the flow field vorticity into three sets. The first group consists of vorticity shed by the cylinder, ω^{shed} . The second group includes external vorticity that is not created by the cylinder, ω^{ext} . This vorticity could arise through a sudden local acceleration of flow, for example a gust. The last group contains the boundary layer vorticity, ω^b , attached to the cylinder surface. The complete vorticity field is therefore given as:

$$\omega = \omega^b + \omega^{shed} + \omega^{ext}. \quad (7.7)$$

Once the vorticity field is split up into the three groups, the force expressed in equation 7.5 can be re-written as,

$$\begin{aligned} L &= \rho \int_{B_b} \underbrace{\frac{dI_y^b}{dt}}_{\text{boundary layer}} dl + \rho \int_{R_L} \left(\overbrace{\frac{dI_y^{shed}}{dt}}^{\text{cylinder-shed vorticity}} + \underbrace{\frac{dI_y^{ext}}{dt}}_{\text{external vorticity}} \right) dR, \\ D &= -\rho \int_{B_b} \underbrace{\frac{dI_x^b}{dt}}_{\text{boundary layer}} dl - \rho \int_{R_L} \left(\overbrace{\frac{dI_x^{shed}}{dt}}^{\text{cylinder-shed vorticity}} + \underbrace{\frac{dI_x^{ext}}{dt}}_{\text{external vorticity}} \right) dR + \rho \frac{d}{dt} \int_{R_b} U_b dR, \end{aligned} \quad (7.8)$$

where

$$\begin{aligned} I_y^b &= x\gamma^b, & I_y^{shed} &= x\omega^{shed}, & I_y^{ext} &= x\omega^{ext} \\ I_x^b &= y\gamma^b, & I_x^{shed} &= y\omega^{shed}, & I_x^{ext} &= y\omega^{ext}. \end{aligned} \quad (7.9)$$

We note that similar to the approach used in previous chapters, boundary layer vorticity is replaced by a vortex sheet γ^b located on the body surface, as permitted by the potential flow framework. The first integral in equation 7.8 is performed over the cylinder surface B_b , whilst the second acts on the area of the remaining flow field. The time derivative has been taken into the integral and the impulse (I_x, I_y) is grouped according to the sets of vorticity. In order to simplify the explanation and to reduce the length of any subsequent equations, all further manipulations are only applied to the lift force but of course remain equally applicable to drag.

The time derivatives in equation 7.8 can now be expanded to reveal force contributions due to the movement and creation of vorticity.

$$L = \rho \int_{B_b} \left(\underbrace{\gamma^b \frac{dx}{dt}}_{\text{motion}} + x \underbrace{\frac{d\gamma^b}{dt}}_{\text{creation}} \right) dl + \rho \int_{R_L} \left(\underbrace{\omega^{shed} \frac{dx}{dt}}_{\text{advection}} + x \underbrace{\frac{d\omega^{shed}}{dt}}_{\text{creation}} + \underbrace{\omega^{ext} \frac{dx}{dt}}_{\text{advection}} + x \underbrace{\frac{d\omega^{ext}}{dt}}_{\text{creation}} \right) dR. \quad (7.10)$$

The change in position of γ^b is linked to the kinematic motion of the cylinder and is therefore labelled as ‘motion’ in equation 7.10. Shed and external vorticity are free to move under the influence of the local flow velocity, where

$$U = \frac{dx}{dt}, \quad (7.11)$$

and the corresponding terms are therefore labelled as ‘advection’. The force due to the rate of change of strength of vorticity is marked as ‘creation’.

Each vortex element, regardless of whether it is part of the boundary layer vortex sheet or whether it resides elsewhere in the flow field, induces a velocity according to the Biot-Savart law

$$u_\theta = \frac{\int_{R_{el}} \omega dR}{2\pi r}, \quad (7.12)$$

where R_{el} is the region associated with a vortex element and r is the distance between the vortex element and a position in the flow field at which the velocity is induced. The flow velocity at any point in the flow field is therefore a superposition of the velocities induced by each vortex element. Thus the velocity field, U_{field} , can be decomposed into a contribution from the boundary layer vortex sheet U_{γ^b} , a contribution from shed vorticity $U_{\omega^{shed}}$ and a contribution from any externally created vorticity $U_{\omega^{ext}}$,

$$U_{field} = U_{\gamma^b} + U_{\omega^{shed}} + U_{\omega^{ext}}. \quad (7.13)$$

Equation 7.10 can now be re-cast with the velocity, which advects the free vorticity, split up into its three contributions,

$$\begin{aligned}
 L = \rho \int_{B_b} \overbrace{\frac{dI_y^b}{dt}}^{\text{change of boundary layer}} dl + \rho \int_{R_L} \left(\overbrace{x \frac{d\omega^{shed}}{dt}}^{\text{new vorticity shed}} + \overbrace{x \frac{d\omega^{ext}}{dt}}^{\text{creation ext. vorticity}} \right. \\
 \left. + \underbrace{U_{\gamma^b} (\omega^{shed} + \omega^{ext})}_{\text{advection by boundary layer}} + \underbrace{U_{\omega^{shed}} (\omega^{shed} + \omega^{ext})}_{\text{advection by shed vorticity}} + \underbrace{U_{\omega^{ext}} (\omega^{shed} + \omega^{ext})}_{\text{advection by ext. vorticity}} \right) dR. \quad (7.14)
 \end{aligned}$$

Equation 7.14 describes the change in momentum and thus the total lift force on the fluid within the control volume. To simplify the formulation, the impulse due to the rate of change of γ^b is written as one term because the vortex sheet elements move with the cylinder surface and develop in accordance with the requirement to ‘mirror’ the vorticity in the flow field rather than advect freely. The remaining two terms of the first line of equation 7.14 are due to new vorticity being shed from the cylinder and any changes in strength of external vorticity. The three terms on the second line of equation 7.14 are due to the advection of free vorticity, caused either by other elements of free vorticity or the boundary layer.

To isolate the force acting on the cylinder and to simplify the expression, a number of terms can be removed from equation 7.14. Saffman [81] shows that two vortices advecting freely under the influence of each other do not generate a force. This is because they do not create a net change in momentum. Therefore, the last two terms in equation 7.14 vanish. On the assumption that the change in strength of external vorticity has not been caused by the cylinder, the creation term associated with external vorticity (third term on the first line in equation 7.14) can also be removed. Implicitly, a change in strength of external vorticity still affects the force acting on the cylinder, as the time variation of the boundary layer vortex sheet is affected. After removing the respective terms, the lift force experienced by the cylinder is,

$$\begin{aligned}
 L_{cyl} = \rho \int_{B_b} \underbrace{\frac{dI_y^b}{dt}}_{\text{change of bound. layer}} dl + \rho \int_{R_L} \left(\underbrace{U_{\gamma^b} (\omega^{shed} + \omega^{ext})}_{\text{advection}} + \underbrace{x \frac{d\omega^{shed}}{dt}}_{\text{creation}} \right) dR. \quad (7.15)
 \end{aligned}$$

The force acting on the cylinder is therefore only dependent on the rate of change of the boundary layer impulse, the creation of new vorticity (ie. vorticity shed by the cylinder) and the advection of surrounding vorticity by the cylinder boundary layer. In the latter, the description ‘surrounding vorticity’ includes all shed vorticity coming from either the cylinder or any other body as well as the vorticity located within the boundary layer of any external object; in short, any vorticity located within the surrounding flow field, and it is mathematically accounted for by the *advection* term in equation 7.15.

Kang et al. [38] rigorously extended Wu's impulse formulation to show that the force affecting a body can be computed by only analysing a finite domain around the body of interest. As such, it becomes possible to determine the force acting on an individual object immersed in a multi-body flow field. On the surface, their formulation looks different to equation 7.15, however, upon expansion and after subsequent simplification, the formulation proposed by the authors recovers equation 7.15. This therefore suggests that equation 7.15 is equally applicable to multi-body flow fields, where the total force on each individual body can be recovered. To illustrate the use of equation 7.15 further, Appendix A applies the result to a steady and accelerating freestream to recover some common theoretical results.

Before attempting to recover the force due to a specific flow feature, it is worth reminding ourselves that we consider the boundary layer vortex sheet, γ^b , to be composed of a number of individual contributions. A first component is created by the kinematic motion of the cylinder γ_{am}^{nc} and can be linked to the added mass force experienced during acceleration. A further contribution to γ^b is due to free vorticity in the flow field. In Chapter 4 this free vorticity was grouped into a component that was shed by the cylinder itself and a second that consisted of externally created vorticity. Here we use the same approach as earlier and let γ_{ext}^{nc} represent the vortex sheet contribution due to externally created vorticity.

To approximate the lift arising from an external flow feature to a first order, we first identify the force component due to the rate of change of the impulse dI^{ext}/dt created by the development of its respective vortex sheet contribution γ_{ext}^{nc} . A second force contribution comes from the advection of this external vorticity. Specifically, the force contribution arises because of the motion induced by the boundary layer vorticity. The effect is quantitatively described by the multiplication of the flow velocity induced by the boundary layer vortex sheet U_{γ^b} and the strength of the free vorticity ω^{ext} . It is worth noting however, that we do not account for changes in the way vorticity sheds from the cylinder, nor for any fundamental and systematic modifications to the flow field dynamics, which may introduce second order force effects. The total force due to an external region of vorticity, such as for example a vortex or a gust shear layer, is therefore

$$L_{ext} = \underbrace{\rho \int_{B_b} \frac{dI_y^{\gamma_{ext}^{nc}}}{dt} dl}_{\text{rate of change of } \gamma_{ext}^{nc}} + \overbrace{\rho \int_{R_L} U_{\gamma^b} \omega^{ext} dR}^{\text{advection of ext. vorticity by boundary layer}}, \quad (7.16)$$

where

$$I_y^{\gamma_{ext}^{nc}} = x \gamma_{ext}^{nc}. \quad (7.17)$$

A schematic illustration of the two contributions to the force, the variation of γ_{ext}^{nc} and the deflection of a vortex as this passes by a cylinder, are shown in figure 7.3.

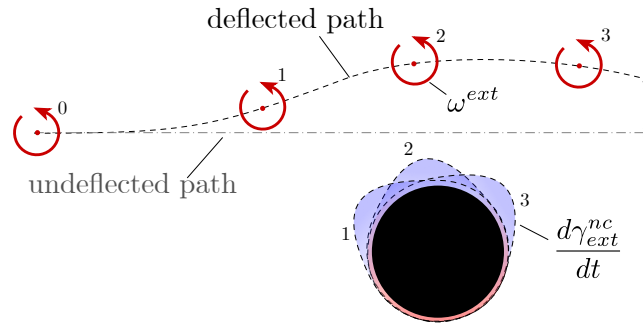


Fig. 7.3 Time variation of γ_{ext}^{nc} and deflection of a free vortex as this passes by a cylinder.

Furthermore, it is worth mentioning that the second term in equation 7.16 could equally be written as the negative of the multiplication of the velocity induced by the external region of vorticity $U_{\omega^{ext}}$ with the boundary layer vortex sheet γ^b , due to the reciprocal relationship between the two,

$$\int_{R_L} U_{\gamma^b} \omega^{ext} dR = - \int_{B_b} U_{\omega^{ext}} \gamma^b dl. \quad (7.18)$$

The derivation discussed above uses a cylinder as the body of interest but there is of course no conceptual difference between for example, a lift-generating spinning cylinder or any other lifting body. This therefore allows us to revisit the work by Martínez-Muriel and Flores [56] who studied a wing encountering a vortical gust. The authors observed that the peak force experienced by the wing was dependent on the average velocity induced onto the wing by the passing vortex. Using equation 7.16 and particularly equation 7.18, we see that the force contribution from an external vortex is, to a first order, dependent on the velocity which it induces onto the boundary layer vortex sheet. It therefore comes as no surprise that Martínez-Muriel and Flores [56] found a corresponding pattern in their experimental results and this serves as an example of how an improved understanding of the force origin can be helpful when interpreting experimental findings.

7.2 Experimental Force Isolation

In equation 7.15, the force acting on a body is broken down into its underlying constituent parts. This makes it possible to recover the force acting on a single object, even when the surrounding flow field is populated with *externally* created vorticity. This external vorticity may come in the form of a freely drifting vortex pair or alternatively, created by other objects that are also present in the flow field. Focusing on the latter as an example, if the vorticity created by all objects is clearly distinguishable and does not mix, it may be tempting to draw a boundary around each individual object as well as its vorticity, as shown in figure 7.4, and simply apply the impulse method to this region in order to obtain the forces. The literature review [7, 38] as well equation 7.15, however clearly demonstrate that the calculation is more involved. Since it is possible to use a force balance to measure the force acting on a single object, we first test our derived force formulation, equation 7.15, on this common multi-body

problem (for which we use the experimental set-up discussed in section 3.4.2), before we move on and use the theory to assess a cylinder-gust encounter in chapter 8.

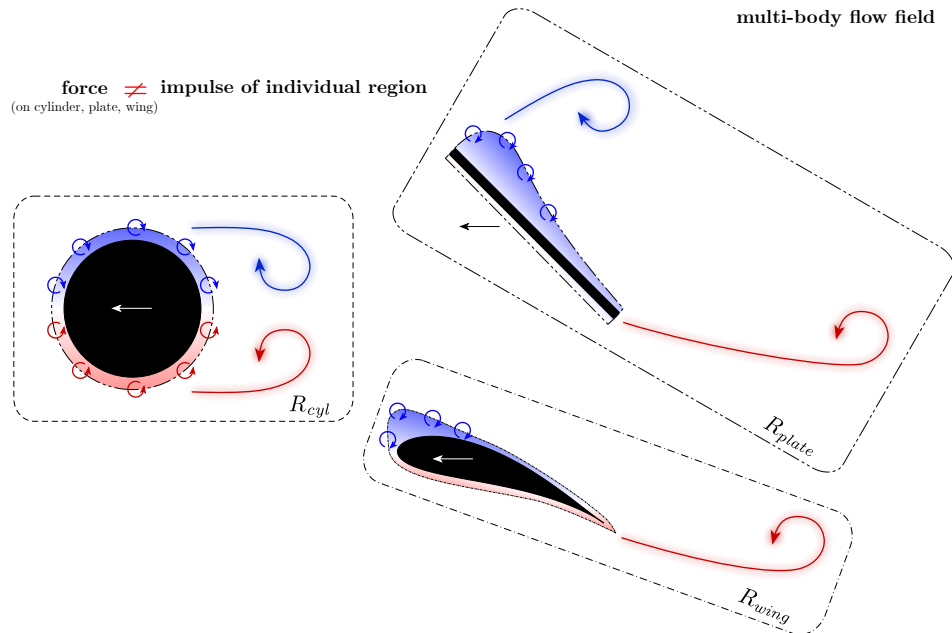


Fig. 7.4 Schematic illustration of the tempting (yet incorrect) approach to calculate the force acting on a single object, part of a multi-body flow field, by only considering the impulse created by the vorticity associated with the individual object.

7.2.1 Force on an Individual Object - Experimental Implementation

Imagine a flow field consisting of a circular cylinder surrounded by shed and externally created vorticity. A direct application of equation 7.15, to identify the force acting on the cylinder, can be cumbersome in an experimental setting. This is because the strength and position of newly shed vorticity must be explicitly identified in order to calculate the *creation* term in equation 7.15. For some geometries this may be easier, for example a flat plate at a high incidence, where vorticity is only shed at the leading and trailing edges. However, for more general bodies such as a circular cylinder, the unsteady separation point moves along the surface and it is therefore difficult to identify the exact position of unsteady separation as well as the magnitude of shed vorticity. Therefore, to circumvent the necessity to explicitly identify these, we use a modified approach that in essence however, is identical to that given by equation 7.15.

The vorticity field is grouped into a region associated with the cylinder, R_{cyl} , as well as into a further area that encloses the externally created vorticity, R_{ext} , as shown in figure 7.5.

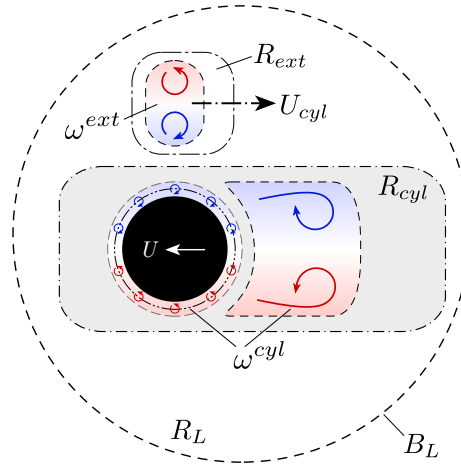


Fig. 7.5 Schematic illustration of a flow field grouped into two sections, one encompasses cylinder related vorticity ω^{cyl} and a second includes only external vorticity ω^{ext} .

To compute the force acting on the cylinder, the impulse

$$I_y^{cyl} = x\omega^{cyl} \quad (7.19)$$

is evaluated directly from the measured vorticity field associated with the cylinder. ω^{cyl} represents both the cylinder boundary layer as well as any cylinder-shed vorticity. Thereafter, the velocity induced by ω^{cyl} at the location of the external vorticity is computed. This determines the relative advection of the external vorticity, which in turn is responsible for an additional force according to equation 7.15. From this it follows that the total lift force acting on the cylinder is,

$$L = \int_{R_{cyl}} \left(\underbrace{\frac{dI_y^{cyl}}{dt}}_{\text{impulse}} + \underbrace{U_{\omega^{cyl}} \omega^{ext}}_{\text{advection}} \right) dR, \quad I_y^{cyl} = x\omega^{cyl}. \quad (7.20)$$

It is worth noting that, as stated earlier, this result is effectively the same as that given by equation 7.15. In fact, equation 7.15 can be recovered from equation 7.20 by expanding the time derivative, splitting up the advection of the free vorticity into the individual induced velocity contributions and by removing the force components due to free vorticity advecting itself.

7.2.2 Cylinder in Isolation

The first experimental case to be explored is that of a cylinder translating in isolation. This is used as a benchmark test case to determine the accuracy of the force calculation when the original impulse formulation derived by Wu [107] is applied to the PIV data. A number of vorticity snapshots of the flow field around the accelerating cylinder are presented in figure 7.6. Initially, vorticity resides only

within the boundary layer. As the cylinder continues to accelerate, vorticity sheds as a shear layer from the top and bottom surface of the cylinder and rolls up into two distinct vortices.

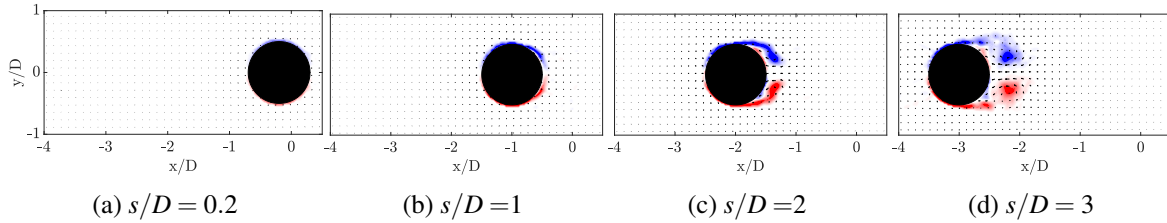


Fig. 7.6 Vorticity contours around a translating cylinder, case m1.

The lift and drag coefficients, C_l and C_d , measured by the force balance as well as those calculated by applying the impulse method to any vorticity located within the flow field are, presented in figure 7.7. The added mass force contribution is also shown. This is determined according to

$$F_{am} = \rho \pi a^2 \frac{dU}{dt}, \quad (7.21)$$

using the measured cylinder acceleration [11]. It can be seen that C_l remains very close to zero throughout the captured translation distance, as well as that force balance and impulse method results are in a good agreement throughout. Furthermore, it is encouraging to see that the drag coefficient is initially dominated by the added mass force. This is expected, because early on, no vorticity has been shed and the force therefore solely comes from the added mass force contribution. With greater translation distance, C_d begins to rise as vorticity sheds from either side of the cylinder. Once more, a very good match is observed between the force balance data and C_d obtained using the impulse method. The results therefore confirm that the impulse method is able to provide a good indication of the forces acting on the cylinder. That is, that the resolution and quality of the PIV data are sufficient to compute the forces.

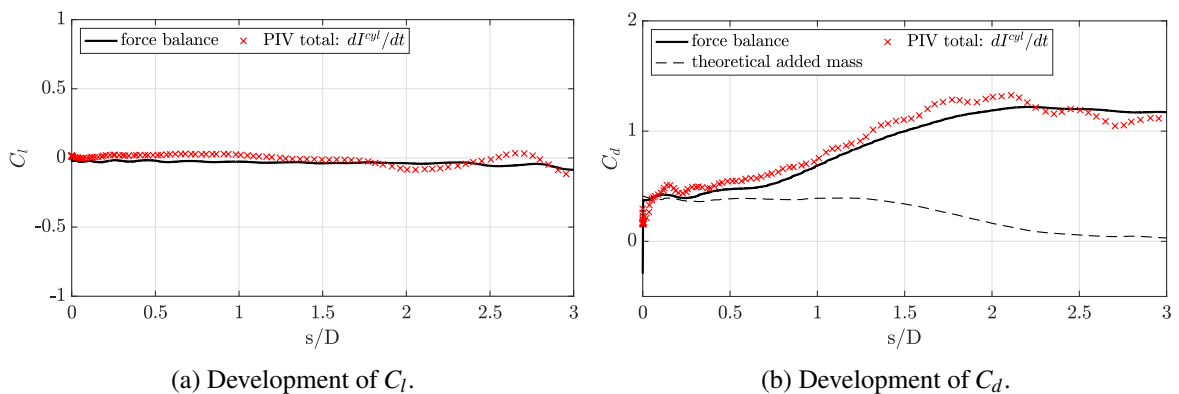


Fig. 7.7 Force history, case m1.

7.2.3 Circular Cylinder in Vicinity of a Small Flat Plate Wing

Having demonstrated that the PIV data is of sufficient quality to enable force calculations, we now consider a scenario where a circular cylinder is placed in close proximity to a lifting body. The development of the unsteady flow field around the, in unison, accelerating circular cylinder and flat plate wing, is shown in figure 7.8. Vorticity is shed from the leading and trailing edges of the plate, where a pronounced leading edge vortex forms and grows in size as the translation distance increases. At the same time, vorticity is shed from either side of the cylinder, where the unsteady separation differs between the top and bottom cylinder surface due to the influence of the plate.

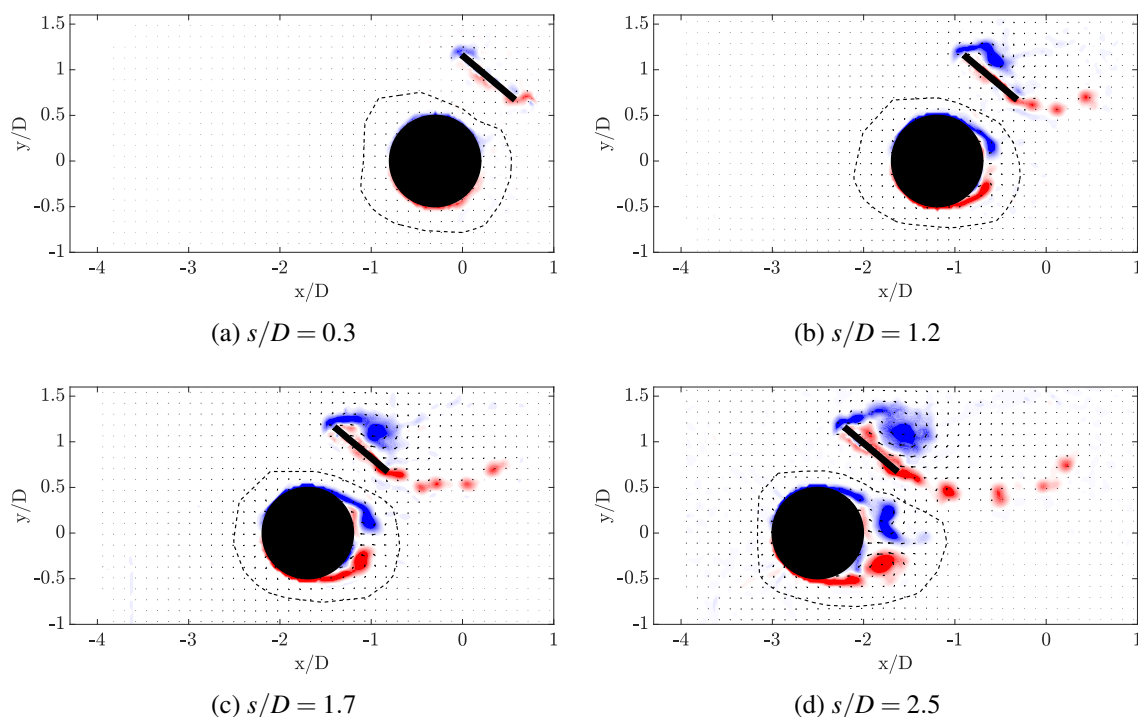


Fig. 7.8 Vorticity contours of the cylinder and plate, case m2. The dashed line marks the region within which vorticity is associated with the cylinder.

The lift and drag force coefficients acting on the cylinder are shown in figure 7.9. In contrast to the cylinder surging in isolation, C_l no longer remains zero but gradually becomes negative until $s/D = 2$. As before, the drag coefficient is initially dominated by the added mass contribution and then rises gradually as vorticity is shed from the cylinder and the plate. The forces are now recovered from the PIV measurements by applying equation 7.20 to the flow field data. The conventional impulse method is applied to the flow field within the dashed loop, encircling the cylinder and its associated vorticity. This resulting ‘impulse’ contribution (blue circles) is then added to the force component created by the ‘advection’ term (green circles) originating from cylinder vorticity advecting any vorticity external to the dashed boundary. The final result (red crosses) is in excellent agreement with the force balance

measurements (black line) throughout the captured translation distance.

It can be seen that the ‘impulse’ and ‘advection’ contributions are of similar magnitude, highlighting that both components are required for an accurate force calculation. Whilst C_l sees a greater contribution from the ‘advection’ term, C_d is dominated by the force calculated from the ‘impulse’ component. This makes sense, since the u -velocity component induced by plate and cylinder vorticity on each other is greater than the induced v -velocity.

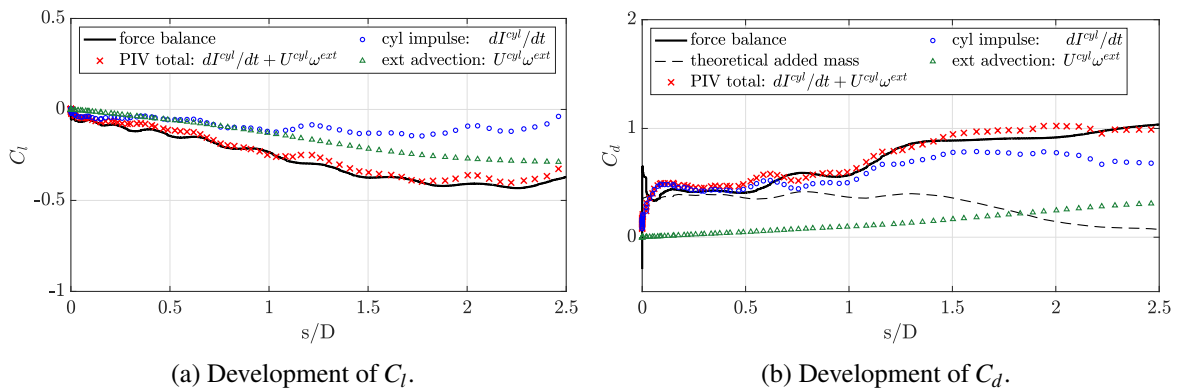


Fig. 7.9 Force history, case m2.

7.2.4 Circular Cylinder in Vicinity of a Large Flat Plate Wing

To test the proposed force formulation in a further flow environment, a large flat plate wing is placed next to the circular cylinder, whilst the Reynolds number is reduced to 10 000 and the acceleration is increased such that it occurs over $0.5 D$.

A selection of snapshots of the vorticity field are shown in figure 7.10. A leading edge vortex forms on the plate and remains close to the leading edge as acceleration begins, whilst small discrete vortices are shed from the trailing edge throughout. At the same time, two distinct vortices develop on either side of the cylinder, where the influence of the plate once more leads to an asymmetric development.

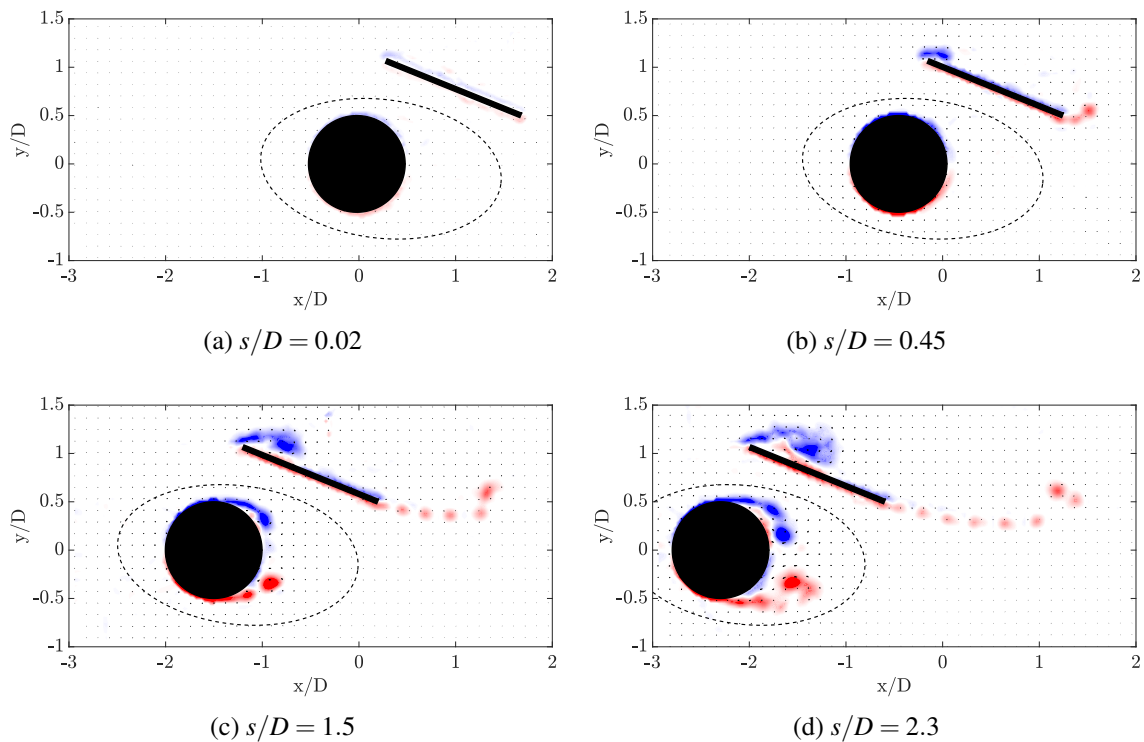


Fig. 7.10 Vorticity contours of the cylinder and plate, case m3. The dashed line marks the region within which vorticity is associated with the cylinder.

The cylinder's force history is shown figure 7.11. The rapid acceleration creates a strong added mass force that is clearly visible in the recorded data. Furthermore, the flow remains largely attached during initial translation and as acceleration ceases, C_d drops accordingly. With the onset of separation from the cylinder around $s/D \approx 0.7$, the drag coefficient increases once more as the force begins to be affected by shed vorticity. The development of C_l on the other hand is much less dramatic and it is marginally negative until $s/D \approx 1.4$ after which it becomes positive.

Figure 7.11 shows the force balance measurements as well as the forces computed from the PIV data. Both the 'impulse' (blue circles) and 'advection' term (green triangles) of equation 7.20 contribute to C_l , and the sum of both (red crosses) matches the force balance measurements well. In contrast, the contribution from the 'advection' term is almost negligible for C_d due to the direction of the induced velocity, which is mainly aligned with the x -axis. The majority of its contribution therefore affects C_l rather than C_d . Once more, a very good match between the drag force balance data and C_d calculated from the vorticity field is achieved. The small discrepancy in the peak drag force during acceleration is most likely caused by vibrations of the flat plate.

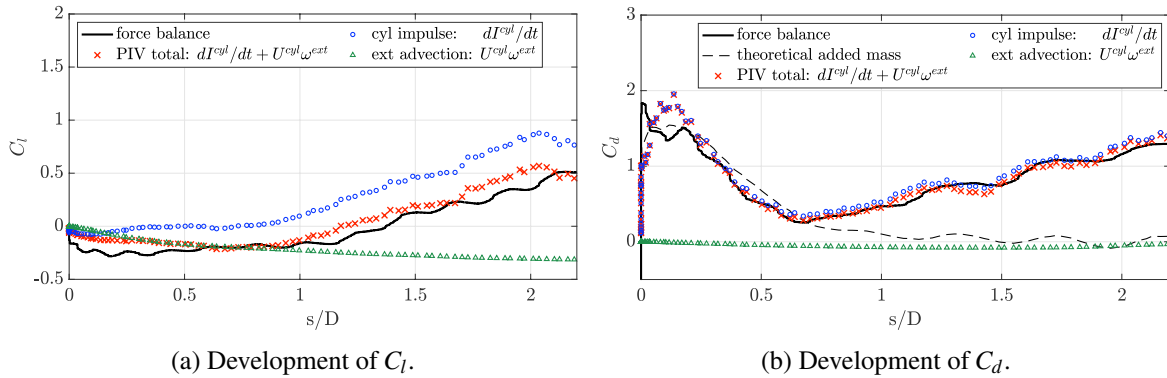


Fig. 7.11 Force history, case m3.

7.3 Summary: Unsteady Force Contributions

A force formulation is proposed that expands the impulse method developed by Wu [107] to isolate the force created by an individual flow feature. It does this by identifying the core contributions to the force using the vorticity field in two-dimensions, for unsteady and incompressible flows. A bi-product of this is that it enables the forces acting on a single object immersed in a multi-body flow field to be found. Since it is easily possible to compare force calculations to force balance measurements of a single object part of such a multi-body flow field, the proposed theory is tested by extracting the forces on a cylinder located in close proximity to a flat plate wing. The lift and drag forces are successfully recovered for as long as there is no significant mixing of vorticity and the flow remains sufficiently two-dimensional.

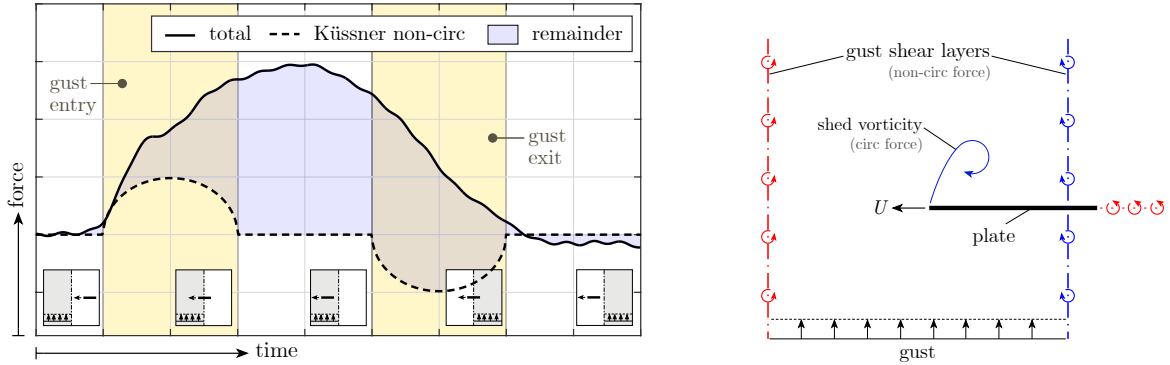
Having tested the proposed methodology on a multi-body flow field, where a direct comparison between force balance measurements and calculations is possible, we move on to evaluate a body-gust encounter in the following chapter. Specifically, the focus will be on how external vorticity located in the gust shear layers affects the entering body and whether their distortion creates a tangible force contribution, warranting an inclusion in a LOM modelling the force.

Chapter 8

Cylinder-Gust Encounter

8.1 Introduction

The aim of this chapter is to apply the theoretical framework, in particular that developed in the last chapter, to a practical use case. Küssner's model [43, 44] is a common analytical method used to approximate forces during a plate-gust encounter. The force experienced by the plate is divided into a circulatory component that arises because of vorticity shed from the trailing edge of the plate as well as into a non-circulatory contribution created by the gust itself, or more specifically the gust shear layers [96, 14]; a more in depth discussion of the force contributions will follow shortly. An example of the force development affecting a flat plate encountering a transverse sharp-edged gust is shown in figure 8.1. The 'gust ratio', GR , measuring the gust velocity relative to the free-stream velocity of the plate, is unity. The measured total force is shown and compared to the non-circulatory component of Küssner's prediction, which can be seen to be greatest when the plate is half-way into (and out of) the gust domain. When the plate is entering, the non-circulatory contribution initially dominates the force response, and at the half-way point is responsible for about 60 % of the total force. An accurate force prediction therefore requires the gust entry (and exit) to be correctly included in an LOM. A core assumption used to simplify the flow in Küssner's model is that the gust shear layers are entirely rigid and non-deforming, even as the body enters the gust. This is understandably not what happens during a real gust encounter and it may therefore not be too controversial to suggest that the true non-circulatory force may deviate from its theoretical calculation, especially when the body entering is of non-zero thickness. It is this assumption that we now seek to explore throughout the chapter and to evaluate whether gust distortion has a significant effect on the non-circulatory force acting on a body.



(a) Total experimental and theoretical non-circulatory Küssner force.

(b) Gust flow field and force association.

Fig. 8.1 Flat plate sharp-edged gust encounter. Note that even for infinitely thin gust shear layers, gust entry (and exit) takes place over one chord length.

The theoretical framework for the idealised non-circulatory force acting on an infinitely thin flat plate is reviewed first and subsequently expanded for a circular cylinder in section 8.2, where the adaptation of Küssner's model for bodies of finite thickness is discussed in detail. Thereafter, the methodology to recover the experimental non-circulatory gust vortex sheet created on the cylinder surface is evaluated in section 8.3.1. Finally, the theoretical and experimental forces acting on the circular cylinder are discussed in section 8.3.2.

8.2 Theoretical Sharp-Edged Gust Encounter

8.2.1 Flat Plate

The Küssner model was derived for flat plates entering a sharp-edged gust. Von Kármán and Sears [96] decomposed the force into a component associated with shed circulation and a second linked to the non-circulatory vortex sheet residing on the plate surface, $\gamma_{\text{Küss}}^{nc}$. The latter is found by von Karman and Sears [96] by using the broken line assumption discussed in section 2.4.2 and thin linear aerofoil theory provided by Durand [22],

$$\gamma_{\text{Küss}}^{nc}(\theta, t) = \sum_{k=1}^{\infty} a_k \frac{\cos(k\theta)}{\sin \theta} \quad (8.1)$$

where

$$a_k(t) = \frac{4V}{\pi} \int_0^{\beta} \sin \theta \sin(k\theta) d\theta. \quad (8.2)$$

The non-circulatory vortex sheet develops while the plate enters (and exits) the gust, as schematically shown for gust entry in figure 8.2.

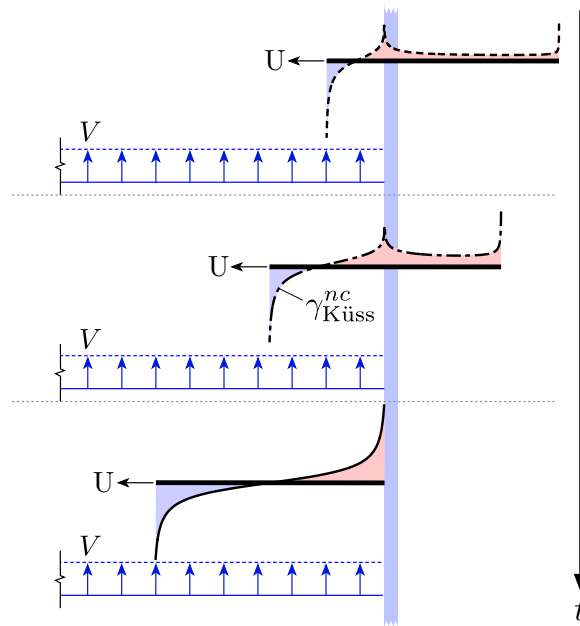


Fig. 8.2 Schematic illustration of a thin flat plate entering a gust and its $\gamma_{Küss}^{nc}$ distribution.

Once the plate is fully immersed in the gust, the vortex sheet distribution is exactly the same as if the plate were in a transverse freestream equal to the gust velocity, as schematically shown in figure 8.3. Von Kármán and Sears therefore called the force created by the rate of change of $\gamma_{Küss}^{nc}$ an *apparent* or *added mass* force. The origin of $\gamma_{Küss}^{nc}$, however, is entirely different to γ_{am}^{nc} and for thin flat plates, Corkery and Babinsky [15] showed that $\gamma_{Küss}^{nc}$ can also be understood as the ‘mirror’ image of the gust shear layer vorticity (ie. $\gamma_{Küss}^{nc} = \gamma_{gust}^{nc}$). Their approach effectively treats the gust edges as regions of external vorticity and thus the associated vortex sheet γ_{gust}^{nc} can be seen as a special case of the vortex sheet generated by *external* vorticity γ_{ext}^{nc} . Moreover, since the development of the vortex sheet, as the plate enters (and exits) the gust, matches that calculated by von Kármán and Sears, the force created by its variation is also identical.

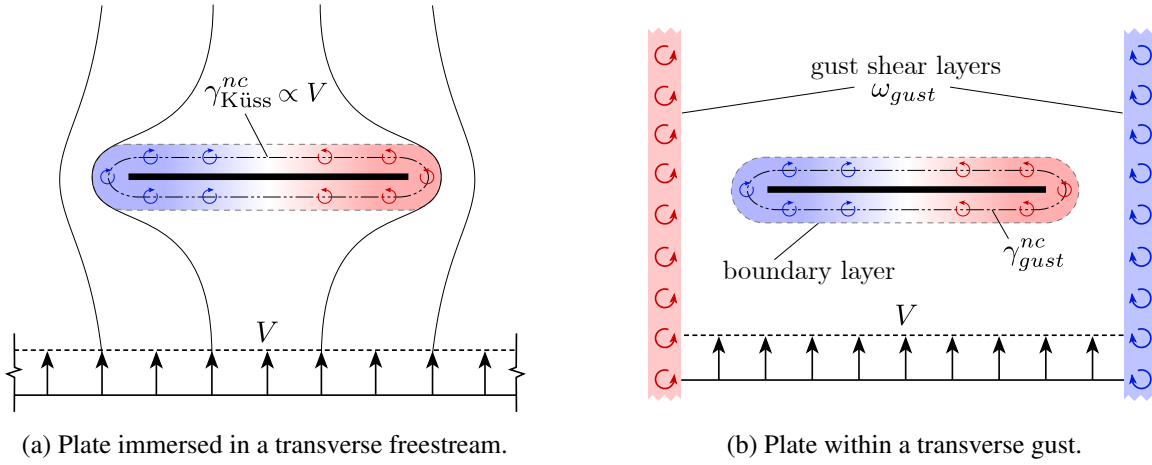


Fig. 8.3 The non-circulatory vortex sheet created around a flat plate immersed in a transverse freestream is identical to the vortex sheet created by the mirror image of the vorticity residing within the gust shear layers.

To compute this non-circulatory force as a flat plate enters the gust, von Kármán and Sears evaluate the impulse created by the evolution of the non-circulatory vortex sheet. The vertical impulse created by a vortex sheet is

$$I_y = \int_0^c x\gamma(x,y) dx. \quad (8.3)$$

This can be written in polar coordinates, where $dx = -c/2 \sin \theta$, and with limits $\theta = \pi$ corresponding to $-c/2$ and $\theta = 0$ equal to $c/2$,

$$I_y = \left(\frac{c}{2}\right)^2 \int_0^\pi \cos \theta \sin \theta \gamma(\theta) d\theta. \quad (8.4)$$

Substituting equation 8.1 for the vortex sheet into the impulse given by equation 8.4 yields

$$I_y = \frac{\pi}{2} \left(\frac{c}{2}\right)^2 a_1, \quad (8.5)$$

where a_1 is given by equation 8.2. Evaluating the time rate of change of the impulse yields the non-circulatory lift force coefficient acting on the plate:

$$C_l^{nc} = 4GR \sqrt{s/c - (s/c)^2}. \quad (8.6)$$

8.2.2 Circular Cylinder

The preceding derivation is valid for infinitely thin flat plates. As a next step, we now evaluate the Küssner model for bodies of volume by applying it to a cylinder sharp-edged gust encounter. The theoretical non-circulatory gust vortex sheet for a cylinder, created by the transverse gust, can be obtained through a variety of methods. In this particular instance we choose to calculate it by

using a simple panel method approach, where each panel distributed along the cylinder surface, represents the vortex sheet strength over its length. To do so the cylinder surface is first deconstructed counter-clockwise into a series of panels. A vortex as well as collocation point, where the no-through flow condition is enforced, are placed one quarter and three quarters along each panel. A transverse velocity V is set at the collocation point for any panel that resides within the gust, whereas $V = 0$ for all others. Thereafter, a system of equations is simultaneously solved to arrive at the required vortex strength needed to enforce the no-penetration condition at each collocation point.

A schematic illustration of the gust encounter is provided in figure 8.4a, and the resulting vortex sheet distribution at various time steps during the gust entry is shown in figure 8.4b. It is observed that, similar to the flat plate case seen in figure 8.2, the vortex sheet distribution varies as the cylinder enters the gust. Once the cylinder is fully immersed in the gust, the vortex sheet distribution is, as expected, equivalent to that of a circular cylinder in cross-flow.

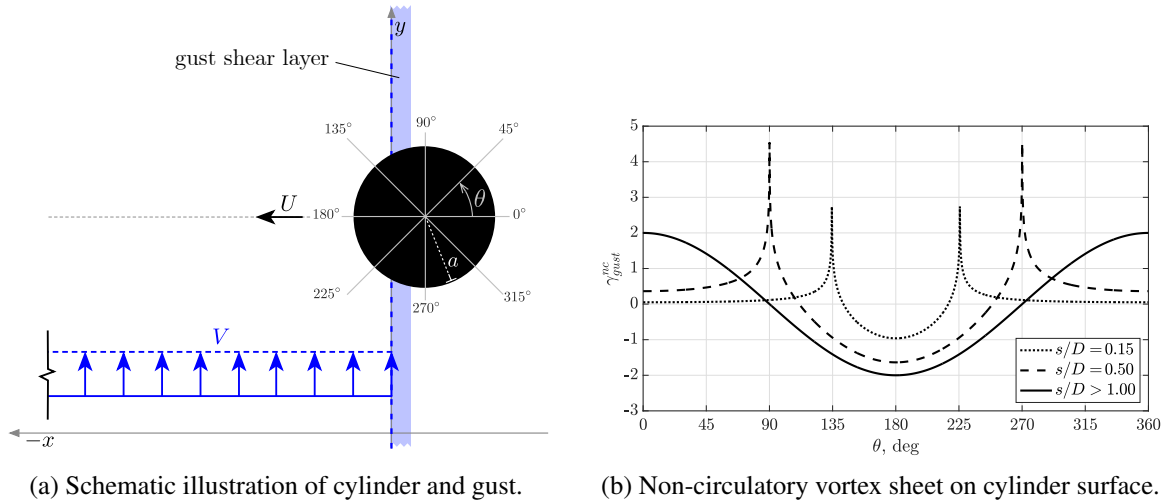


Fig. 8.4 Cylinder entering a rigid non-deforming gust.

Assessing the rate of change of the vortex sheet attributed to the gust shear layers gives the related non-circulatory Küssner force

$$\hat{C}_{l\text{Küssner}}^{nc} = \frac{dI_{gust}^{nc}/dt}{1/2U^2D}, \quad (8.7)$$

where U is the translation velocity and D represents the cylinder diameter. I_{gust}^{nc} represents the flow impulse, which for a vertical force, is defined as

$$I_{gust}^{nc} = \int_{B_b} x \gamma_{gust}^{nc} dx, \quad (8.8)$$

where x is the coordinate aligned with the horizontal axis and the integration is performed over the surface B_b of the cylinder. For the cylinder, the rate of change of the non-circulatory gust vortex

sheet results in the *uncorrected* non-circulatory Küssner force $\widehat{C}_{l\text{Küssner}}^{nc}$ shown in figure 8.5, which is non-zero only when the cylinder intersects the gust shear layers.

While the cylinder is outside of the gust, there is uniform transverse flow momentum inside the gust domain. However, as the cylinder encroaches on the gust, it begins to occupy some of its volume. By doing so, any transverse gust momentum in the region occupied by the cylinder is replaced by horizontal momentum related to the translation velocity of the cylinder, as schematically shown in figure 8.6.

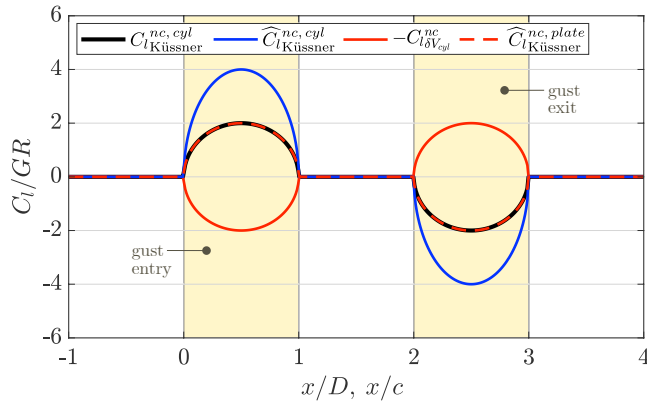


Fig. 8.5 Force coefficient contributions as the cylinder or plate intersects the rigid gust shear layers when entering and exiting a top-hat gust.

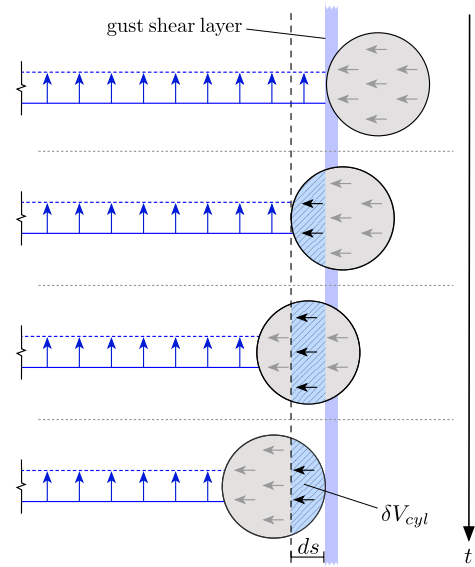


Fig. 8.6 Schematic illustration indicating the change in transverse momentum as the cylinder enters the gust.

As each new section of the cylinder enters the gust, more of the transverse gust momentum is removed. The rate at which this occurs can in turn be linked to a force. In reality the momentum occupied by the cylinder is, of course, not ‘lost’ but rather re-distributed as the gust flow deflects around the cylinder. Unfortunately, the rigid shear layer assumption does not allow for this and creates an additional force contribution. This can be corrected by removing the additional force due to the momentum change caused by the cylinder volume. The force coefficient due to this body volume effect is:

$$C_{l\delta V_{cyl}}^{nc} = \frac{2GR}{U_\infty D} \frac{dV_{cyl}}{dt}, \tag{8.9}$$

where $\frac{dV_{cyl}}{dt}$ is the rate at which the volume of the cylinder inside the gust changes. The contribution due to the ‘lost’ transverse momentum inside the cylinder $C_{l\delta V_{cyl}}^{nc}$ turns out to be exactly half of

$\widehat{C}_{l_{\text{Küssner}}}^{nc}$, as seen in figure 8.5. Removing its contribution from $\widehat{C}_{l_{\text{Küssner}}}^{nc}$,

$$C_{l_{\text{Küssner}}}^{nc} = \widehat{C}_{l_{\text{Küssner}}}^{nc} - \underbrace{C_{l_{\delta V_{\text{cyl}}}}^{nc}}_{\text{effect of lost gust momentum}} \quad (8.10)$$

results in the same non-circulatory Küssner force as calculated for a thin flat plate, as shown in figure 8.5. $C_{l_{\text{Küssner}}}^{nc}$ will be referred to as the corrected Küssner force for a circular cylinder, where the effect due to lost gust momentum as a result of body volume, has been accounted for.

8.2.3 Accounting for further Gust Idealization

Further to the discrepancy caused by the non-rigid nature of real gusts, the infinitely thin and non-deforming gust shear layer assumption may lead to further mismatches between theory and reality:

- A realistic transverse gust is not perfectly sharp-edged. Instead, viscous effects thicken the gust shear layers and the gust velocity is reached over a short distance, δw_{gust} . This implies that the actual gust entry starts somewhat earlier and spreads over a longer distance, which results in a different (lower) force than predicted by Küssner's model.
- Due to flow entrainment there may exist a small yet non-zero transverse velocity outside the gust. As the cylinder translates it may thus experience a small non-zero lift force before it reaches the first gust shear layer.

A schematic illustration of these effects and the corresponding velocity distributions is shown in figure 8.7. To isolate the impact that gust shear layer distortion has on the non-circulatory force, the two effects described above must be accounted for in the theoretical calculation, in order to arrive at a fair comparison.

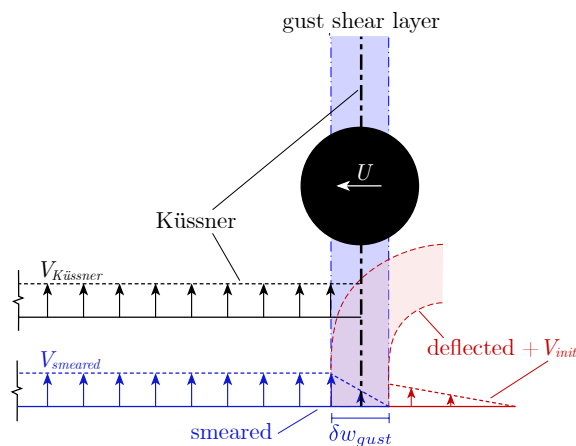


Fig. 8.7 Variations of the gust shear layer: The velocity profile for the Küssner and smeared gust are indicated as well as the non-zero velocity outside the gust.

Effect of Gust Shear Layer Thickness

The thickness of the gust shear layers can be accounted for theoretically by using a Duhamel integral. Using this approach, the gust velocity profile is split up into a number of discrete top-hat shaped gusts. Each of these discrete gusts contributes to the overall force coefficient acting on the cylinder according to

$$K(s/D) = 4GR\sqrt{s/D - (s/D)^2}, \quad (8.11)$$

as derived by von Kármán and Sears [96] and given by equation 8.6 earlier. Superposing the effect from each element, as the cylinder enters the gust, recovers the force coefficient due to the *smear*d gust,

$$C_{l_{\text{Küssner}}}^{nc, smeared} = \int_0^{s/D} \frac{dK(\sigma)}{d\sigma} \iota(s/D - \sigma) d\sigma. \quad (8.12)$$

where σ is a non-dimensional position inside the gust. $\iota(s/D - \sigma)$ ranges from 0 to 1 and corresponds to the gust velocity profile. It is assumed that, to a first order, the velocity rise occurs linearly over the shear layer width, from zero velocity outside the gust to the target velocity inside the gust. The resulting gust velocity profile and the non-circulatory gust force for a range of shear layer widths, δw_{gust} , is plotted in figure 8.8¹. It can be seen that with increasing gust shear layer width the initial rise in C_l is less rapid and has a lower peak value than the corrected non-circulatory Küssner force. It can further be noted that the transverse velocity upstream of the first gust shear layer V_{init} can equally be modelled using a Duhamel approach.

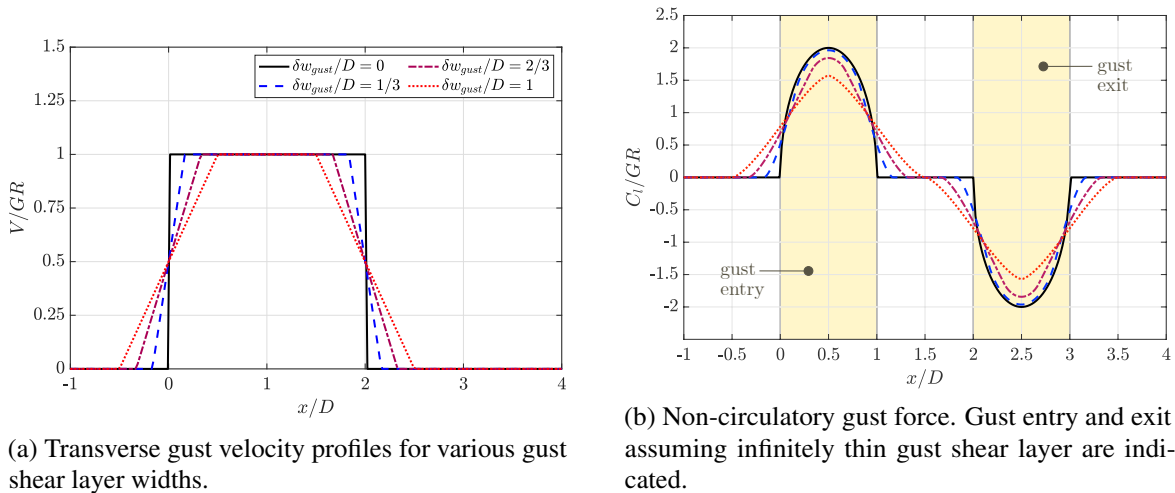


Fig. 8.8 Effect of smeared gust shear layers.

Isolating the Effect of Gust Shear Layer Deflection

The effect of gust distortion on the non-circulatory force is found by isolating the experimentally determined force and comparing it to its theoretical equivalent. Any difference between the two can

¹The rate of change of momentum inside the cylinder has also been accounted for, as described in section 8.2.2.

subsequently be attributed to gust shear layer deflection.

To calculate the non-circulatory force for the experimental gust encounter, equation 7.16 is used. The vortex sheet created by the gust is first extracted (discussed next in section 8.3.1) after which the force, due to the rate of change of the impulse created by the gust vortex sheet, is obtained. This force component is added to the contribution created by the advection of gust vorticity by the cylinder boundary layer vortex sheet to give the total non-circulatory force. γ^b is recovered using the *wedge* method discussed in section 3.5 and the velocity induced at the location of each element of gust vorticity is found using the Biot-Savart law.

8.3 Experimental Gust Encounter

8.3.1 Recovering the Cylinder Gust Vortex Sheet

The generic flow field around a cylinder immersed in a sharp-edged gust is shown in figure 8.9. Vorticity resides in the gust shear layers and is also shed by the cylinder itself.

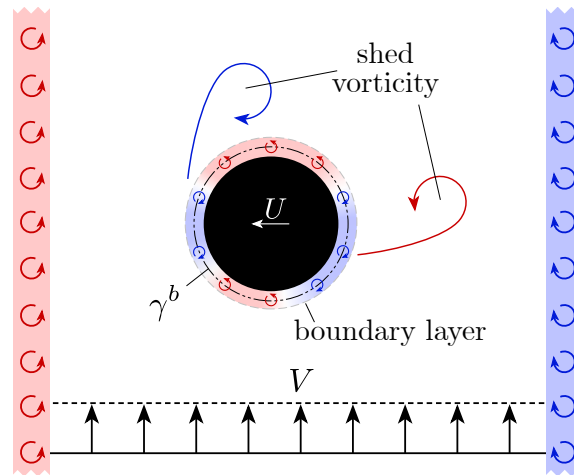


Fig. 8.9 Schematic illustration of a cylinder inside an idealised rigid top-hat shaped gust.

As stated in equation 4.37, the boundary layer vortex sheet surrounding the cylinder is made up of a component associated with the translation velocity, γ_{am}^{nc} , a further arising due to shed circulation, γ^{shed} , and a final contribution created by external vorticity, which takes the form of gust shear layer vorticity γ_{gust}^{nc} . The latter can be isolated by re-arranging the vortex sheet contributions:

$$\overbrace{\gamma_{gust}^{nc}}^{\text{gust vorticity}} = \underbrace{\gamma^b}_{\text{translation}} - \overbrace{\gamma^{shed}}^{\text{shed vorticity}} - \underbrace{\gamma_{am}^{nc}}_{\text{translation}}, \quad (8.13)$$

which is akin to the approach outlined by Corkery & Babinsky [15] for flat plates.

γ_{am}^{nc} , which forms when the cylinder initially accelerates to its steady-state velocity, is found from potential theory and equal to $-2U \sin \theta$ as discussed in section 4.1.1. The boundary layer vortex sheet γ^b is obtained by applying the *wedge* method outlined in section 3.5. To obtain γ^{shed} , we first isolate only cylinder-shed vorticity. Thereafter, it is possible to compute γ^{shed} from the slip velocity induced at the cylinder surface by shed vorticity and the corresponding mirror counterparts as discussed in section 4.1.2. Cylinder-vorticity is isolated by applying a mask to each frame that removes any gust shear layer vorticity. The mask is created by manually drawing a contour around the region of cylinder-shed vorticity for every 15th frame and linearly interpolating between these successive loops for each individual frame. An example of the result is shown for case g1 in figure 8.10. This process is rather straightforward when the cylinder is fully inside the gust, and an example is shown for case g1 in figure 8.10. When the cylinder intersects the gust shear layers, it becomes more difficult to correctly attribute vorticity to either the gust or the cylinder. Results during this phase should therefore be treated with caution, since incorrectly assigned vorticity in close proximity to the cylinder can have a significant effect on the resulting vortex sheet distribution.

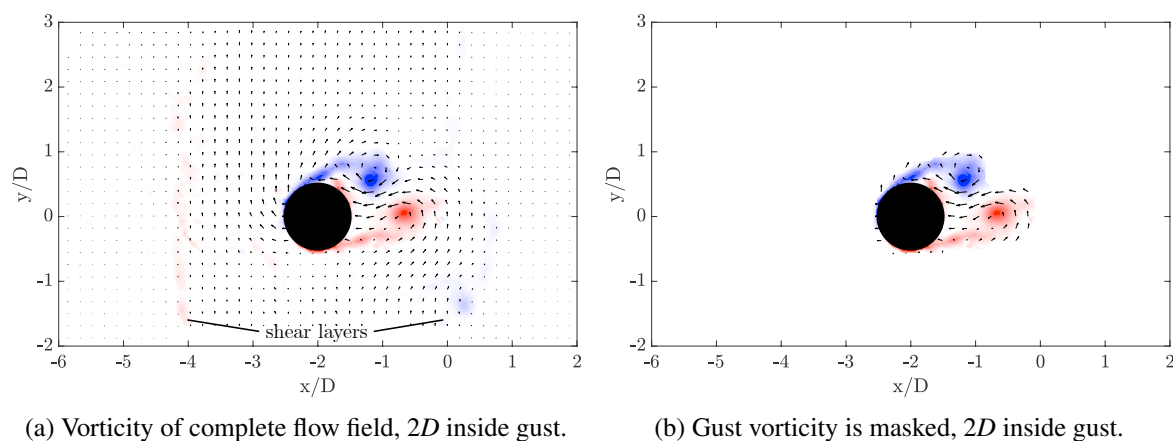


Fig. 8.10 Normalised vorticity field used to calculate γ^{shed} for case g1, $GR = 0.5$.

γ_{gust}^{nc} does not vary when the cylinder is completely inside the gust, regardless of cylinder position. As a result, the measurement of γ_{gust}^{nc} can be averaged over all time instances whilst the cylinder is immersed in the gust; reducing the noise in the data. The theoretical distribution of γ_{gust}^{nc} is calculated with knowledge of the transverse gust velocity distribution and is $2V \cos \theta$. This is equal to the vortex sheet on a cylinder in a transverse freestream and the derivation of this is identical to that performed in section 4.1; the only difference is the angle of the incoming freestream.

Figures 8.11a through 8.11c show the vortex sheet distributions for nominal gust ratios of 0.5, 1 and 1.5. It is observed that γ_{gust}^{nc} matches the theoretical distribution obtained from potential flow theory in all cases. Furthermore, since the magnitude of γ_{gust}^{nc} is directly proportional to the gust

strength, the vortex sheets collapse onto each other when non-dimensionalised by gust ratio as shown in figure 8.11d.

Some small discrepancies can be seen between $270^\circ < \theta < 320^\circ$ and around $\theta = 135^\circ$. These locations correspond to the regions where flow separation occurs. Due to the nature of how shed vorticity leaves the cylinder surface, some of the vorticity in close proximity to the cylinder is incorrectly associated with γ^b instead of with γ^{shed} , and therefore causes local errors in the experimentally recovered γ_{gust}^{nc} distribution. These errors can be as high as approximately 20 % and from a quantitative perspective are therefore large. However, from a qualitative standpoint, they do not deter from the overall good match between the theoretical and experimental vortex sheet distribution, as these errors are only associated with small, limited regions along the cylinder surface.

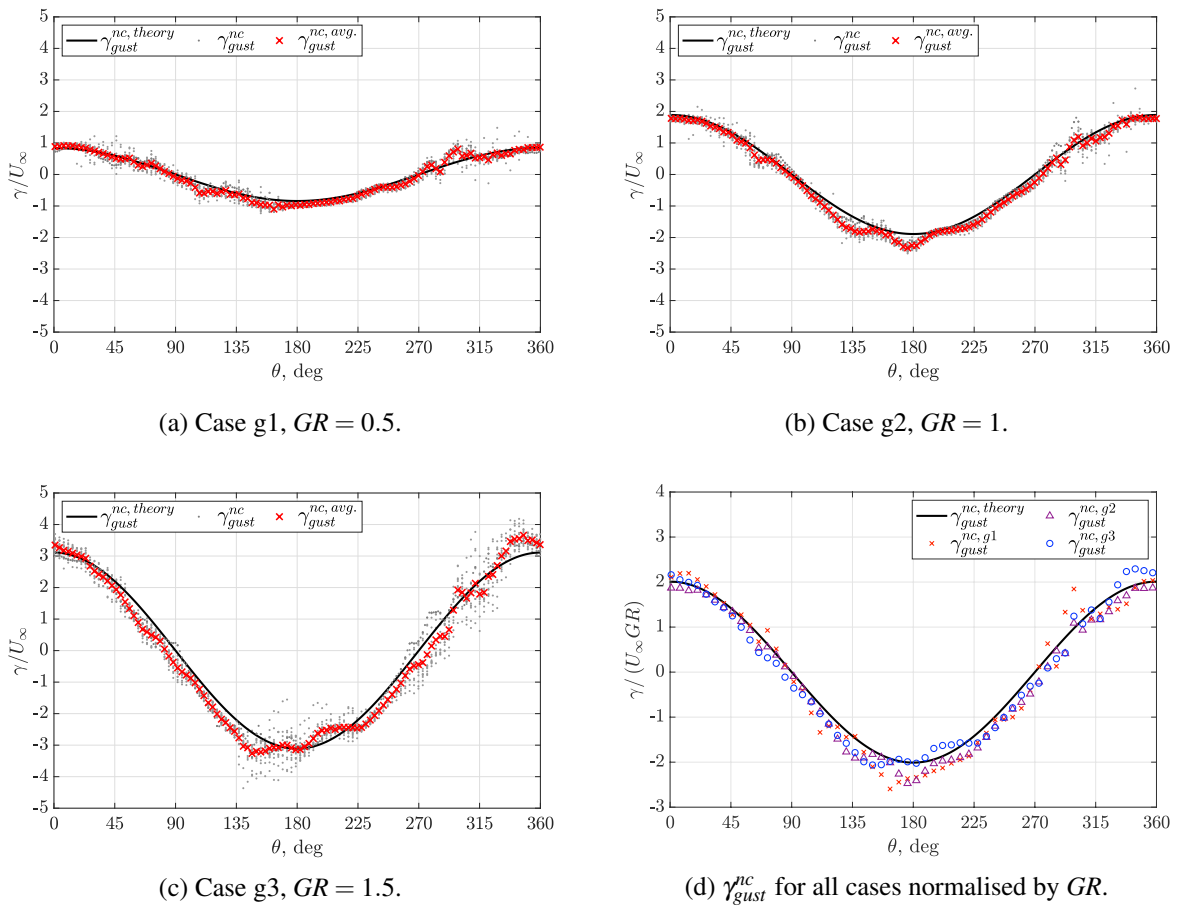


Fig. 8.11 Comparison between the theoretical and experimental distribution of γ_{gust}^{nc} .

It is now possible to demonstrate that the γ_{gust}^{nc} distributions shown in figure 8.11 are a consequence of gust shear layer vorticity. To do so, vorticity residing within the gust shear layers is isolated and the resulting vortex sheet contribution is calculated by applying the methodology discussed in section 4.1.2. The masked flow field, at an instance in time when the cylinder is fully inside the gust,

is shown in figure 8.12 as well as the vortex sheet (blue circles) computed from the remaining vorticity. Whilst the distribution is correct in shape, the magnitude is too small. This asks the question of whether gust distortion causes this discrepancy. At the same time however, we must note that the field of view only includes a small portion of the gust shear layers. Therefore, to provide a more complete representation of the gust, we augment the shear layers by point vortices at the same x -location. These extend for a further 60 cylinder diameters, as shown in figure 8.12a, and help model the uniform transverse gust. By incorporating the additional point vortices in the computation of the vortex sheet (red crosses), we now successfully recover the theoretical distribution. Moreover, this suggests that once the cylinder is sufficiently far inside the gust, shear layer distortion has no significant effect on the distribution of the non-circulatory gust vortex sheet.

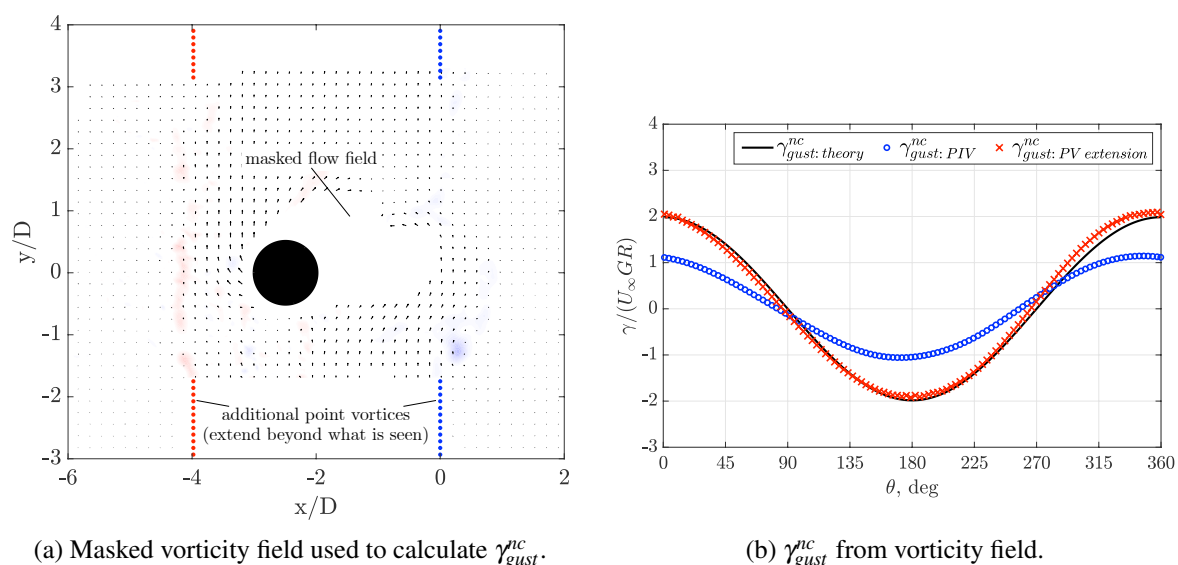


Fig. 8.12 Flow field and non-circulatory gust vortex sheet γ_{gust}^{nc} as a result of extending the gust shear layers and masking any cylinder-shed vorticity. Case g1, $GR = 0.5$.

The experiments demonstrate that the non-circulatory gust vortex sheet recovered from a knowledge of the gust shear layer vorticity distribution is identical to the vortex sheet attributed to an added mass effect by von Kármán and Sears, even for bodies of volume. An added mass force arises due to body acceleration, occurring in unidirectional or oscillatory motion. Because the gust encounter involves no such body acceleration (apart from the initial start to achieve the freestream velocity), the results further confirm the suggestion by Corkery [14] that it seems more appropriate to attribute this force to gust vorticity instead of added mass. While this distinction may seem a somewhat pedantic question of semantics, it becomes significant when attributing forces to vorticity external to the body, as any inclusion of gust shear layer vorticity as well as an added mass effect would lead to ‘double-counting’ the same physics. This also applies to other problems where vorticity is shed from more than one source, for example from two individual wings or when measurement data includes the boundary layer in a wind tunnel.

8.3.2 Non-Circulatory Gust Force

The confirmation that we can isolate Küssner's non-circulatory vortex sheet created by the gust shear layers paves the way for us to assess the effect that gust distortion has on the non-circulatory gust force. The final experimental data set that the reader is subjected to as part of this thesis, is that of the circular cylinder entering the top-hat shaped gust. Snapshots of the vorticity field during gust entry at nominal gust ratios of 0.5, 1 and 1.5 are shown in figure 8.13, to provide a visual overview of the gust encounter. The cylinder starts from a stationary start just upstream of the first shear layer. As a result, vorticity is only just about to shed from the top and bottom surface of the cylinder, as the cylinder reaches the upstream shear layer. Once the cylinder is fully inside the gust, two distinct vortices have been shed from either side, and these grow in size and are advected further upwards with increasing gust ratio. Moreover, significant gust shear layer deflection is observed, as seen in the right column of figure 8.13.

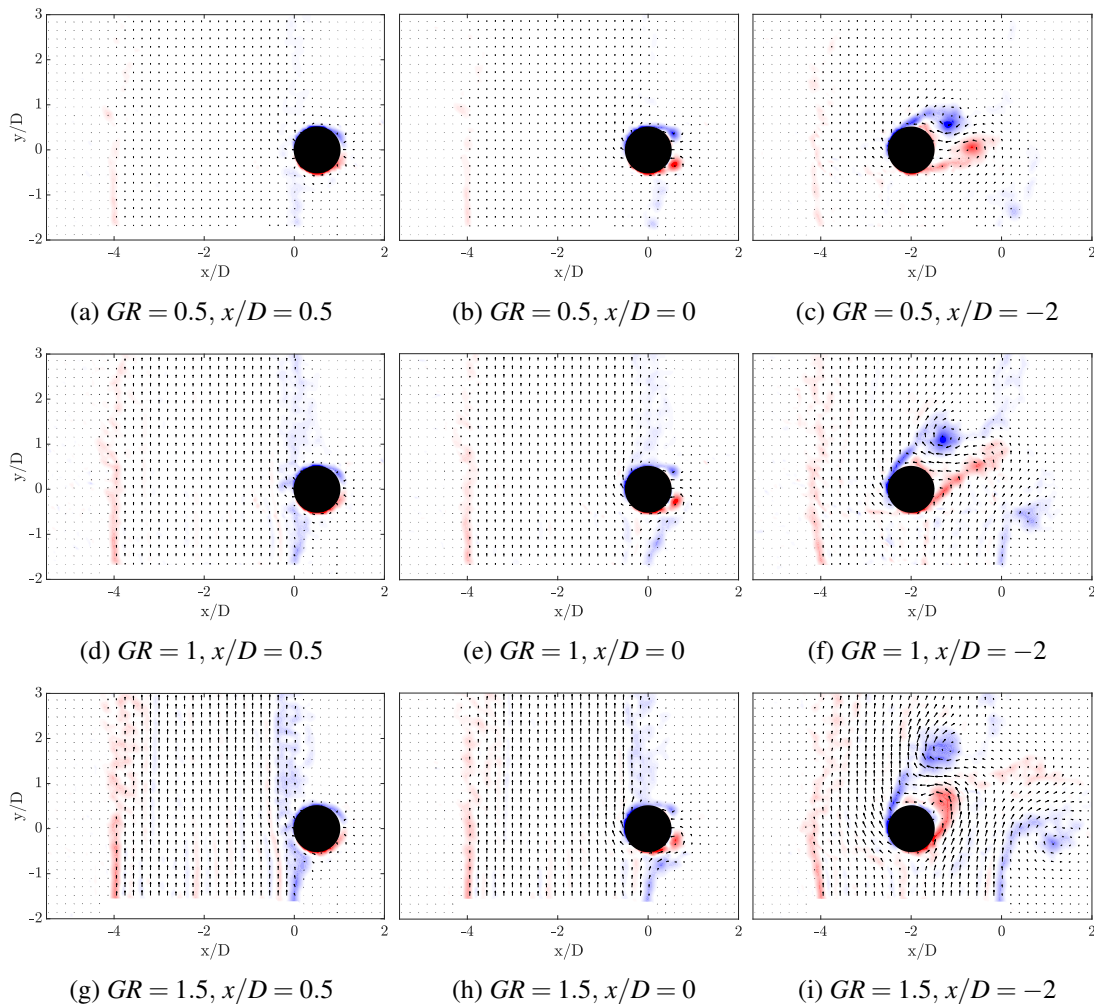


Fig. 8.13 Vorticity contours of a circular cylinder entering a top-hat shaped gust at $GR = 0.5$ (a-c), $GR = 1.0$ (d-f), $GR = 1.5$ (g-i).

The force balance measurements C_l^{fb} for the surging cylinder are shown in figure 8.14. For all gust ratios, C_l^{fb} rises quickly when the cylinder enters the gust and reaches a maximum soon after the cylinder is completely immersed at roughly $x/D = 1.5$. Thereafter, the lift force decreases and for $GR = 0.5$ continues on a downwards trajectory until the cylinder leaves the gust. Conversely at the highest gust ratio, C_l^{fb} increases once more from $x/D \approx 2.4$ onwards and reaches a lower high just prior to gust exit. Furthermore, a small positive force exists at all gust ratios whilst the cylinder is still upstream of the gust. This is likely caused by the transverse velocity upstream of the first shear layer, as first seen in figure 3.18.

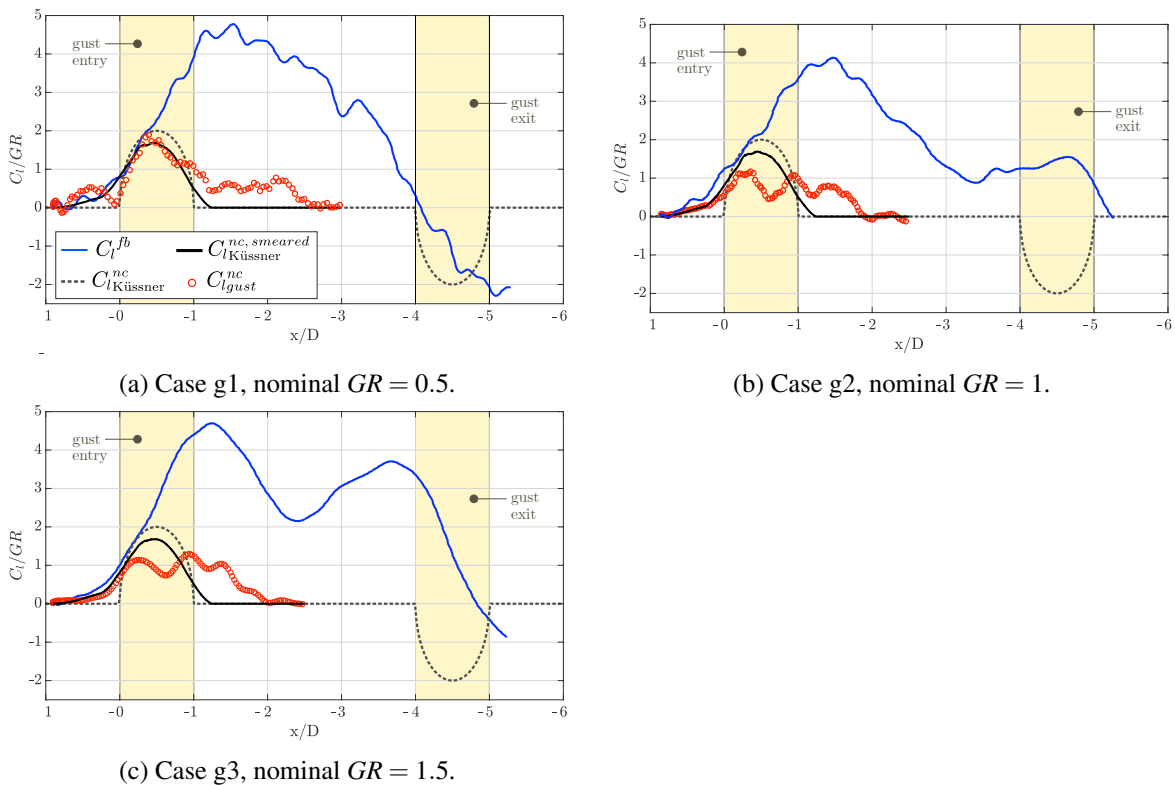


Fig. 8.14 Theoretical and experimental forces acting on the cylinder.

Figure 8.14 also shows the corrected theoretical non-circulatory Küssner force $C_{l_{Küssner}}^{nc}$, assuming rigid infinitely thin shear layers. Further to this, the smeared equivalent $C_{l_{Küssner}}^{nc, smeared}$, calculated according to section 8.2.3, is also included and the volume correction discussed in section 8.2.2 has been applied to both forces. For $C_{l_{Küssner}}^{nc, smeared}$, the gust shear layer thickness is set to $0.5D$ and the transverse velocity upstream of the first gust shear layer is assumed to increase linearly from zero to a maximum of $0.15GR$. It naturally follows that the smeared Küssner force (black line) has a lower and more spread out force contribution during gust entry compared to $C_{l_{Küssner}}^{nc}$ (dark grey dashed line), which assumes a perfectly sharp edged gust. This is because the more benign gust profile causes the non-circulatory gust vortex sheet to grow to its final state more slowly, thereby creating a lower force

contribution. Furthermore, the corrected and smeared non-circulatory Küssner force are of the right order of magnitude during gust entry compared to the force balance measurements. A non-circulatory gust force is also present when the cylinder exits the gust. However, by now a considerable amount of shed vorticity is present in the flow field and the circulatory force contribution therefore dominates and obscures any non-circulatory force effect.

The impact of gust shear layer distortion can be assessed by comparing the theoretical non-circulatory force $C_{l_{\text{Küssner}}}^{nc, smeared}$ with the experimental counterpart $C_{l_{\text{gust}}}^{nc}$ (red circles), which also features in figure 8.14. The latter is calculated from the measured flow field as described in section 8.2.3 and is only computed for gust entry. During gust exit, significant amounts of shear layer and cylinder-shed vorticity leave the field of view, making a force computation no longer possible. For the lowest gust ratio, the experimental force tracks the theoretical force history well, as the cylinder enters the gust. A discrepancy appears when the cylinder has supposedly fully entered the gust according to the Küssner's model at $x/D > 1.25$. The theoretical non-circulatory force has now vanished, whilst $C_{l_{\text{gust}}}^{nc}$ remains non-zero. A similar effect can be seen for the two higher gust ratios. $C_{l_{\text{gust}}}^{nc}$ persists for substantially longer compared to $C_{l_{\text{Küssner}}}^{nc, smeared}$ and also reaches a lower peak force.² The discrepancy between the forces arises, even though the measured and theoretical non-circulatory gust vortex sheets are identical once the cylinder is fully inside the gust as discussed in section 8.3.1. The difference in force must therefore come from a slower growth rate of $\gamma_{\text{gust}}^{nc}$. As the cylinder enters and distorts the gust, the transverse flow is disrupted and the cylinder effectively sees a more gradual entry into the gust. A natural consequence of this is that it takes $\gamma_{\text{gust}}^{nc}$ longer to develop to its final state and thereby limits the rate of change of the impulse created by $\gamma_{\text{gust}}^{nc}$. As a result the force peak is reduced and spread out over a larger translation distance.

Viewing the contribution of the non-circulatory force component in the context of the total force acting on the cylinder offers insight into its relative impact on the overall gust encounter. From this it can be seen, that very early on when the cylinder has just entered the gust, the total force is governed by the non-circulatory force component. However, as soon as vorticity sheds, the associated force contribution begins to dominate the response and the total force considerably exceeds the non-circulatory component. When the cylinder experiences the peak force, $C_{l_{\text{gust}}}^{nc}$ contributes of the order of 10 - 20 % to the total force, whilst the theoretical contribution has returned to zero by this point. Even though $C_{l_{\text{gust}}}^{nc}$ is therefore not entirely negligible, the vast majority of the force is created by cylinder-shed vorticity. It therefore appears sensible to suggest that more time should be devoted to accurately modelling the circulatory force contribution rather than capturing the influence of gust distortion, since the effects due to gust shear layer deflection are only of secondary importance.

²The 'waviness' in the experimental force comes from the contribution created by the rate of change of the gust vortex sheet. Due to the experimental nature of the measurements, and their sensitivity to correctly associating vorticity with the gust and the cylinder, errors can arise whilst the cylinder intersects the gust shear layers. The force results should therefore not be taken as an exact quantitative result but rather as a qualitative indication of the development.

8.4 Summary: Cylinder-Gust Encounter

Significant forces can develop when an object enters a transverse gust. Küssner developed a simplified force prediction by reducing the complexity of the flow field and representing the gust through a sharp edged, top-hat shaped velocity distribution with infinitely thin and rigid shear layers. Using the methodology developed in chapter 7, making it possible to attribute a force contribution to a particular flow feature, the chapter assessed Küssner's model to better understand what the consequences of the rigid gust assumption are. To this end, a cylinder-gust encounter of varying strengths is investigated.

By applying potential flow concepts and assuming two rigid gust shear layers, a theoretical non-circulatory gust vortex sheet, located on the cylinder surface, can be calculated. The presence of this vortex sheet is experimentally confirmed for all three gust ratios studied and its origin is attributed to vorticity residing within the gust shear layers. To correctly calculate the theoretical non-circulatory gust force created during gust entry (and exit), the volume of the cylinder needs to be accounted for. This is because the rigid gust shear layer assumption otherwise incorrectly enforces that all of the transverse gust momentum inside the region occupied by the cylinder is lost, and thereby leads to an over estimation of the force.

Comparing the theoretical force predictions to measurements of the equivalent non-circulatory gust force indicates that shear layer deflection reduces the non-circulatory gust force and prolongs the time over which it acts. This appears to be because gust distortion reduces the growth rate of the non-circulatory gust vortex sheet, which therefore takes significantly longer to develop to its final state. Depending on the required accuracy of a low order model, gust distortion may therefore need to be accounted for. However it should be noted that the majority of the force still comes from the circulatory contribution created by cylinder-shed vorticity. It may therefore prove to be more beneficial to devote resources to getting this correct, rather than to account for gust shear layer deflection.

Chapter 9

Conclusions and Future Work

9.1 General Comments

The aim of this work is to facilitate the development of low order models (LOMs) for unsteady low Reynolds number flow. Many LOMs split the force into simple more tractable problems, which they solve independently and superpose thereafter. In general, the force can be related to the rate of change in strength and relative motion of vorticity, where the vorticity can be bound to the surface of an object or freely moving in the flow field. The literature review revealed that despite the fact that identifying the origin and behaviour of this vorticity is crucial for an accurate force estimation, limited understanding of the underlying flow physics regarding its development exists. Boundary layer vorticity is found to be composed of numerous independent contributions, however, no assessment of these has been made for bodies of volume in viscous flow. Moreover, there remains some ambiguity about the true origin of the vortex sheet when it is the fluid, rather than the body, accelerating or similarly, when the flow field is occupied by vorticity which is not shed from the body itself. In addition, even though the boundary layer is explicitly or implicitly used to predict the position of unsteady separation as well as the rate at which vorticity is shed, factors affecting the evolution of the boundary layer vorticity are not fully understood. Furthermore, although LOMs ideally only include the most dominant flow physics to save time, there is a lack in ability to identify how much a single flow feature contributes to the force, which would otherwise enable an informed decision as to which flow structures to include and which to neglect.

To provide insight into these areas of low Reynolds number fluid mechanics, experiments were performed in the towing tank facilities at the University of Cambridge. To create a range of unsteady flows around a lifting body with volume, a translating and rotating circular cylinder was used. Its constant surface curvature creates a dynamically changing unsteady separation point, whilst its thickness enables an assessment of body volume effects. In addition, an accelerating fluid around a stationary flat plate was recreated in the towing tank to further assess the creation of boundary layer vorticity. Ultimately, the cylinder is augmented with a flat plate wing as well as subjected to a sharp

edged top-hat shaped gust encounter to provide insight into unsteady force generation. The Reynolds numbers for all experiments are between 4000 and 20000.

9.2 Boundary Layer and Free Vorticity

Boundary layer vorticity is integral for the prediction of the unsteady separation point as well as the rate at which vorticity is released into the flow. Further yet, its variation equally affects the force. To therefore gain a better understanding of its evolution globally as well as at the unsteady separation point, its development around a stationary flat plate immersed in a moving freestream and around a translating and rotating cylinder is investigated in chapter 4. The key findings from this are:

- The vortex sheet contribution created by an accelerating freestream on a stationary flat plate, although identical in shape to the added mass vortex sheet seen when the plate accelerates in a quiescent fluid, forms as a result of external vorticity created at the interface of the moving external flow and its surrounding. Externally created vorticity therefore equally contributes to the boundary layer vortex sheet and a clear distinction between the added mass vortex sheet due to translation and the contribution due to an accelerating freestream must be made, as to avoid double counting this component.
- The vortex sheet contributions around a rotating and translating circular cylinder are identified in viscous flow, thereby verifying that grouping boundary layer vorticity according to individual contributions is equally valid for bodies of volume as it is for idealized infinitely thin objects. The evolution of the total boundary layer vortex sheet can therefore be traced back to the development of its constituent parts, originating from motion kinematics and free vorticity.
- The vortex sheet contribution due to free vorticity is proposed to be split into a local and far-field component. The far-field contribution grows in time as vorticity accumulates far away from the cylinder and is responsible for a uniform shift of the total vortex sheet forming around the circular cylinder. Normalising the vortex sheet by instantaneous velocity and removing the contribution due to far-field vorticity causes the adjusted vortex sheet to remain largely invariant upstream of the separation point as the unsteady flow field develops.
- A similar invariance is observed for the vortex sheet strength at the unsteady separation point. By further removing the vortex sheet contribution due to rotation, the strength at the separation point collapses for all investigated cylinder kinematics, as long as no second vortex is shed from the same side. This invariance of the *adjusted* vortex sheet strength indicates that the most dominant factors affecting boundary layer vorticity are identified. Moreover, the variation in the raw vortex sheet strength at the separation point further suggests that it cannot be used as an indicator for unsteady separation.

Any vorticity that has been shed into the flow field must have originated from a surface boundary layer. Chapter 5 therefore explored the link between the rate at which vorticity sheds and the boundary layer vortex sheet contributions, where the main results are:

- The vorticity flux of the boundary layer can be expressed in terms of the individual vortex sheet contributions. From this it can be deduced, that the rate at which vorticity sheds is proportional to the difference between the total boundary layer vortex sheet and the rotational component at the separation point. Alternatively, the vorticity shedding rate is proportional to the strength of the vortex sheet due to translation and free vorticity at the point of separation.
- When the unsteady separation point is known, the rate at which vorticity is shed can therefore be predicted by any potential flow model as well as from experimental measurements of the boundary layer vortex sheet. In turn and the opposite way round, the strength of the boundary layer vortex sheet at the separation point can be estimated by measuring the rate at which vorticity sheds.
- Variations in the rate at which vorticity is shed as the flow field evolves, can be explained by changes in strength of the boundary layer vortex sheet contributions. Whilst acceleration leads to an increased shedding rate, vorticity of the same sign as that being shed populating the far-field, has the opposite effect.

Chapter 6 discussed the real world implications of the findings regarding vortex sheet and vorticity shedding rate development. In particular it was noted that:

- The alternate vortex shedding pattern, often observed behind bluff bodies, can be explained through a vortex sheet perspective. The cyclic shedding pattern can be linked to the effect that an imbalance of positive and negative vorticity, residing in the far-field, has on the boundary layer vortex sheet. This net difference in far-field vorticity alternately increases the vorticity shedding rate from one side of the cylinder, whilst simultaneously decreases it from the other, thereby creating the commonly observed alternate vortex shedding pattern.
- The unsteady force development is similarly affected by an imbalance of positive and negative shed vorticity. Moreover, Prandtl's theoretical maximum force for a spinning and translating cylinder can equally be recovered using a vortex sheet approach.

9.3 Unsteady Force Response

LOMs used for gust mitigation must not only accurately predict the force but they must likewise be able to do this in real time. It is therefore crucial, that their computational effort is reduced to a minimum. This can be achieved by only modelling the flow physics that most strongly contribute to the force. To help determine how much a single flow feature affects the force, chapter 7 outlines a

methodology that approximates the force due to an individual flow structure by analyzing the vorticity field, making it possible to quantitatively assess whether it must be included in the LOM.

- To a first order, the force acting on an object, due to a surrounding flow structure, is a function of the rate of change of the boundary layer vortex sheet created on the object by this flow structure as well as by how much the flow feature is advected by the velocity induced by the objects boundary layer.

Chapter 8 builds on these findings and explores a cylinder sharp-edged transverse gust encounter. Particularly, the chapter focuses on the rigid gust shear layer assumption that is part of Küssners model. The main conclusions are:

- The rigid gust shear layer assumption requires Küssners theoretical non-circulatory gust force to be modified for bodies of finite thickness, since it otherwise significantly overestimates the force.
- Shear layer deflection changes the non-circulatory force acting on the cylinder, especially when the gust ratio is high. At the same time, the relative importance of the non-circulatory force was found to reduce as the gust ratio increases. This suggests that ‘correcting’ the non-circulatory gust force by accounting for shear layer deflection may be less crucial than accurately modelling the force due to shed vorticity.

9.4 Recommendations and Future Work

A key finding from this thesis is that the *adjusted* vortex sheet strength at the unsteady separation point on a circular cylinder remains constant as the flow field develops and for different kinematic cases. However, there is missing physical understanding as to why this is the case. An avenue for future work could therefore be to explore this further, in order to gain a better insight into the physical mechanisms at play. Furthermore, a parametric study assessing whether this observation carries forward to different geometries and flow fields would also be beneficial.

In regards to the examined transverse gust encounter of the circular cylinder, it was noted that whilst gust distortion affected the non-circulatory gust force, the overall impact on the force was comparatively small. Here, it could be of interest to explore how gust distortion affects the force development on an entering lifting wing, since significant gust distortion could be expected here and this would perhaps also be more representative of an actual gust encounter experienced in real life. Furthermore, the force analysis could be extended to vortical gusts, where a flow disturbance is created by a passing vortex. By using the proposed methodology discussed in chapter 7, assessing the impact of an individual flow structure on the force, it could be explored whether the mutual interaction between a wing and a vortical gust significantly changes the force and whether this effect

must therefore be included in an LOM.

In summary, the work presented here can hopefully be combined in future to advance the development of novel LOMs. By understanding better what influences boundary layer vorticity globally as well as at the separation point, improved methods to predict unsteady separation can perhaps be developed. In addition, rather than guessing which flow features are important and need to therefore be included in an LOM, a quantitative assessment of the flow now allows for a detailed analysis to determine which flow structures dominate the force response and which are negligible. These stepping stones therefore aim to remove some of the guess work when developing LOMs and hope to enable a more targeted and time-efficient approach.

There is still a long way to go before we can confidently navigate unsteady flows, however, every new piece of information helps us move on step further away from the first human flight of Otto Lilienthal and closer to the aerodynamic designs of the future, for which I hope that this work has played its small, yet informative, part.

References

- [1] Adrian, R. J. and Westerweel, J. (2011). *Particle Image Velocimetry*. Cambridge University Press.
- [2] Akkala, J. M. and Buchholz, J. H. J. (2017). Vorticity Transport Mechanisms Governing the Development of Leading-Edge Vortices. *Journal of Fluid Mechanics*, 829:512–537.
- [3] Anderson, J. D. (2010). *Fundamentals of Aerodynamics*. Tata McGraw-Hill Education, London.
- [4] Andreu-Angulo, I., Babinsky, H., Biler, H., Sedky, G., and Jones, A. R. (2020). Effect of Transverse Gust Velocity Profiles. *AIAA Journal*, 58(12):5123–5133.
- [5] Badr, H. M., Coutanceau, M., Dennis, S. C. R., and Ménard, C. (1990). Unsteady Flow Past a Rotating Circular Cylinder at Reynolds Numbers $10e3$ and $10e4$. *Journal of Fluid Mechanics*, 220:459.
- [6] Badr, H. M. and Dennis, S. C. R. (1985). Time-Dependent Viscous Flow Past an Impulsively Started Rotating and Translating Circular Cylinder. *Journal of Fluid Mechanics*, 158(-1):447.
- [7] Bai, C., Li, J., and Wu, Z. (2014). Generalized Kutta-Joukowski Theorem for Multi-Vortex and Multi-Airfoil Flow with Vortex Production - A General Model. *Chinese Journal of Aeronautics*, 27(5):1037–1050.
- [8] Bennett, L. (1970). Insect Flight: Lift and Rate of Change of Incidence. *Science*, 167(3915):177–179.
- [9] Bisplinghoff, R. L., Ashley, H., and Halfman, R. L. (1955). *Aeroelasticity*. Addison-Wesley series in mechanics. Addison-Wesley, Cambridge, MA.
- [10] Blevins, R. D. (1977). *Flow-Induced Vibration*. van Nostrand Reinhold, New York.
- [11] Brennen, C. E. (1982). A Review of Added Mass and Fluid Inertial Forces. *Ocean Engineering*, (January):50.
- [12] Burgess, M. (2016). Facebook’s Aquila Drone Crash Landed because it was too Windy.
- [13] Cavaliere, L. A. (1992). The Wright brother’s Odyssey: Their Flight of Learning. *New Directions for Adult and Continuing Education*, 1992(53):51–59.
- [14] Corkery, S. J. (2019). *Unsteady Aerodynamics of Wing Gust Encounters*. Phd thesis, University of Cambridge.
- [15] Corkery, S. J. and Babinsky, H. (2019). An Investigation into the Added Mass Force for a Transverse Wing-Gust Encounter. *AIAA Scitech 2019 Forum*.
- [16] Corkery, S. J., Babinsky, H., and Graham, W. R. (2019). Quantification of Added-Mass Effects Using Particle Image Velocimetry Data for a Translating and Rotating Flat Plate. *Journal of Fluid Mechanics*, 870:492–518.

- [17] Coutanceau, M. and Menard, C. (1985). Influence of Rotation on the Near-Wake Development Behind an Impulsively Started Circular Cylinder. *J. Fluid Mech*, 158:399–446.
- [18] Darwin, C. (1953). Note on Hydrodynamics. *Mathematical Proceedings of the Cambridge Philosophical Society*, 49(2):342–354.
- [19] Deparday, J. and Mulleners, K. (2019). Modeling the Interplay Between the Shear Layer and Leading Edge Suction During Dynamic Stall. *Physics of Fluids*, 31(10).
- [20] Didden, N. (1979). On the Formation of Vortex Rings: Rolling-up and Production of Circulation. *Journal of Applied Mathematics and Physics (ZAMP)*, 30.
- [21] Durand, W. F. (1935a). *Aerodynamic Theory: General Aerodynamic Theory*. Springer, Berlin.
- [22] Durand, W. F. (1935b). *Aerodynamic Theory: General Aerodynamic Theory*. Springer, Berlin.
- [23] Eldredge, J. D. (2010). A Reconciliation of Viscous and Inviscid Approaches to Computing Locomotion of Deforming Bodies. *Experimental Mechanics*, 50(9):1349–1353.
- [24] Eldredge, J. D. (2019). *Mathematical Modeling of Unsteady Inviscid Flows*. Springer.
- [25] Eldredge, J. D. and Jones, A. R. (2019). Leading-Edge Vortices: Mechanics and Modeling. *Annual Review of Fluid Mechanics*, 51(1):75–104.
- [26] Fage, A. and Johansen, F. C. (1927). On the Flow of Air behind an Inclined Flat Plate of Infinite Span.
- [27] Farren, W. S. (1935). Reaction on a Wing Whose Angle of Incidence is Changing Rapidly. Technical report, London.
- [28] Francis, R. H. and Cohen, J. (1933). The Flow Near a Wing which Starts Suddenly from Rest and then Stalls. *Rep Memo Aeronaut Res Comm*, 1561.
- [29] Garrick, I. E. (1936). Propulsion of a Flapping and Oscillating Airfoil. Technical report.
- [30] Goldstein, S. (1938). *Modern Developments in Fluid Dynamics: an Account of Theory and Experiment Relating to Boundary Layers, Turbulent Motion and Wakes*. Clarendon Press.
- [31] Graham, W. R., Pitt Ford, C. W., and Babinsky, H. (2017). An Impulse-Based Approach to Estimating Forces in Unsteady Flow. *Journal of Fluid Mechanics*, 815:60–76.
- [32] Grasmeyer, J. M. and Keennon, M. T. (2001). Development of the Black Widow Micro Air Vehicle. *39th Aerospace Sciences Meeting and Exhibit*, (January).
- [33] Green, G. (1835). Researches on the Vibration of Pendulums in Fluid Media. *Transactions of the Royal Society of Edinburgh*, 13(1):54–62.
- [34] He, X. and Williams, D. R. (2020). Unsteady Aerodynamic Loads on an Airfoil at High Angle of Attack in a Randomly Surging Flow. *AIAA Scitech 2020 Forum*, (January).
- [35] Hodara, J., Lind, A. H., Jones, A. R., and Smith, M. J. (2016). Collaborative Investigation of the Aerodynamic Behavior of Airfoils in Reverse Flow. *Journal of the American Helicopter Society*, 61(3):1–15.
- [36] Johnson, W. (1986). The Magnus Effect-Early Investigations and a Question of Priority. *International Journal of Mechanical Sciences*, 28(12):859–872.

- [37] Jones, A. R. and Babinsky, H. (2011). Reynolds Number Effects on Leading Edge Vortex Development on a Waving Wing. *Experiments in Fluids*, 51(1):197–210.
- [38] Kang, L. L., Liu, L. Q., Su, W. D., and Wu, J. Z. (2018). Minimum-Domain Impulse Theory for Unsteady Aerodynamic Force. *Physics of Fluids*, 30:016107.
- [39] Keennon, M., Klingebiel, K., Won, H., and Andriukov, A. (2012). Development of the Nano Hummingbird: A Tailless Flapping Wing Micro Air Vehicle. *50th AIAA Aerospace Sciences Meeting Including the New Horizons Forum and Aerospace Exposition*, (January):1–24.
- [40] Kelvin, L. (1869). On Vortex Motion. *Trans. Roy. Soc. Edinb.*, 25:217–260.
- [41] Kramer, V. M. (1932). Die Zunahme des Maximalauftriebes von Tragflugeln bei plotzlicher Anstellwinkervergrosserung (Boeneffekt). *Z. Flugtech. Motorluftschiff*, 23:185–189.
- [42] Kravchenko, S. A. (1995). Wing Tip Lifting Surfaces: Aerodynamic Design and Comparative Analysis. *Aircraft Engineering, Technology, and Operations Congress*.
- [43] Küssner, H. G. (1932). Stresses produced in Airplane Wings by Gusts. *National Advisory Committee for Aeronautics*, 654.
- [44] Küssner, H. G. (1936). Untersuchung der Bewegung einer Platte beim Eintritt in eine Strahlgrenze. *Zentrale für techn.-wiss. Berichtswesen*, 13:425–429.
- [45] Lam, K. M. (2009). Vortex Shedding Flow Behind a Slowly Rotating Circular Cylinder. *Journal of Fluids and Structures*, 25(2):245–262.
- [46] Lamb, H. (1932). *Hydrodynamics*.
- [47] Lee, T. and Gerontakos, P. (2006). Effect of Winglet Dihedral on a Tip Vortex. *Journal of Aircraft*, 43(1):117–124.
- [48] Leishman, G. J. (2006). *Principles of Helicopter Aerodynamics*. Cambridge University Press, New York, 2 edition.
- [49] Li, J. and Wu, Z. N. (2018). Vortex Force Map Method for Viscous Flows of General Airfoils. *Journal of Fluid Mechanics*, 836:145–166.
- [50] Li, Z.-y., Feng, L.-h., Kissing, J., and Tropea, C. (2020). Experimental Investigation on the Leading-Edge Vortex Formation and Detachment Mechanism of a Pitching and Plunging Plate. *J. Fluid Mech.*, 901:A17.
- [51] Lighthill, J. (1986). *An Informal Introduction to Theoretical Fluid Mechanics*. Oxford University Press, New York.
- [52] Lilienthal, O. (1896). Practical Experiments for the Development of Human Flight. *The Aeronautical Annual*, pages 7–20.
- [53] Lissaman, P. B. S. (1983). Low-Reynolds-Number Airfoils. pages 223–239.
- [54] Magnus, G. (1852). On the Deflection of a Projectile. *Abhandlungen der Akademie der Wissenschaften, Berlin, Germany*.
- [55] Martín-Alcántara, A., Sanmiguel-Rojas, E., and Fernandez-Feria, R. (2015). On the Development of Lift and Drag in a Rotating and Translating Cylinder. *Journal of Fluids and Structures*, 54:868–885.

- [56] Martínez-Muriel, C. and Flores, O. (2020). Analysis of Vortical Gust Impact on Airfoils at Low Reynolds Number. *Journal of Fluids and Structures*, 99:103138.
- [57] Mathioulakis, D. S. and Telionis, D. P. (1987). Velocity and Vorticity Distributions in Periodic Separating Laminar Flow. *Journal of Fluid Mechanics*, 184:303–333.
- [58] Matsumoto, M. (1999). Vortex Shedding of Bluff Bodies: a Review. *Journal of Fluids and Structures*, 13(7-8):791–811.
- [59] Melius, M. S., Mulleners, K., and Cal, R. B. (2018). The Role of Surface Vorticity During Unsteady Separation. *Physics of Fluids*.
- [60] Milne-Thomson, L. M. (1996). *Theoretical Hydrodynamics*. Courier Corporation.
- [61] Mittal, S. and Kumar, B. (2003). Flow Past a Rotating Cylinder. *Journal of Fluid Mechanics*, 476(476):303–334.
- [62] Mohamed, A., Abdulrahim, M., Watkins, S., and Clothier, R. (2016). Development and Flight Testing of a Turbulence Mitigation System for Micro Air Vehicles. *Journal of Field Robotics*, pages 639–660.
- [63] Moore, F. K. (1958). On the Separation of the Unsteady Laminar Boundary Layer. In *Grenzschichtforschung/Boundary Layer Research*, pages 296–311. Springer.
- [64] Nobach, H. and Bodenschatz, E. (2009). Limitations of Accuracy in PIV due to Individual Variations of Particle Image Intensities. *Experiments in Fluids*, 47(1):27–38.
- [65] Noca, F., Shiels, D., and Jeon, D. (1997). Forces on Bodies , Using Only Velocity. *Journal of Fluids and Structures*, 11:345–350.
- [66] Noca, F., Shiels, D., and Jeon, D. (1999). A Comparison of Methods for Evaluating Time-Dependent Fluid Dynamic Forces on Bodies, using only Velocity Fields and their Derivatives. *Journal of Fluids and Structures*, 13(5):551–578.
- [67] Padrino, J. C. and Joseph, D. D. (2006). Numerical Study of the Steady-State Uniform Flow Past a Rotating Cylinder. *Journal of Fluid Mechanics*, 557:191–223.
- [68] Perry, A. E., Chong, M. S., and Lim, T. T. (1982). The Vortex-Shedding Process Behind Two-Dimensional Bluff Bodies. *Journal of Fluid Mechanics*, 116:77–90.
- [69] Pitt Ford, C. W. (2013). *Unsteady Aerodynamic Forces on Accelerating Wings at Low Reynolds Numbers*. Phd thesis, University of Cambridge.
- [70] Prandtl, L. (1904). Über Flüssigkeitsbewegung bei sehr kleiner Reibung. In *Verhandl. III, Internat. Math.-Kong., Heidelberg, Teubner, Leipzig*, pages 484–491.
- [71] Prandtl, L. (1926). Application of the "Magnus Effect" of the Wind Propulsion of Ships. *National Advisory Commitee For Aeronautics*.
- [72] Raffel, M., Willert, C. E., Wereley, S. T., and Kompenhans, J. (1998). *Particle Image Velocimetry - A Practicle Guide*. Springer, 1 edition.
- [73] Ramanathan, H., Narsipur, S., and Gopalarathnam, A. (2019). Boundary-Layer Characteristics at the Onset of Leading-Edge Vortex Formation on Unsteady Airfoils. *AIAA Aviation 2019 Forum*, (June):1–12.

- [74] Ramesh, K. (2020). On the Leading-Edge Suction and Stagnation-Point Location in Unsteady Flows Past Thin Aerofoils. *Journal of Fluid Mechanics*, 886.
- [75] Ramesh, K., Gopalarathnam, A., Granlund, K., Ol, M. V., and Edwards, J. R. (2014). Discrete-Vortex Method with Novel Shedding Criterion for Unsteady Aerofoil Flows with Intermittent Leading-Edge Vortex Shedding. *Journal of Fluid Mechanics*, 751:500–538.
- [76] Ramesh, K., Granlund, K., Ol, M. V., Gopalarathnam, A., and Edwards, J. R. (2018). Leading-Edge Flow Criticality as a Governing Factor in Leading-Edge Vortex Initiation in Unsteady Airfoil Flows. *Theoretical and Computational Fluid Dynamics*, 32(2):109–136.
- [77] Rival, D. E. and van Oudheusden, B. (2017). Load-Estimation Techniques for Unsteady Incompressible Flows. *Experiments in Fluids*, 58(3):1–11.
- [78] Roberts, S. C. (1966). An Investigation of End Plates to Reduce the Drag of Planar Wings. *USAAVLABS TECHNICAL REPORT*, pages 65–79.
- [79] Roshko, A. (1961). Experiments on the Flow Past a Circular Cylinder at Very High Reynolds Number. *J. Fluid Mech.*, pages 345–356.
- [80] Rott, N. (1956). Unsteady Viscous Flow in the Vicinity of a Stagnation Point. *Quarterly of Applied Mathematics*, 13(4):444–451.
- [81] Saffman, P. G. (1992). *Vortex Dynamics*. Cambridge University Press.
- [82] Saffman, P. G. and Schatzman, J. C. (1982). An Inviscid Model for the Vortex-Street Wake. *Journal of Fluid Mechanics*, 122:467–486.
- [83] Sane, S. P. and Dickinson, M. H. (2001). The Control of Flight Force by a Flapping Wing: Lift and Drag Force Production. *Journal of Experimental Biology*, 204:2607–2626.
- [84] Sarpkaya, T. (1975). An Inviscid Model of Two Dimensional Vortex Shedding for Transient and Asymptotically Steady Separated Flow over a Cylinder. 6.
- [85] Sarpkaya, T. and Isaacson, M. (1981). *Mechanics of Wave Forces on Offshore Structures*. New York: van Nostrand Reinhold, New York.
- [86] Sears, W. R. and Telionis, D. P. (1975). Boundary-Layer Separation in Unsteady Flow. *SIAM Journal on Applied Mathematics*, 28(1):215–235.
- [87] Seifert, J. (2012). A Review of the Magnus Effect in Aeronautics. *Progress in Aerospace Sciences*, 55:17–45.
- [88] Shumway, N. M. and Jones, A. R. (2020). The Initial Growth of Normalized Circulation of the Leading-Edge Vortex on Surging and Rotating Wings. *AIAA Scitech 2020 Forum*, 1 PartF(January):1–12.
- [89] Smith, M. J., Komerath, N., Ames, R., Wong, O., and Pearson, J. (2001). Performance Analysis of a Wing with Multiple Winglets. *19th AIAA Applied Aerodynamics Conference*, (June).
- [90] Stevens, P. R. R. J. (2015). *Unsteady Low Reynolds Number Aerodynamic Forces*. Phd thesis, University of Cambridge.
- [91] Stevens, P. R. R. J. and Babinsky, H. (2017). Experiments to Investigate Lift Production Mechanisms on Pitching Flat Plates. *Experiments in Fluids*, 58(1):1–17.
- [92] Thompson, L. M. M. (1968). *Theoretical Hydrodynamics*. Macmillan, New York, 5 edition.

- [93] Thouault, N., Breitsamter, C., Adams, N., Seifert, J., Badalamenti, C., and Prince, S. (2012). Numerical analysis of a rotating cylinder with spanwise disks. *AIAA Journal*, 50(2):1–14.
- [94] Thwaites, B. (1949). Approximate Calculation of the Laminar Boundary Layer. *Aeronautical Quarterly*, pages 245–280.
- [95] Tokumaru, P. T. and Dimotakis, P. E. (1993). The Lift of a Cylinder Executing Rotary Motions in a Uniform Flow. *Journal of Fluid Mechanics*, 255(1993):1–10.
- [96] von Karman, T. and Sears, W. R. (1938). Airfoil Theory for Non-Uniform Motion. *Journal of the Aeronautical Sciences*, 5.
- [97] Walshe, D. E. J. (1972). *Wind-Excited Oscillation of Structures*. H.M. Stationary Office.
- [98] Watkins, S., Milbank, J., Loxton, B. J., and Melbourne, W. H. (2006). Atmospheric Winds and Their Implications for Microair Vehicles. *AIAA Journal*, 44(11):2591–2600.
- [99] Watkins, S., Thompson, M., Loxton, B., and Abdulrahim, M. (2010). On Low Altitude Flight Through The Atmospheric Boundary Layer. *International Journal of Micro Air Vehicles*, 2(2):55–68.
- [100] Whitcomb, R. T. (1976). A Design Approach and Selected Wind Tunnel Results at High Subsonic Speeds for Wing-Tip mounted Winglets. *Nasa Tn D-8260*, (July):1–33.
- [101] White, C., Lim, E. W., Watkins, S., Mohamed, A., and Thompson, M. (2012). A Feasibility Study of Micro Air Vehicles Soaring Tall Buildings. *Journal of Wind Engineering and Industrial Aerodynamics*, 103:41–49.
- [102] Widmann, A. and Tropea, C. (2015). Parameters Influencing Vortex Growth and Detachment on Unsteady Aerodynamic Profiles. *Journal of Fluid Mechanics*, 773:432–459.
- [103] Wieneke, B. (2015). PIV Uncertainty Quantification from Correlation Statistics. *Measurement Science and Technology*, 26(7):074002.
- [104] Wienke, F., Raffel, M., and Dillmann, A. (2021). Wind-Tunnel Testing of Otto Lilienthal’s Production Aircraft from 1893. *AIAA Journal*, 59(4):1342–1351.
- [105] Wojcik, C. J. and Buchholz, J. H. (2014). Vorticity Transport in the Leading-Edge Vortex on a Rotating Blade. *Journal of Fluid Mechanics*, 743:249–261.
- [106] Wong, J. G. and Rival, D. E. (2015). Determining the Relative Stability of Leading-Edge Vortices on Nominally Two-Dimensional Flapping Profiles. *Journal of Fluid Mechanics*, 766:611–625.
- [107] Wu, J. C. (1981). Theory for Aerodynamic Force and Moment in Viscous Flows. *AIAA Journal*, 19(4):432–441.
- [108] Wu, J. C. (2018). *Elements of Vorticity Aerodynamics*. Springer.
- [109] Xia, X. and Mohseni, K. (2017). Unsteady Aerodynamics and Vortex-Sheet Formation of a Two-Dimensional Airfoil. *Journal of Fluid Mechanics*, 830:439–478.

Appendix A

Reconciling Force Calculations with Legacy Theory

This appendix aims to relate the proposed force calculation discussed in Chapter 7 with some common theoretical results.

A.1 Steady Flow: Kutta-Joukowski Lift

Although equation 7.15 is intended for unsteady flow, it must also be applicable to steady flow. As such, two steady-state flow fields are considered. Imagine a cylinder translating from right to left at a steady velocity in quiescent fluid, with the starting vortex infinitely far away. Alternatively, the cylinder is stationary in a uniform freestream with the starting vortex advecting at constant velocity.

The lift force in the first example is easily calculated. The strength of the starting vortex is Γ_∞ . In turn the boundary layer circulation is $-\Gamma_\infty$. The u -velocity component induced on the starting vortex by the boundary layer approaches zero, as the vortex is located infinitely far away. Thus, if the cylinder is translating at a velocity U_∞ , then using equation 7.15, the Kutta-Joukowski lift is recovered, $L = -\rho\Gamma_\infty U_\infty$.

The more interesting example may therefore perhaps be the case of a stationary cylinder immersed in a uniform steady-state freestream. Initially, one may worry that this violates a core assumption in the impulse formulation; that requires the velocity at the boundary of the domain to approach zero. However, the uniform flow in the vicinity of the cylinder could be created by two external point vortices located far away, as shown in figure A.1. If the boundary B_L is sufficiently far away, the induced velocity therefore again, approaches zero on B_L , thus complying with all assumptions made

by Wu [107]. The u -velocity component of two external vortices located at η along the y -axis is

$$U(y) = \frac{\Gamma_{ext}}{\pi} \left(\frac{\eta}{\eta^2 - y^2} \right). \quad (\text{A.1})$$

The strength of a pair of external vortices located at infinity required to induce a velocity U at $y = 0$ is therefore

$$\Gamma_{ext} = \pm\pi\eta U. \quad (\text{A.2})$$

We now assume a flow field that consists of two such external vortices that induce a velocity U along $y = 0$. A body residing in the flow field has shed a vortex of strength Γ_∞ which is located at infinity and is advecting at a constant velocity. No more vorticity is shed thereafter. The bound circulation of the body is therefore of strength $-\Gamma_\infty$ and uniformly distributed about the body surface. The flow field is schematically illustrated in figure A.1.

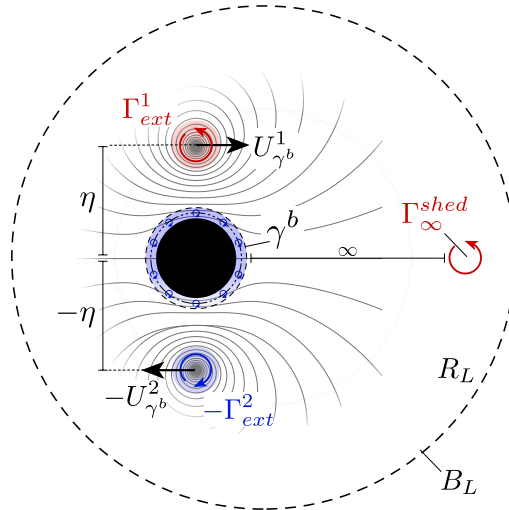


Fig. A.1 Schematic illustration of the steady-state flow field. A single vortex has been shed to infinity and a uniform freestream is induced by two external vortices.

To compute the force acting on the body, equation 7.15 is used. The boundary layer strength remains constant, therefore, does not contribute to the force. Similarly, the force due to advection of the shed vortex by the cylinder boundary layer is also zero, as the induced velocity approaches zero. The induced velocity at the external vortices by the boundary layer is

$$U_{\gamma^b} = \frac{\Gamma_\infty}{2\pi\eta}. \quad (\text{A.3})$$

The force due to the advection of the two external vortices by the boundary layer therefore is

$$\begin{aligned} L &= \rho \left(U_{\gamma^b}^1 \Gamma_{ext}^1 + U_{\gamma^b}^2 \Gamma_{ext}^2 \right) \\ &= -\rho \left(\frac{\Gamma_\infty}{2\pi\eta} \pi\eta U + \frac{\Gamma_\infty}{2\pi\eta} \pi\eta U \right). \end{aligned} \quad (\text{A.4})$$

Equation A.4 simplifies to

$$L = -\rho \Gamma_\infty U \quad (\text{A.5})$$

and thus recovers the expected Kutta-Joukowski lift formulation.

A.2 Accelerating Flow

A further flow scenario is that of a stationary body in an accelerating fluid. Without loss of generality, the freestream is once more assumed to be created through a pair of external point vortices, as schematically shown in figure A.2.

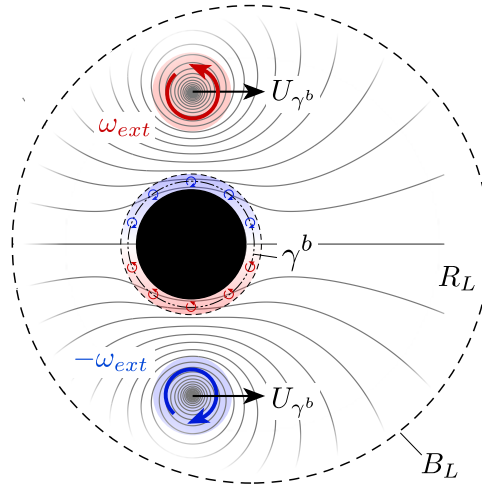


Fig. A.2 Schematic illustration of the flow field due to an external vortex pair that induces uniform freestream at the location of the cylinder.

The two external vortices and their mirror images result in a vortex sheet distribution,

$$\gamma^b = \gamma^{ext} = -2U \sin \theta. \quad (\text{A.6})$$

$\gamma^b = \gamma^{ext}$ since there is no further vorticity in the flow field, and the cylinder is stationary. As the external vortices grow in strength, the uniform freestream accelerates and γ^b grows. This results in a

force. Using the vortex sheet distribution, the impulse

$$I_x = \oint y \gamma^b dl \quad (\text{A.7})$$

can be obtained, where dl is the element length of the vortex sheet. Since $y = a \sin \theta$ and $dl = a d\theta$, the impulse is

$$I_x = a^2 \oint_0^{2\pi} \gamma^b \sin \theta d\theta. \quad (\text{A.8})$$

Substituting γ^b , equation A.6, into equation A.8 and evaluating the integral gives

$$I_x = -2\pi U a^2. \quad (\text{A.9})$$

The drag force acting on the cylinder can now be found by using equation 7.15 together with impulse I_x given by equation A.9,

$$\begin{aligned} F_x &= -\rho \frac{dI_x}{dt} + \rho \int_{R_L} V_{\gamma^b} \omega^{ext} dR + \rho \frac{d}{dt} \int_{R_b} U_b dR \\ &= 2\rho \pi a^2 \frac{dU}{dt}. \end{aligned} \quad (\text{A.10})$$

The second term on the first row goes to zero since the cylinder boundary layer induces zero vertical velocity onto the two external vortices and the third term is equally zero since the cylinder is stationary. As such, equation A.10 recovers the same drag force acting on the cylinder that is otherwise obtained when solving the unsteady Bernoulli's equation for the pressure on the body surface [14].

The current and preceding section therefore show that it makes no difference when implementing the impulse formulation whether the body or flow are accelerating. Furthermore, the flow field can uniquely be described only in terms of vorticity. Therefore, when calculating the force, equation 7.15 can be used with no further components due to a freestream or an added mass force that need to be added. This reduces the risk of double counting a force contribution by mistake.